FREE-SURFACE TURBULENT SHEAR FLOWS

Thesis by

Patrice M. Maheo

In Partial Fulfillment
of the Requirements for the Degree of
Doctor of Philosophy.

California Institute of Technology,
Pasadena, California
1999

(Submitted October 26, 1998)

© 1999

Patrice M. Maheo
All Rights Reserved

"Road: a strip of ground over which one walks.
A highway differs from a road not only because
it is solely intended for vehicles, but also because
it is merely a line that connects one point with another.
A highway has no meaning in itself;
its meaning derives entirely from the two points that it connects.
A road is a tribute to space.
Every stretch of road has a meaning in itself
and invites us to stop.
A highway is the triumphant devaluation of space,
which thanks to it has been reduced to
a mere obstacle to human movement and a waste of time.
Before roads and paths disappeared from the landscape,
they had disappeared from the human soul:
man stopped wanting to walk,
to walk on his own feet and to enjoy it.
What's more, he no longer saw his own life as a road,
but as a highway: a line that led from one point to another,
from the rank of captain to the rank of general,
from the role of wife to the role of widow.
Time became a mere obstacle to life,
an obstacle that had to be overcome by ever greater speed"

Milan Kundera.

This work is dedicated to Ping Xie,
who stood by me no matter what.
She brightened my life and
broadened my horizons by showing me
what life outside the Caltech walls truly is,
in all its many splendors.

Patrice M. Maheo

Acknowledgments

I would like to express my deepest gratitude to my advisor, Professor Morteza Gharib, who, with his unique dedication and kindness, saw me through every aspect of this work. His enthusiasm for fluid mechanics is contagious and is a great source of inspiration for all his students. I would like to thank him in particular for the freedom he allowed in the course of this investigation and the ways he showed me to approach scientific as well as real life phenomena.

I wish to thank all the members of the Caltech community and in particular the people of GALCIT for making the Caltech adventure a memorable one. For lending their time, interest and insight I wish to sincerely thank the members of my Examining Committee: Pr. Hans Hornung, Pr. Anthony Leonard, Pr. Frederich Raichlen and Pr. Theodore Wu.

Among the several contributions made to this thesis and the author himself, both personal and scientific, I wish to distinguish those made by Flavio Noca. The present work has benefited tremendously from his insightful ideas, as he has been a kind mentor and an invaluable friend throughout these years. I would like to thank Pr. Thomas Roesgen and Dr. Ron Henderson for their availability and the many inspirational discussions. I would also like to thank the past and present members of Dr. Gharib's research group for sharing their individual talents. My sincere thanks to Chris Willert, Mustapha Hammache and Dana Dabiri for sharing their knowledge of the DPIV technique; to Alex Weigand, who spent a great deal of time introducing me to my new home: the "laboratory"; to Brad Dooley for his friendship and his dedication during long and tough seances of data acquisition; to Haitao Huang, David Jeon and Fred Taugwalder for sharing their computer expertise.

I want to thank my friends, some of whom I already named above, whose love and warmth is what kept me going many times these years.

Finally, it is my deepest pride to thank here my ***parents*** and ***grandparents***. My journey has been their journey and this thesis is dedicated to their love.

I gratefully acknowledge the financial support of the Office of Naval Research, contract number N00014-92-J-1618, and the University Research Initiative, contract number N00014-92-J-1610, under the supervision of Dr. Edwin Rood.

Abstract

The structure and dynamics of turbulent wakes and shear layers in the presence of a clean free surface have been investigated experimentally using digital particle image velocimetry (DPIV). The purpose of this study was to determine the extent and characteristics of the influence, if any, of the free surface on these underlying turbulent shear flows.

The free surface was found to affect the dynamics of turbulence within a *surface layer* on the order of one half-width of the submerged wake and one half of the local vorticity thickness of the submerged shear layer. Within this layer, the vertical velocity fluctuations are inhibited and the turbulence kinetic energy is redistributed to the horizontal components. The self-induced motion of surface-parallel vortical structures under the influence of their images was shown to lead to large-scale mean streamwise secondary flows and associated outward *surface currents* — symmetric for the wake and asymmetric for the shear layer. This motion was the origin of the significantly higher lateral spreading rates of these surface shear flows compared to the spreading rates of their fully-submerged counterparts — 20% and 25% for the wake and shear layer respectively. In addition, the evolution of the streamwise and surface-normal enstrophy components within the *surface layer* was consistent with the normal connection of vortical structures required at a free surface.

The influence of the secondary flows was tracked back to the splitter plate's turbulent boundary layers where they were hence deduced to originate. A simple analysis of the mixed-boundary corner flows of the splitter plate made using the mean streamwise vorticity equation coupled with the evolution of the values of the transverse velocity confirmed the latter. In this picture of the mean flow, the secondary flows present in the near-surface edges of these shear flows were related to the pair of outer secondary *vortices* generated thereby. Furthermore, using a simplified equation for the surface-normal Reynolds stress, it was shown that the mutual interaction of the surface-parallel vortical structures with their images yielded a decrease in vertical velocity fluctuations as the free surface was approached. This equation shed further light on the redistribution of the vertical kinetic energy of turbulence into the other two Reynolds normal stresses. The resulting free-surface Reynolds-stress anisotropy in turn gave birth to the two streamwise secondary flows.

Table of Contents

List of Tables

Chapter III

Chapter IV

List of Figures

Chapter I

Chapter II

Chapter III

Chapter IV

Chapter V

Appendices

Nomenclature

b	halfwidth of the wake
$c_o = \sqrt{gH}$	wavespeed of an infinitesimal shallow-water surface wave
C_δ	growth-rate constant of a shear layer
d_P	mean diameter of the tracer particles
f	frequency
$Fr \equiv \frac{U_S}{\sqrt{gH}}$	Froude number
$\mathbf{g}$	gravity vector
H	water channel depth
k	turbulence kinetic energy
$\mathbf{n}$	surface normal vector
N_I	image density
P	pressure
$\mathbf{r}$	surface normal coordinate
$r \equiv \frac{U_2}{U_1}$	freestream velocity ratio of a shear layer
R	radius of curvature of the free surface at a point
$Re_\delta \equiv \frac{\delta w_o}{\nu}$ or $\frac{\delta \Delta U}{\nu}$	Reynolds number
$\mathbf{s}$	surface tangential coordinate
$\mathbf{u} = \begin{pmatrix} u \\ v \\ w \end{pmatrix}$	velocity vector
$\overline{\mathbf{u}} = \begin{pmatrix} \overline{u} \\ \overline{v} \\ \overline{w} \end{pmatrix}$	mean velocity vector
U_∞	freestream velocity
$U_C \equiv (U_1 + U_2)/2$	convective velocity of a shear layer
U_1	freestream velocity of the high-speed side
U_2	freestream velocity of the low-speed side
U_S	surface velocity

$\sqrt{\overline{u'^2}}$	root-mean-square of the streamwise velocity fluctuations
$\sqrt{\overline{v'^2}}$	root-mean-square of the transverse velocity fluctuations
$\sqrt{\overline{w'^2}}$	root-mean-square of the normal velocity fluctuations
$-\rho\,\overline{u'v'}$	turbulent Reynolds shear stress
$W^2 \equiv \frac{w_o^2 x}{U_\infty^2 \theta}$	maximum-velocity-defect parameter of the wake
W^*	asymptotic value of W
$We \equiv \frac{\rho U_S^2 H}{\sigma}$	Weber number
w_o	maximum velocity defect of the wake
x	streamwise, or downstream, distance
x_o	"mean" virtual origin
y	transverse, or spanwise, distance
z	normal distance
δ	measure of the (local) transverse extent of the turbulent shear flow
δ_ω	vorticity (or maximum slope) thickness
$\Delta \equiv \frac{\delta_\omega}{x}$	growth-rate parameter for a shear layer
$\Delta^2 \equiv \frac{b^2}{x\theta}$	growth-rate parameter for a wake
Δ^*	asymptotic value of Δ
ΔT	time delay between two images of a DPIV pair
$\Delta U = U_1 - U_2$	velocity difference across a shear layer
κ^s	dilatational viscosity of a surfactant (monolayer) film
μ	dynamic viscosity of the fluid (water)
μ^s	shear viscosity of a surfactant (monolayer) film
ν	kinematic viscosity of the fluid (water)
ν_T	eddy viscosity
θ	angle between the gravity vector **g** and the free surface
θ_i	initial integral thickness
θ_o	far-wake momentum thickness

ρ	density of the fluid (water)
ρ_p	density of the tracer particles
σ	surface tension
τ	typical timescale in the flow
τ_K	Kolmogorov timescale
τ_P	time response of the tracer particles
τ_r	normal stress
τ_{rs}	shear stress
$\boldsymbol{\omega} = \begin{pmatrix} \omega_x \\ \omega_y \\ \omega_z \end{pmatrix} \equiv \nabla \times \mathbf{u}$	vorticity vector
$\overline{\boldsymbol{\omega}} = \begin{pmatrix} \overline{\omega_x} \\ \overline{\omega_y} \\ \overline{\omega_z} \end{pmatrix}$	mean vorticity vector

"The lame in the path outstrip the swift who wander from it."
Francis Bacon.

INTRODUCTION

CHAPTER I

1. Introduction

1.1. The ship wake problem

The wakes produced at the sea surface by various types of ocean-going vessels have been of interest to scientists and sailors for centuries. They continue to be, especially now that they can be observed, photographed, and imaged by remote sensors from space platforms. An important catalyst for the present interest in "free-surface turbulence" has indeed come as a result of recent advances in remote sensing. Techniques such as synthetic-aperture radar (SAR) capable of detecting the free-surface disturbances created by the flow about a surface ship many kilometers behind the ship, and sometimes hours after the ship has passed (Reed et al.[1], 1990), are expected to allow worldwide monitoring of maritime traffic in the foreseeable future.

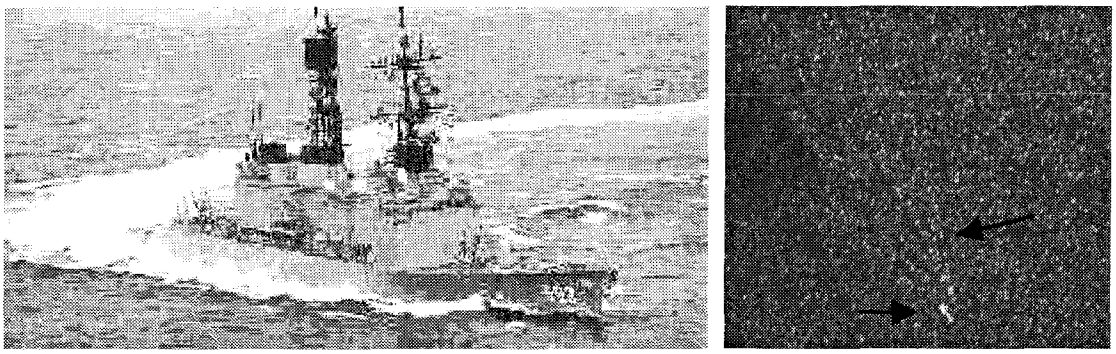

Fig. 1.1. Photograph of the surface signature of a destroyer and a typical SAR image of a ship wake. It is interesting to note that the boat is not at the apex of its wake on the SAR image: this results from an additional Doppler shift due to its relative motion to the satellite.

A moving vessel expends energy to overcome water resistance, creating eddies in the turbulent wake and generating a wave wake. The resulting ship wake comprises a number of complex phenomena: longitudinal waves, known as Kelvin waves, which move steadily with the ship at an angle of about $\pm 19.5^{\circ}$ off the ship track; transverse waves which form immediately behind the ship and propagate at a right angle to the direction the ship is traveling; a turbulent momentum wake; helical vortices associated with the propellers, rudders and hydrofoils; axial vortices

[1] Reed, A.M., Beck, R.F. Griffin, O.M. & Peltzer, R.D. 1990 Hydrodynamics of remotely sensed surface-ship wakes. Trans. Soc. Naval Archit. Mech. Engrs. **98**, 319-363.

generated in the bow region as a consequence of wave breaking; stern and bilge vortices; a large amount of foam and bubbles created by wave breaking and cavitation from the propellers; and, if the ocean is stratified, internal waves.

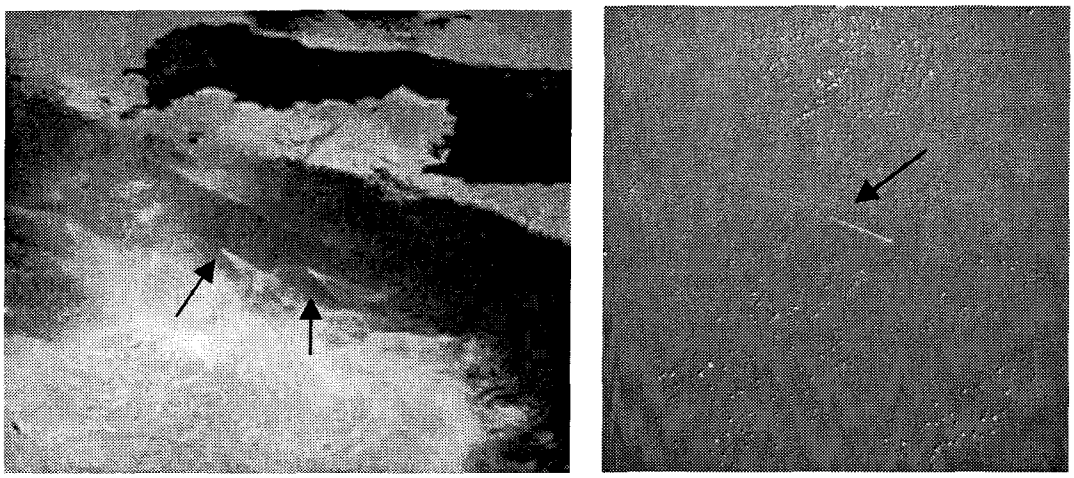

Fig. 1.2. Photographs taken from the space shuttle Challenger. The left picture shows a set of nested-V wakes off the coast of Crete, while the right picture is that of stern wake in the Atlantic Ocean.

Recent SAR imagery of the open ocean have revealed the existence of a narrow V-shaped wake extending 10 kilometers or more behind surface ships with a half angle between 2° and 3° (Vesecky and Stewart[2], 1982; Shemdin[3], 1987; Milgram[4], 1988; Ochadlick et al.[5], 1992). The length of such arms in general depends on the sea state, and the half angle varies from ship to ship and depends on ship speed and radar wavelength. The usual presence of sea-slicks (organic films of biological origin) enhances the visibility of these tracks, while wind-induced surface roughness reduces the visibility of both the slicks and the ship wakes. From visual observations and photography (see Fig. 1.2), astronauts aboard the space shuttle provided information that differed from that obtained from a spaceborne SAR. Stern wakes

[2] Vesecky, J.F. & Stewart, R.H. 1982 The observation of ocean surface phenomena using imagery from the Seasat synthetic aperture radar: an assessment. J. Geophys. Res. **87** (C5), 3397-3430.

[3] Shemdin, O.H. 1987 SAR imaging of ship wakes in the Gulf of Alaska. Final Rep. N00014-84-WRM-2212, Office of Naval Research, Arlinton, VA.

[4] Milgram, J.H. 1988 Theory of radar backscatter from short waves generated by ships, with application to radar (SAR) imagery. J. Ship Res. **32**, 54-69.

[5] Ochadlick, A.R. Jr., Cho, P. & Evans-Morgis, J. 1992 Synthetic aperture radar observations of currents colocated with slicks. J. Geophys. Res. **97**, 5325-5330.

extending behind a ship for more than 200 kilometers were observed routinely (Scully-Power[6], 1986). Perhaps the most surprising, and intriguing, however, were the nested-V bow waves photographed during the 1984 and 1985 shuttle missions (Munk et al.[7], 1987).

These new discoveries were surprising and have sparked considerable speculation. The persistence of these observed features were uniquely puzzling in that they did not obey any known decay laws of fully-submerged flows. This phenomenon could not indeed be explained in light of the fact that a submerged jet in a helical mode, similar to a propeller thrust wake, decays exponentially and that the diverging Kelvin waves at the observed angles are short and should disperse in a matter of meters.

Both sun-glint and SAR imageries map the reflectivity of the ocean surface and thus a surface modification should be expected in the region through which the ship's hull has traversed. The radar return from the sea surface is, to first order, the result of Bragg scattering which selects a single wavenumber of the water surface configuration pointing in the same direction as the radar does. For the Seasat SAR, the surface-wavelength selected by Bragg scattering was about 30cm. It was found that these surface waves were neither part of the well-known Kelvin-wave pattern nor created by ship-generated internal waves. A new mechanism proposes that these V-like wakes are mainly generated by incoherent point sources behind the ship (Munk et al.[7], 1987).

Careful, in-situ measurements of surface tension across the ship's wake (Peltzer et al.[8], 1992) showed a central region of high surface tension (clean water) bordered by two narrow bands of concentrated surface contaminants. The redistribution of the surface contaminants was also observed to persist for long times (>100 minutes) while their separation grows linearly with time (ship distance). The damping of short wavelength surface waves ($\leq$20 cm) by these surface contaminant bands makes the wake region visible to both the eye and SAR imaging. Another proposed mechanism is that the underlying far-wake flow acquires a large scale geometry that has much resemblance to that of a pair of trailing vortices, although, to date, no concentrated vorticity has been observed to exist. Such vortical structures would result in an upwelling in the center of the wake which brings up fresh, clean water from the bulk fluid and pushes to the side the contaminated water that consisted of the ocean surface. The demarcation between the clean and contaminated surfaces is

[6] Scully-Power, P. 1986 Navy oceanographer shuttle observations, Mission report, Rep. STSS 41-G, NUSC Tech. Doc. 7611, Nav. Underwater Syst. Cent., Newport, R.I., March 26, 1986.

[7] Munk, W.H., Scully-Power, P. & Zachariasen, F. 1987 Ships from space. Proc. R. Soc. Lond. A **412**, 231-254.

[8] Peltzer, R.D., Griffin, O.M., Barger, W.R. & Kaiser, J.A.C. 1992 High-resolution measurement of surface-active film redistribution in ship wakes. J. Geophys. Res. C **104**, 245-258.

marked by what is known as a Reynolds ridge. The contaminated surface, or bands into which the surfactants have been compressed, damps any waves in that area making the distinction with the clean surface easily visible.

Whatever the mechanism might be, the surface signature of a ship is caused by a complex interaction of wake turbulence with surface waves, further influenced by the presence of bubbles and possibly natural slicks. Typical ship wakes possess Reynolds numbers in excess of 10^8 which, in combination with the complex nature of these turbulent flows, makes their full simulation in a laboratory environment difficult, if not impossible, to perform. Their computational simulation faces even more drastic restrictions in the parameter space. Rather than studying this flow in its full complexity, a common approach in the scientific community has been to focus on the nature of its elemental components. The insight gained from the elemental features can then be integrated into a flow model of the ship wake and its associated surface signatures.

1.2. Elemental components of ship wakes

The subject of "free-surface turbulence" is not as advanced as other areas of turbulent flow research, and in fact remains in a primitive state despite the rapid progress that has been made in the past decade. The vorticity / free-surface interaction or mutual modification requires a deep understanding of the physics of multiple phenomena, particularly when the vorticity is in a turbulent state. The research scene is hence still dominated by efforts that focus on the understanding of the interaction of canonical flows, such as isotropic turbulence, jets, wakes, mixing layers and, on a more elementary level, vortex pairs and rings, with free surfaces.

Various turbulent shear flows near free surfaces have been examined in recent years. The problem of a vortex ring or a vortex pair approaching a boundary with a free-slip or no-slip condition (whether it is solid or deformable) received much attention as the most elemental constituent of vortex / free-surface interactions. The pioneering work of Sarpkaya & Henderson[9] (1985), and subsequent important studies of Ohring & Lugt[10] (1991) and Dommermuth[11] (1992) on the vortex-pair problem, and the work of Bernal & Kwon[12] (1989) on the vortex-ring problem opened a new

[9] Sarpkaya, T. & Henderson, D.O. 1985 Free surface scars and striations due to trailing vortices generated by a submerged lifting surface. AIAA Paper 85-0445.

[10] Ohring, S. & Lugt, H.J. 1995 Interaction of a viscous vortex pair with a free surface. J. Fluid Mech. **227**, 47-70.

[11] Dommermuth, D.G. 1992 The formation of U-shaped vortices on vortex tubes impinging on a wall with applications to free surfaces. Phys. Fluids A **4**, 757-769.

[12] Bernal, L.P. & Kwon, J.T. 1989 Vortex ring dynamics at a free surface. Phys. Fluids A **1**, 449-451.

era in our understanding of vortex / free-surface interactions. In those studies, vortex trajectories and surface signatures such as 'scars' and 'striations' have been investigated extensively. Bernal & Kwon showed furthermore that as a vortex ring approaches the free surface at an oblique angle, the upper part of the vortex rings deforms and opens its ends to reconnect to the surface. Weigand & Gharib[13] (1996) identified the physical mechanisms that are responsible for the self-disconnection of vortex filaments in the near-surface region and the subsequent connection of disconnected vortex elements to the free surface. Numerical simulations of this phenomenon by Zhang & Yue[14] (1996) have shown similar results.

Shear-free turbulence near a free surface has been studied experimentally, numerically and theoretically. The early evolution of turbulence near a solid wall with zero mean shear has been considered theoretically by Hunt & Graham[15] (1978). In particular, they found that the tangential velocity fluctuations are elevated over a region roughly half the integral scale of turbulence, and the surface-normal fluctuations are reduced over a region which is about twice as thick. Brumley & Jirka[16] (1987) investigated a stirred fluid with zero mean velocity, generated by an oscillating grid below a free surface. Their results were in approximate agreement with the theory for the stress anisotropy of Hunt & Graham. Walker, Leighton & Garza-Rios[17] (1996) used direct numerical simulation to examine the evolution of shear-free, initially homogeneous turbulence near a flat free surface. They concluded that Reynolds stresses are anisotropic over a region roughly equal to the turbulent lengthscale and noted a decrease in vertical fluctuations near the free surface. Furthermore, the turbulent kinetic energy and mean pressure were observed to rise in the near-surface region.

Turbulent jets interacting with a free surface have also received considerable attention in recent years. Liepmann[18] (1990) showed that instabilities in the near-field region of a round jet are strongly influenced by the presence of a free surface, and that the jet flow field is altered through changes in the entrainment field near the free

[13] Gharib, M. and Weigand, A. 1996 Experimental studies of vortex disconnection and connection at a free surface. J. Fluid Mech. **321**, 59-86.

[14] Zhang, C. & Yue, D.P. 1996 On vortex connection at a free surface. *Private communication.*

[15] Hunt, J. & Graham, J. 1978 Free stream turbulence near plate boundaries. J. Fluid Mech. **84**, 178-209.

[16] Brumley, B. & Jirka, H. 1987 Near-surface turbulence in a grid stirred tank. J. Fluid Mech. **183**, 235-263.

[17] Walker, D.T., Leighton, R.I. & Garza-Rios, L.O. 1996 Shear-free turbulence near a flat free surface. J. Fluid Mech. **320**, 19-51.

[18] Liepmann, D. 1990 The near-field dynamics and entrainment field of submerged and near-surface jets. Ph.D. thesis, University of California, San Diego.

surface. Swean et al.[19] (1989) made measurements in a developing planar surface jet and noted a decrease in vertical fluctuations near the free surface. Anthony & Willmarth[20] (1992) examined a circular jet, at single Reynolds and Froude numbers, issuing below and parallel to a free surface using a three-component laser velocimeter. They also noted that the vertical velocity fluctuations were damped near the free surface and identified several, other interesting effects. Most notable was the existence of a flow outward, away from the jet axis in a thin layer near the free surface. On the basis of flow visualization, they concluded that this outward flow, or *surface currents*, was comprised mainly of vortical structures ejected from the main jet. An outward flow similar to that observed by Anthony & Willmarth[20] was observed at the surface by Walker & Johnston[21] (1991) in moderate- to high-Reynolds-number model-ship wakes using flow visualization and by Hoekstra[22] (1991) using velocity measurements. Both Davis & Winarto[23] (1980) and Launder & Rodi[24] (1983) observed similar spreading near the wall in initially axisymmetric wall jets. The occurrence of these similar results in both wall and free-surface jets led Anthony & Willmarth[20] to conclude that the *surface currents* must be caused by the common kinematic boundary condition on the surface-normal velocity (i.e., it vanishes at the boundary), not the differing conditions on the tangential velocities. Walker[25] (1997) developed the mean momentum equations of a turbulent jet in the near-surface region and showed that these *surface currents* can be explained in terms of Reynolds stress anisotropy. This analysis was consistent with earlier explanations by Anthony & Willmarth[20] and Walker et al.[26] (1995) in terms of vortex / free-surface interaction, since both explanations can be ultimately traced to the kinematic boundary condition on the surface-normal velocity.

---

[19] Swean, T.F. Jr., Ramberg, S.E. & Miner, E.W. 1991 Anisotropy in a turbulent jet near a free surface. J. Fluid Eng. **113**, 430-438.

[20] Anthony, D.G. & Willmarth, W.W. 1992 Interaction of a submerged jet with a free surface. J. Fluid Mech. **243**, 699-720.

[21] Walker, D.T. & Johnson, V.G. 1991 Observations of turbulence near the free surface in the wake of a model ship. In Dynamics of bubbles and vortices near a free surface (ed. I. Sahin & G. Tryggvason), ASME AMD-**119**.

[22] Hoekstra, M. 1991 Macro wake features of a range of ships. MARIN Rep. 410461-1-P. Maritime Research Institute Netherlands.

[23] Davis, M.R. & Winarto, H. 1980 Jet diffusion from a circular nozzle above a solid wall. J. Fluid Mech. **101**, 201-221.

[24] Launder, B.E. & Rodi, W. 1983 The turbulent wall jet measurements and modeling. Ann. Rev. Fluid Mech. **15**, 429-459.

[25] Walker, D.T. 1997 On the origin of the 'surface currents' in turbulent free-surface flows. J. Fluid Mech. **339**, 275-285.

[26] Walker, D.T., Chen, C.-Y. & Willmarth, W.W. 1995 Turbulent structure in free-surface jet flows. J. Fluid Mech. **291**, 223-261.

Turbulent open channel flow, in which turbulence generated by a solid bottom wall interacts with the free surface, was examined by Lam & Banerjee[27] (1988) and Handler et al.[28] (1993) among others. The turbulent flow along a corner formed by a vertical wall and a horizontal free surface was investigated experimentally and numerically by Grega et al.[29] (1995) and Longo et al.[30] (1997). The most significant result was the identification of inner and outer secondary flow regions in the corner, similar to the secondary flows formed in turbulent rectangular channel flow (Gessner & Jones[31], 1965; Perkins[32], 1970). The inner secondary motion was characterized by a weak slowly evolving vortex with negative streamwise vorticity, while the outer secondary motion was characterized by an upflow along the wall and outflow away from the wall at the free surface.

The interaction of a turbulent wake with a free surface, at a low Froude number and moderate Reynolds number, was investigated experimentally by Logory et al.[33] (1996). Their LDV measurements showed the existence of a shallow surface layer where the wake width approximately doubles. Flow visualization using laser-induced fluorescence (LIF) revealed the existence of surface-parallel structures. The mutually induced velocity by these structures and their images above the free surface was believed to generate outward *surface currents*, thus carrying low momentum fluid outwards and widening the wake. They further conjectured that these free-surface structures were quasistreamwise vortices, which originated in the flat-plate turbulent boundary layers, and so did the wake widening. However, the apparent differences between their results and those of Longo et al. were not elucidated.

Finally, the reader is referred to Stern et al.[34] (1993) and Warncke[35] (1997) for discussions on the effects of various amplitude waves on turbulent wakes and on the

---

[27] Lam, K. & Banerjee, S. 1992 On the conditions of streak formation in a bounded turbulent flow. Phys. Fluids A **4** (2), 306-320.

[28] Handler, R.A., Swean, T.F. Jr., Leighton, R.I. & Swearingen, J.D. 1993 Length scales and the energy balance for turbulence near a free surface. AIAA J. **31**, 1998-2007.

[29] Grega, L.M., Wei, T., Leighton, R.I. & Neves, J.C. 1995 Turbulent mixed-boundary flow in a corner formed by a solid wall and a free surface. J. Fluid Mech. **294**, 17-46.

[30] Longo, J., Huang, H.P. & Stern, F. 1998 Solid / free-surface juncture boundary layer and wake. Exp. Fluids **25** (4), 283-297.

[31] Gessner, F.B. & Jones, J.B. 1965 On some aspects of fully-developed turbulent flow in rectangular channels. J. Fluid Mech. **23**, 689-713.

[32] Perkins, H.J. 1970 The formation of streamwise vorticity in turbulent flow. J. Fluid Mech. **44**, 721-740.

[33] Logory, L.M., Hirsa, A. & Anthony, D.G. 1996 Interaction of wake turbulence with a free surface. Phys. Fluids **8** (3), 805-815.

[34] Stern, F., Choi, J.E. & Hwang, W.S. 1993 Effects of waves on the wake of a surface-piercing flat plate: experiment and theory. J. Ship Res. **37**, 102-118.

[35] Warncke, A. 1997 The effects of surfactants on free-surface flows. Ph.D. thesis, California Institute of Technology, Pasadena.

effects of surfactants on free surface flows respectively. The effects of waves and surfactants are believed to be small in the present shear-flow experiments.

1.3. Objectives

When a turbulent shear flow approaches a clean free surface, its spectrum of eddies has to adjust to the boundary condition of zero shear stress. This boundary condition requires that vortex lines, which terminate at the free surface, be surface normal. The overall dynamics of turbulence near a free surface is the result of a delicate balance between the dynamics of two classes of structures: vortex tubes which are connected to the free surface and vortex tubes which are oriented parallel to the free surface. The depth to which the free surface influences the underlying turbulent flow is generally not known, but its influence on the decay of turbulence at a free surface appears to be significant. Recent studies of surface jets and grid-generated flows have identified a shallow layer beneath the free surface, within which turbulent flow properties are modified. In this *surface layer*, the vertical fluctuations decrease rapidly with a concomitant redistribution of energy to the horizontal components. The objective of the present study is to unravel the existence, extent and origins of such a surface-influenced layer for other turbulent surface flows, which have, until now, received little or no attention, that is, wakes and shear layers.

To assess the effect of the free surface upon the underlying turbulent flows, a splitter plate was aligned with the flow direction and pierced the free surface. The plate extended far enough below the surface to produce shear flows that become nearly *two-dimensional* with depth, that is, away from the free surface, the turbulence quantities become homogeneous in the vertical direction. Instantaneous, full-field measurements of the velocity were made using digital particle image velocimetry (DPIV) in image planes throughout these free-surface flows. Large data sets of DPIV realizations were acquired to obtained well-converged Reynolds-averaged quantities. The statistics of these turbulent flows were subsequently obtained, in order to quantify the differences between the mean and turbulent properties of these turbulent shear flows as the free surface was approached.

1.4. Organization

The present chapter detailed the recent discoveries, which gave fresh impetus to the experimental and numerical investigations of the near-surface turbulent flows. It further reviewed the results from previous investigations of turbulent flows bounded by a free surface, and presented the objective of this thesis. *Chapter 2* of the thesis is a mathematical description of vorticity interactions with a free surface. The results

developed in this chapter have received corroboration from physical experiments investigating various vortical structures, such as closed loops and line pairs. They also provide a helpful background for understanding the complex nature of the problem. *Chapter 3* describes the experimental setup and the latest improvements in the DPIV (Digital Particle Image Velocimetry) technique, which made the measurements possible. *Chapter 4* presents the results from the study of the interaction of a turbulent wake with a free surface. *Chapter 5* reports the results of a similar study of a turbulent surface shear layer. *Chapter 6* sheds light on the origin of the secondary corner flows and their subsequent downstream evolution into the resulting turbulent shear flow. Finally, in *Chapter 7*, the conclusions from this work are presented along with some recommendations for future studies.

"Men who have excessive faith in their theories or ideas are not only ill-prepared for making discoveries; they also make poor observations."
Claude Bernard.

THEORETICAL BACKGROUND

CHAPTER II

2. Theoretical Background

2.1. Introduction

Mass, momentum, vorticity, and heat fluxes across a deformable, two-dimensional, curved interface, separating two contiguous bulk-fluid phases of different densities and viscosities depend, in general, on the coupled hydrodynamic interactions between the adjacent layers over the broad range of spatial and temporal scales. The analysis of the motion of the primary phase (often a liquid) may be considerably simplified if it is hypothesized that the hydrodynamic and physic-chemical characteristics of its interior surface are not affected by those of the adjacent phase (often a gas). The surface is then said to be free. The two fluid phases may now exert only a constant normal stress on one another; there are no shear stresses on the outward surfaces of each other. Although the exterior of a free surface is free from externally imposed shear, the interior is not necessarily free from the shear generated internally. In fact, surface deformations and contaminants give rise to surface-tension gradients and tangential stresses on the internal side of the bounding surface. From a mathematical viewpoint, a free surface means that the density and viscosity of the upper fluid are zero and that the existence of a continuum above the interface is inconsequential. From a practical point of view, the free surface means that the dynamics of the continuum above the interface has negligible influence on the lower phase, i.e. a free surface is a simplifying approximation for an almost free surface. Only the comparison of numerical simulations, based on the free-surface hypothesis, with physical experiments, carried out under laboratory conditions, may help to assess the range of the governing parameters and the type of boundary conditions for which the free-surface hypothesis is valid.

The following paragraphs are a mathematical discourse on vorticity interactions with a free surface, with appropriate physical interpretation. The fluids are of (different) constant density on either side of the interface, although the equations can be easily extended to incompressible variable density flow and to compressible flow.

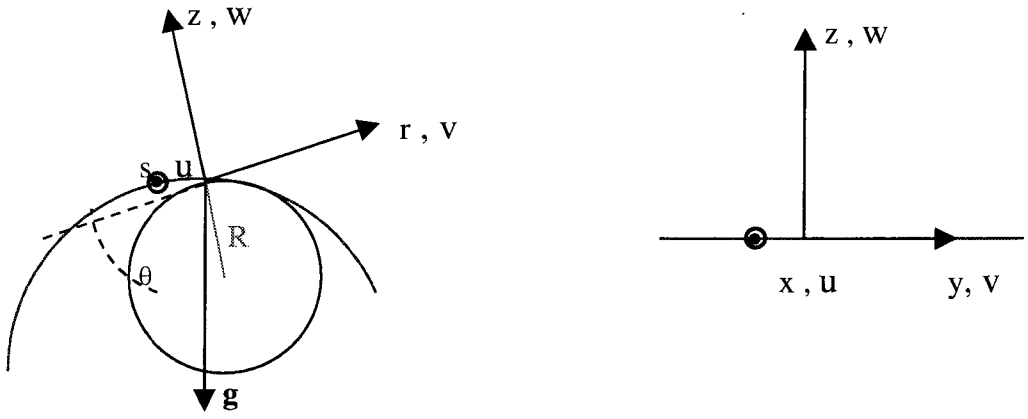

(a) (b)

Fig. 2.1. Coordinate systems: (a) curvilinear, (b) cartesian

2.2. Coordinate systems

When studying a free surface, which by definition is free to move and deform, it is best to define a local curvilinear coordinate system as that depicted in Fig. 2.1. Here **s** is the surface tangential coordinate, **r** is the surface normal coordinate, and **z** is the normal to the plane defined by **r** and **s**. In the subsequent analysis, curvature will only be assumed to exist in the **rs** plane, and the radius of curvature of the free surface at a point is denoted by R. In addition, the angle of the free surface is also measured with respect to **g**, the gravity vector, pointing downwards, and is denoted by θ.

However, for some of the results to be presented it is realized that the free surface deformation is negligible with respect to the magnitude of the velocity field. Some results will then be presented in a global orthogonal **xyz** coordinate system (see Fig. 2.1) with **x** corresponding to **s** and **z** corresponding to **r** at the free surface. In this coordinate system u,v,w are the corresponding components of the velocity vector **u**. The vorticity vector is then defined as:

$$\boldsymbol{\omega} = \begin{pmatrix} \omega_x \\ \omega_y \\ \omega_z \end{pmatrix} \equiv \nabla \times \mathbf{u} = \begin{pmatrix} \dfrac{\partial w}{\partial y} - \dfrac{\partial v}{\partial z} \\ \dfrac{\partial u}{\partial z} - \dfrac{\partial w}{\partial x} \\ \dfrac{\partial v}{\partial x} - \dfrac{\partial u}{\partial y} \end{pmatrix}$$

2.3. Stress conditions at a free surface

Let us develop and analyze the stress conditions at an interface between two fluids, as derived by Rood[1] (1995), and then specialize those conditions for a free surface. In this analysis, air and water represent the two fluids to make it easier to differentiate the fluids and because the interface between air and water is generally a free surface in the absence of wind.

At the interface between the two fluids the stresses must be in balance:

$$(\text{stress})_{\text{water side of interface}} + (\text{stress})_{\text{air side of interface}} + (\text{stress})_{\text{surface}} = 0$$

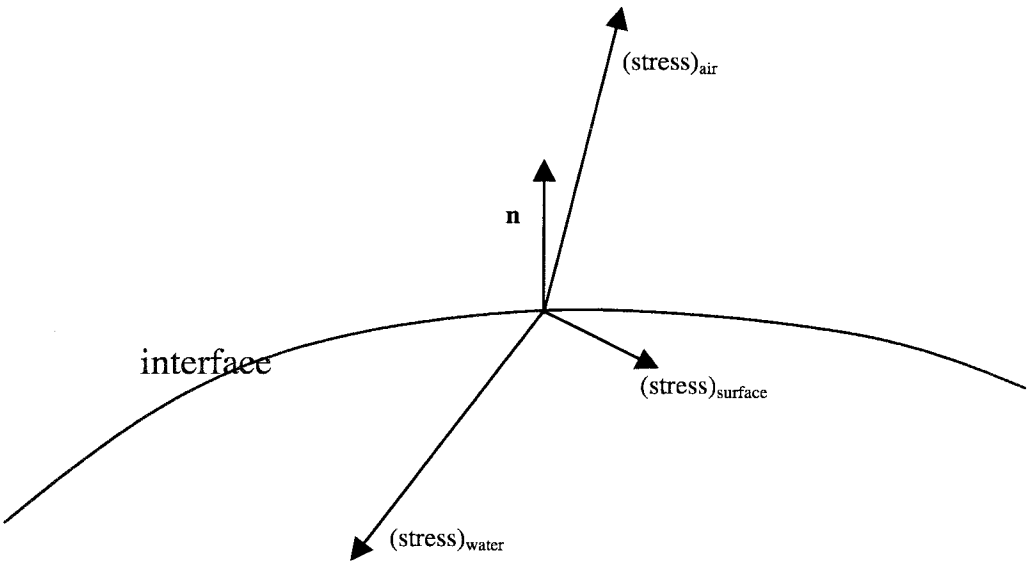

Fig. 2.1. Schematic of the force balance at the free surface

[1] Rood, E.P. 1995 Free surface vorticity. In Fluid Vortices, ed. S.I. Green, 687-730. Norwell, MA: Kluwer.

The stresses on the interface shown in Fig. 2.1 are given by the following expressions:

$$(\text{stress})_{\text{water side}} = -\left[(-p_{\text{water}} + (\tau_r)_{\text{water}})\,\mathbf{n} + (\tau_{rs})_{\text{water}}\,\mathbf{s}\right]$$

$$(\text{stress})_{\text{air side}} = (-p_{\text{air}} + (\tau_r)_{\text{air}})\,\mathbf{n} + (\tau_{rs})_{\text{air}}\,\mathbf{s}$$

$$(\text{stress})_{\text{surface}} = -\frac{\sigma}{R}\,\mathbf{n} + \left(\frac{\partial \sigma}{\partial s} + (\kappa^s + \mu^s)\frac{\partial^2 u_s}{\partial s^2}\right)\mathbf{s}$$

where

σ is the surface tension,

κ^s and μ^s are the dilatational and shear viscosities of a surfactant (monolayer) film,

τ_r and τ_{rs} are the normal and the shear stresses.

These expressions can be plugged into the stress balance equation to obtain:

$$-\left[(-p_{\text{water}} + (\tau_r)_{\text{water}})\,\mathbf{n} + (\tau_{rs})_{\text{water}}\,\mathbf{s}\right] + \left[(-p_{\text{air}} + (\tau_r)_{\text{air}})\,\mathbf{n} + (\tau_{rs})_{\text{air}}\,\mathbf{s}\right] + \left[-\frac{\sigma}{R}\,\mathbf{n} + \left(\frac{\partial \sigma}{\partial s} + (\kappa^s + \mu^s)\frac{\partial^2 u_s}{\partial s^2}\right)\mathbf{s}\right] = 0$$

The stress balance equation can be simplified for air and water under conditions producing a free surface for the interface between the fluids. For such a free surface, the stress condition at the interface is that one of the fluids, the air, applies a constant surface-normal stress but essentially no surface-parallel viscous stress at the interface. "Essentially no surface-parallel viscous stress" means that the surface-parallel stress at the interface is much smaller than the stress in the flow interior. Indeed, in practical situations, for the interaction of underwater disturbances with the free surface under calm wind conditions, the fact that:

$$\mu_{\text{air}} << \mu_{\text{water}}$$

$$\rho_{\text{air}} << \rho_{\text{water}}$$

leads to the surface-normal and surface-parallel stress conditions:

$$p_{\text{air}} - (\tau_r)_{\text{air}} \cong \text{constant}(= p_{\text{Atm}})$$

$$(\tau_{rs})_{\text{air}} << (\tau_{rs})_{\text{water}}$$

The surface-normal and surface-parallel components of the simplified equation are thus found to be:

$$(-p_{water} + (\tau_r)_{water}) + p_{Atm} = -\frac{\sigma}{R}$$

$$(\tau_{rs})_{water} = \frac{\partial \sigma}{\partial s} + (\kappa^s + \mu^s)\frac{\partial^2 u_s}{\partial s^2}$$

For a clean free surface, the latter equation can be further simplified to:

$$(\tau_{rs})_{water} = 0$$

2.4. Vortical elements and free surface

A flat surface condition can be used to demonstrate the special condition that a vortex filament has to follow in order to connect to a free surface. The flat surface condition is proper when the radius of curvature approaches infinity. In a local Cartesian coordinate system, using the flat surface condition (w = constant) and the zero shear-stress condition ($(\tau_{rs})_{water} \cong 0 \Rightarrow \tau_{zx} = 0$ and $\tau_{zy} = 0$), we have

$$\frac{\partial w}{\partial x} = 0 \qquad \frac{\partial w}{\partial y} = 0$$

$$\tau_{zx} = \mu\left(\frac{\partial w}{\partial x} + \frac{\partial u}{\partial z}\right) = 0 \qquad \tau_{zy} = \mu\left(\frac{\partial w}{\partial y} + \frac{\partial v}{\partial z}\right) = 0$$

$$\Rightarrow \quad \frac{\partial w}{\partial x} = \frac{\partial w}{\partial y} = \frac{\partial u}{\partial z} = \frac{\partial v}{\partial z} = 0$$

Thus,

$$\omega_x = \frac{\partial w}{\partial y} - \frac{\partial v}{\partial z} = 0$$

$$\omega_y = \frac{\partial u}{\partial z} - \frac{\partial w}{\partial x} = 0$$

$$\omega_z = \frac{\partial v}{\partial x} - \frac{\partial u}{\partial y}$$

This leaves only the surface-normal component of the vorticity remaining at a flat free surface and forces vortex lines to terminate normal to the surface. In contrast, the no-slip wall only permits the existence of wall-parallel vorticity. The surface-normal termination of vortex lines applies only at the free surface. Immediately below the surface, surface-parallel vorticity can exist without violating any surface condition. However, as a consequence of the kinematic condition, vortex filaments cannot terminate within the fluid, and disconnected filaments will have a tendency to connect normally to the free surface.

2.5. Vorticity and vorticity flux

The unique boundary conditions present at the air/water interface give rise to unique mechanisms of vorticity generation. The next paragraphs outline the derivation of a general expression for the vorticity component parallel to a free surface. The local analysis is done in the orthogonal curvilinear coordinate system previously defined.

The shear stress τ_{rs} on the surface can be expressed in the most general way as follows:

$$\tau_{rs} = \tau_{air} + \frac{\partial \sigma}{\partial s} + (\kappa^s + \mu^s)\frac{\partial^2 u_s}{\partial s^2}$$

The interfacial shear stress is balanced by the stress on the fluid element below the surface:

$$\tau_{rs} = \mu\left(\frac{\partial u_s}{\partial r} - \frac{u_s}{R_s + r} + \frac{R_s}{R_s + r}\frac{\partial u_r}{\partial s}\right)$$

which is a general expression set forth by Schlichting[2] (1987) for the formulation of the momentum equation in curvilinear coordinates. The corresponding vorticity component parallel to the boundary (i.e., the free surface here) is given as

$$\omega_y = \left[-\frac{\partial u_s}{\partial r} - \frac{u_s}{R_s + r} + \frac{R_s}{R_s + r}\left(\frac{\partial u_r}{\partial s}\right)\right]_{r=0}$$

[2] Schlichting, H. 1979 Boundary-Layer Theory, 7th ed. (reissued 1987) McGraw-Hill.

Using the stress equations, the parallel vorticity component may be rewritten as

$$\omega_y = -\frac{\tau_{air}}{\mu} - \frac{1}{\mu}\left(\frac{\partial \sigma}{\partial s} + \left(\kappa^s + \mu^s\right)\frac{\partial^2 u_s}{\partial s^2}\right) - 2\frac{u_s}{R_s} + 2\frac{\partial u_r}{\partial s}$$

This equation, as shown in part by Lugt[3,4] (1987, 1988), Lundgren[5] (1988) and Gharib and Weigand[6] (1995), manifests the four contributions to the vorticity that can be present at a free surface. These are:
(1) the shear stress imposed by the adjoining fluid which in the case of air is considered negligible,
(2) the effects of surfactants from surface tension gradients and acceleration / decceleration of the monolayer film,
(3) the curvature of the free surface, and
(4) the vertical motions of the free surface which is only present in the case of unsteady flows.

Using the same coordinate system, the vorticity flux or vorticity transport equation at a free surface is derived (Rood[1], 1995; Gharib[7], 1994). The equation of continuity in a curvilinear coordinate system (evaluated at the free surface) is written as

$$\frac{\partial u_s}{\partial s} + \frac{\partial u_r}{\partial r} + \frac{u_r}{R} = 0$$

and the s-momentum equation as

$$\frac{\partial u_s}{\partial t} + u_s\frac{\partial u_s}{\partial s} + u_r\frac{\partial u_s}{\partial r} + \frac{u_s u_r}{R} =$$

$$-\frac{1}{\rho}\frac{\partial p}{\partial s} - g\cos\theta + \nu\left(\frac{\partial^2 u_s}{\partial s^2} + \frac{\partial^2 u_s}{\partial r^2} + \frac{1}{R}\frac{\partial u_s}{\partial r} - \frac{u_s}{R^2} + \frac{2}{R}\frac{\partial u_r}{\partial s} - \frac{u_r}{R^2}\frac{\partial R}{\partial s}\right)$$

[3] Lugt, H.J. 1987 Local flow properties at a viscous free surface. Phys. Fluids **30**, 3647-3652.
[4] Lugt, H.J. 1988 Fundamental viscous flow properties at a free surface. Fluid Dyn. Trans. **14**, 1-20.
[5] Lundgren, T.S. 1988 A free surface vortex method with weak viscous effects. Proceedings of the Workshop on Mathematical Aspects of Vortex Dynamics, Leesburg, VA, 68-79.
[6] Weigand, A. and Gharib, M. 1995 Turbulent vortex ring/surface interaction. J. Fluid Eng. Trans. ASME **117**, 374-381.
[7] Gharib, M. 1994 On some aspects of near vortices. In Proc. Twelfth US National Congress of Applied Mechanics, June 1994, Seattle, WA (ed. A.S. Kobayashi), Appl. Mech. Rev. **47**, S157-S162.

which was first derived by Lugt (1987).
Differentiating with respect to r, one derives an equation for the surface-parallel vorticity flux at the free surface as

$$\nu\left[\frac{\partial\omega_y}{\partial r}\right]_{r=0} = -\frac{\partial^2 u_s}{\partial r^2} - \frac{1}{R}\frac{\partial u_s}{\partial r} + \frac{u_s}{R^2} - \frac{1}{R}\frac{\partial u_r}{\partial s} + \frac{\partial^2 u_r}{\partial r \partial s}$$

Next, differentiating the continuity equation with respect to s and evaluating it at the free surface (r = 0), the last term in equation is also represented as

$$\frac{\partial^2 u_r}{\partial r \partial s} = \frac{u_r}{R^2}\frac{\partial R}{\partial s} - \frac{1}{R}\frac{\partial u_r}{\partial s} - \frac{\partial^2 u_s}{\partial s^2}$$

Substituting into, the equation simplifies to

$$-\nu\left[\frac{\partial\omega_y}{\partial r}\right]_{r=0} = \frac{\partial u_s}{\partial t} + u_s\frac{\partial u_s}{\partial s} + u_r\left(\frac{\partial u_s}{\partial r} + \frac{u_s}{R}\right) + \frac{1}{\rho}\frac{\partial p}{\partial s} + g\cos\theta$$

Because the coordinate system is defined locally with the origin at the free surface and moving with it, u_r is equal to zero and the above equation becomes

$$\nu\left[\frac{\partial\omega_y}{\partial r}\right]_{r=0} = -\left(\frac{\partial u_s}{\partial t} + u_s\frac{\partial u_s}{\partial s} + \frac{1}{\rho}\frac{\partial p}{\partial s} + g\cos\theta\right)$$

This is the vorticity transport equation at a free surface where a positive value of the right-hand side denotes a positive flux of vorticity at the free surface into the fluid. The right-hand side can be categorized into an unsteady term and a change of total head, H, along s where H is defined as:

$$H \equiv \frac{1}{2}u_s^2 - \frac{1}{\rho}\frac{\partial p}{\partial s} - g\cos\theta$$

2.6. Dimensionless numbers

The non-dimensional numbers characterizing the free-surface turbulence are defined below.

First, the Reynolds number Re_δ, which reflects the balance between dynamical forces (inertia) and viscous forces, is given by

$$Re_\delta \equiv \frac{\delta \, \Delta U}{\nu}$$

where δ is a measure of the (local) transverse extent of the turbulent shear flow region, ΔU is the velocity difference across the turbulent region ($\Delta U \equiv w_o$ for the wake where w_o is the maximum velocity defect and $\Delta U \equiv U_1 - U_2$ for the shear layer where U_1 and U_2 are the freestream velocities on each side of the shear layer), and ν is the flow kinematic viscosity.

Then, two parameters govern the degree to which a free surface deforms: gravity g and surface tension σ. The former is incorporated in the non-dimensional Froude number, which reflects the balance between the inertial forces and the gravitational restoring forces. The more common definition, which is the ratio of the surface velocity U_S and the wavespeed ($c_o = \sqrt{gH}$) of an infinitesimal shallow-water surface wave, leads to the following expression

$$Fr \equiv \frac{U_S}{\sqrt{gH}}$$

where H is the water channel depth and U_S is the freestream velocity ($= U_\infty$) for the wake and the convection velocity ($= U_C \equiv \frac{U_1 + U_2}{2}$) for the shear layer.

Surface tension (σ) counteracts the level of surface deformation by keeping the surface flat. The corresponding non-dimensional Weber number, which reflects the balance between inertial forces and surface tension forces, is given by

$$We \equiv \frac{\rho U_S^2 H}{\sigma}$$

"The experiment serves two purposes, often independent one from the other: it allows the observation of new facts, hitherto either unsuspected, or not yet well defined; and it determines whether a working hypothesis fits the world of observable facts."

Rene J. Dubos.

EXPERIMENTAL METHODS

CHAPTER III

3. Experimental Methods

3.1. Experimental facility

3.1.1. Free-surface shear layer facility

The experiments were conducted in the free-surface shear layer facility at the Graduate Aeronautical Laboratories of the California Institute of Technology (GALCIT). Top and side view schematic diagrams of the facility are shown in Fig. 3.1. It was designed by Dr. Gharib and manufactured by Engineering Laboratory Design, Inc., in 1993.

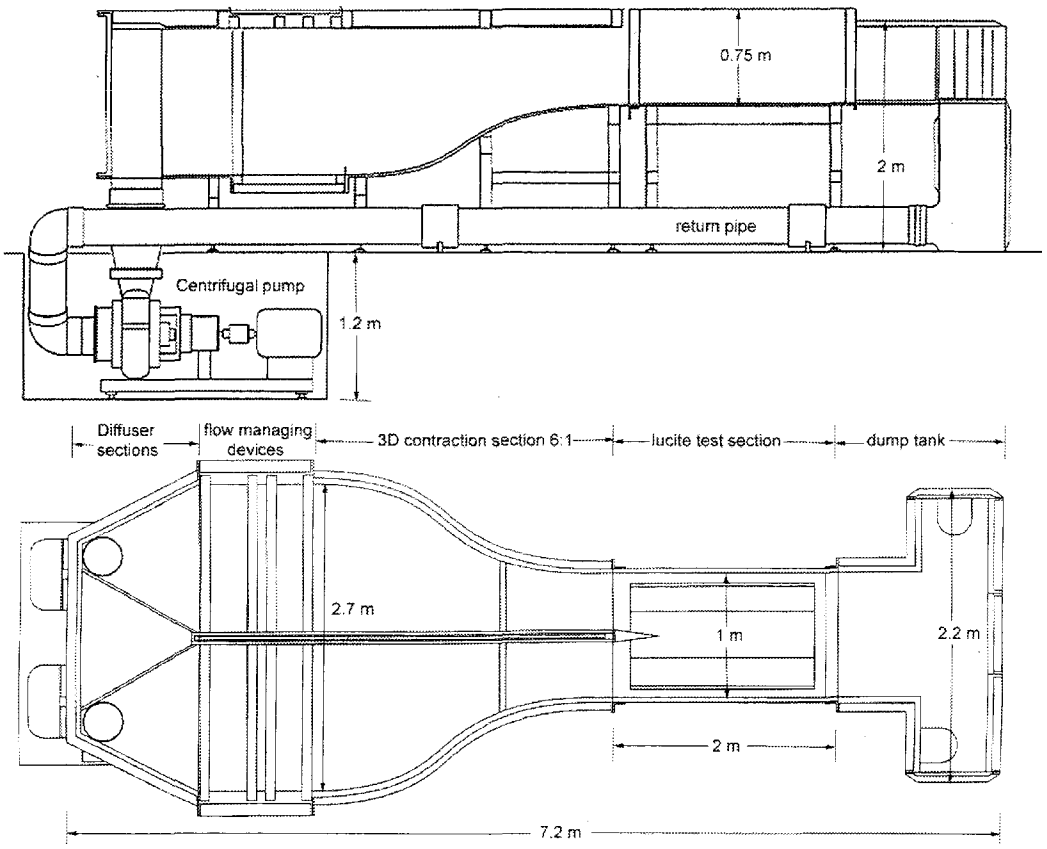

Fig. 3.1. Schematic views of the free-surface shear layer facility

This facility is a recirculating watertunnel with two different streams that are separated by a long dividing plate and that can be controlled independently. The flow from each return pipe empties in a 28° half-angle diffuser. A perforated plate is installed in each diffuser to provide the pressure drop that matches the pressure rise in order to prevent severe separation from the diffuser walls. Each stream then passes into a straight-wall settling chamber, which contains more flow manipulators, including a perforated plate, a honeycomb and three turbulence-reducing screens. Both quieted streams flow through a three-dimensional 6:1 contraction section and enter the test section, where they merge at the end of the splitter plate tip, hence generating a wake or a shear layer depending on the velocity ratio. The tunnel's test section is 2 m long, 1 m wide, and 0.56 m deep and is made of lucite with the bottom positioned 1.2 m above ground to allow optical access from the bottom and both sides. The smooth lucite bottom allowed optical access from below thereby excluding the refraction problems due to surface disturbances present when accessing the flow through the free surface. At the end of the test section, two sets of vanes deflect the flow on each side of the tunnel, through a set of honeycombs in the downstream settling chamber. This downstream section was optimized to prevent air entrainment from bath-tube vortices. Each stream subsequently flows in its respective return line towards each pump.

Each stream was independently driven by a 20 hp end suction centrifugal type pump. Variable-speed controllers were used to set the flow rate between 2 and 20 m^3/min. With the test section completely filled, the maximum flow rate corresponded to a mean freestream velocity of approximately 60 cm/s.

Deionized water was used in the watertunnel and residual surfactants were removed by surface drainage prior to each experiment. Fig. 3.1 shows a schematic of the filtering and cleaning systems. During the tunnel operation, any surfactants adsorbed on the surface were convected downstream to the settling chamber, leaving the test section free of surface contamination.

3.1.2. Splitter plate

The shear flows were generated by a sharp, smooth, two-dimensional splitter plate, which extended through the free surface. The plate was made of a non-corrosive material - PolyVinyl Chloride - to allow prolonged submersion in water. It was mounted at the tip of the tunnel dividing plate using stainless steel screws. The latter were covered with tape to avoid any local tripping of the boundary layers. The plate was linearly tapered from an initial thickness of 7.3cm to a 1mm sharp tip at a half-angle of 4.5° (Fig. 3.2). This half-angle value was small enough to prevent separation and high enough to favor earlier transition of the boundary layers to turbulence over the range of experimental speeds.

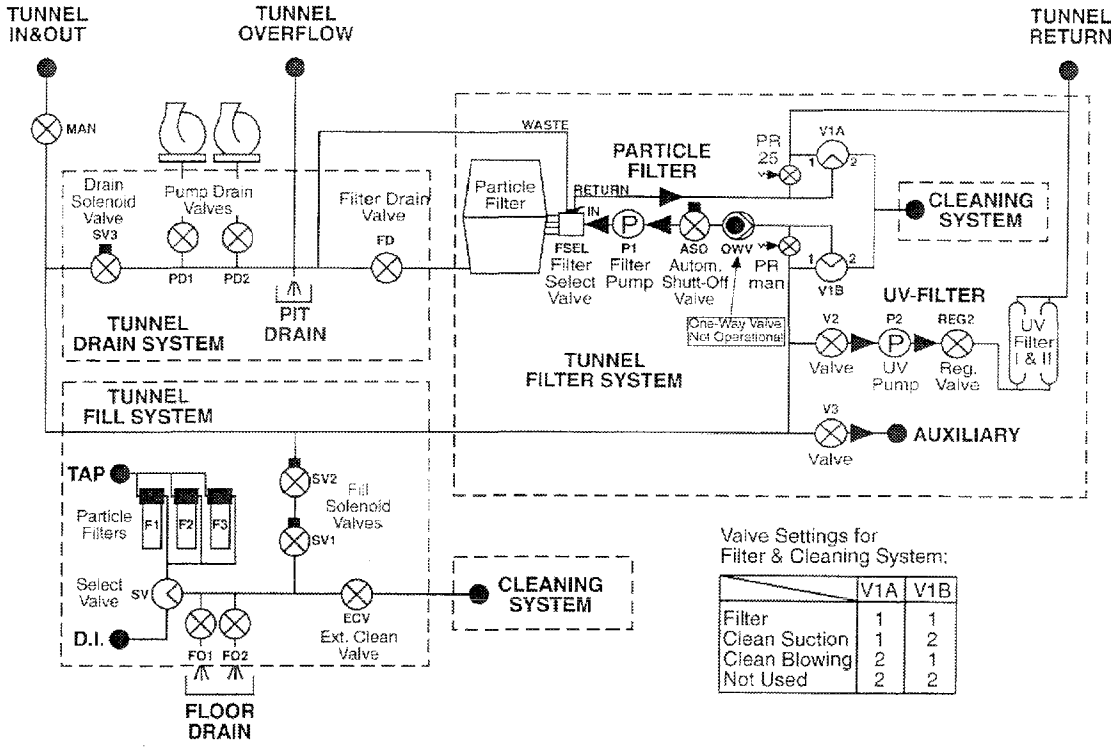

Fig. 3.1. Schematic diagram of filling, draining, filtering and cleaning systems

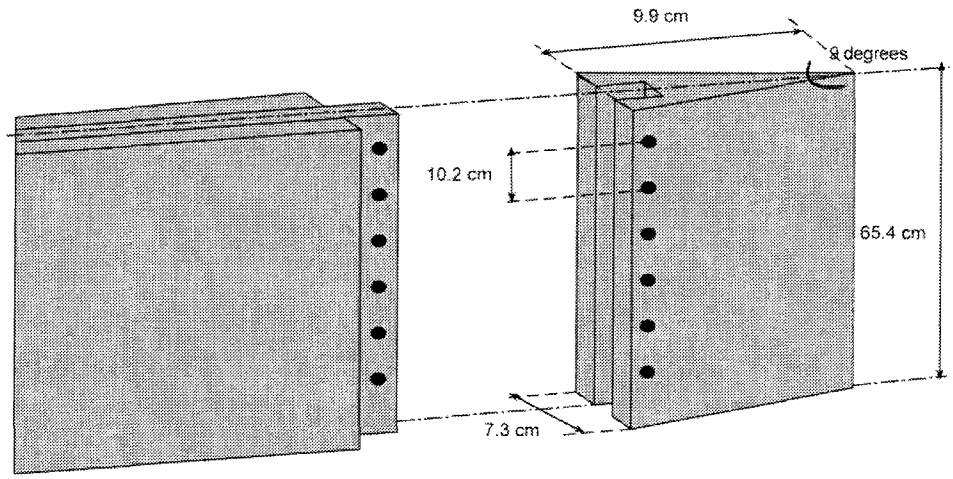

Fig. 3.2. Splitter Plate (not to scale)

3.1.3. Facility calibration: LDV and hot-film measurements

Prior to the free-surface shear flow studies, the flow quality of this newly-built facility was investigated using laser-Doppler velocimetry (LDV) and hot-film anemometry.

(a) LDV measurements

LDV measurements were made to calibrate the speed controllers' settings and to check the flow uniformity. A two-component backscattering LDV (Dantec 2D FiberFlow) probe was mounted on a three-axis positioning system (Velmex series 8300) placed under the tunnel's test section. The output signal of the photomultiplier tube was sent to a burst spectrum analyzer (IDSA) enabling us to measure the freestream velocity on each side of the dividing plate. The LDV measuring volume was approximately 1mm in length and 0.1mm in diameter. For these measurements, the tunnel was seeded with the same 40μm silver-coated glass spheres used for the DPIV measurements. The position of the measuring volume and the acquisition of data from the burst spectrum analyzer were controlled by a personal computer. At each measurement point, 1024 velocity samples were obtained. From each ensemble, the mean velocity $\bar{u}$ was obtained with a measurement uncertainty of 1%.

The measuring volume was positioned at the center of each channel flow at the upstreammost location optically accessible, that is x = −200mm, y = ±254mm, z = −280mm. The coordinate system used to report the subsequent measurements is shown in Fig. 3.1. It is a Cartesian coordinate system with the origin at the intersection of the undisturbed free surface and plate leading edge. The (x,y,z) axes are directed downstream, transverse, and upward, respectively. The results of this study, which are assembled in Appendix A, indicate the good uniformity of the flow.

(b) Hot-film measurements

Hot-film measurements were made in both streams to measure the freestream turbulence level. The facility was run in *wake mode*, that is with the same freestream velocity on both sides. A hot-film sensor (TSI model 1210-20 Pt), which was mounted at the end of a 0.64 cm diameter steel sting reinforced by an airfoil to avoid any vibrations, was positioned at the center of each channel (x = −200mm, y = ±254mm, z = −280mm). Its output was passed through a constant-temperature linearized anemometer (TSI IFA 100) and then filtered with a bandpass filter with cut-off frequencies set at 1 Hz and 200 Hz. The frequencies below 1 Hz were removed to eliminate the effect of U-tube oscillations

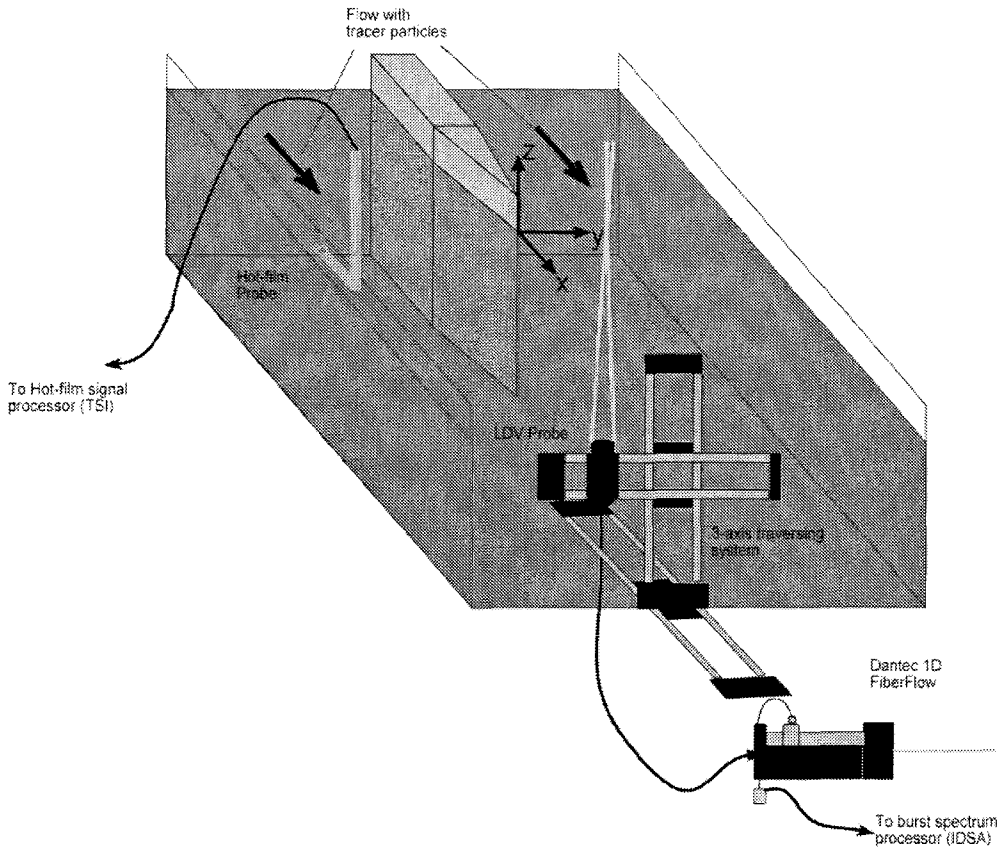

Fig. 3.1. Experimental setups and laboratory coordinate system

$(f = \frac{\omega_o}{2\pi} = \frac{1}{2\pi}\sqrt{\frac{2g}{l_{Tunnel}}} \approx 0.2Hz)$ which are characteristic of such facilities and were not expected to contribute significantly to the studied flow patterns. The frequencies above 200 Hz were removed to eliminate the instrument noise revealed by a HP spectrum analyzer. The filtered signal was sent to a computer-controlled analog-to-digital data collection system. The system was composed of a Macintosh Power PC with a Mac Adios II analog-to-digital (A/D) converter, consisting of a printed circuit board mounted in the computer bus slots and a connection box at the end of a ribbon cable. The A/D converter has 32-bit resolution over an input range of 10 volts, has a maximum sample conversion rate of 10 Mhz, and can collect up to 16 channels. The board is designed so that at slower collection rates, data may be continuously read off of the board and into the computer memory. This feature was used to collect large amount of data directly to the disk drive. The superscope II software provided by the

manufacturer was very adequate for these experiments. A *hot-film* instrument was designed to compute the turbulence level using the collected data.

The aim of these measurements being the quantification of each freestream turbulence level, the hot-film probe was not calibrated and the velocity fluctuations were found in a manner presented in Appendix B.

The table below shows the resulting freestream turbulence levels hence obtained.

U(cm/s)	T (%) for side 1	T (%) for side 2
10	0.06	0.05
20	0.04	0.03
30	0.03	0.02
40	0.05	0.05
50	0.10	0.03
60	0.14	0.04

Table 3-1. Freestream turbulence levels for both sides of the facility

Therefore, the free-surface shear layer facility has a very low freestream turbulence level, that is on the order of 0.1% or less.

It is worth noting that both LDV and hot-film measurements were performed in the same conditions used with digital particle image velocimetry (DPIV), that is with 40 μm seeding tracer particles.

3.2. DPIV Data Acquisition System

3.2.1. Introduction

Flow visualizations clearly show that turbulence is not a random process, but consists of coherent flow structures (Brown and Roshko[1], 1974). With flow visualization we only obtain a qualitative picture of these structures. Traditional instruments like the hot-wire or laser-doppler anemometer are one-point measurement techniques, and therefore not able to reveal the instantaneous spatial structure of a

[1] Brown, G.L. & Roshko, A. 1974 On density effects and large structures in turbulent mixing layers. J. Fluid Mech. **64**, 775-816.

flow. With the aid of a new observation technique called "particle image velocimetry" (PIV), quantitative, two-dimensional information of the velocity field is obtained. These data enable us to compute other flow quantities, such as vorticity and deformation, directly related to the flow dynamics. Although this technique is still young, a number of excellent review papers have already been published, of which we may mention the review by Adrian[2] (1991), which together describe the historical development, measurement technique, and applications of PIV. The original method for PIV image analysis yields accurate results with high spatial resolution, but is very time-consuming. This is a major problem in the application of PIV to study the dynamics of coherent structures in turbulent flows, which requires the analysis of a large number of images. A digital implementation of the PIV method (Willert and Gharib[3], 1991) considerably reduces the processing time, at the cost of a reduction in spatial resolution but virtually no effect on the measurement accuracy (Willert and Gharib[3], 1991; Westerweel et al.[4], 1991). This has proven to be a feasible solution to process large quantities of PIV images.

Fig. 3.1 briefly explains a typical set-up for digital particle image velocimetry recording in a watertunnel.

Small tracer particles are added to the flow. A plane (light sheet) within the flow is illuminated twice by means of a laser (the time delay between pulses depending on the mean flow velocity and the magnification at imaging). It is assumed that the tracer particles move with local flow velocity between the two illuminations. The light scattered by the tracer particles is recorded via a high quality lens on two separate frames of a charge-coupled device (CCD) sensor. The output of the CCD sensor is stored in real time on a laser video disk or directly in the memory of a computer.

For evaluation the digital PIV recording is divided in small subareas called *interrogation windows*. The local displacement vector for the images of the tracer particles of the first and second illuminations is determined for each interrogation window by means of statistical methods (cross-correlation for DPIV). The projection of the vector of the local flow velocity into the plane of the light sheet (two-component velocity vector) is calculated taking into account the time delay between the two illuminations and the magnification at imaging.

[2] Adrian, R.J. 1991 Particle-imaging techniques for experimental fluid mechanics. Ann. Rev. Fluid Mech. **23**, 261-304.

[3] Willert, C.E. & Gharib, M. 1991 Digital particle image velocimetry. Exp. in Fluids **10**, 181-193.

[4] Westerweel, J., Flör, J.B. & Nieuwstadt, F.T.M. 1991 Measurement of dynamics of coherent flow structures using particle image velocimetry. Appl. Laser Tech. Fluid Mech. (eds Adrian, R.J. et al.), Berlin: Springer, 476-499.

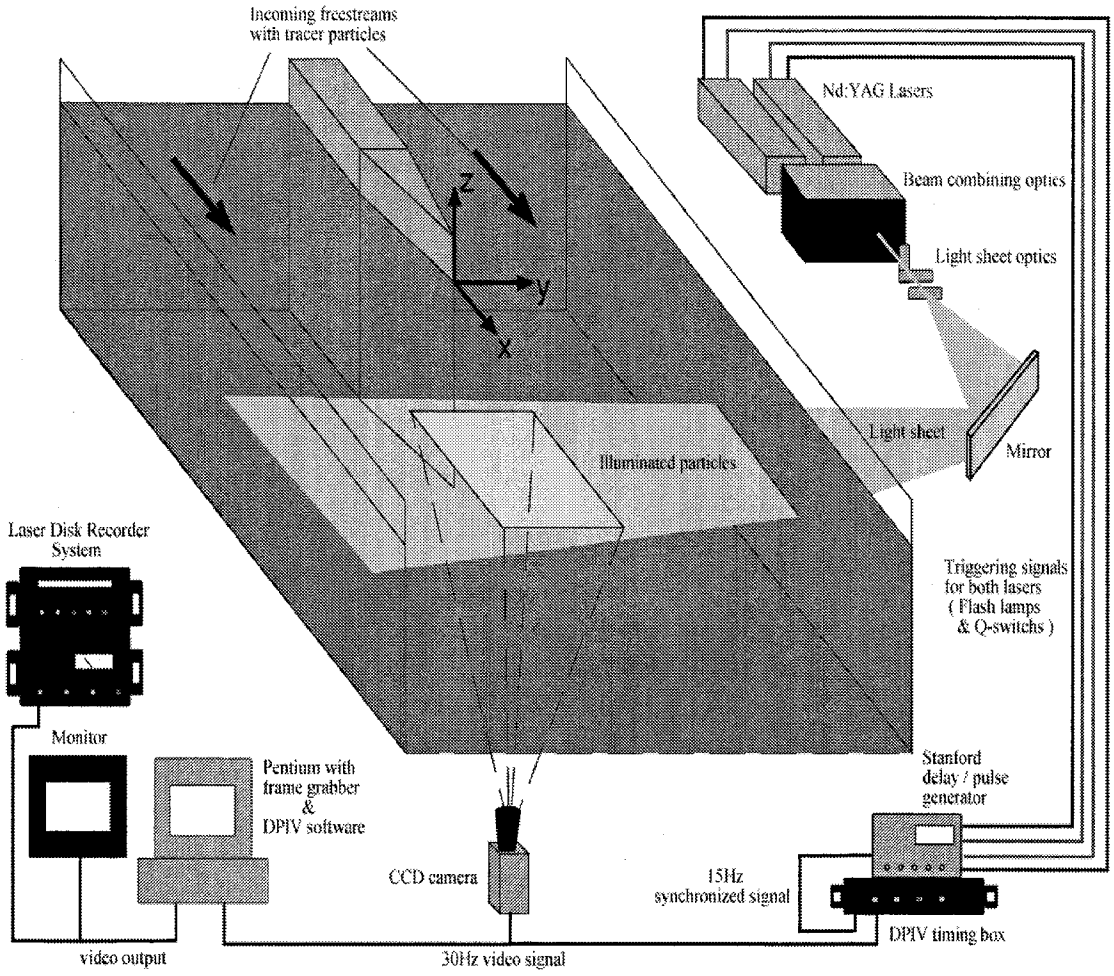

Fig. 3.1. Experimental arrangement for particle image velocimetry

The process of interrogation is repeated for all interrogation windows of the PIV recording. With modern video cameras (768 x 480 sensor elements) it is possible to capture more than 100 PIV recordings per minute. The evaluation of one video PIV recording with 1300 instantaneous velocity vectors (depending on the size of the recording and of the interrogation window) is of the order of a few seconds with standard computers. Second-order differential quantities like vorticity and strain rates, and integral quantities such as the stream function and circulation, are then numerically computed.

One of the most challenging applications of particle image velocimetry (PIV) is measurement of turbulence. For example, the measurement in a turbulent wake may require an image size large enough to include the flow from one edge of the wake to the other with a resolution that is sufficient to resolve the small-scale motions. In addition, the measurement error needs to be small enough in order to measure the small velocity fluctuations throughout the shear flows. Finally, the investigation of turbulent flows with PIV will require the analysis of large number of images, e.g., to determine the flow statistics or to investigate the dynamics of coherent flow structures from image sequences.

The following paragraphs address all these DPIV issues that need to be satisfied to obtain accurate results. The parameters of the wake flow will be mostly used for numerical estimates.

3.2.2. Seeding

For accurate PIV measurements the tracer particles should (1) be distributed homogeneously over the fluid, (2) not alter the properties of the fluid or the flow, (3) accurately follow the motions of the fluid, and (4) scatter or emit enough light to adequately expose an imaging device.

For these measurements the flow is seeded with silver-coated glass spheres (*Conduct-O-Fil* from Potters Industries Inc., Carlstadt, NJ) which have a nominal diameter of 40 μm and a density that makes them almost neutrally buoyant in water. The seeding concentration is about 0.75 g/l, which corresponds to a number density of 0.6 mm^{-3} and a volume fraction of $5x10^{-6}$.

We satisfy the first condition by allowing sufficient time for the seeding material to become evenly distributed over the flow volume before we carry out the measurements.

Acccording to Elghobashi[5] (1994) the effects of the tracer particles on the flow can be disregarded for a volume fraction of less than 10^{-6} (for mono-disperse particles). We approximately comply with this criterion, and therefore the tracer particles will have a negligible effect on the overall state of the flow.

The ability of the tracer particles to follow the motions of the fluid is characterized by the particle time response

$$\tau_P = \frac{\rho_P}{\rho} \frac{d_p^2}{18\,\nu},$$

where ρ_P/ρ is the ratio of the density of the tracer particles with respect to the density of the fluid and d_P the diameter of the tracer particle. For $\rho_P/\rho \approx 0.8$ and

[5] Elghobashi, S. 1994 On predicting particle-laden turbulent flows. Appl. Sci. Res. **52**, 309-329.

$d_P = 40\ \mu m$, we find $d_P = 40\ \mu m$, which is considerably smaller than the Kolmogorov time scale τ_K (τ K , where δ and τ are respectively the wake length and time scales) for the wake flow, i.e., $\tau_K \approx 5$ ms. Hence, we conclude that these tracer particles are able to accurately follow the fluid motions.

From the previous equation it can be seen that the diameter of the particles should be very small in order to ensure good tracking of the fluid motion. On the other hand, the particle diameter should not be too small as light (Mie) scattering properties have also to be taken into account. Therefore, it is clear that a compromise has to be found for conditions (3) and (4) to be satisfied at the same time.

3.2.3. Light sheets

Two DPIV set-ups were used during the course of the experiments, one for measurements in x-y surface-parallel planes, and another for measurements in y-z flow-normal planes. In both set-ups, the green line (532nm) from a pair of frequency-doubled Nd:YAG lasers (Spectra-Physics GCR-18S) were used for illumination. Both lasers operated at 15 Hz with a pulse duration of 10 ns and at an energy level of 0.3 J/pulse. Synchronization of the two lasers was achieved with a digital delay/pulse generator, and the lasers were triggered sequentially with a 1/30s delay (camera frame rate) between them.

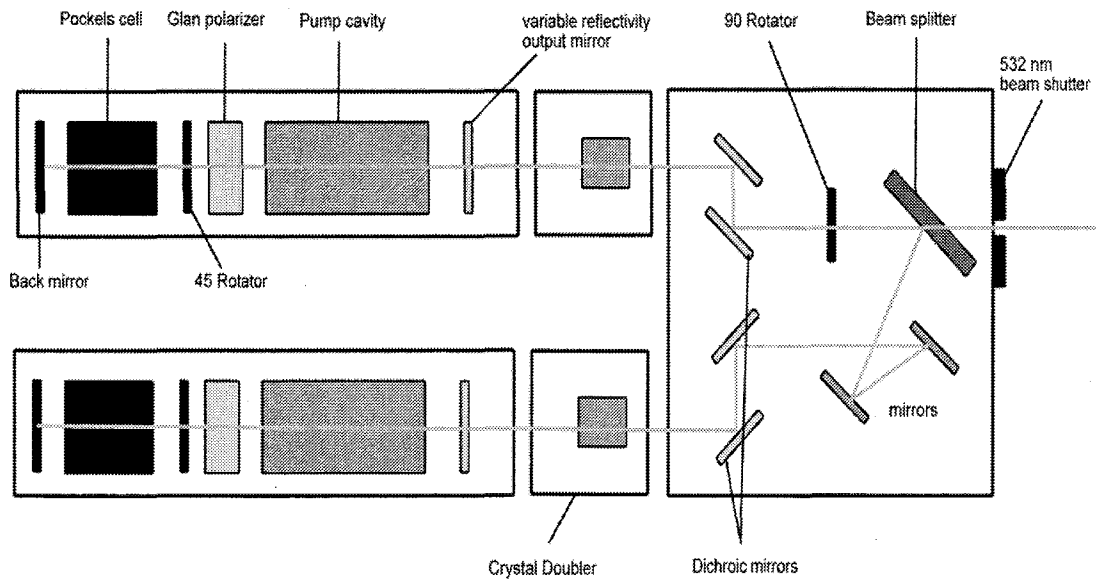

Fig. 3.1. Double oscillator laser system with critical resonators

The beam combining optical system shown schematically in Fig. 3.1 is based on the beam polarizations. Each beam goes through a pair of dichroics to obtain a 98% pure monochromatic vertically polarized beam (532nm). The infrared component is trapped using a beam dump. A 90° polarization rotator is introduced in the first beam path to flip its polarization. The latter beam continues through a polarizing beamsplitter that transmits horizontally polarized light and reflects vertically polarized light and is thus fully transmitted. On the other hand, the second beam is fully reflected by the polarizing beamsplitter. Furthermore, a set of two mirrors are found on the path of the second beam to enable its fine spatial adjustment. As a result, the output is a pair of 15Hz-pulsed normally-polarized laser beams which coincide spatially. All routing optics are located in a dust-free enclosure to prevent mirror damages.

The sheet generating optical system shown schematically in Fig. 3.2 is composed of three cylindrical lenses. The first lens is a –60mm focal-length cylindrical lens, which expands each laser beam into a sheet. The next two cylindrical lenses, of respective focal lengths 100mm and –200mm, form a telescope, which controls the sheet thickness. The reason why a diverging lens has been used first is that focal lines should be avoided. In high power pulse lasers focal points have to be avoided, as otherwise the air close to the focal point will be ionized. Focal lines usually do not ionize the air but dust particles might be burned if the area in the vicinity of the line is not covered or evacuated. In both cases acoustic radiation will occur and the beam properties will change significantly.

Sets of 45° front-surface mirrors mounted on linear and rotation stages are then used to position the sheets normally or parallel to the flow and at the proper location.

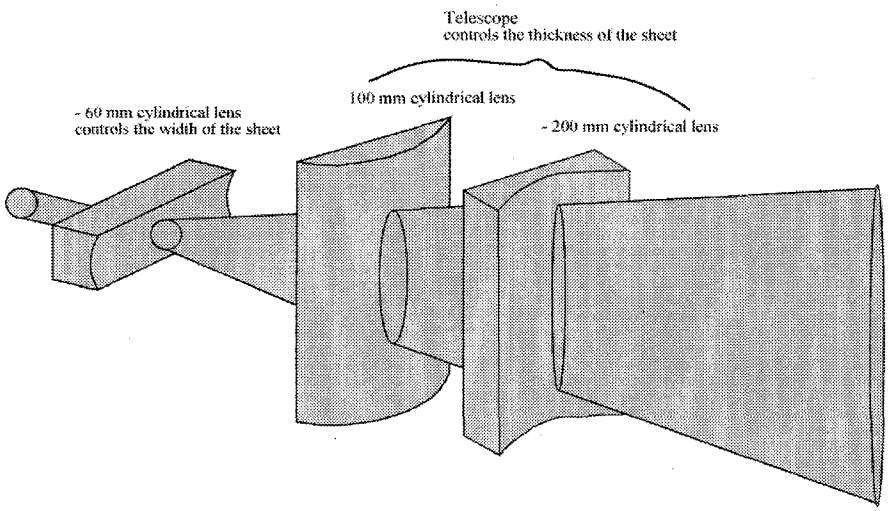

Fig. 3.2. Light sheet optics using three cylindrical lenses

3.2.4. Image recording

A 50 mm focal-length lens (Nikkor) with a numerical aperture of f#=4 was mounted on a charge-coupled device (CCD) video camera (Pulnix TM9700), with the optical axis of the lens perpendicular to the plane of the light sheet. The typical view area was 20cm x 15cm. Particle images of an image pair were obtained asynchronously. The triggering of the lasers was synchronized with the video camera using a digital delay/pulse generator, as shown in Fig. 3.1. The timing diagram in Fig. 3.1 illustrates this further.

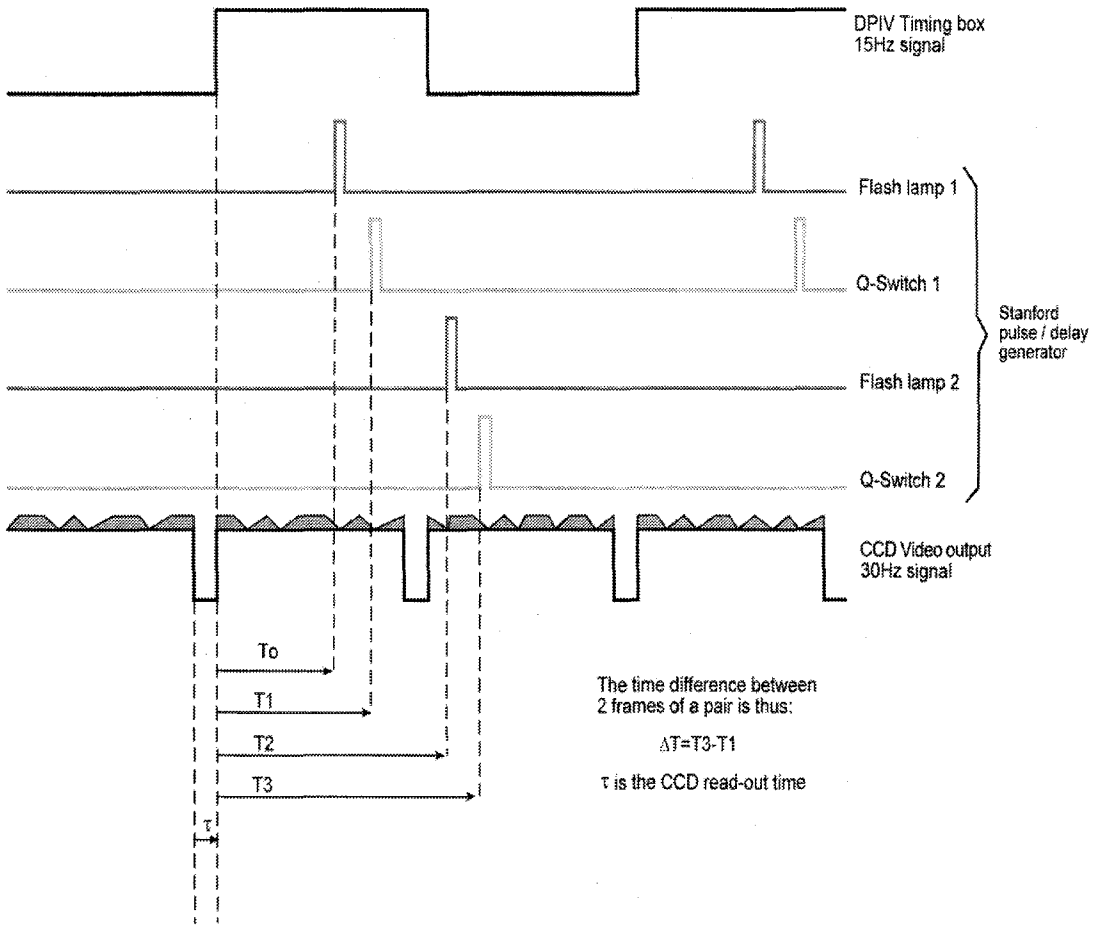

Fig. 3.1. Timing diagrams for PIV recordings

In specific, the camera's sensor was illuminated by the first laser sheet just prior to a frame transfer event. The entire frame was transferred to a read-out buffer within a few microseconds wherefore the CCD sensor could be re-exposed by the second light sheet. In this way, image pairs with an exposure time difference down to a few microseconds can be generated. To properly acquire images the video frame rate that is obtained from the input video signal was divided by two by a timing box. The resulting 15 Hz output signal was then sent to a digital delay/pulse generator (Stanford) which controlled the flash-lamp and Q-switch signals of both Nd:YAG lasers. The time delay (ΔT) between two particle images of a pair was typically on the order of 5 ms. The mean in-plane displacement of the tracer particles was ($U_\infty \Delta T$=) 1.68mm which corresponds to about 1/4th of the width of the interrogation region and complies with the value recommended by Keane and Adrian[6] (1991). The cycle rate of the image pairs is half of the camera frame rate, that is 15 Hz (two images for one displacement field measurement). Particle images were stored on analog laser video disks (Sony LVM 3AA0/3) using a Sony Recorder-Processor system (LVR-5000A & LVS-5000A), subsequently digitized (8 bit A/D conversion to 768x480 pixels^2) by a frame grabber (Epix board model 10-8MB) and then downloaded to a Silicon Graphics to be processed by the DPIV software.

3.2.5. Interrogation analysis

Particle displacement vectors were obtained from successive images by cross-correlating corresponding sampling windows in the frame pair. The cross-correlation was obtained by complex conjugate multiplication in the spatial frequency domain (Willert and Gharib[3], 1991), and the vorticity normal to each field was calculated from the velocity gradients, obtained by numerical differentiation.

The cross-correlation technique utilized to obtain particle displacements from sampling windows in successive video frames amounts to a low-pass spatial filtering of the image data and results in a trade-off between spatial resolution and measurement accuracy. The size of the sampling window must be chosen large enough that sufficient particles remain within the window during successive frames, yet small enough that the velocity of all the particles within the window is essentially uniform. The average number of particle-image pairs per interrogation region, or image density N_I, is 12, which roughly complies with the value recommended by Keane and Adrian[6] (1991). For the present study, a method of successive window

[6] Keane, R.D. & Adrian, R.J. 1991 Optimization of particle image velocimeters. Part II: Multiple-pulsed systems. Meas. Sci. Technol. **2**, 963-974.

refinement was devised using the window shifting technique (Westerweel, Dabiri and Gharib[7], 1997).

The particle displacements were originally determined using a coarse 32x32–pixel sampling window at intervals of 16 pixels (i.e., a 50% overlap). A refined sampling window (16x16–pixel) was then used, displaced between successive frames by an amount equal to the measurement determined from the coarse window. No overlap of the sampling window was used, and the resulting field consisted of approximately 1300 measured independent displacement vectors. Since the location of the cross-correlation peak can be resolved with a sub-pixel accuracy of better than 0.05 pixel (Willert and Gharib[3], 1991), the maximum uncertainty based on the local velocity and vorticity magnitude is $\pm$ 1% and $\pm$ 3%, respectively. For a full error analysis, see Willert and Gharib[3] (1991).

Each image pair yields a data set of 29 rows of 46 vectors each. The set of image pairs is processed on a Silicon graphics workstation, which completes the analysis (DPIV and window shifting technique) of one pair in less than 30 s.

3.2.6. Data validation

As a consequence of the stochastic nature of the number of tracer particles that appear in the interrogation area, a certain number of interrogations is based on insufficient particle pairs and results in a spurious measurement of the displacement. Each data set is subject to a validation procedure to detect and replace spurious measurements of the displacement. The automated scheme used here scans the displacement differences of a displacement vector to each of its eight neighbors. A data-point in question is tagged for each difference exceeding a certain threshold. If a point had been tagged for more than four instances, it would be discarded and re-interpolated from the surrounding untagged displacement vectors typically using a bi-linear approach. The absolute velocity data was first processed and all vectors that deviate more than 33.5 mm/s (viz. 1 pixel) from its neighbors were identified as *spurious*. The average fraction of detected spurious vectors per image was less than 1%.

However, the efficiency of any detection procedure cannot be 100% perfect (Westerweel[8], 1994). This procedure was no exception to that, so a small fraction of spurious displacements remains undetected and a small fraction of valid data may have been labeled mistakenly as *spurious*. A second iteration of the detection procedure was implemented, but now for the fluctuating velocity (i.e., we subtract at

[7] Westerweel, J., Dabiri, D. & Gharib M. 1997 The effect of a discrete window offset on the accuracy of cross-correlation analysis of digital PIV recordings. Exp. Fluids **23**, 20-28.

[8] Westerweel, J. 1994 Efficient detection of spurious vectors in particle image velocimetry data sets. Exp. Fluids **16**, 236-247.

each location the appropriate mean velocity). For the second iteration, we label all vectors that deviate more than 16 mm/s from its neighbors. No further improvement is expected for additional iterations, since the latter detection level is already close to a situation where the random measurement errors are of the same level as the small-scale velocity fluctuations.

3.2.7. Resolution

(a) spatial

For the present investigation, the objective was to determine the structure of large scales in the flow. The measured velocity with DPIV at a certain location is actually an average over the interrogation volume. One-millimeter thick sheets were found to be thin enough to provide good spatial resolution, yet thick enough so that the percentage of particles leaving the sheets between two consecutive video frames was small. In order to insure sufficient spatial resolution, each surface-parallel plane was made of several overlapping measurement regions, which could be combined into a mosaic of the entire test section. The image size of each measurement region was furthermore made large enough to include the wake flow from one edge to the other at the downstreammost location in order to maximize spatial resolution. Similarly, the image size of each flow-normal plane was large enough to capture the flow large scales (see Fig. 3.1). In both DPIV setups, the 16–pixel resolution corresponded to approximately 4mm in the flow. Although the Kolmogorov lengthscale $\delta\,\mathrm{Re}_\delta^{-3/4}$ (where $\delta \approx 10\,\mathrm{cm}$ is a mean measure of the wake width) for the wake flow was calculated to be on the order of 0.2mm, the 4mm resolution of the DPIV measurements was adequate to resolve the large scales in the wake flow. The DPIV spatial resolution was of the order of magnitude of the flow Taylor microscale (estimated at 2mm).

(b) temporal

For these experiments thousands of image pairs (typically 5000, i.e., 4 Gbytes) were recorded at a frame rate of 15 Hz at each downstream station. At this particular frame rate the time between consecutive frames is about three times less than the estimated integral scale of the wake flow (i.e., $\delta/U_\infty \approx 0.2\,\mathrm{s}$). Hence, this frame rate enables us to follow the motion of coherent structures as they pass along the view area of the camera. However, the measurement results for each of the image pairs are not statistically independent and the sampling error does not converge as quickly as for fully independent data. Nevertheless, large enough data sets were acquired to

obtain well-converged Reynolds-averaged quantities. The sampling error for the flow statistics is not simply determined by the size of the data set; a more appropriate way to link the size of the data set to the sampling error is to consider the "equivalent measurement time" expressed in integral time scales. Dividing the measurement time ($(5000/3)(\delta/U_\infty) \approx 330$ s) by the integral time scale ($\delta/U_\infty \approx 0.2$ s) yields a value of about 1667. The sampling error for the flow statistics is inversely proportional to the square root of the corresponding measurement time, that is about 0.025.

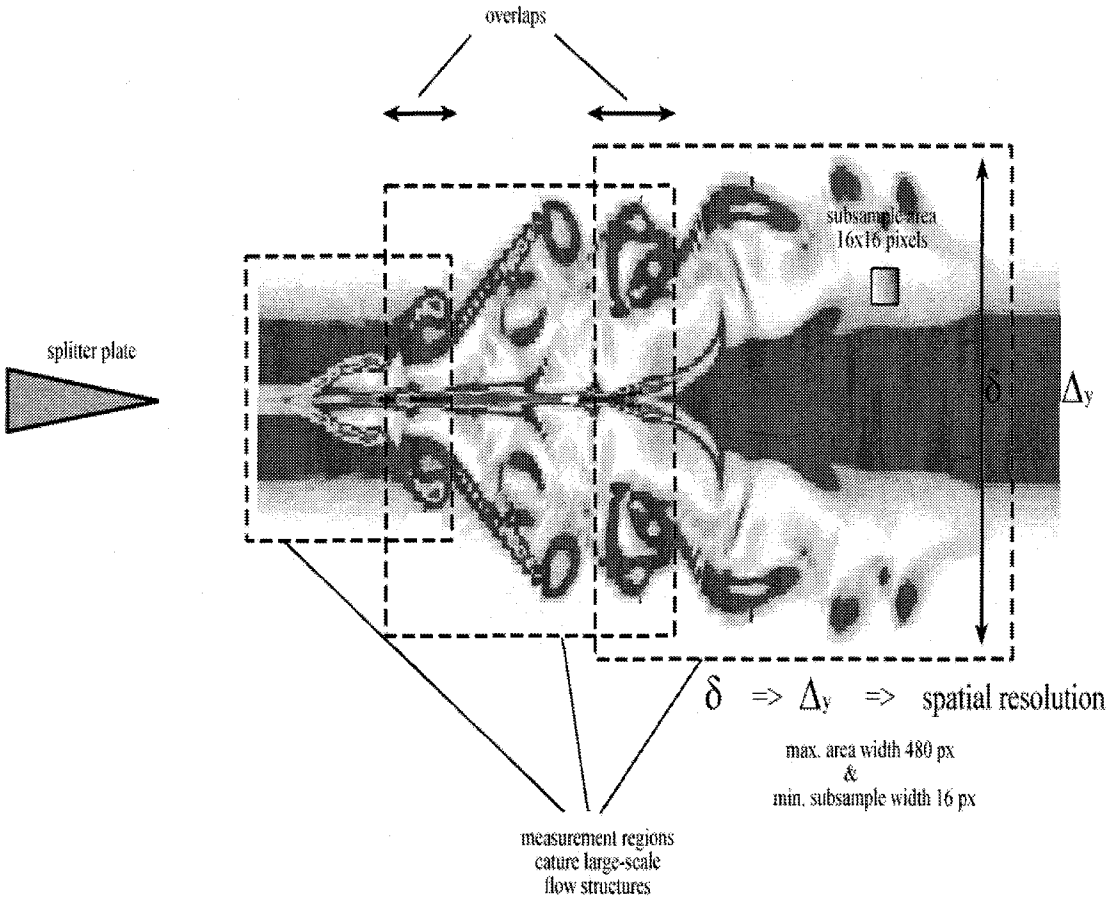

Fig. 3.1. PIV overlapping measurement regions and spatial resolution

3.2.8. Conventional & flow-normal PIV techniques

In addition to the conventional PIV technique set up for measurements in flow-parallel planes, a flow-imaging technique had to be devised for convective flows. Measurements in y-z flow-normal planes had to be performed to probe the spatial extent of the free surface on the underlying turbulent shear flow and thus guide the positioning of the x-y surface-parallel planes in the very near-surface region. The concept of this technique is not new by any means and it has already been applied successfully in experimental studies particularly in tow-tanks and most recently in a watertunnel[9]. This optical configuration of the digital PIV system allowed for measurements in which the mean flow was normal to the plane of the light sheet, as depicted in Fig. 3.1. The laser beams were made into individual light sheets using the sheet-generating optical system presented in Fig. 3.2. In this case, however, the two sheets were spaced a few millimeters apart. The sheet thickness of the first sheet was about 1mm while that of the second depended on the normal flow field (typically a few millimeters). This was necessary in order that the same particles were imaged in successive frames of each frame pair. However, this set-up led to a systematic error as a result of perspective, as shown in Appendix C. A particle image was synthetically obtained through numerical simulation, in which randomly distributed particles were generated. This particle image was carefully positioned in each light plane and numerous recordings were made by the CCD sensor. These image sets were then processed using the DPIV software, and the "source-like" velocity field due to this perspective (also called parallax) effect was obtained and subsequently digitally removed.

Systematic and random errors were estimated for these measurements using the large data sets obtained and are presented in the next tables.

[9] Kuzo, D.M. 1996 An experimental study of the turbulent transverse jet. Ph.D. thesis, California Institute of Technology, Pasadena.

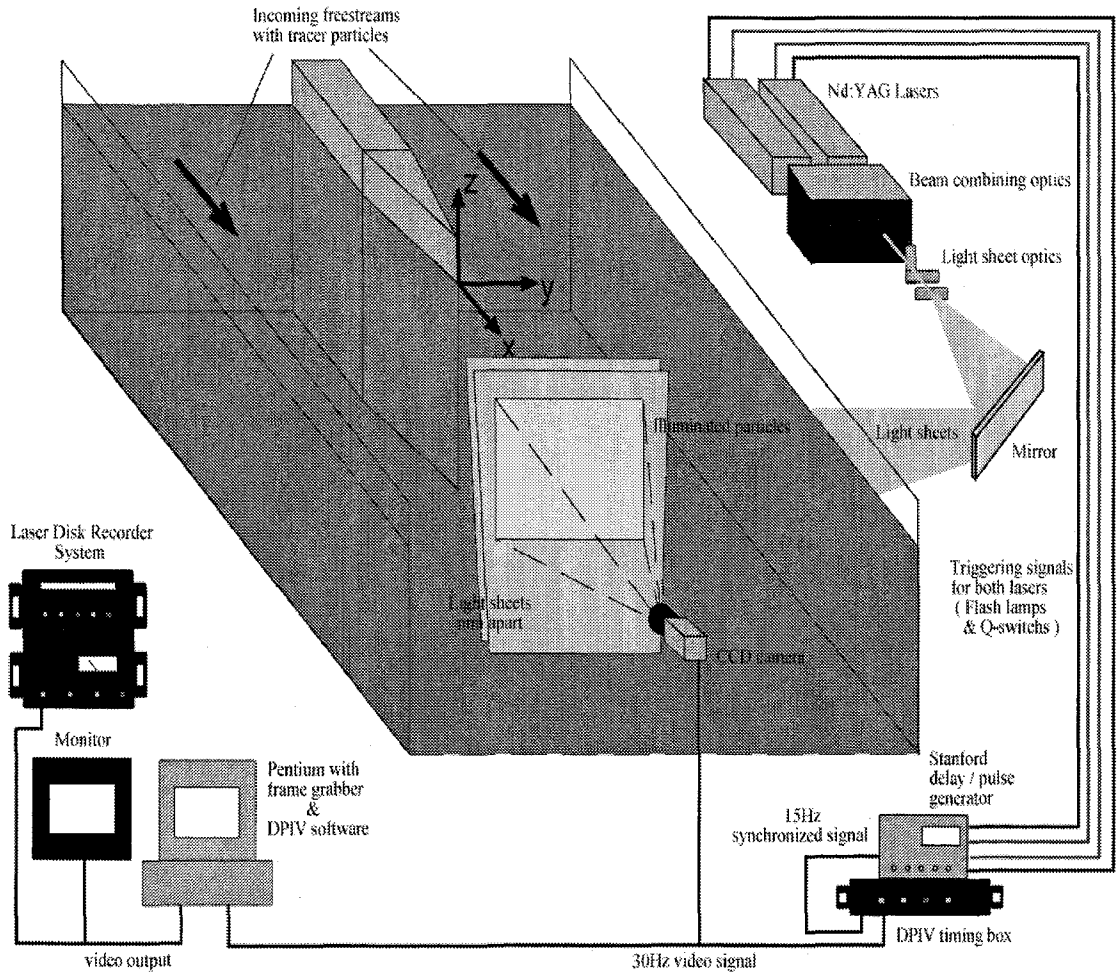

Fig. 3.1. Schematics of the DPIV setup for measurements in flow-normal y-z planes

	Near Field	Intermediate Field
U (mm/sec)	300	300
$\overline{U}$ (mm/sec)	300	300
$\sqrt{\overline{u'^2}}$ (mm/sec)	25	10
σ_U (%)	1	1
$\sigma_{\overline{U}}$ (%)	0.5	0.5
$\sigma_{\sqrt{\overline{u'^2}}}$ (%)	15	15
V (mm/sec)	25	10
$\overline{V}$ (mm/sec)	5	0.5
$\sqrt{\overline{v'^2}}$ (mm/sec)	20	10
σ_V (%)	15	30
$\sigma_{\overline{V}}$ (%)	15	15
$\sigma_{\sqrt{\overline{v'^2}}}$ (%)	15	15
$\overline{u'v'}$ (mm^2/sec^2)	100	50
$\sigma_{\overline{u'v'}}$ (%)	10	10

Table 3-2. Estimate of measurement errors in surface-parallel planes

	Intermediate Field
V (mm/sec)	15
$\overline{V}$ (mm/sec)	10
$\sqrt{\overline{v'^2}}$ (mm/sec)	5
σ_V (%)	15
$\sigma_{\overline{V}}$ (%)	10
$\sigma_{\sqrt{\overline{v'^2}}}$ (%)	15
W (mm/sec)	10
$\overline{W}$ (mm/sec)	5
$\sqrt{\overline{w'^2}}$ (mm/sec)	5
σ_W (%)	20
$\sigma_{\overline{W}}$ (%)	10
$\sigma_{\sqrt{\overline{w'^2}}}$ (%)	15

Table 3-3. Estimate of measurement errors in flow-normal planes

3.3. DPIV measurement procedure

The digital particle image velocimetry (DPIV) technique of Dr. Gharib's research group was used to obtain instantaneous two-dimensional velocity measurements in image planes throughout the investigated shear flows.

Prior to each data acquisition, the Nd:YAG lasers were "warmed up" for about fifteen minutes to optimize the repeatability of their operation. The two laser beams were carefully aligned with respect to one another through a series of pinholes positioned in front of and after the test section at the preset downstream station. The laser sheets were generated by the optical set-up, which was presented in paragraph 3.2.3. These sheets were carefully positioned in the following manner.

3.3.1. Measurements in x-y surface-parallel planes

The first laser sheet was aligned with the free surface at rest and then carefully positioned at the preset depth using precise traversing systems. The second light sheet was aligned to the first by matching them precisely at each end of the test section. The CCD camera was traversed to the preset downstream position and then placed normal to the free surface (and thus the light sheets) using its reflection. The watertunnel was then turned on at preset flow conditions of Reynolds number and velocity ratio. Next, particle concentration and suspension in the facility were issues, with extensive effort given to assuring correct particle count levels. This level was set mostly by hands-on experience: too-small a particle count made for poor image correlation during processing, while too-high a count diminished image quality due to (light) scattering. Following all of these inspections and corrections (if necessary), sufficient time was allowed for the flow to become steady-state if a disturbance was created during any modification or correction. Once optimum conditions had been established, room lights and any other extraneous light sources were doused, and attention turned to the next procedures for data acquisition. The time delay (ΔT) between two particle images of a pair was set so that the mean in-plane displacement of the tracer particles was about 1/4th of the width of the interrogation region and complied with the value recommended by Keane and Adrian[6] (1991). A few image pairs were then digitized by a frame grabber and processed on a PC to check the data quality. After strict quality checks were met (less than 1% of outliers), particle images were stored on an analog laser video disk using a Sony Recorder-Processor system.

3.3.2. Measurements in y-z flow-normal planes

Measurements in y-z flow-normal planes had to be performed to probe the spatial extent of the free surface on the underlying turbulent shear flow and thus guide the positioning of the x-y surface-parallel planes in the very near-surface region. The first laser sheet was positioned normally to the free surface and the splitter plate and then carefully positioned at the preset downstream station. The second light sheet was aligned to the first by matching them precisely and then displaced by a few millimeters to improve the signal-to-noise ratio and its thickness adjusted based on the measured normal flow field at that location. The CCD camera was placed normally to the light sheet to image the flow in this plane. The watertunnel was then turned on at preset flow conditions and tracers were added to the flow to assure correct particle count levels. After inspections and possible corrections were performed, sufficient time was allowed for the flow to become steady-state if a disturbance was created during any modification or correction. Once optimum conditions had been established, room lights and any other extraneous light sources were doused, and attention turned to data acquisition procedures. The time delay (ΔT) between two particle images of a pair was varied about the estimated value so that the same particles were imaged in successive frames of each frame pair. Image pairs were digitized by a frame grabber and processed on a PC to check the data quality. When the percentage of outliers was less than 1%, particle images were then stored on an analog laser video disk using a Sony Recorder-Processor system.

As the above outlined procedure required several hours, it is clear that one data set per day was the rule, with the remainder of the time spent in preparation or data processing. In addition, at the end of each data acquisition, ruler, target and particle images were taken for calibration and correction purposes.

"With accurate experiment and observation to work upon, imagination becomes the architect of physical theory."
Tyndall.

TURBULENT WAKES

CHAPTER IV

4. Turbulent wakes

4.1. Fully-submerged turbulent wakes

4.1.1. Two-dimensional turbulent wakes

In this section we review some of the background of turbulent plane wakes. The reader already familiar with this material is invited to proceed to section 4.1.2. Turbulent, plane wakes generated by circular cylinders in the absence of a pressure gradient have been the subject of numerous experimental investigations, the most notable of which are those by Townsend[1,2] (1947, 1949). The results of these studies, along with results obtained in other free shear flows, led to the early ideas of self-preservation and Reynolds number independence proposed by Townsend[3] (1956). It was postulated that, sufficiently far downstream from the wake generator, an asymptotic self-preserving state is achieved for which the flow can be described by a single velocity scale w_o and a single length scale b (see Fig. 4.1). That is, the transverse distributions of mean velocity and Reynolds stress must be independent of the streamwise coordinate x when normalized by these scales. This can be expressed in the form

$$\begin{aligned}
\overline{u} &= U_\infty - w_o f(\eta), \\
\overline{v} &= w_o h(\eta), \\
\sqrt{\overline{u'^2}} &= w_o g_{11}(\eta), \\
\overline{u'v'} &= w_o^2 g_{12}(\eta), \\
\sqrt{\overline{v'^2}} &= w_o g_{22}(\eta), \\
\sqrt{\overline{w'^2}} &= w_o g_{33}(\eta),
\end{aligned}$$

where $\eta \equiv \frac{y}{b}$ and w_o and b are the maximum velocity defect and the half-width of the wake respectively, as defined in Fig. 4.1.

---

[1] Townsend, A.A. 1947 Measurements in the turbulent wake of a cylinder. Proc. R. Soc. Lond. A **190**, 551-561.

[2] Townsend, A.A. 1949 The fully developed turbulent wake of a circular cylinder. Austral. J. Sci. Res. **2**, 451-468.

[3] Townsend, A.A. 1956 The structure of turbulent shear flows. Cambridge University Press, Cambridge.

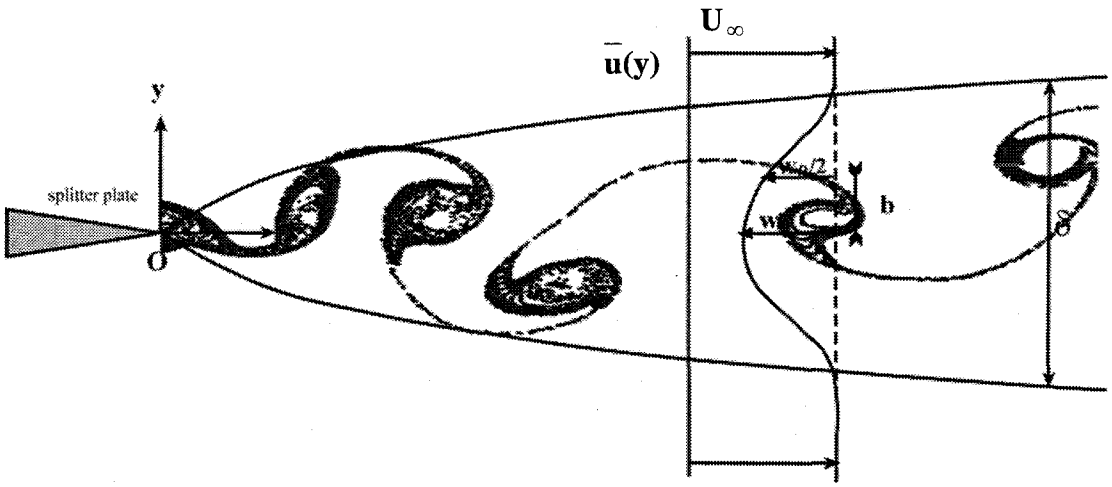

Fig. 4.1. The plane turbulent wake: definition of the nomenclature

For the small-deficit far wake, i.e., $\frac{w_o}{U_\infty} << 1$, in the absence of pressure gradient and at sufficiently large Reynolds numbers, the equations governing the mean velocity field are given by

$$\frac{\partial \bar{u}}{\partial x} + \frac{\partial \bar{v}}{\partial y} = 0$$

$$U_\infty \frac{\partial \bar{u}}{\partial x} = -\frac{\partial}{\partial y}(\overline{u'v'})$$

The conditions under which self-preserving flow is possible can be obtained by substituting the self-preserving distributions into the equation of mean momentum,

$$\frac{U_\infty}{w_o^2} b \frac{dw_o}{dx} f(\eta) - \frac{U_\infty}{w_o} \frac{db}{dx} \eta \frac{df(\eta)}{d\eta} = \frac{dg_{12}(\eta)}{d\eta}$$

leading to

$$\frac{b}{w_o^2}\frac{dw_o}{dx} = \text{constant} \quad \text{and} \quad \frac{1}{w_o}\frac{db}{dx} = \text{constant}$$

whose general solution is $b \propto x^n$ and $w_o \propto x^{n-1}$.

The momentum integral provides an additional constraint that makes the result determinate

$$\theta = \int_{-\infty}^{+\infty} \frac{\bar{u}}{U_\infty}(1-\frac{\bar{u}}{U_\infty})\,dy \approx \int_{-\infty}^{+\infty} \frac{w_o f(\eta)}{U_\infty} b\,d\eta = \frac{w_o b}{U_\infty} \underbrace{\int_{-\infty}^{+\infty} f(\eta)d\eta}_{I_1}$$

$$\Rightarrow w_o b = \text{constant}$$

$$\text{which implies that } n = \frac{1}{2}.$$

Therefore, the normalized velocity and length scales should vary as

$$\frac{U_\infty}{w_o} = A[\frac{x-x_o}{\theta}]^{\frac{1}{2}}$$

$$\frac{b}{\theta} = B[\frac{x-x_o}{\theta}]^{\frac{1}{2}}$$

where x_o is the "mean" virtual origin. The deviation from the power laws can be represented by a shift of the virtual origin of the wake. However, as shown by Townsend[3] (1956), virtual origins for the velocity and length scales are different, even though most experimental works are not sufficiently precise to make this distinction and a mean virtual origin is used.

It should also be noted that the Reynolds number defined by w_o and b is constant. Thus, once turbulent, a plane wake remains turbulent.

Substituting these relations into the momentum equation, we obtain

$$-\frac{1}{2}\frac{B}{A}\frac{d}{d\eta}(\eta f(\eta)) = \frac{d}{d\eta} g_{12}(\eta)$$

In order to proceed, we need a relation between f and g_{12}. This is the classical closure problem encountered for turbulent flows. If we define an eddy viscosity ν_T by

$$-\overline{u'v'} \equiv \nu_T \frac{\partial \bar{u}}{\partial y}$$

and further assume that ν_T is constant, we get

$$\frac{d^2}{d\eta^2}f(\eta)+\alpha\frac{d}{d\eta}(\eta f(\eta))=0$$

$$\text{in which}\quad \alpha\equiv\frac{1}{2}\frac{B^2U_\infty\theta}{\nu_T}$$

$$\text{whose solution is}\quad f(\eta)=\exp(-\frac{1}{2}\alpha\eta^2)$$

In accordance with the definition of w_o and b, we have

$$w(0)=w_of(0)=w_o=\max_\eta(w(\eta))$$

$$w(1)=w_of(1)=w_o\exp(-\frac{1}{2}\alpha)=\frac{w_o}{2}\Rightarrow\alpha=2\ln 2$$

Hence, the mean velocity distribution is

$$\frac{U_\infty-\bar{u}}{w_o}\equiv\frac{w(\eta)}{w_o}=f(\eta)=\exp\left[-(\ln 2)\eta^2\right]$$

Both the observed and predicted velocity distributions resemble in shape the Gaussian error function, except near the edges of the wake where the approach to the freestream velocity is more rapid. As pointed out by Townsend[3] (1956), the assumption of an eddy viscosity used to derive the mean velocity distribution is untenable on physical grounds, and the very good agreement of the Gaussian distribution with observation should be regarded as useful but accidental.

Plugging the Gaussian velocity distribution in the momentum equation gives the following Reynolds shear stress distribution

$$\frac{\tau}{\rho w_o}=-\frac{\overline{u'v'}}{w_o^2}=-g_{12}(\eta)=2\ln 2(\frac{\nu_T}{w_ob})\eta\exp\left[-(\ln 2)\eta^2\right]$$

The rate of approach to equilibrium strongly depends on the initial conditions and the wake generator. Indeed, Townsend[2] (1949) showed that the wake behind a circular

cylinder attains its self-preservation state for $\frac{x}{\theta} \geq 10^3$, whereas equilibrium was attained much earlier for Prabhu and Narasimha's twin plate[4] as well as Pot's flat plate[5] ($\frac{x}{\theta} \geq 350$).

It is useful to consider the development of two-dimensional turbulent wakes in terms of the non-dimensional parameters

$$\Delta^2 \equiv \frac{b^2}{x\theta}$$

and

$$W^2 \equiv \frac{w_o^2 x}{U_\infty^2 \theta}$$

defined by Narasimha and Prabhu[4]. It is expected that in the limit of small defect ratios, the above two parameters tend asymptotically to certain constant values, say $(\Delta^*)^2$ and $(W^*)^2$.

Indeed,

$$\Delta^2 \equiv \frac{b^2}{x\theta} = \frac{(b/\theta)^2}{(x/\theta)} = \frac{B^2\left(\frac{x-x_o}{\theta}\right)}{\left(\frac{x}{\theta}\right)} = B^2\left(1-\frac{x_o}{x}\right) \xrightarrow{\text{for large } x} B^2 \equiv (\Delta^*)^2$$

$$W^2 \equiv \frac{w_o^2 x}{U_\infty^2 \theta} = \frac{(x/\theta)}{(U_\infty/w_o)^2} = \frac{\left(\frac{x}{\theta}\right)}{A^2\left(\frac{x-x_o}{\theta}\right)} = \frac{1}{A^2\left(1-\frac{x_o}{x}\right)} \xrightarrow{\text{for large } x} \frac{1}{A^2} \equiv (W^*)^2$$

In light of experimental data on numerous wake generators, Sreenivasan[6] (1981) concluded that these two parameters are universal numbers characteristic of the plane

[4] Narasimha, R. & Prabhu, A. 1972 Equilibrium and relaxation in turbulent wakes. J. Fluid Mech. **54**, 1-17.

[5] Pot, P.J. 1979 Measurements in a 2-D wake and in a 2-D wake merging into a boundary layer. Data report, NLR TR-79063 U, the Netherlands.

[6] Sreenivasan, K.R. 1981 Approach to self-preservation in plane turbulent wakes. AIAA J.**19**, 1365-1367.

equilibrium wake. On the other hand, experimental results by Wygnanski et al.[7] (1986) indicated that the normalized velocity and length scales were dependent on the initial conditions and the nature of the wake generator.

Wake Generator	Source	W^*	Δ^*	$W^*\Delta^*$
flat plate	Pot	1.63	0.300	0.489
twin plate	Prabhu et al.	1.63	0.300	0.489
circular cylinder	Chapman	1.74	0.288	0.501
circular cylinder	Wygnanski et al.	1.75	0.289	0.506
screen (σ=70%)	Wygnanski et al.	1.67	0.302	0.504
solid strip	Wygnanski et al.	1.88	0.270	0.508
airfoil	Wygnanski et al.	1.56	0.320	0.500
flat plate	Wygnanski et al.	1.71	0.297	0.508

Table 4-1. Effects of the shape of the wake generator on its parameters

The momentum integral equation provides a redundant condition

$$\theta = \int_{-\infty}^{+\infty} \frac{\bar{u}}{U_\infty}\left(1-\frac{\bar{u}}{U_\infty}\right)dy \approx \frac{bw_o}{U_\infty} I_1 \Rightarrow \left(\Delta^*\right)^2\left(W^*\right)^2 I_1^2 = 1 \quad \text{where } I_1 = \int_{-\infty}^{+\infty} f(\eta)d\eta$$

that needs to be satisfied and serves to confirm the values of the wake parameters $\left(\Delta^*\right)^2$ and $\left(W^*\right)^2$.

Furthermore, since all experimenters agree on the universal nature of the mean velocity distribution $f(\eta)$ (even though their fits differ slightly), the integration of the linearized mean momentum equation which yields to

$$-\frac{\overline{u'v'}}{w_o^2} = -g_{12}(\eta) = \frac{\Delta^*}{2W^*}\eta f(\eta)$$

[7] Wygnanski, I., Champagne, F. & Marasli, B. 1986 Structures in two-dimensional, small-deficit, turbulent wakes. J. Fluid Mech. **168**, 31-71.

indicates the influence of the values of the wake parameters on the universality of $g_{12}(\eta)$ and thus on the existence of the wake equilibrium state.

Indeed, since $\frac{\Delta^*}{2W^*}$ varies by 43% between the solid strip and the symmetrical airfoil according to Wygnanski et al.[7], so does $g_{12}(\eta)$ which provides evidence for the lack of universality of the turbulent structures of two-dimensional far wakes.

In addition, using the Gaussian mean velocity distribution and Sreenivasan and Narasimha's values[8] of the wake parameters Δ^* and W^*, we can estimate the maximum value of the normalized Reynolds shear stress

$$\left|\frac{-\overline{u'v'}}{w_o^2}\right|_{max} = \frac{\Delta^*}{2W^*}\frac{1}{\sqrt{2\ln 2}}\exp(-\frac{1}{2}) \approx 0.0474$$

which compares quite well with Prabhu and Narasimha's value[4] (0.045).

Finally, the mean transverse velocity of the equilibrium wake can also be deduced from the continuity equation

$$\frac{\partial \bar{u}}{\partial x} + \frac{\partial \bar{v}}{\partial y} = 0$$

$$\text{with} \quad \frac{U_\infty - \bar{u}}{w_o} \equiv \frac{w(\eta)}{w_o} = f(\eta) = \exp(-\ln 2\eta^2)$$

$$\Rightarrow \frac{\partial \bar{v}}{\partial y} = -\frac{\partial}{\partial x}\left[U_\infty - w_o(x)\exp\{-\ln 2(\frac{y}{b(x)})^2\}\right]$$

Integrating the right-hand side from 0 to y and using the previous laws of the wake as well as the fact that $\bar{v} = 0$ at $y = 0$ by symmetry, a new expression is obtained

$$\bar{v}(x,y) = \underbrace{\left[\frac{-U_\infty}{2\Delta^*(W^*)^3}\right]\left(\frac{\theta_o}{b(x)}\right)^2}_{<0} \underbrace{\int_0^{y/b}\left[1-(2\ln 2)t^2\right]\exp\left[-(\ln 2)t^2\right]dt}_{\substack{>0 \text{ for } y>0 \\ <0 \text{ for } y<0}}$$

This expression simply translates that fluid is entrained in the turbulent wake, hence enabling its growth.

[8] Sreenivasan, K.R. & Narasimha, R. 1982 Equilibrium parameters for two-dimensional turbulent wakes. J. Fluid Eng. **104**, 167-170.

4.1.2. Fully-submerged wake measurements

Digital PIV measurements were made in the deep wake ($z/\theta_o \approx -100$) of the surface-piercing splitter plate to determine its mean flow field, turbulent intensities, and Reynolds stresses. The freestream velocity (33.5 cm/sec), and plate length L (3 m), resulted in a Reynolds number of about 10^6. The boundary layers were not tripped in order to avoid triggering any undesired free-surface effects. But, in the present conditions, the angle of the splitter plate (about 4.5°) was small enough to prevent separation from occurring and large enough to favor earlier transition of the boundary layers to turbulence as dye visualization did reveal. Measurements carried out in the fully-submerged wake showed that the Reynolds number based on the wake width δ, i.e., $Re_\delta \equiv \frac{\Delta U \delta}{\nu}$, was 2500. In this investigation, surface wave amplitudes were small and the water surface remained free of surfactant as indicated by the values of Froude and Weber numbers, that is, respectively 0.15 and 2700, and consequently neither of those effects was expected to be significant.

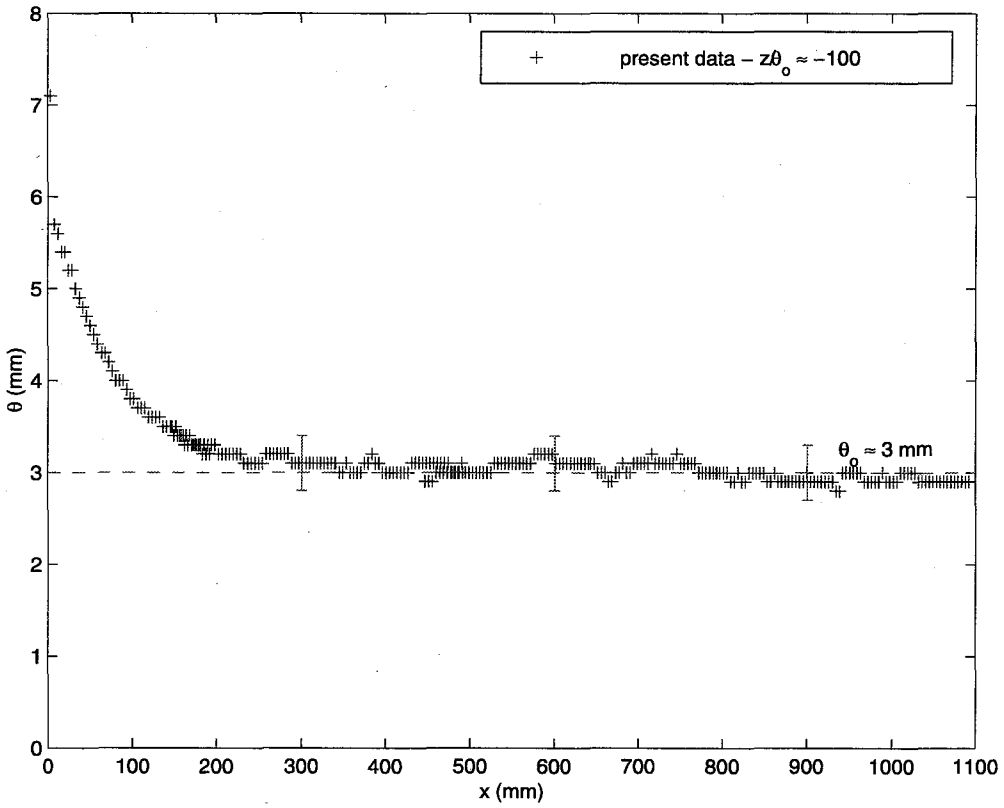

Fig. 4.1. Evolution of the momentum thickness with the downstream distance

(a) behavior of the mean flow in the wake

Data were obtained at distances ranging from 0 to 300 momentum thicknesses downstream of the tip of the splitter plate. The wake momentum thickness is plotted as a function of the downstream distance in Fig. 4.1. As expected, since there is no significant pressure gradient in this flow, except in the near-wake region where the transverse velocity was not negligible at the edges of the measurement region, the momentum thickness was found to be a constant whose value is $\theta_o \approx 3$mm. Fig. 4.1 shows approximately 200 defect velocity profiles obtained for $x/\theta_0 \geq 100$. When normalized, these mean velocity profiles collapse quite well onto a single curve described by the traditional Gaussian error function

$$f(\eta) \equiv \frac{w(\eta)}{w_o} = \exp[-(\ln 2)\eta^2].$$

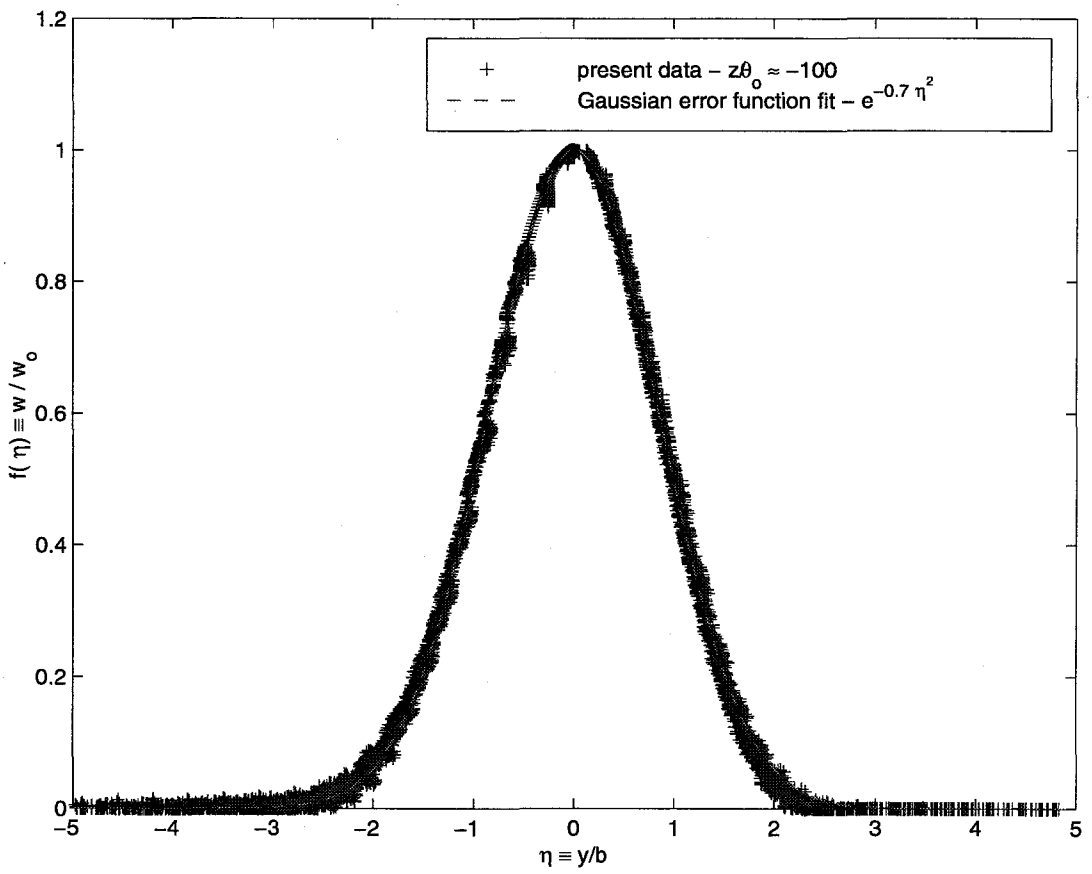

Fig. 4.1. Mean velocity defect distribution for the fully-submerged wake

The wake profiles are found to be closely symmetric, but all the parameters were evaluated using the complete velocity profile rather than one half of it. Furthermore, the defect velocity profiles were plotted for $x/\theta_o \geq 100$, the point after which the non-dimensional parameter Δ^2 reaches its asymptotic state, as shall be seen below. It is interesting to note then that the mean streamwise velocity profile reaches its asymptotic profile quite rapidly, i.e., for $x/\theta_o \geq 100$.

The next two figures, Fig. 4.2 and Fig. 4.3, present the evolution of the two non-dimensional wake parameters Δ^2 and W^2, as defined by Prabhu and Narasimha[4], with the normalized downstream distance.

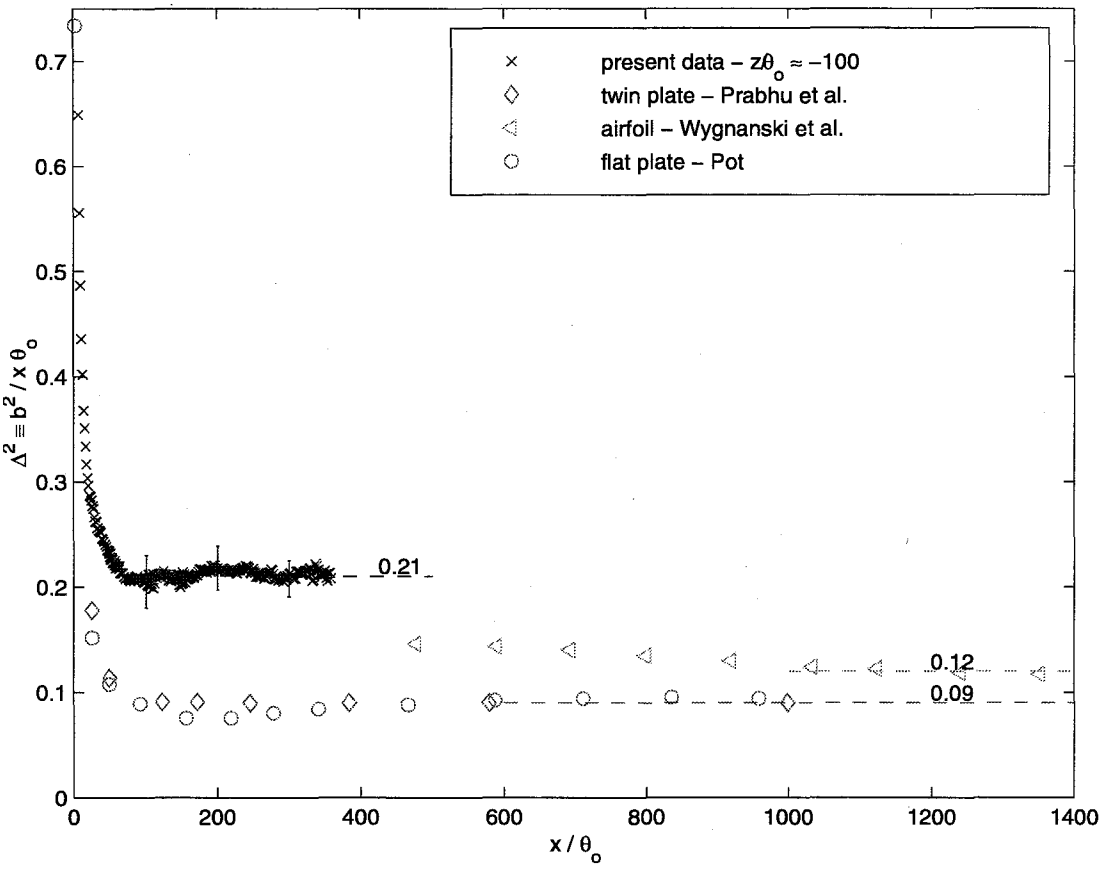

Fig. 4.2. Evolution of the growth rate parameter Δ^2 with the normalized downstream distance x/θ_o

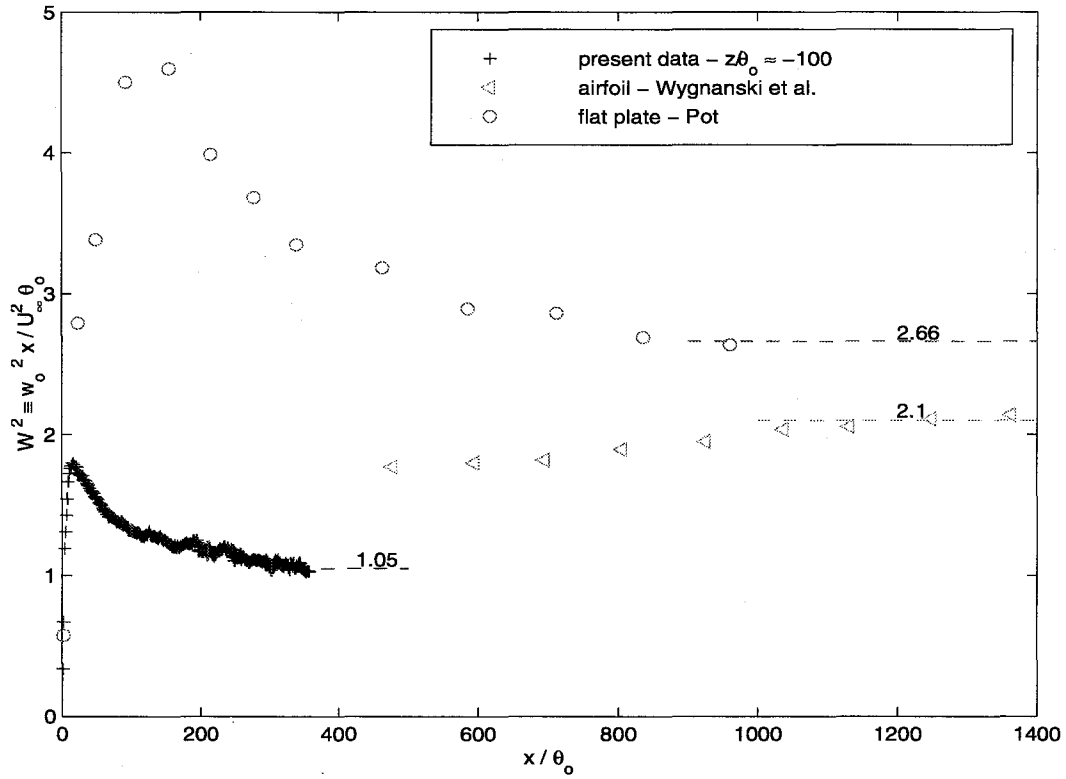

Fig. 4.3. Evolution of the maximum velocity defect parameter W^2 with the normalized downstream distance x/θ_o

Sufficiently far from the wake generator, these two parameters converge toward asymptotic values

$$\left(\Delta^*\right)^2 \approx 0.21, \text{ for } x/\theta_o \geq 100,$$
$$\left(W^*\right)^2 \approx 1.05, \text{ for } x/\theta_o \geq 300.$$

One of the important issues that arise in the discussion of wake development is concerned with the downstream distance from the trailing edge beyond which the wake can be regarded as having reached an asymptotic state. By the asymptotic self-preserving state, we mean here that the mean velocity and the Reynolds-stress distributions are independent of the streamwise position when normalized by the same velocity and length scales. It is interesting to point out that the wake half-width b reaches its asymptotic growth rate much faster than the maximum wake velocity defect w_o. The importance of this issue is reinforced by the fact that the present values

are quite different from those obtained in earlier studies. However, the wake parameters satisfy the momentum integral constraint

$$\left(\Delta^*\right)^2\left(W^*\right)^2 I_1^2 = 0.21*1.05*\frac{\pi}{\ln 2} = 0.9994 \approx 1$$

and are consistent with the higher values of the Reynolds stresses found throughout these experiments, as will be shown in the next section.

Nevertheless, previous researchers did speculate that the scatter found amongst those values was due to measurements too close to the trailing edge. Indeed, it shall be shown in the next section that the turbulent flow quantities become self-similar only for $x/\theta_o \geq 300$ in this study, as well. However, the scatter found in the values of $\left(\Delta^*\right)^2$ observed in the literature (see Ramaprian et al.[9] for instance) and

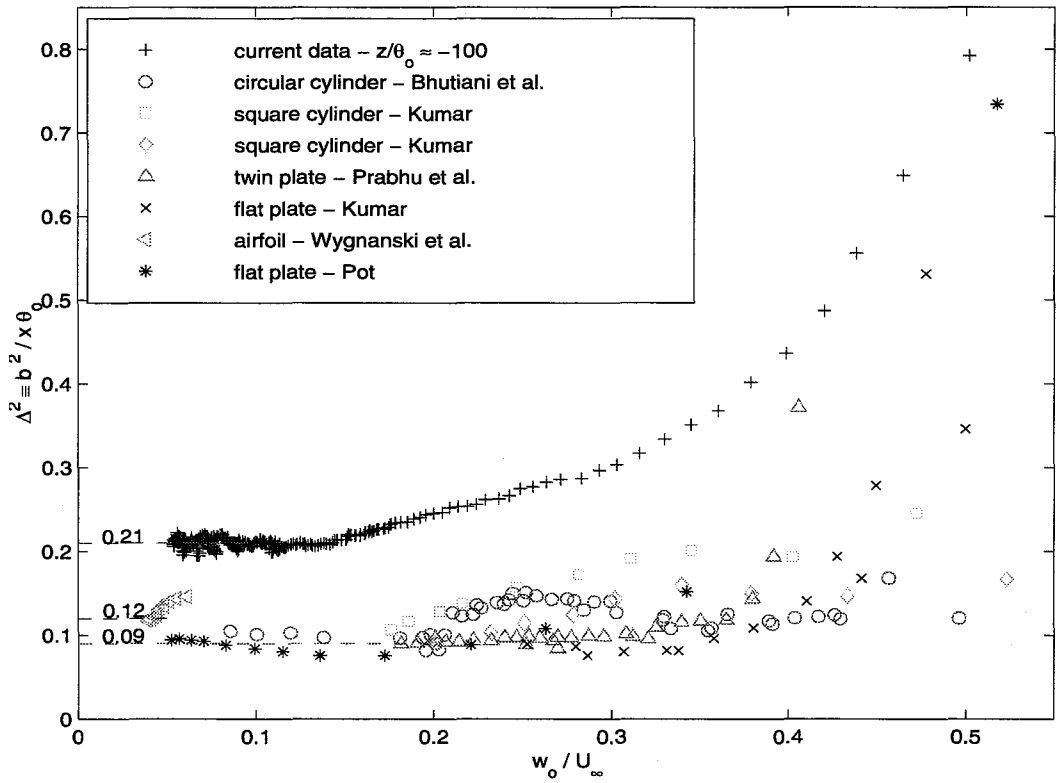

Fig. 4.4. Variation of the growth rate parameter Δ^2 with the maximum defect velocity ratio w_o/U_∞

[9] Ramaprian, B.R., Patel, V.C. & Sastry, M.S. 1982 The symmetric turbulent wake of a flat plate. AIAA J. **20**, 1228-1235.

attributed to measurements being too close to the trailing edge does not appear to hold up here since Δ^2 rapidly converges toward its asymptotic value. In addition, Sreenivasan[6] indicated that scatter might be due to the fact that the ratio w_o/U_∞ was not sufficiently small. He indeed showed that the correction terms in the evaluation of the wake parameters were of the order of $O(w_o/U_\infty)$. The next two plots, Fig. 4.4 and Fig. 4.5, address this issue and show that the "small-deficit wake" approximation is valid at distances much smaller than $x/\theta_o = 300$ for the splitter-plate wake generator. In contrast to the variable routes followed by other wake generators, the variation of the parameters Δ^2 and W^2 with w_o/U_∞ exhibits a simple behavior to approach their asymptotic values for the splitter-plate wake generator. The absence of scatter in the routes followed by Δ^2 and W^2 to approach $(\Delta^*)^2$ and $(W^*)^2$ coupled with the low values of w_o/U_∞ further stress the validity of the asymptotic values found in this study.

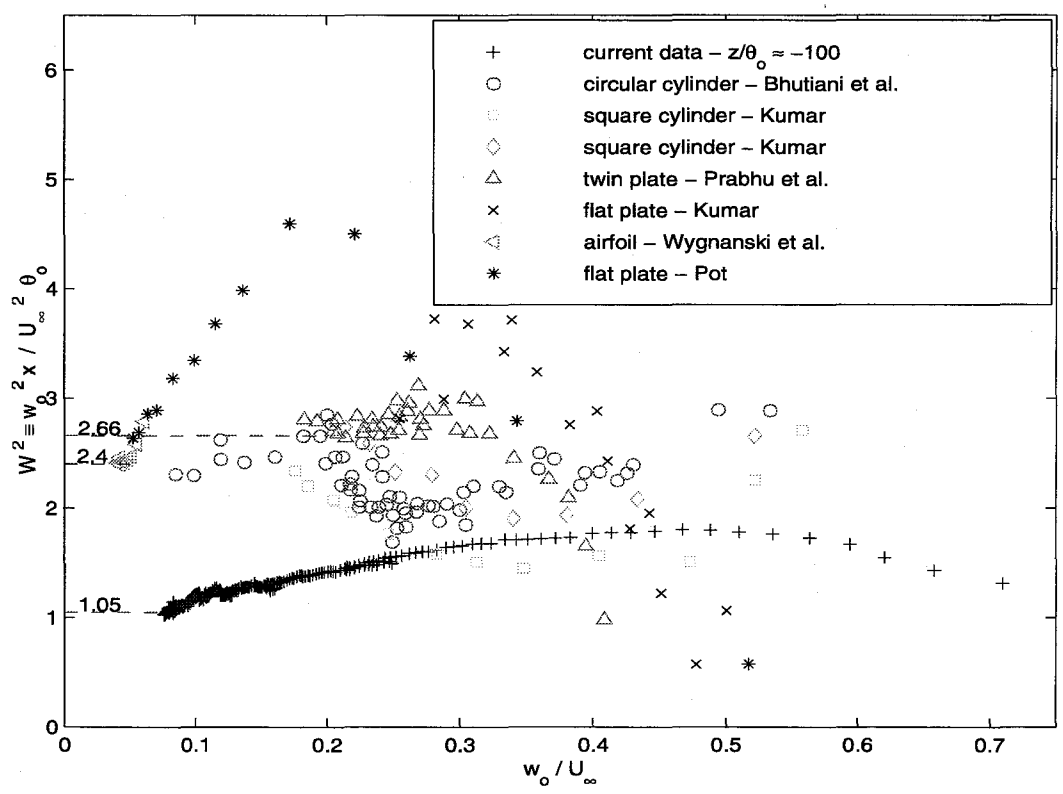

Fig. 4.5. Variation of the maximum velocity defect parameter W^2 with the maximum defect velocity ratio w_o/U_∞

(b) turbulence structure in the wake

The measured distributions of the normalized root-mean-square of the streamwise velocity fluctuations $g_{11}(\eta)$ are plotted at several downstream stations in Fig. 4.1.

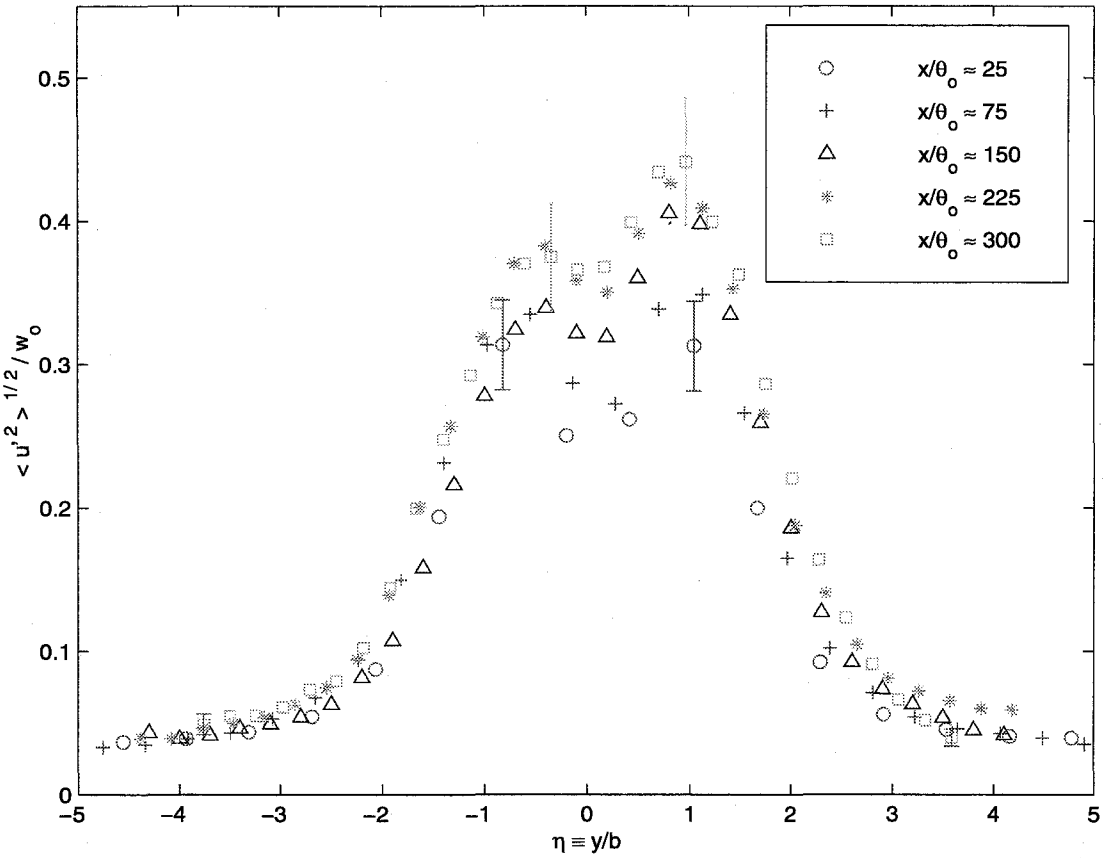

Fig. 4.1. Distribution of the streamwise velocity fluctuations at several downstream stations

The degree to which the wake approaches a self-preserving state can be determined from Fig. 4.2, which shows the downstream variation of $\sqrt{\overline{u'^2_{max}}}/w_o$. For a self-preserving state, this statistic should be a constant, independent of x. The present results show that this is indeed the case at the end of the intermediate region ($x/\theta_o \geq 300$). It is interesting to note that the maximum normalized streamwise velocity fluctuation increases toward its far-wake value while this quantity was found to decrease toward its asymptotic value in previous experiments[7]. Furthermore, in

previous mixing-layer experiments[10], the values of $\sqrt{u'^2_{max}}/\Delta U$ were found to increase with the downstream distance for nonturbulent boundary layers whereas they were found to decrease for turbulent boundary layers. In addition, the values of the maximum normalized root-mean-square of the streamwise velocity fluctuations did converge toward the same value at large downstream stations ($x/\theta_o \geq 10^3$) for both turbulent and nonturbulent boundary layers. We can conjecture that the state of the boundary layers, being turbulent but not fully-developed, could be an important factor in the evolution of the wake since this was a major difference between this and the previous studies. Furthermore, it is an implicit assumption in such studies that the behavior of a turbulent flow can be characterized by local flow parameters, at least in a statistical sense, at high-enough Reynolds numbers.

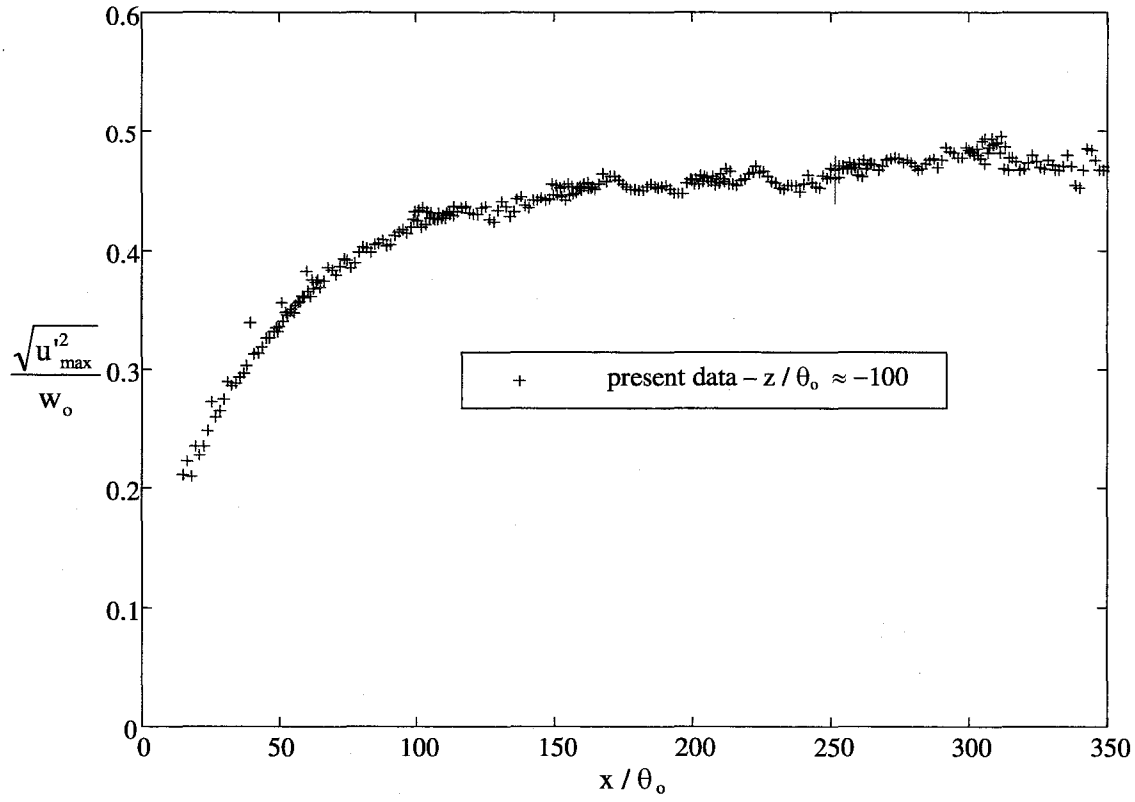

Fig. 4.2. The downstream variation of $(g_{11})_{max}$ for the fully-submerged wake

[10] Browand, F.K. & Latigo, B.O. 1979 Growth of the two-dimensional mixing layer from a turbulent and a nonturbulent boundary layer. Phys. Fluids **22(6)**.

The requirement that the local Reynolds number must be large enough stems from the need to have Reynolds stresses dominate viscous stresses, but also in such a way that three-dimensional small scales can be generated and sustained. Based on a relatively-well-defined mixing transition in shear layers[11] and other shear flows, Dimotakis[12] proposed the following minimum local Reynolds number

$$\mathrm{Re}_\delta \equiv \frac{\Delta U \delta}{\nu} \geq 10^4$$

or so, after which turbulence is *fully-developed.* An examination of the present and previous wake studies reveals that the local Reynolds numbers fall short of the aforementioned criterion. In this respect, the scatter found amongst the values of the resulting wake parameters might also be Reynolds-number dependent.

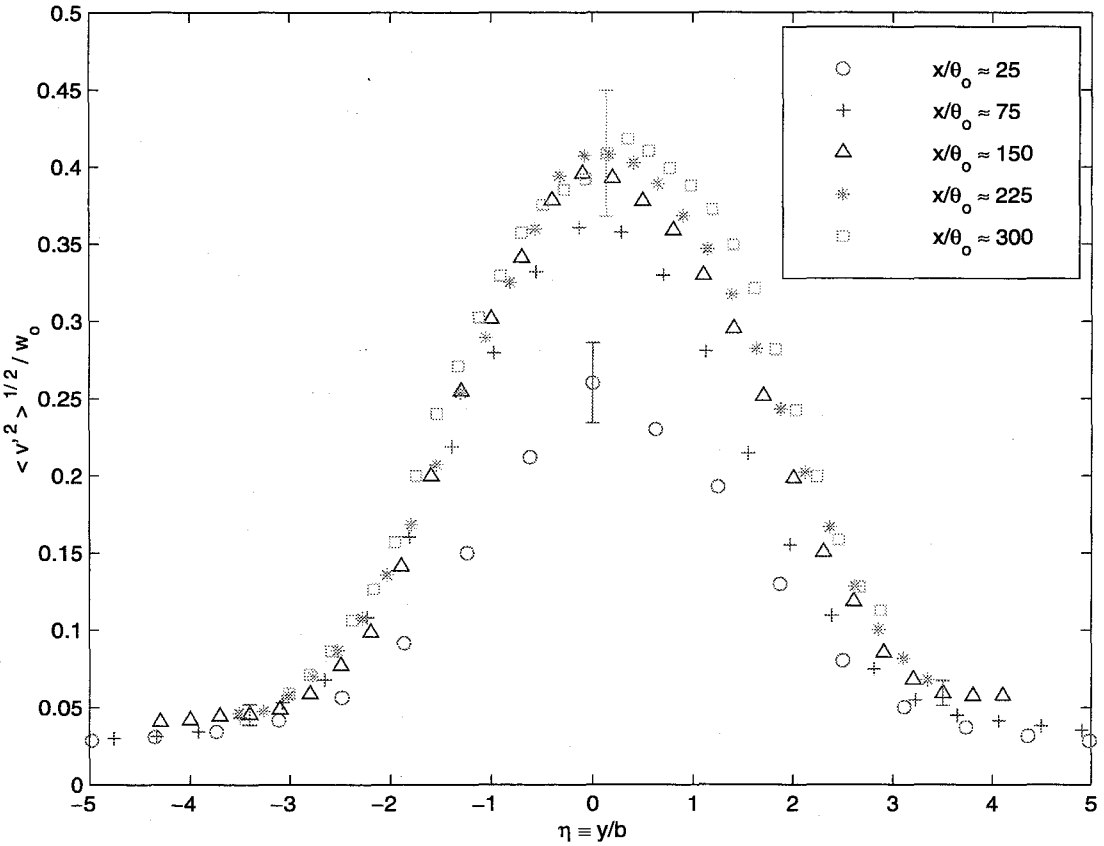

Fig. 4.3. Distribution of the transverse velocity fluctuations at several downstream stations

[11] Konrad, J.H. 1976 An experimental investigation of mixing in two-dimensional turbulent shear flows with applications to diffusion-limited chemical reactions. Ph.D. thesis, California Institute of Technology, Pasadena.

[12] Dimotakis, P.E. 1993 Some issues on turbulent mixing and turbulence. GALCIT report **FM93-1a.**

Similar results were obtained for the distributions of the normalized root-mean-square of the transverse velocity fluctuations $g_{22}(\eta)$ and the normalized Reynolds stresses $g_{12}(\eta)$ (see Fig. 4.3 and Fig. 4.4). In particular, the Reynolds stress profile also attains its theoretical asymptotic profile at the end of the intermediate region. Using the Gaussian mean velocity distribution and the values of the wake parameters Δ^* and W^* obtained hereby, the maximum value of the normalized turbulent Reynolds stress was estimated to be

$$\left|\frac{-\overline{u'v'}}{w_o^2}\right|_{max} = \frac{\Delta^*}{2W^*}\frac{1}{\sqrt{2\ln 2}}\exp(-\frac{1}{2}) \approx 0.11$$

which compares quite well with the experimental values found at the end of the intermediate region as shown in Fig. 4.4.

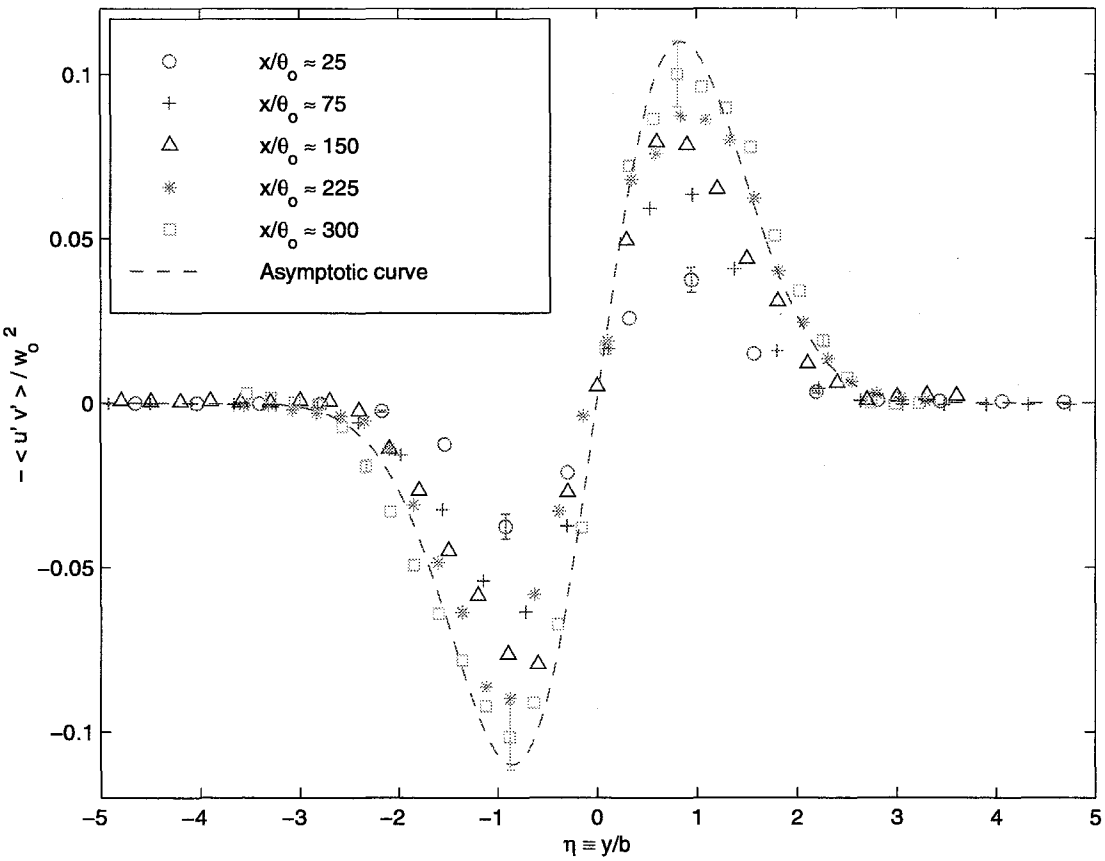

Fig. 4.4. The measured distribution of the turbulent Reynolds stress at several downstream stations

The present results would give credence to the universal equilibrium concept suggested by Sreenivasan and Narasimha[8], except that the asymptotic values of the constants given by these authors were quite different. Therefore, these results indicate that the normalized characteristic velocity and length scales as well as the normalized distributions of the Reynolds stresses depend on the inflow conditions or the nature of the wake generator. In contrast, the shape of the normalized mean velocity profile is independent of these conditions. As has been pointed out above, it is believed that the state of the boundary layers, turbulent but not fully-developed, and the relatively low value of the Reynolds number are some of these important conditions resulting in such different, but consistent, wake parameters.

(c) turbulent features of the wake

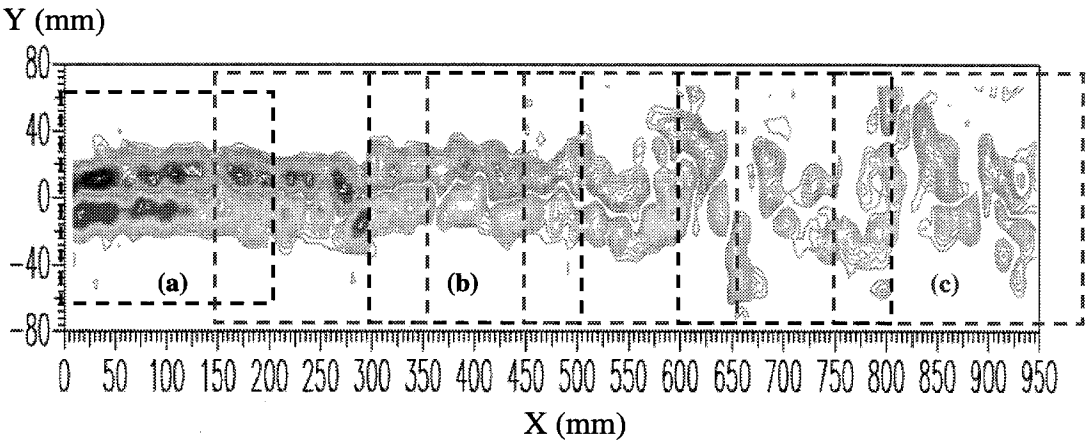

Fig. 4.1. Composite instantaneous normal vorticity contours at $z/\theta_o \approx -100$

Fig. 4.1 shows a typical "instantaneous" vorticity field of the fully-submerged wake. In fact, this picture is made of several instantaneous vorticity fields captured in overlapping measurement regions (6 dashed rectangles), which combine into a mosaic of the entire test section at $z/\theta_o \approx -100$. The transverse scale, i.e., Y, was considerably stretched to favor the visibility of the structures. This figure sheds some light on the turbulent features of the wake behind the splitter plate. The turbulent boundary layers on the two sides of the splitter plate merge slowly and transform into the wake as the sudden disappearance of the wall shear stress diffuses outward. Regions of oppositely-signed vorticity are apparent on each side of the wake with little mixing across the wake centerline until $x = 600\,\text{mm}\,(x/\theta_o \approx 200)$. This

interesting aspect was also pointed out by Chevray and Kovasznay[13] in their investigation of the turbulent wake behind a flat plate when they noticed that the large scale quasi-periodic motion often associated with the wakes of two-dimensional blunt bodies was conspicuously absent. Then, the turbulent wake seems to "break up" and mixing is enhanced along the centerline as the wake evolves downstream with vortical structures reminiscent of the Kàrmàn vortex street. This interesting observation was addressed by Wygnanski et al.[7] who pointed out that long distances are required in small-deficit, plane wakes for unstable waves to amplify.

Fig. 4.2 presents three instantaneous vorticity fields captured at different stages in the development of the wake. The associated measurement regions, indicated by the letters (a), (b), and (c) in Fig. 4.1, correspond to the near, early intermediate and late intermediate fields respectively. These images capture in further detail the evolution of the turbulent structures of the wake. Image (a) shows how the turbulent boundary layers on the two sides of the splitter plate merge slowly and transform into the wake. Image (b) shows how the two shear layers "break up" into "individual" vortical structures, as regions of oppositely-signed vorticity cross-diffuse into one another at certain locations in the wake. Image (c) shows the resulting large-scale structures, which are reminiscent of the Kàrmàn vortex street.

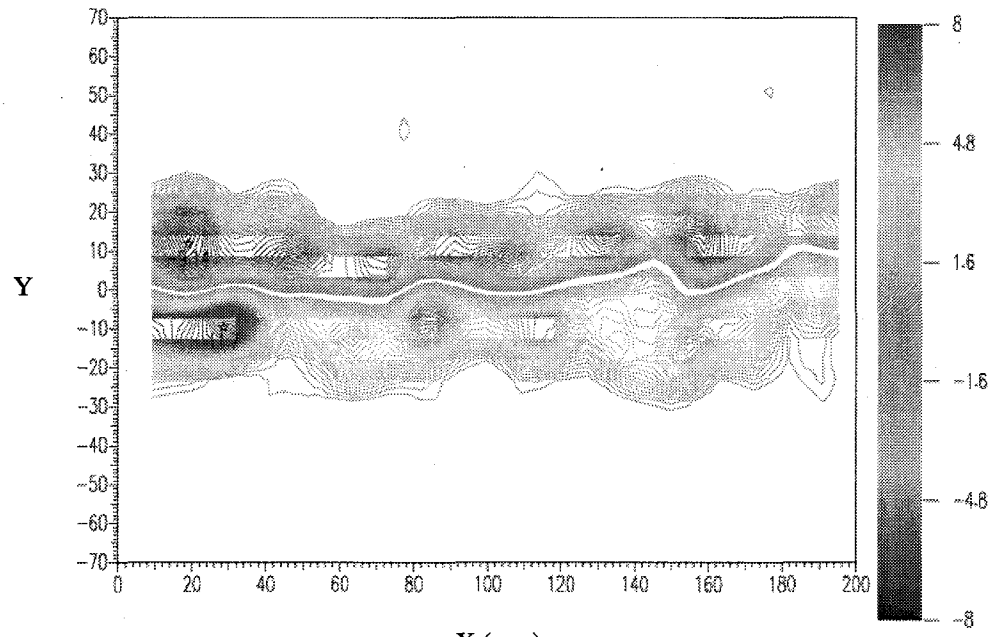

(a)

[13] Chevray, R. & Kovasznay, L.S.G. 1969 Turbulence measurements in the wake of a thin flat plate. AIAA J. **7**, 1641-1643.

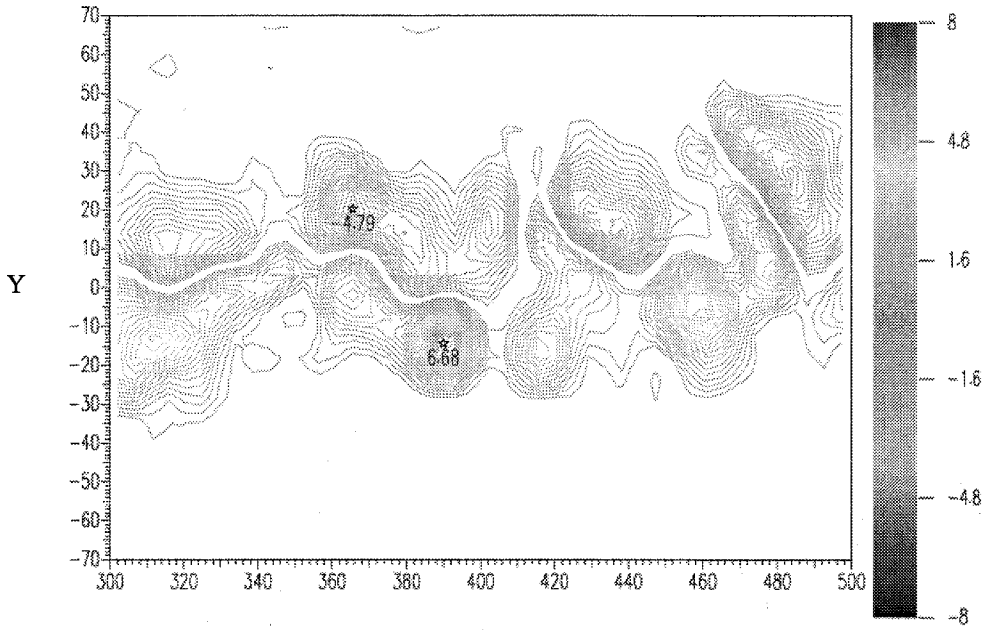

(b)

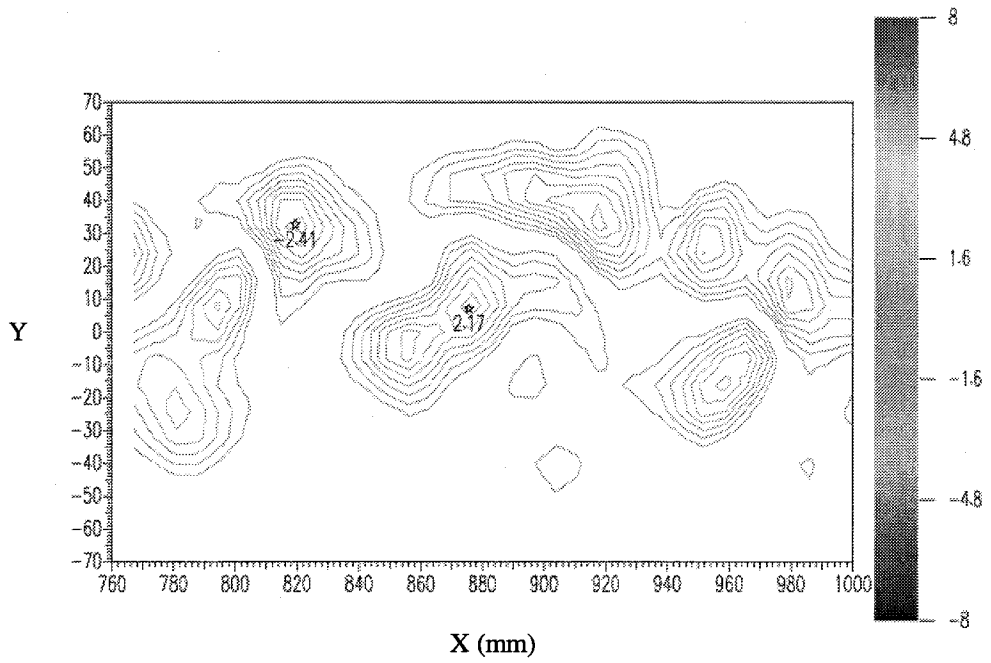

(c)

Fig. 4.2. Instantaneous normal vortical fields at different stages for the fully-submerged wake: (a) $0 \leq x \leq 200$, (b) $300 \leq x \leq 500$, (c) $770 \leq x \leq 1000$, with x in mm.

4.2. Free-surface turbulent wakes

4.2.1. Flow-normal plane measurements

(a) behavior of the mean flow in the wake

Data were acquired in y-z flow-normal planes at different downstream stations ($x/\theta_o \approx$ 85, 165, 250 and 330) in order to probe the spatial extent of the free-surface influence on the underlying turbulent wake and thus guide the positioning of our x-y surface-parallel planes in the near-surface region.

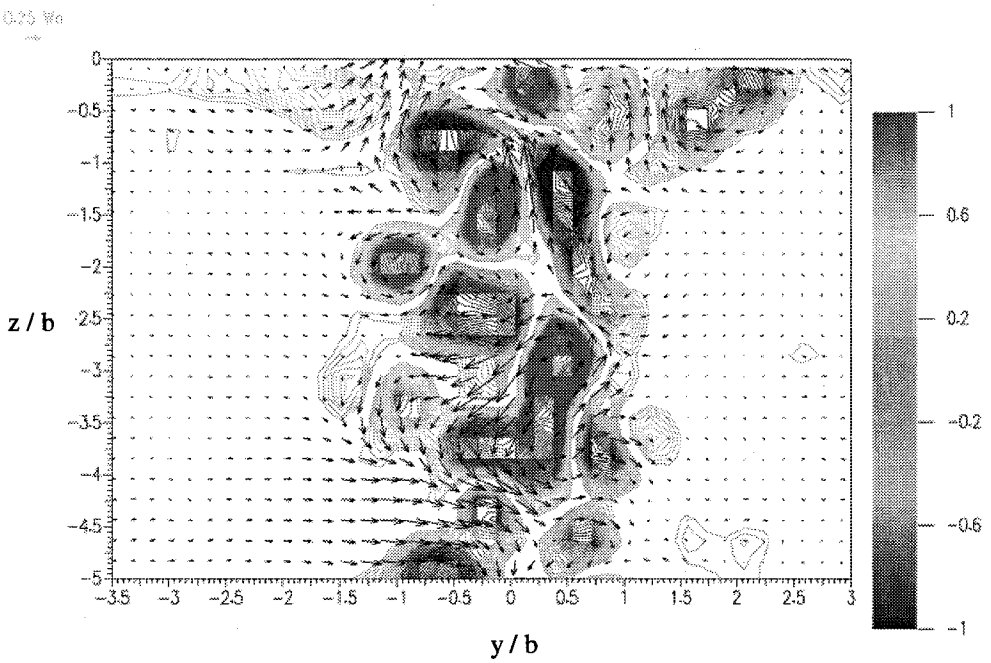

Fig. 4.1. Instantaneous velocity & vorticity fields in the flow-normal plane at $x/\theta_o \approx 165$

Fig. 4.1 shows a representative instantaneous vorticity field on which its associated velocity field is superimposed obtained in such a flow-normal plane at $x/\theta_o \approx$ 165. The flow is normal to the page; z = 0 is at the free surface. Contour plots of the normalized streamwise vorticity $(\omega_x/(w_o/b))$ indicate that the wake is composed of numerous streamwise vortical structures believed to originate from the plate's turbulent boundary layers. It also appears from this instantaneous flow picture that the wake widens at the free surface. These instantaneous measurements depicted

here are representative of the wake flow but they do not necessarily encompass all possible flow features observed in the wake. In order to obtain a better picture of the underlying mean characteristics of this flow, long-term averages over thousands of realizations were performed at these stations ($x/\theta_o \approx$ 85, 165, 250 and 330).

Long-time averages (of six minutes that is about 5,000 image pairs) clearly reveal the presence of two counter-rotating streamwise secondary flows in the near-surface region persisting at all stations (as shown in Fig. 4.2). Fig. 4.3 and Fig. 4.4 show the distributions of the mean streamwise vorticity respectively along a transverse cut running through the core centers ($z/b \approx -0.25$) and along a normal cut running through a core center from the free surface to the fluid bulk ($y/b \approx \pm 1.75$). The first figure indicates that the mean streamwise vorticity profiles reach self-similarity for $x/\theta_o \geq 165$ with $\left(\overline{\omega_x}\right)_{max}/(w_o/b) \approx 0.9$ at $(y/b, z/b) \approx (\pm 1.75, -0.25)$. These values are of the same order of magnitude as that obtained for the mean normal vorticity, i.e., $\left(\overline{\omega_z}\right)_{max}/(w_o/b)$ (≈ 0.7) (see Fig. 4.3). The next figure quantifies the depth to which these secondary flows extend below the free surface. Their region of influence, also called "surface layer" in the literature, is about 1b or roughly $5\theta_o$ in the mean (that is, at the middle of the test section). The latter result is crucial to the positioning of our x-y surface-parallel measurement planes in the near-surface region and thus to investigate the wake in the *surface layer*. The instantaneous vortical structures present in the deep wake canceled out during the averaging process as was expected if one is to obtain a fully-submerged turbulent wake two-dimensional in the mean. An interesting question that arises is concerned with the origin of these near-surface secondary flows. This issue will be tackled extensively in section 4.2.3 with the use of the mean streamwise vorticity equation. In addition, in contrast to previous free-surface flow studies using single-point measurement techniques, new light will also be shed on the instantaneous flow features using the spatio-temporal information obtained through the intensive use of digital PIV.

The velocity fields depicted in Fig. 4.2 show some of the hallmarks of a vortex pair interacting with a flat shear-free boundary such as the orbital motions observed in the flow beneath the free surface. The now well known *surface currents*[14] can be simply understood in terms of mean induced velocity field of the secondary flows at the free-surface boundary in this context. As pointed out by Walker[15], these *surface currents* appear to be ubiquitous features of turbulent free-surface flows.

[14] Anthony, D.G. & Willmarth, W.W. 1992 Interaction of a submerged jet with a free surface. J. Fluid Mech. **243**, 699-720.

[15] Walker, D.T. 1997 On the origin of the 'surface currents' in turbulent free-surface flows. J. Fluid Mech. **339**, 275-285.

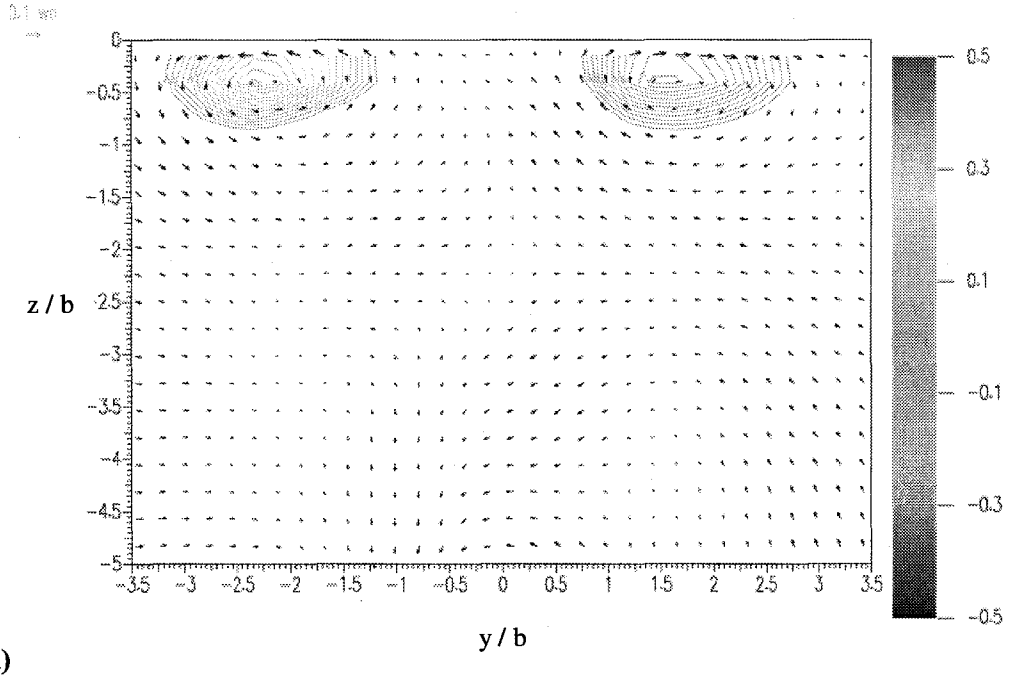
z / b
y / b
0
-0.5
-1
-1.5
-2
-2.5
-3
-3.5
-4
-4.5
-5
-3.5 -3 -2.5 -2 -1.5 -1 -0.5 0 0.5 1 1.5 2 2.5 3 3.5
0.5
0.3
0.1
-0.1
-0.3
-0.5

(a)

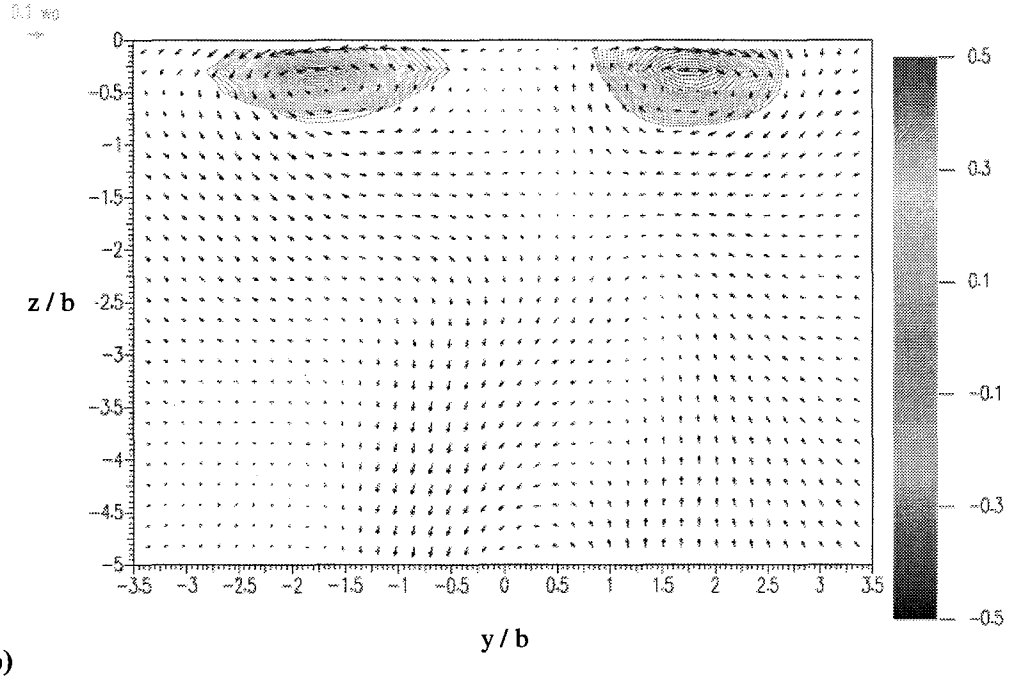
z / b
y / b
0
-0.5
-1
-1.5
-2
-2.5
-3
-3.5
-4
-4.5
-5
-3.5 -3 -2.5 -2 -1.5 -1 -0.5 0 0.5 1 1.5 2 2.5 3 3.5
0.5
0.3
0.1
-0.1
-0.3
-0.5

(b)

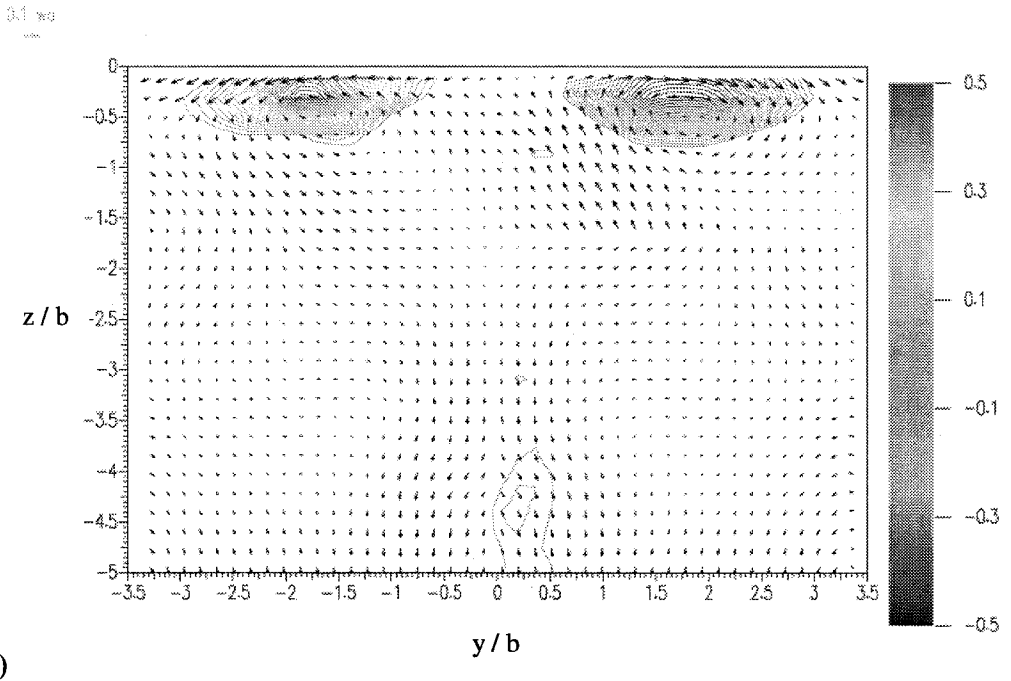

(c)

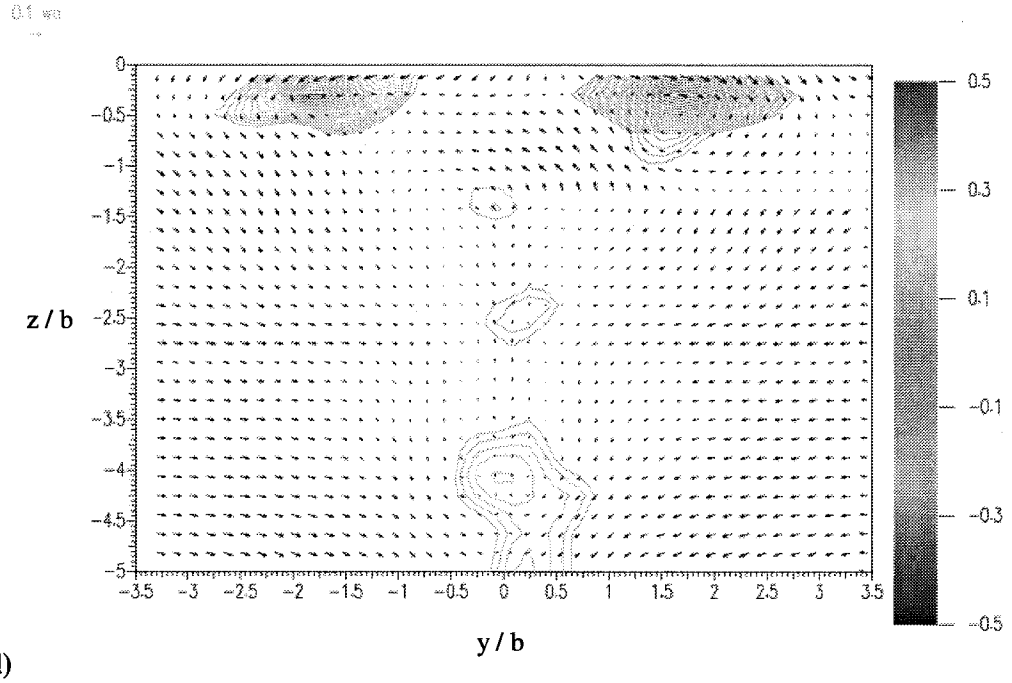

(d)

Fig. 4.2. Normalized Reynolds-averaged velocity & vorticity fields obtained in the flow-normal planes: (a) $x/\theta_o \approx 85$, (b) $x/\theta_o \approx 165$, (c) $x/\theta_o \approx 250$, (d) $x/\theta_o \approx 330$

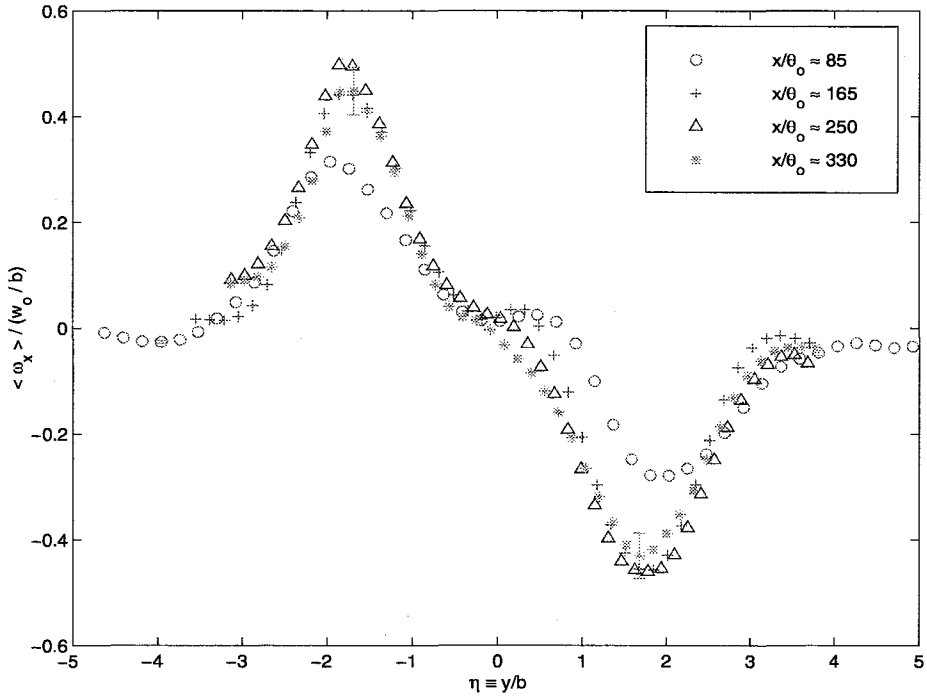

Fig. 4.3. Distribution of the mean streamwise vorticity along $z/b \approx -0.25$

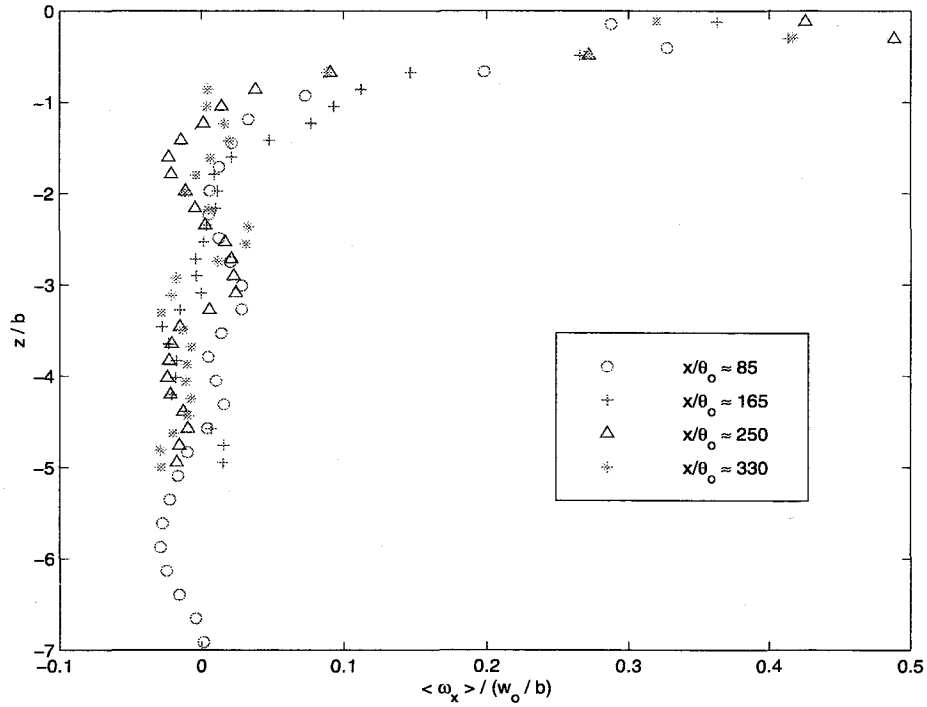

Fig. 4.4. Distribution of the mean streamwise vorticity along $y/b \approx \pm 1.75$

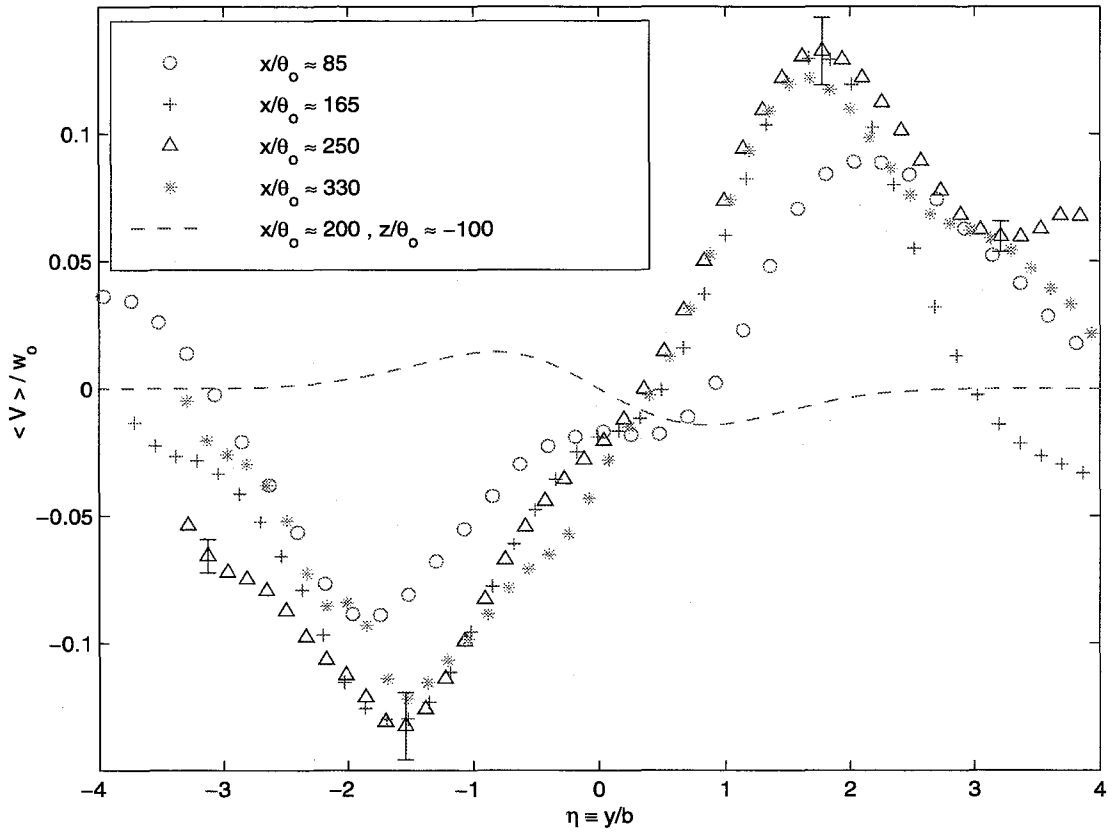

Fig. 4.5. Profiles of the Reynolds-averaged transverse velocity at $z/\theta_o \approx -1$

Plotting the mean transverse velocity profiles in the surface-parallel plane just beneath the free surface, that is, at $z/\theta_o \approx -1$, clearly reveals the presence of these outward currents adjacent to the free surface. Fig. 4.5 shows that these near-surface velocity profiles have similar shape as those found in the deep turbulent wake, but they are of opposite sign and of larger amplitude. The data obtained just beneath the free surface thus show the mean flow to be everywhere outward, away from the wake centerline, rather than entraining at the edges and enabling its growth as in the case of the fully-submerged wake. Therefore, one issue that naturally arises is the influence of the near-surface secondary flows and their associated free-surface currents on the development of the wake (its growth in particular) and its mean and turbulent properties at the free surface. This question will be addressed in the following section with the help of surface-parallel measurements in the *surface layer*.

(b) turbulence structure in the wake

Measurements of the turbulent transverse and normal velocity fluctuations as well as the streamwise vorticity fluctuations were also obtained in these flow-normal planes.

The contours of the root-mean-square of the normalized transverse velocity fluctuations are plotted in Fig. 4.1. The magnitude of $\sqrt{\overline{v'^2}}/w_o$ remains essentially constant with the depth in the central region of the wake for $|y/b| \leq 1.5$ but increases along the edges of the wake for $1.5 \leq |y/b| \leq 3.5$ as the free surface is approached ($|z/b| \leq 0.5$). Comparison between the profiles of the root-mean-square of the normalized transverse velocity fluctuations at constant depth near the free surface ($z/\theta_o \approx -1$) and in the fluid bulk ($z/\theta_o \approx -30$) confirms this analysis. Furthermore, Fig. 4.2 also reveals the difference in shape between the profiles of the free-surface wake and its fully-submerged counterpart. Indeed, $\sqrt{\overline{v'^2}}/w_o$ has a Gaussian-shaped profile evolving toward its asymptotic curve in the fully-submerged wake while its profile at the free surface is much fuller ranging from -3b to 3b with a non-Gaussian but symmetric characteristic shape.

The contours of the root-mean-square of the normalized normal velocity fluctuations are also plotted in Fig. 4.3. The magnitude of $\sqrt{\overline{w'^2}}/w_o$ decreases sharply as the free surface is approached while its profile widens at the same time. Similar comparison between the profiles of the root-mean-square of the normalized normal velocity fluctuations at constant depth near the free surface ($z/\theta_o \approx -1$) and in the fluid bulk ($z/\theta_o \approx -30$) clearly shows this sharp decrease by a factor of about 3 (i.e., 66%) as the free surface is approached (cf Fig. 4.4). The shape of this distribution remains the same, that is, a double-hump profile, but it is flattened and it increases to a width of about 6b as the free surface is reached.

A striking feature of these results is the free-surface anisotropy. At this low Froude number, the free surface seems to behave much like a flat, shear-free boundary and, hence, vertical momentum is deflected in the horizontal direction by the free surface. This results in a reduction in $\sqrt{\overline{w'^2}}/w_o$ and an increase in $\sqrt{\overline{v'^2}}/w_o$. This trend will be further detailed when the results obtained in the streamwise direction are presented in the next section.

The values of the Reynolds stress $\overline{v'w'}$, which were also measured, were under-resolved in this study as they were expected[16] to be nearly zero in both the deep and free-surface wakes.

Fig. 4.5 shows the contours of the root-mean-square of the normalized streamwise vorticity fluctuations. The magnitude of $\sqrt{\overline{\omega'^2_x}}/(w_o/b)$ remains essentially constant with the depth until the near-free-surface region ($|z/b| \le 0.75$). As the free surface is approached, it decreases in the central region of the wake for $|y/b| \le 1.5$ while it increases along the edges of the wake for $1.5 \le |y/b| \le 3.5$. Comparison between the profiles of the root-mean-square of the normalized streamwise vorticity fluctuations at constant depth near the free surface ($z/\theta_o \approx -1$) and in the fluid bulk ($z/\theta_o \approx -30$) confirms the decrease of $\sqrt{\left(\overline{\omega'^2_x}\right)_{max}}/(w_o/b)$ by a factor of about 2. Fig. 4.6 also shows that the shape of the profiles are similar (with a double hump) but it is flattened and increases to a width of about 6b as the free surface is reached.

These results are consistent with previous and present experimental results. Indeed, only the surface-normal component of the vorticity remains at a flat free surface and forces vortex lines to terminate normal to the surface. Thus, $\sqrt{\overline{\omega'^2_x}}/(w_o/b)$ decreases as the free surface is reached as vortex filaments tend to connect to the free surface. However, the surface-normal termination of vortex lines applies only at the free surface and immediately below the surface, surface-parallel vorticity can exist without violating any surface condition. The presence of higher values of $\sqrt{\overline{\omega'^2_x}}/(w_o/b)$ for $1.5 \le |y/b| \le 3.5$ and $|z/b| \le 0.75$ is furthermore consistent with the discovery of streamwise vortical structures present at the edges of the wake at the free surface. The reader is referred to section 4.2.3(b)(ii) for a closer look at these instantaneous near-surface streamwise vortical structures.

[16] Walker, D.T., Chen, C.-Y. & Willmarth, W.W. 1995 Turbulent structure in free-surface jet flows. J. Fluid Mech. **291**, 223-261.

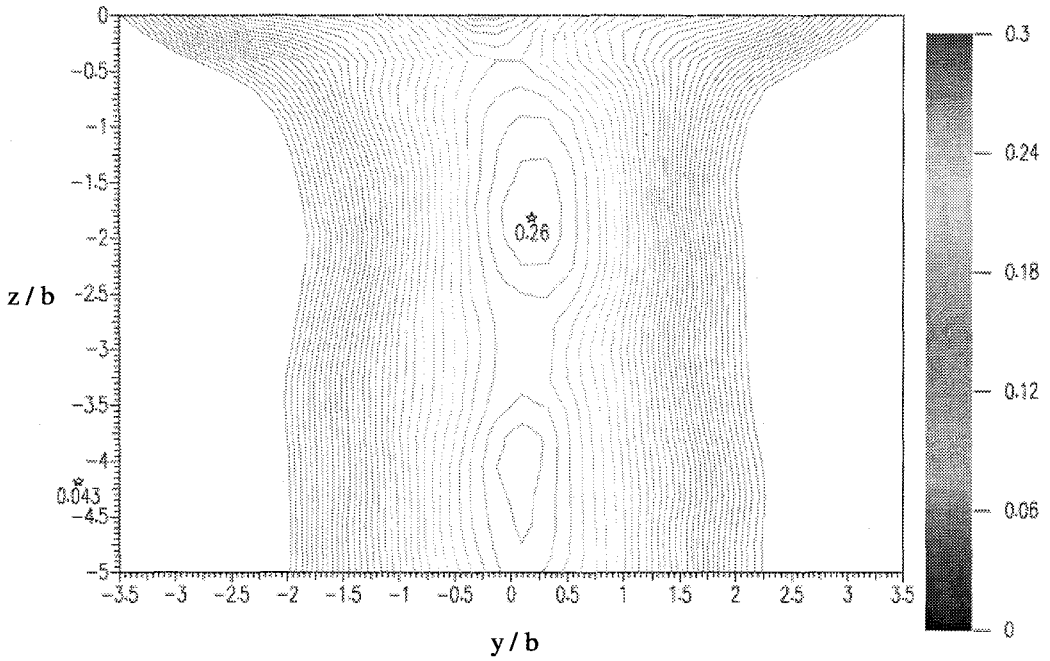
0
-0.5
-1
-1.5
-2
-2.5
-3
-3.5
-4
-4.5
-5
z / b
0.26
0.043
-3.5 -3 -2.5 -2 -1.5 -1 -0.5 0 0.5 1 1.5 2 2.5 3 3.5
y / b
0.3
0.24
0.18
0.12
0.06
0

(a)

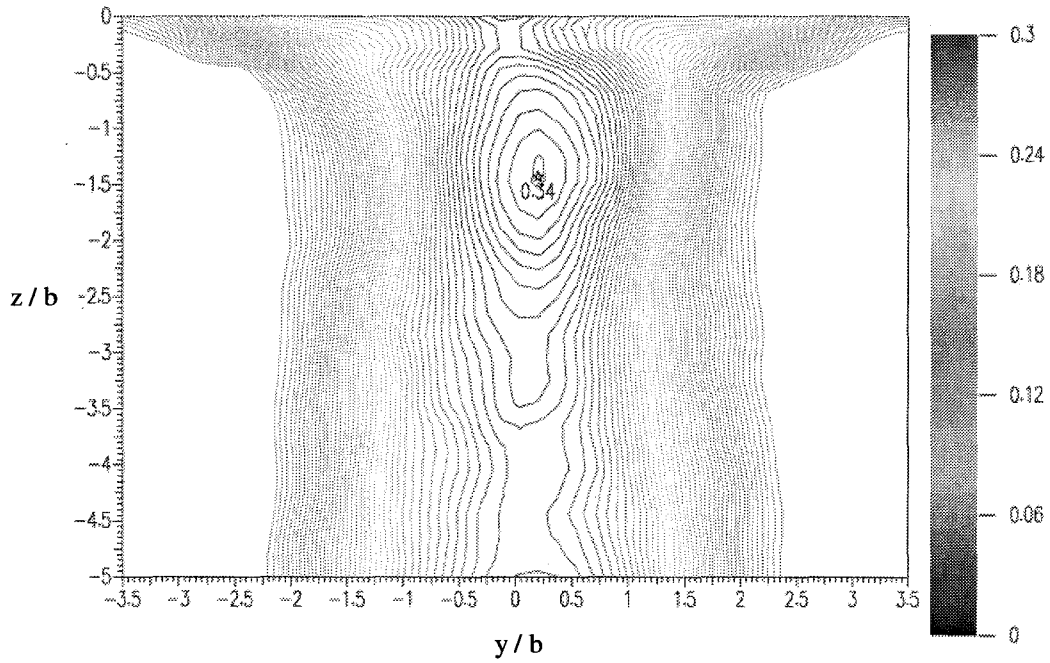
0
-0.5
-1
-1.5
-2
-2.5
-3
-3.5
-4
-4.5
-5
z / b
0.34
-3.5 -3 -2.5 -2 -1.5 -1 -0.5 0 0.5 1 1.5 2 2.5 3 3.5
y / b
0.3
0.24
0.18
0.12
0.06
0

(b)

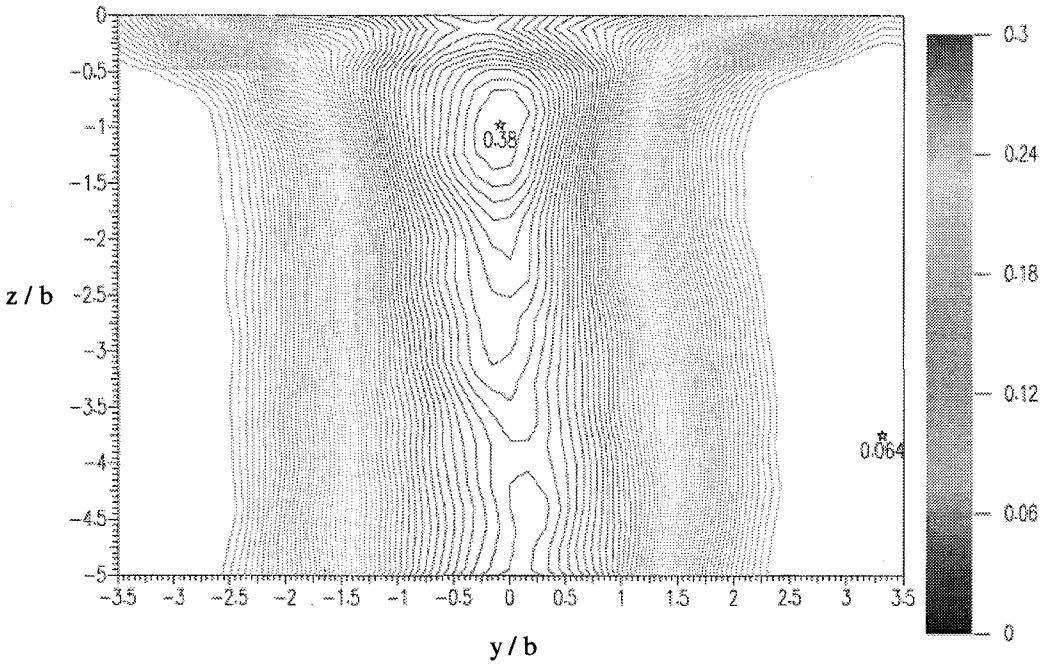

(c)

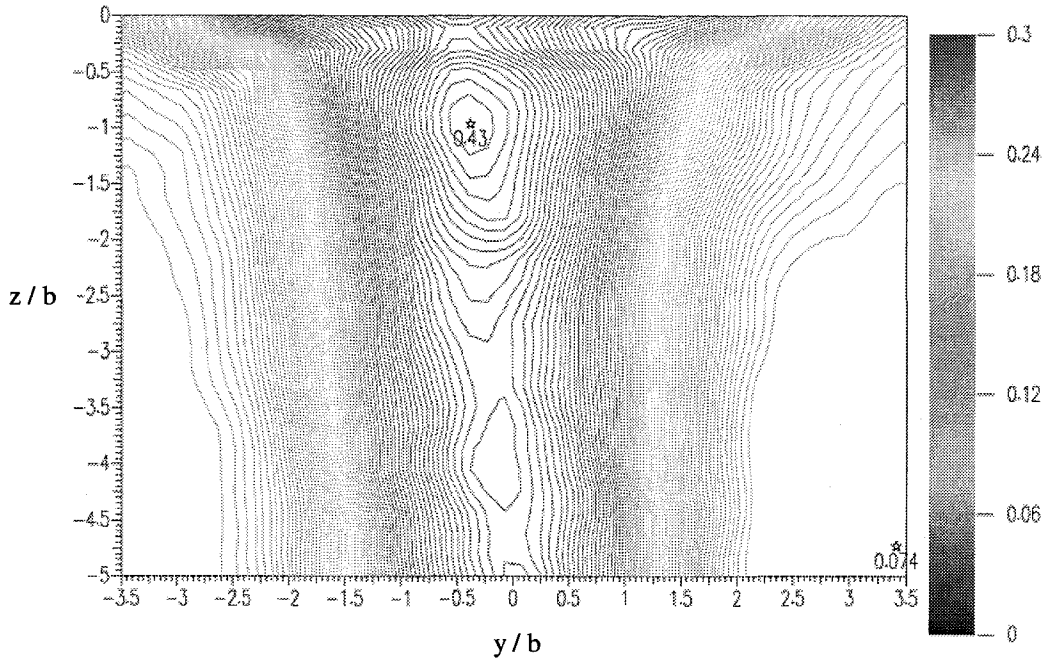

(d)

Fig. 4.1. Contours of the normalized transverse velocity fluctuations in the flow-normal planes: (a) $x/\theta_o \approx 85$, (b) $x/\theta_o \approx 165$, (c) $x/\theta_o \approx 250$, (d) $x/\theta_o \approx 330$

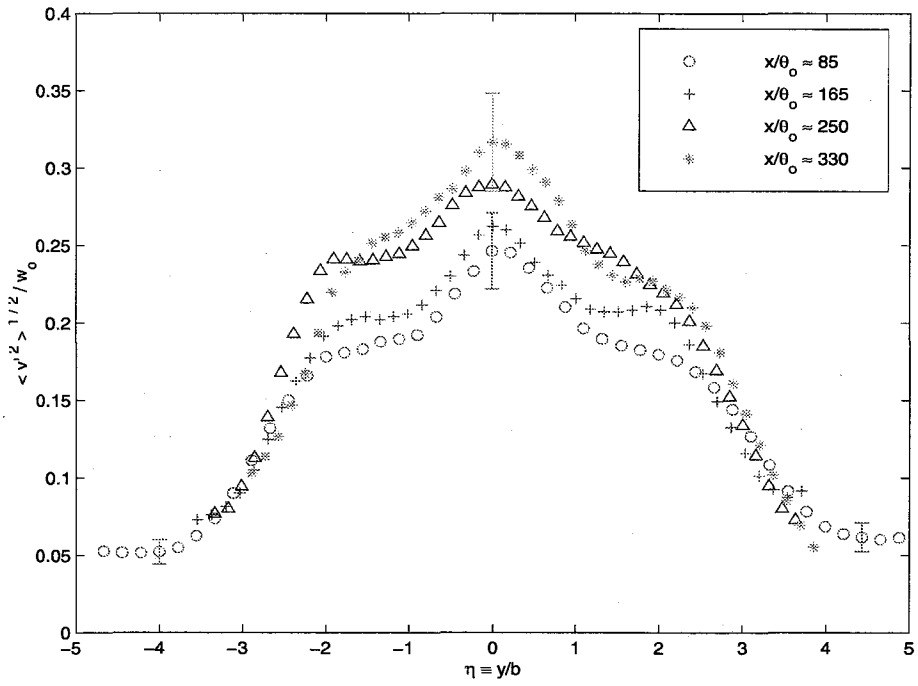

(a)

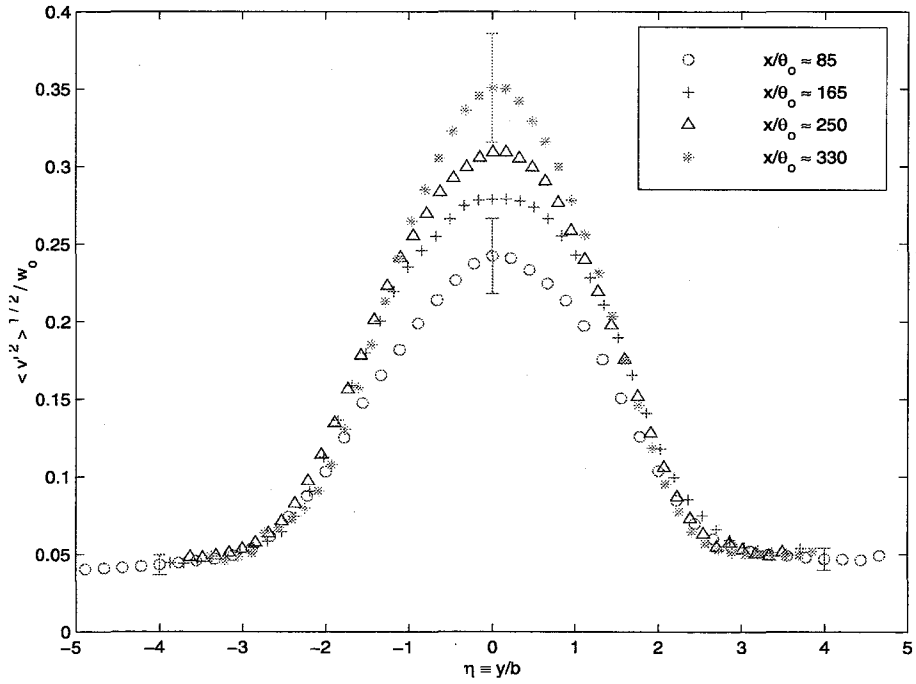

(b)

Fig. 4.2. Profiles of the normalized transverse velocity fluctuations in the flow-normal planes at: (a) $z/\theta_o \approx -1$, (b) $z/\theta_o \approx -30$

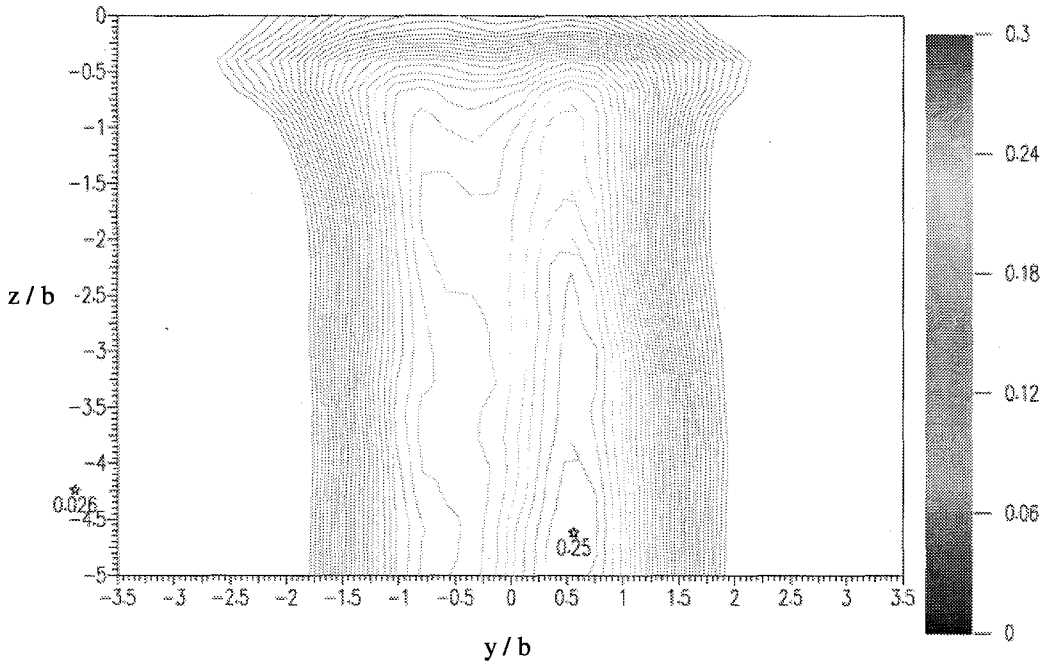
z / b
y / b
0.026
0.25
0.3
0.24
0.18
0.12
0.06
0

(a)

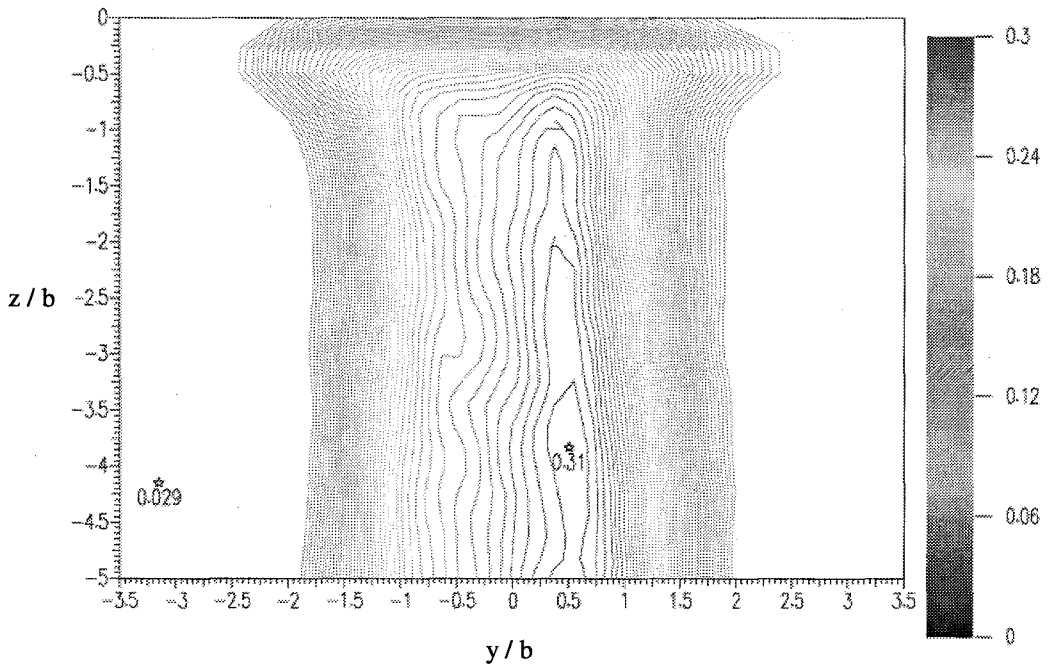
z / b
y / b
0.029
0.31
0.3
0.24
0.18
0.12
0.06
0

(b)

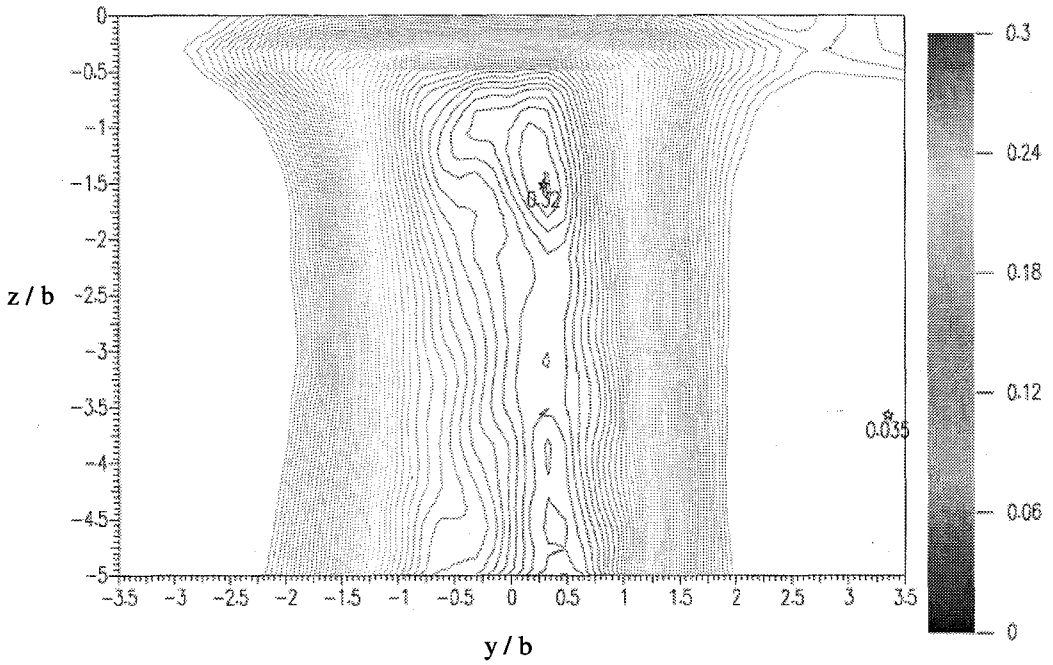

(c)

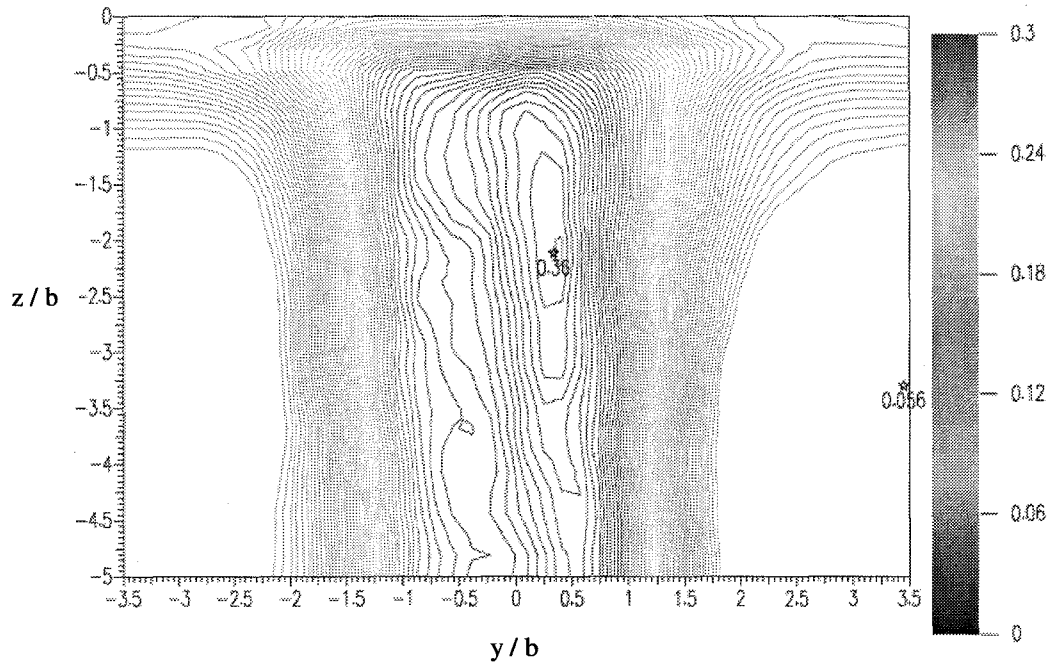

(d)

Fig. 4.3. Contours of the normalized normal velocity fluctuations in the flow-normal planes: (a) $x/\theta_o \approx 85$, (b) $x/\theta_o \approx 165$, (c) $x/\theta_o \approx 250$, (d) $x/\theta_o \approx 330$

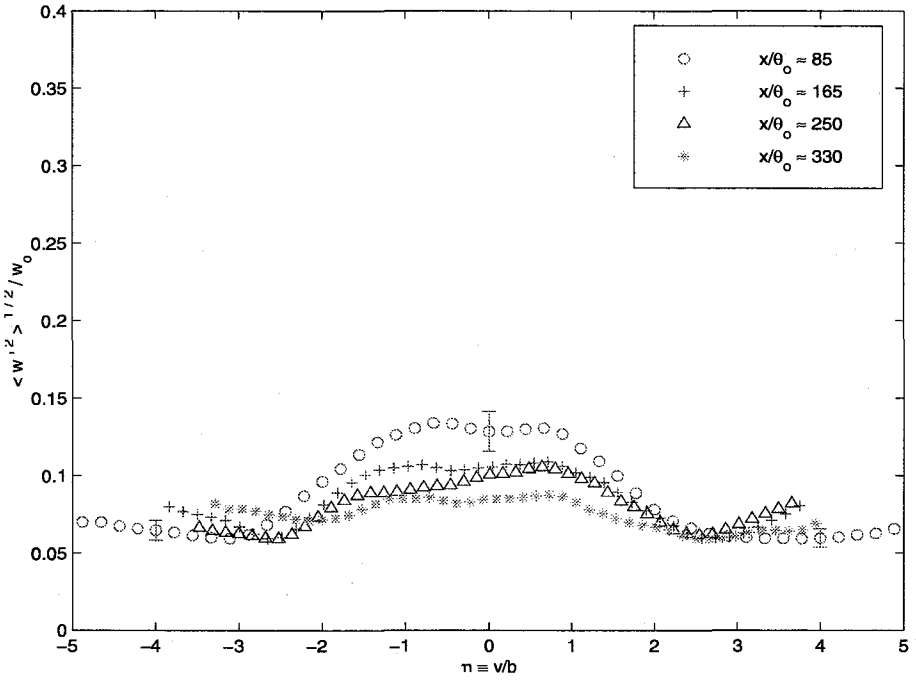

(a)

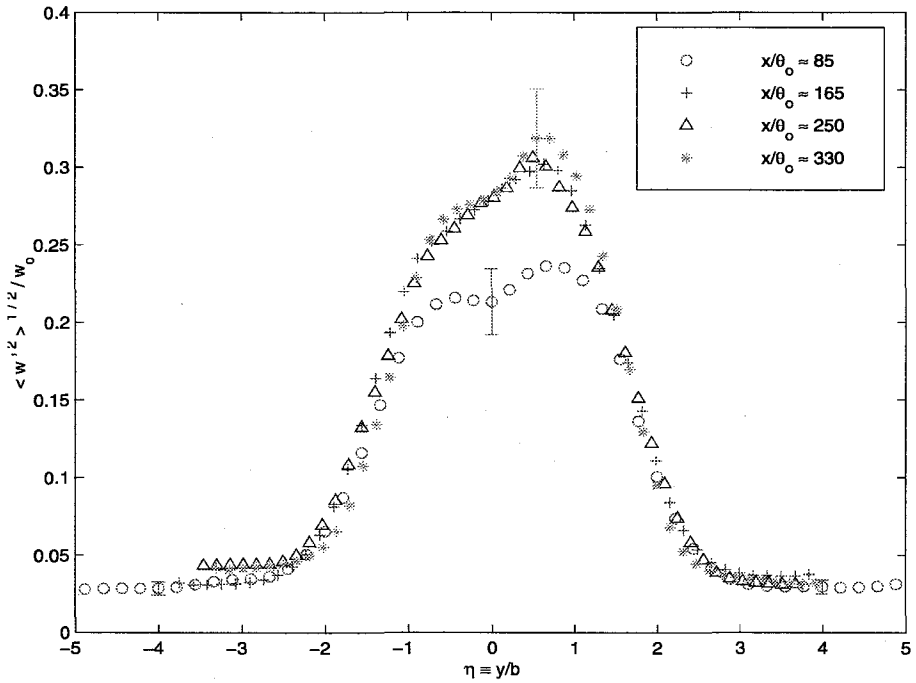

(b)

Fig. 4.4. Profiles of the normalized normal velocity fluctuations in the flow-normal planes at: (a) $z/\theta_o \approx -1$, (b) $z/\theta_o \approx -30$

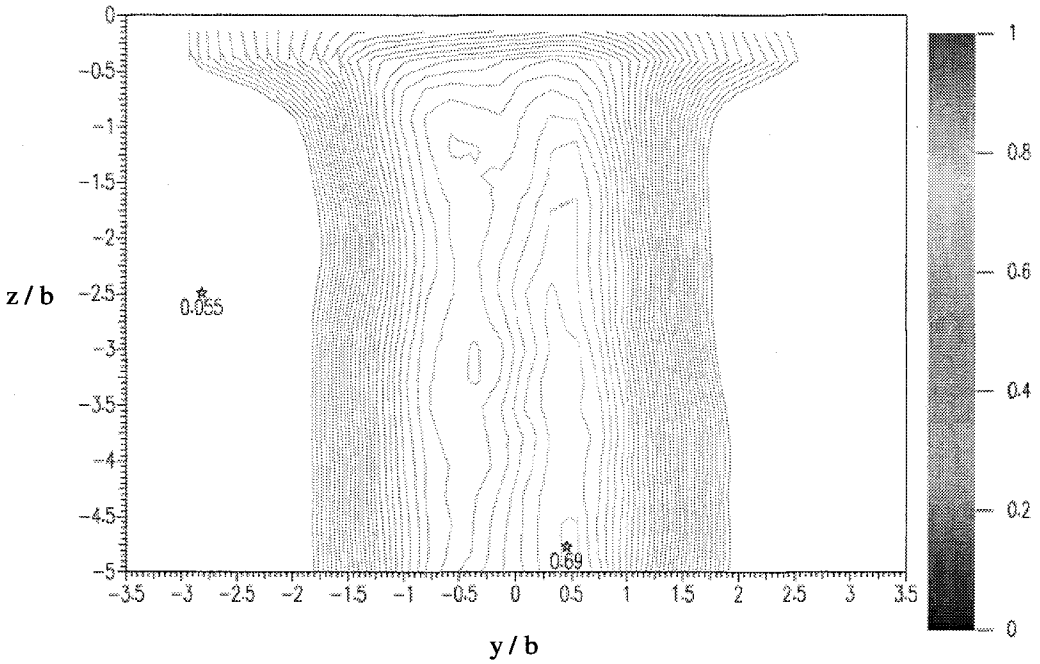
z / b
y / b
0.065
0.69
0
-0.5
-1
-1.5
-2
-2.5
-3
-3.5
-4
-4.5
-5
-3.5
-3
-2.5
-2
-1.5
-1
-0.5
0
0.5
1
1.5
2
2.5
3
3.5
1
0.8
0.6
0.4
0.2
0

(a)

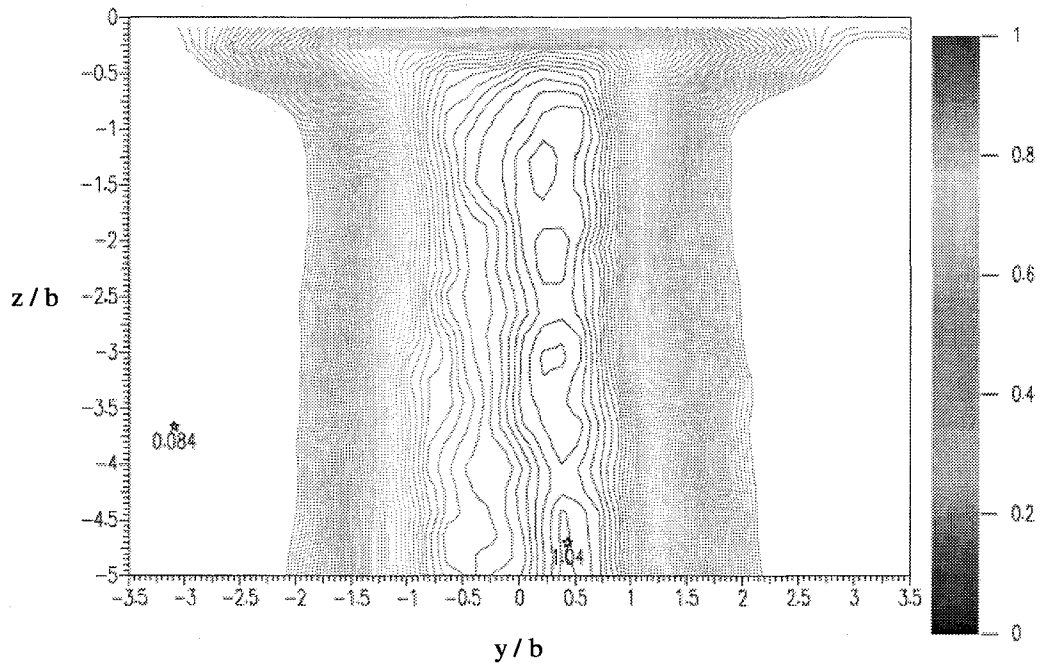
z / b
y / b
0.084
1.04
0
-0.5
-1
-1.5
-2
-2.5
-3
-3.5
-4
-4.5
-5
-3.5
-3
-2.5
-2
-1.5
-1
-0.5
0
0.5
1
1.5
2
2.5
3
3.5
1
0.8
0.6
0.4
0.2
0

(b)

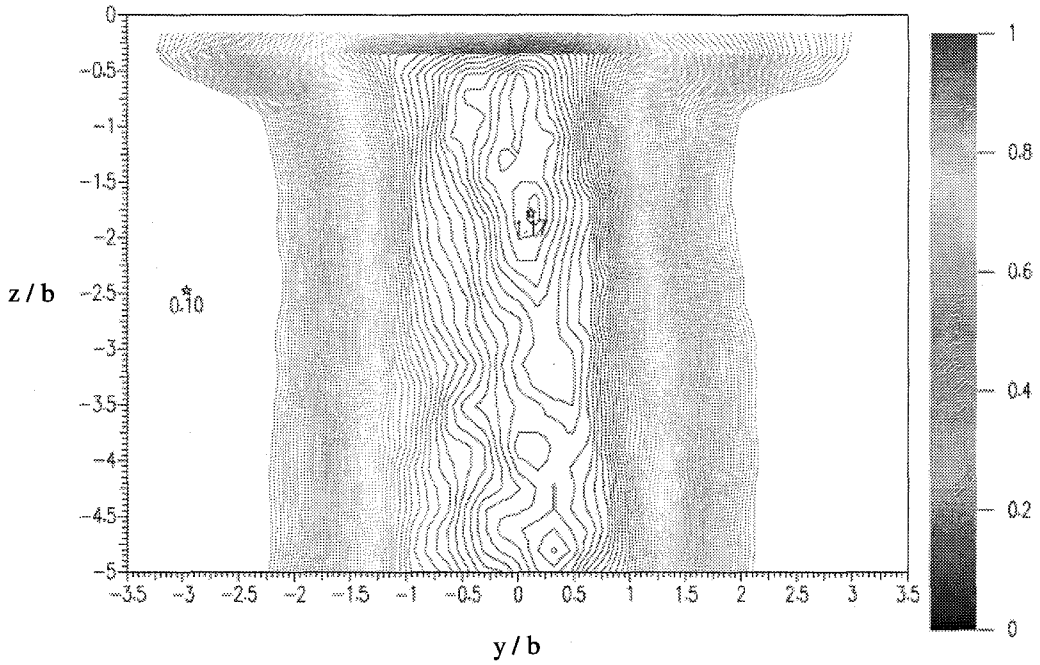

(c)

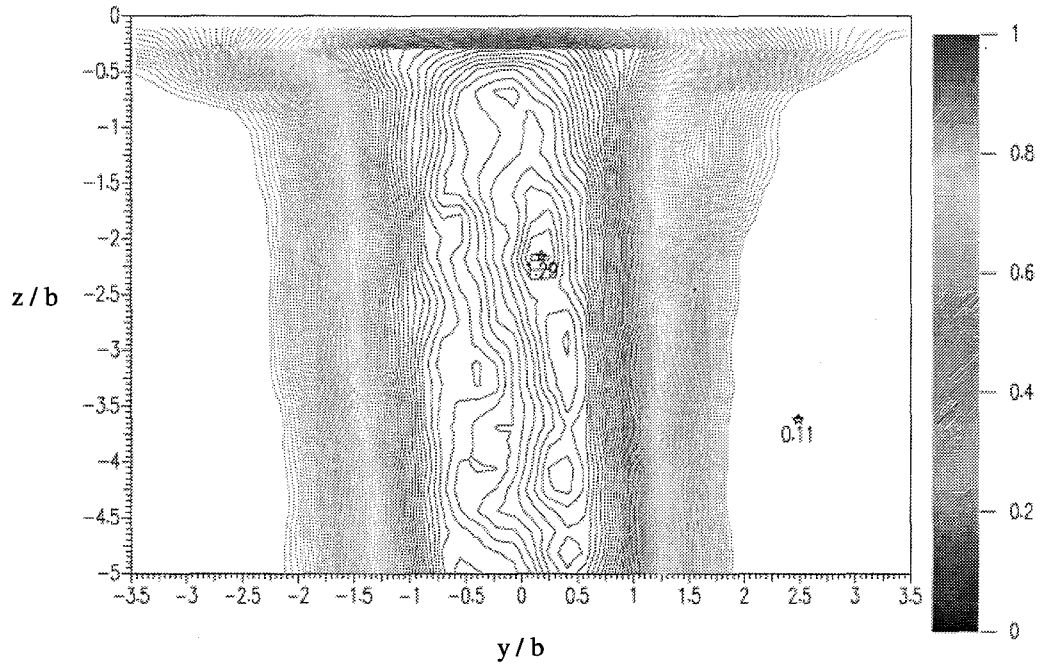

(d)

Fig. 4.5. Contours of the normalized streamwise vorticity fluctuations in the flow-normal planes: (a) $x/\theta_o \approx 85$, (b) $x/\theta_o \approx 165$, (c) $x/\theta_o \approx 250$, (d) $x/\theta_o \approx 330$

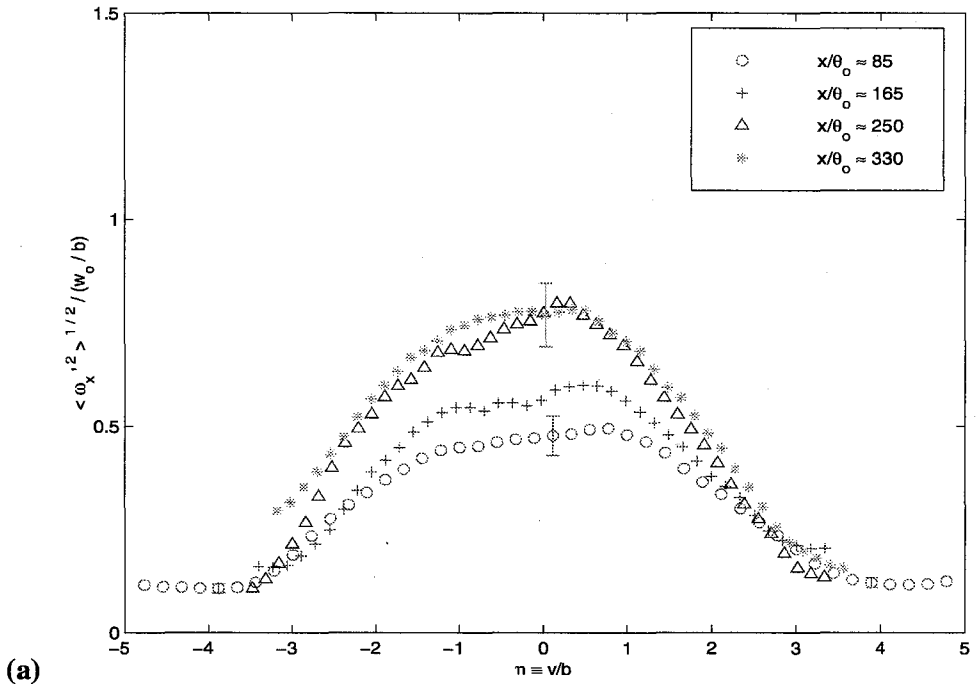

(a)

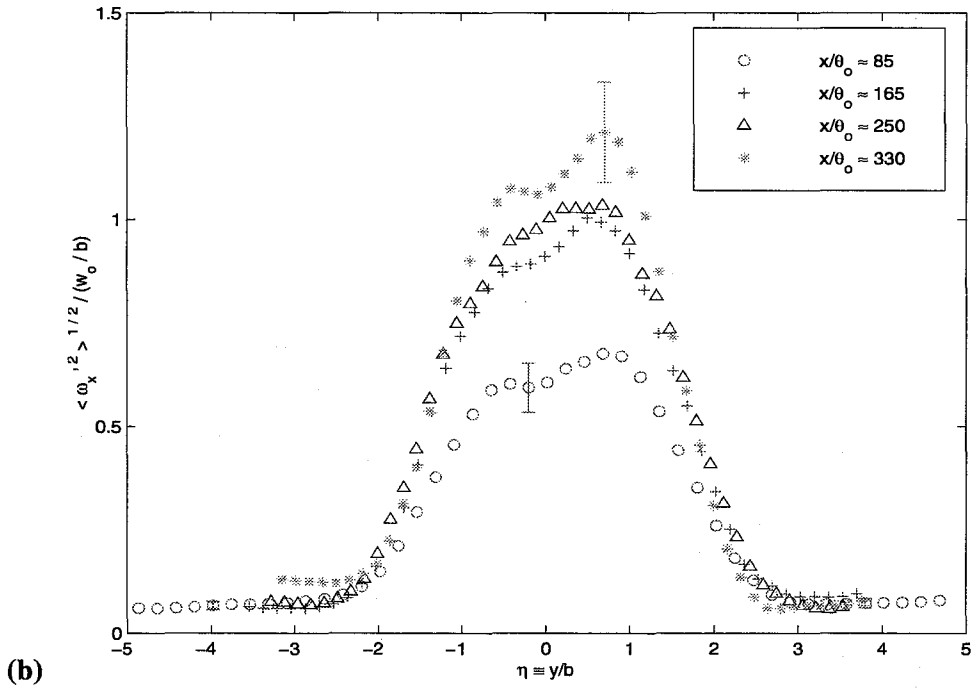

(b)

Fig. 4.6. Profiles of the normalized streamwise vorticity fluctuations in the flow-normal planes at: (a) $z/\theta_o \approx -1$, (b) $z/\theta_o \approx -30$

4.2.2. Free-surface plane measurements

Surface-parallel measurement planes were then positioned in the estimated region of influence of the near-surface secondary flows to investigate their influence on the underlying turbulent wake. Data were thus acquired in x-y surface-parallel planes at several depths in the *surface layer* at $z/\theta_o \approx -1, -2$ and -4.

(a) behavior of the mean flow in the wake

Values of the half-width parameter b were determined in these surface-parallel planes to quantify the influence of the secondary flows on the wake's growth rate in the *surface layer*. The notations $b_{(z/\theta_o \approx -1, -2, \text{and } -4)}$ represent these values. We are here interested in the variation of the wake's width as the free surface is reached in relation to the location of the secondary flows. In this scope, the positions of the secondary vorticity extrema were also determined. This was achieved in two different ways. First, these values were readily available from the data captured in the four flow-normal planes. They enabled us to compute the distance between the mean streamwise vorticity extrema and the centerline (y = 0), defined as the positive quantity $(\Delta y_{|\omega_x|_{max}}/2 \equiv (y(\omega_x = (\omega_x)_{min}) - y(\omega_x = (\omega_x)_{max}))/2 \geq 0)$. Then, these values were also inferred from the data gathered in the surface-parallel plane $z/\theta_o \approx -1$. Since the secondary flows showed some of the hallmarks of a vortex pair interacting with a flat shear-free boundary, it was speculated that the extrema of the mean streamwise vorticity should correlate quite well with the extrema of the mean transverse velocity. This turned out to be indeed the case (see the coincidence between the red squares and the blue crosses in the plot below). As a result, the secondary flows could not only be tracked at four single downstream stations but throughout the wake development. The half "distance" between the maximum and minimum values of the mean transverse velocity, defined as $\Delta y_{|V|_{max}}/2 \equiv (y(V = V_{max}) - y(V = V_{min}))/2$, was then computed. The latter "distance" was purposely defined such that it could be positive or negative. We will see shortly that this definition helps to unveil some fundamental characteristics of the near-wake flow field (indeed the vertical blue dash line divides the figure in two parts; it particularly stresses the fact that this parameter takes negative values for $x/\theta_o \leq 45$, whose meaning will be discussed below). All these parameters were nondimensionalized by the value of the half-width parameter b (= $b_{deep\ wake}$) of the deep turbulent wake and are plotted in Fig. 4.1 as a function of the normalized downstream distance.

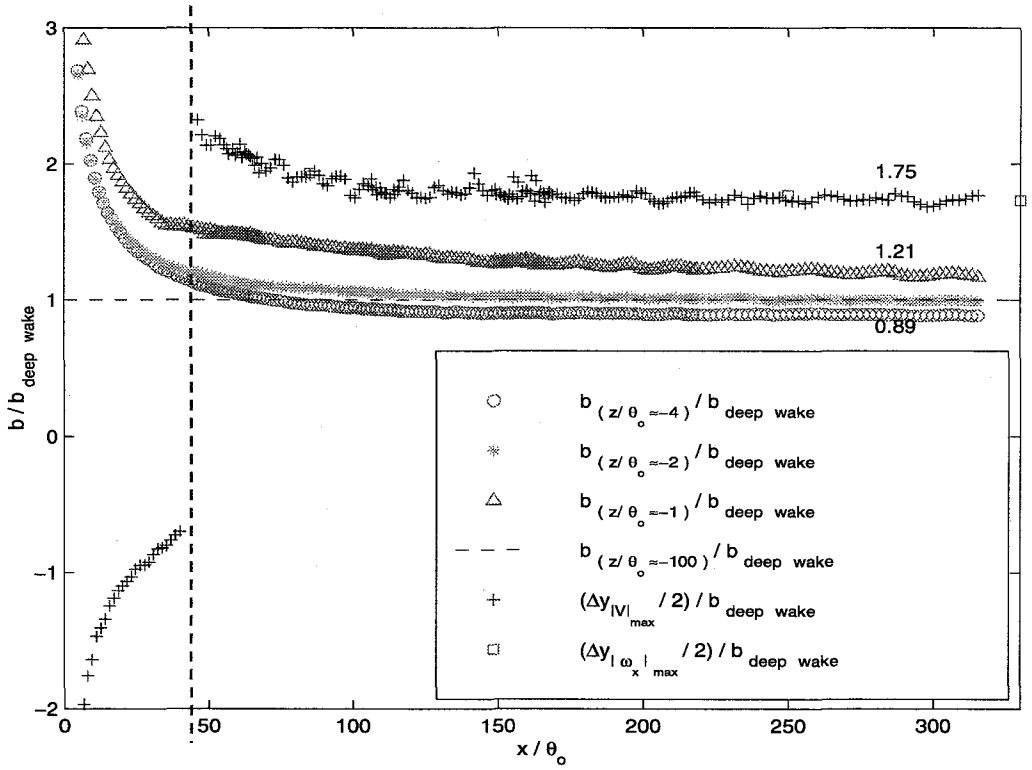

Fig. 4.1. Evolution of halfwidth-wake ratios and secondary-vorticity-maximum positions with the downstream distance

However, the half-width parameter b is an arbitrary measure of the wake's extent unlike its name might imply. Indeed, a better estimate of the width of the fully-submerged wake, δ, can be expressed as:

$$\exp(-\ln 2\left(\frac{\delta}{2b}\right)^2) = w(\eta \equiv \frac{\delta/2}{b}) = \frac{1}{100} \Rightarrow \delta = 2\sqrt{\frac{2}{\log 2}}\, b \approx 5b.$$

Values of the "physical" lateral extent of the wake can then be estimated using the previous results. Based on these geometrical parameters, a simple schematic of the wake's topology is sketched in Fig. 4.2. The results shows that, as the free surface is approached, the 5b-wide fully-submerged wake first narrows to 4.5b (about 10% decrease) at $z/\theta_o \approx -4$ before widening to 6b (about 20% increase) at $z/\theta_o \approx -1$. These findings can be fully explained in terms of the near-surface secondary flows, which are located at $(y/b,\ z/b) \approx (\pm 1.75,\ -0.25)$. Indeed, they are responsible for transporting fluid elements with higher mean velocities toward the centerline at $z/\theta_o \approx -4$, thus reducing the width of the wake at this depth, while transporting fluid elements with low mean velocity outward at $z/\theta_o \approx -1$ (inducing the well known "surface currents"), and hence increasing its width. Furthermore, the coincidence

between the extrema of the mean streamwise vorticity and the extrema of the mean transverse velocity shows that this influence on the free-surface wake can be traced back to the plate's turbulent boundary layers. As will be further argued in the next section, each secondary vortical flow is believed to be the outer vortex of the corner vortices formed in each of the wall / free-surface juncture flows.

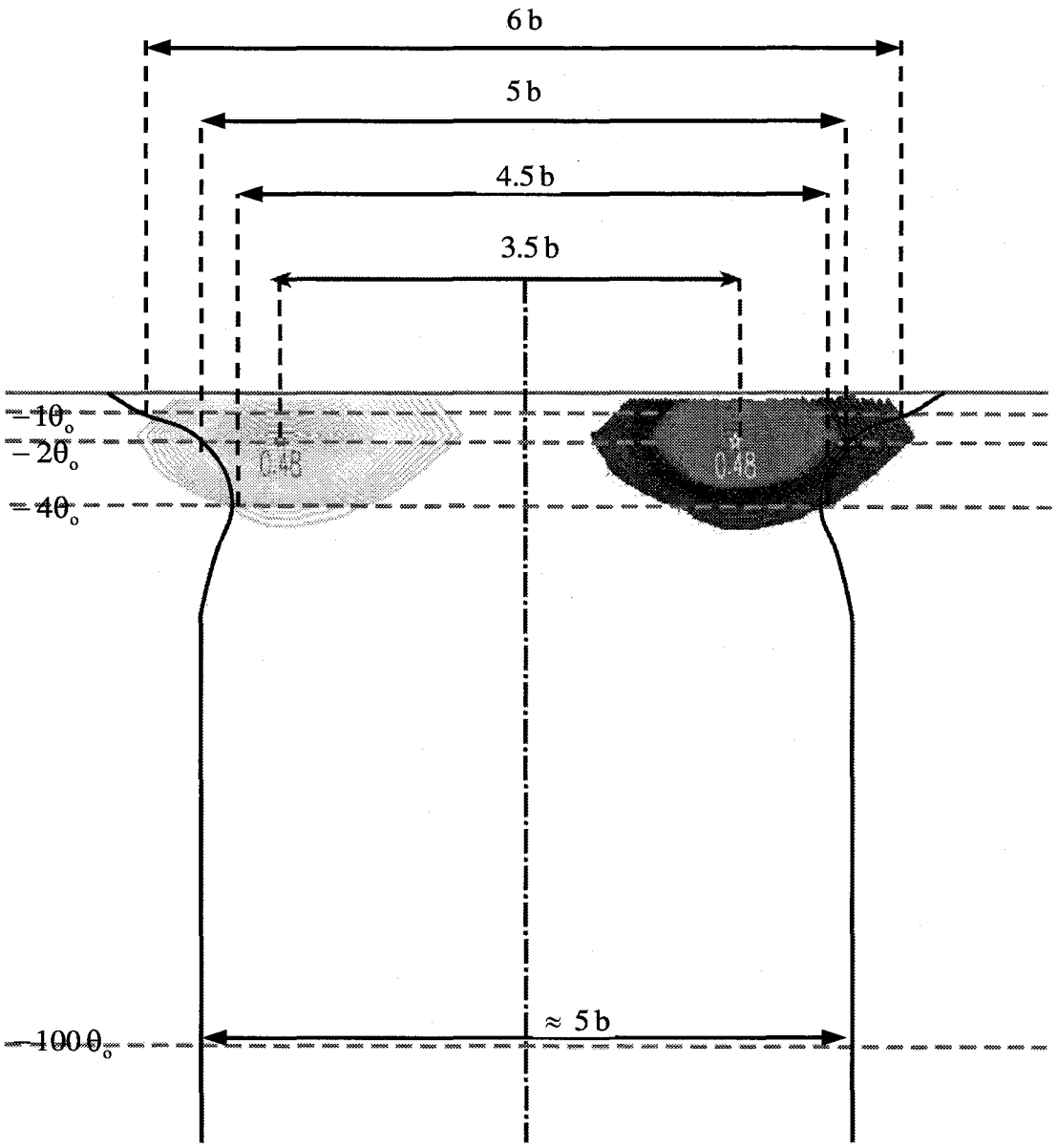

Fig. 4.2. Variation of the main geometrical parameters of the wake with the channel depth

Fig. 4.3 displays several mean transverse velocity profiles obtained in the very near-surface measurement plane, which is located at $z/\theta_o \approx -1$. These profiles are, as expected, not only consistent with the presence of "surface currents" at the free surface but they also match the profiles gathered in the flow-normal planes — in particular $\left(\overline{v}/w_o\right)_{min,\,max} \approx \pm 0.135$ at $\eta \equiv y/b \approx \pm 1.75$. As previously mentioned, there is very good agreement between the locations of the extrema of the mean vorticity distributions and the locations of the extrema of the mean transverse velocity at the free surface. In this context of a "mean" vortex pair interacting with the free surface, these "surface currents" can be simply interpreted as mutual interaction between the streamwise vortical structures and their "images" above the free surface. However, in addition to these outward currents, the aforementioned measurements also reveal the presence of inward surface currents in the near-wake region. Indeed, another pair of extrema can still be noticed in the profile at $x/\theta_o \approx 85$. The magnitude of these currents is larger than their outward counterparts in the near-wake region but decreases steadily and rapidly until these inward currents completely disappeared. The negative values taken by the blue crosses in Fig. 4.3 indicates the near-wake region $(x/\theta_o \leq 45)$ where these currents are stronger in magnitude than the corresponding outward surface currents. These currents are believed to be the signatures of the inner vortices of the corner vortices formed in the juncture flows.

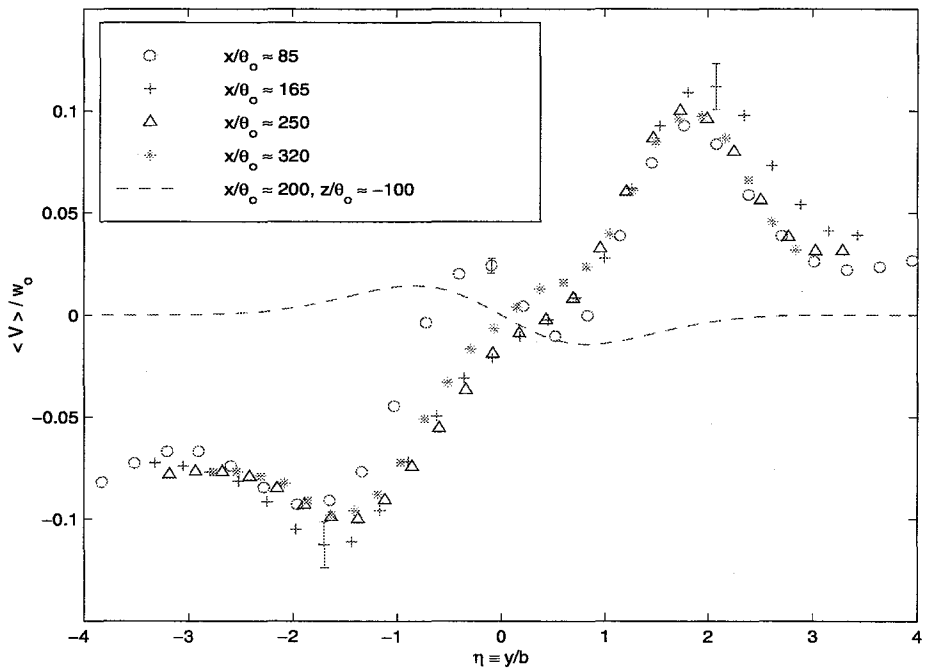

Fig. 4.3. Profiles of the Reynolds-averaged transverse velocity at $z/\theta_o \approx -1$

(b) turbulence structure in the wake

Measurements of the turbulent streamwise and transverse velocity fluctuations, the turbulent Reynolds shear stress as well as the normal vorticity fluctuations were also obtained in these surface-parallel planes.

Profiles of the root-mean-square of the normalized streamwise velocity fluctuations found in the three near-surface-parallel planes are compared to the fully-submerged wake distributions in Fig. 4.1. The shape of the double-hump distributions for $\sqrt{\overline{u'^2}}/w_o$ is conserved as the free surface is approached. However, the lateral extent and maximum value of these profiles do vary. The values of the lateral extent are consistent with the values of the half-width of the wake measured in these planes (see Fig. 4.1). The magnitude of $\sqrt{\overline{(u'^2)}}_{max}/w_o$ increases by about 20% with respect to its fully-submerged counterpart to a value of 0.55 at $z/\theta_o \approx -4$ before decreasing to 0.5 at $z/\theta_o \approx -2$ and 0.45 at $z/\theta_o \approx -1$ which corresponds to the maximum value it attained in the fully-submerged wake.

Profiles of the root-mean-square of the normalized transverse velocity fluctuations, which are shown in Fig. 4.2, display a similar trend. Indeed, the lateral extent of these profiles varies from 5b at $z/\theta_o \approx -100$ to 4.5b at $z/\theta_o \approx -4$ and to 6b at $z/\theta_o \approx -1$ while $\sqrt{\overline{(v'^2)}}_{max}/w_o$ increases by about 5% with respect to its fully-submerged counterpart to a value of 0.425 at $z/\theta_o \approx -4$ and at $z/\theta_o \approx -2$ before decreasing to 0.4 at $z/\theta_o \approx -1$ which corresponds to the maximum value it attained in the fully-submerged wake. However, this plot reveals the difference in shape between the profiles of the free-surface wake and its fully-submerged counterpart. Indeed, $\sqrt{\overline{v'^2}}/w_o$ has a Gaussian-shaped profile evolving toward its asymptotic curve in the fully-submerged wake while its profile at the free surface is much fuller with a non-Gaussian characteristic shape. These results are consistent with the previous results obtained for $\sqrt{\overline{v'^2}}/w_o$ in flow-normal planes.

The present results, coupled with the previous ones gathered in flow-normal planes, corroborate the free-surface anisotropy: vertical momentum is deflected in the horizontal direction by the free surface. The sharp reduction in $\sqrt{\overline{w'^2}}/w_o$ — by 66% in magnitude — is accompanied by an increase in both $\sqrt{\overline{u'^2}}/w_o$ and $\sqrt{\overline{v'^2}}/w_o$. The maximum value of the streamwise velocity fluctuations increases far more than its transverse counterpart — 20% vs. 5% — but the width of both associated profiles increase by the same amount — 20%.

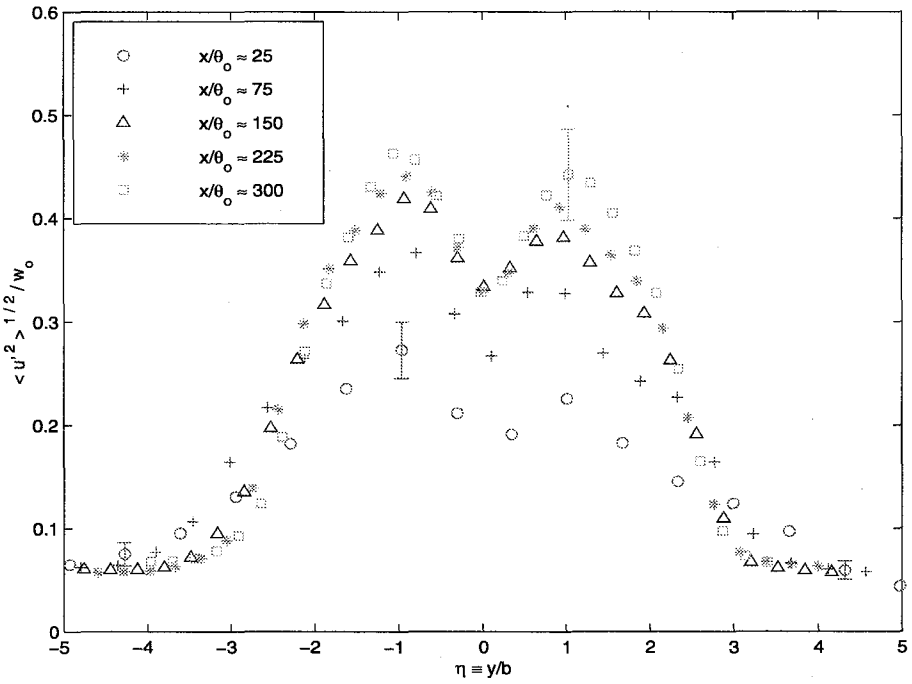
x/θo ≈ 25
x/θo ≈ 75
x/θo ≈ 150
x/θo ≈ 225
x/θo ≈ 300
< u'2 >1/2 / wo
η ≡ y/b

(a)

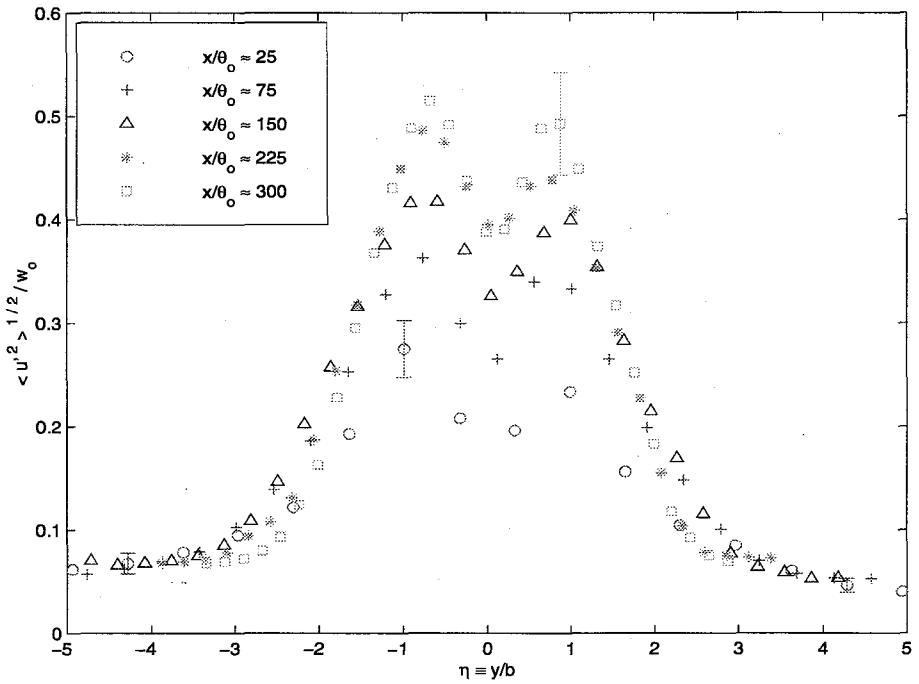
x/θo ≈ 25
x/θo ≈ 75
x/θo ≈ 150
x/θo ≈ 225
x/θo ≈ 300
< u'2 >1/2 / wo
η ≡ y/b

(b)

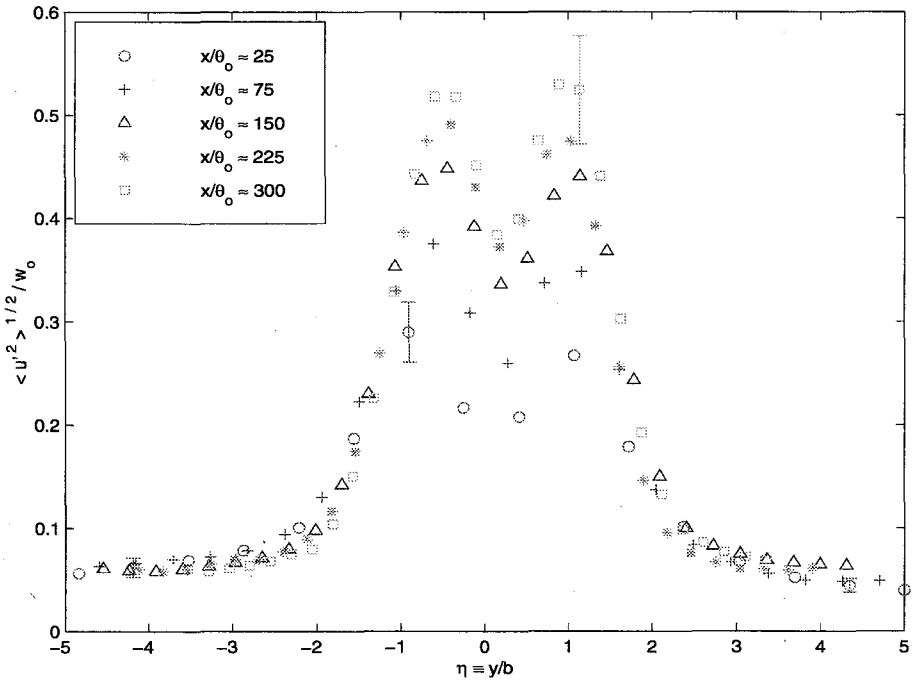

(c)

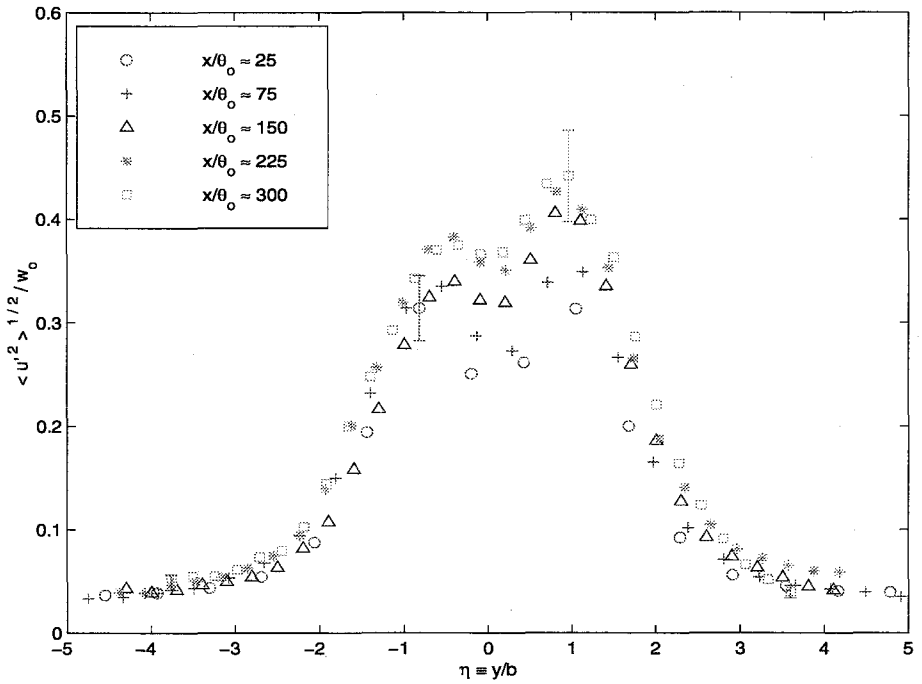

(d)

Fig. 4.1. Profiles of the normalized streamwise velocity fluctuations in the surface-parallel planes at: (a) $z/\theta_o \approx -1$, (b) $z/\theta_o \approx -2$, (c) $z/\theta_o \approx -4$, (d) $z/\theta_o \approx -100$

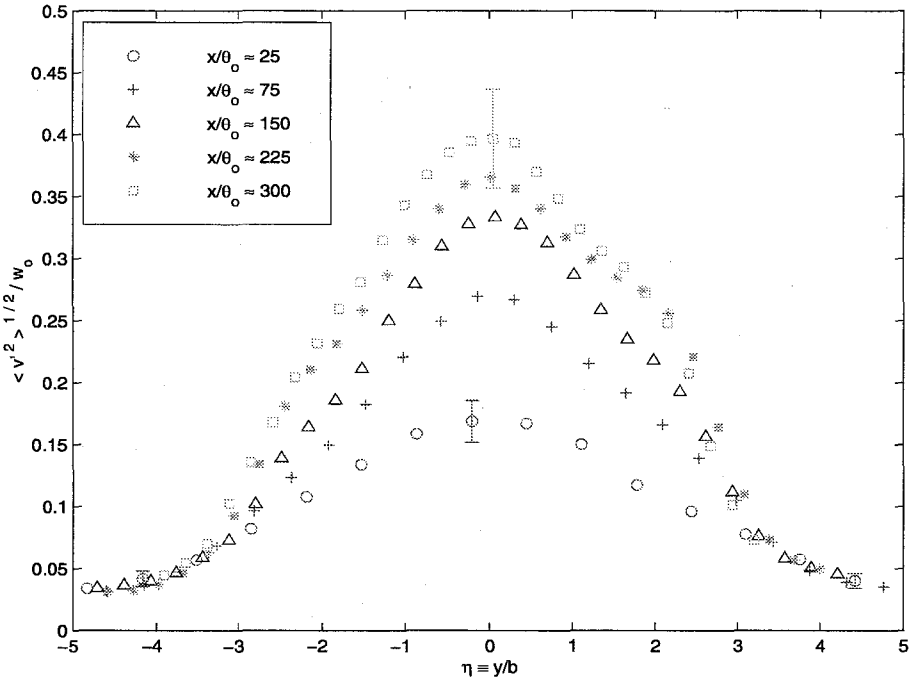
x/θo ≈ 25
x/θo ≈ 75
x/θo ≈ 150
x/θo ≈ 225
x/θo ≈ 300
<v'2>1/2/wo
η ≡ y/b

(a)

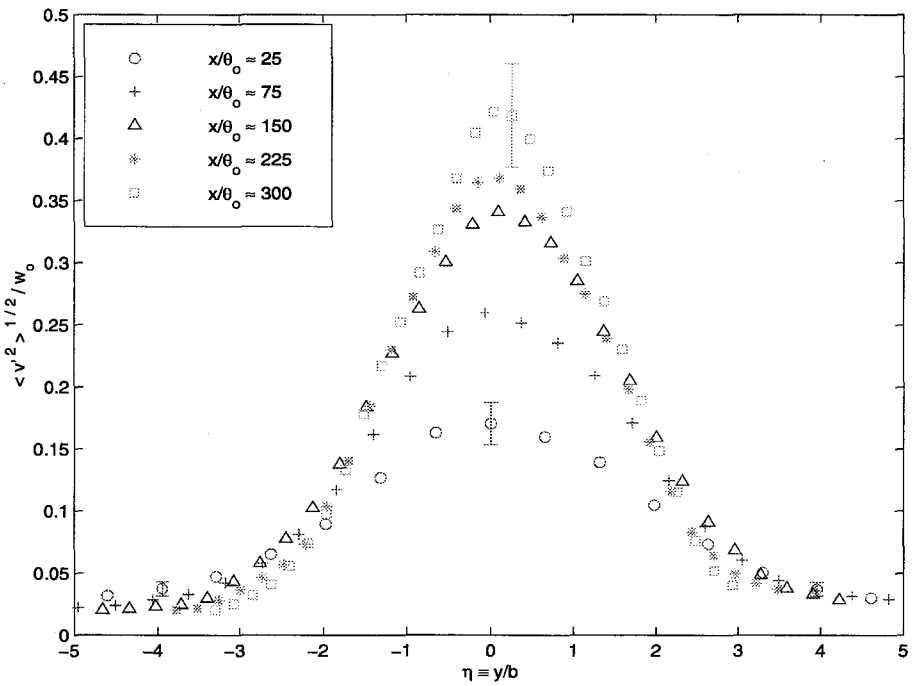
x/θo ≈ 25
x/θo ≈ 75
x/θo ≈ 150
x/θo ≈ 225
x/θo ≈ 300
<v'2>1/2/wo
η ≡ y/b

(b)

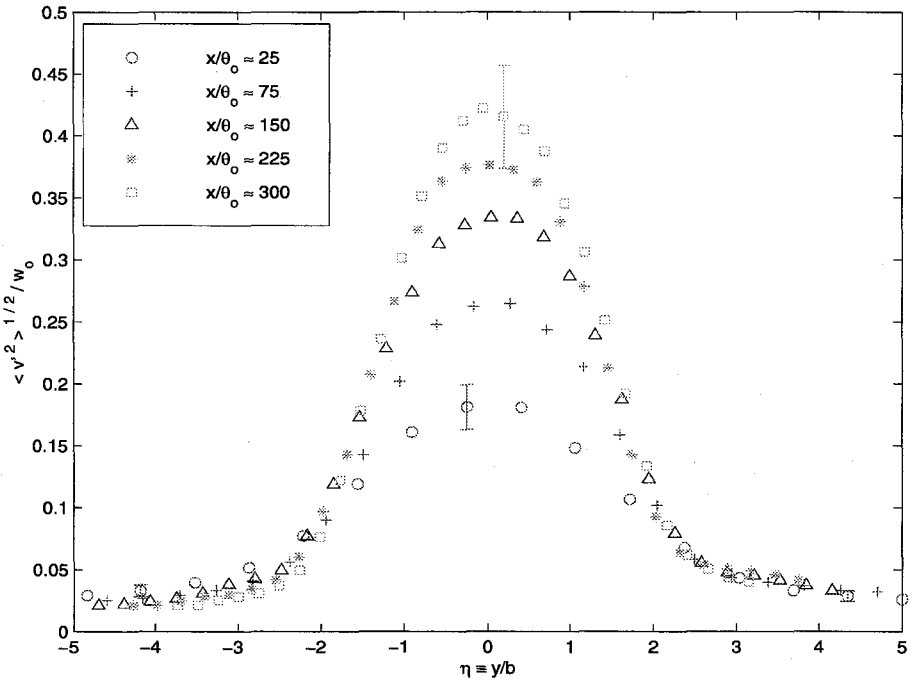

(c)

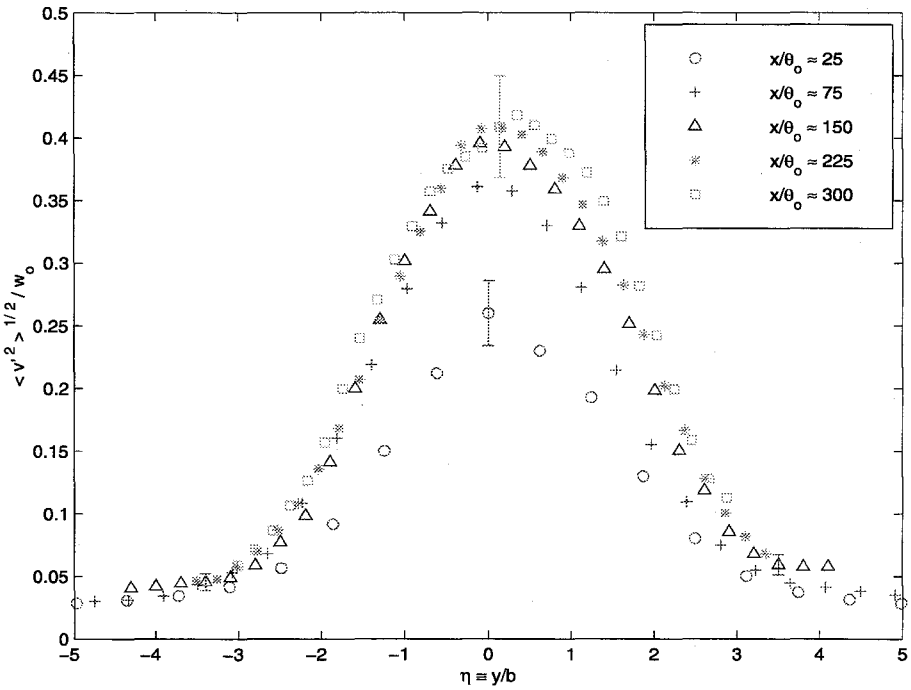

(d)

Fig. 4.2. Profiles of the normalized transverse velocity fluctuations in the surface-parallel planes at: (a) $z/\theta_o \approx -1$, (b) $z/\theta_o \approx -2$, (c) $z/\theta_o \approx -4$, (d) $z/\theta_o \approx -100$

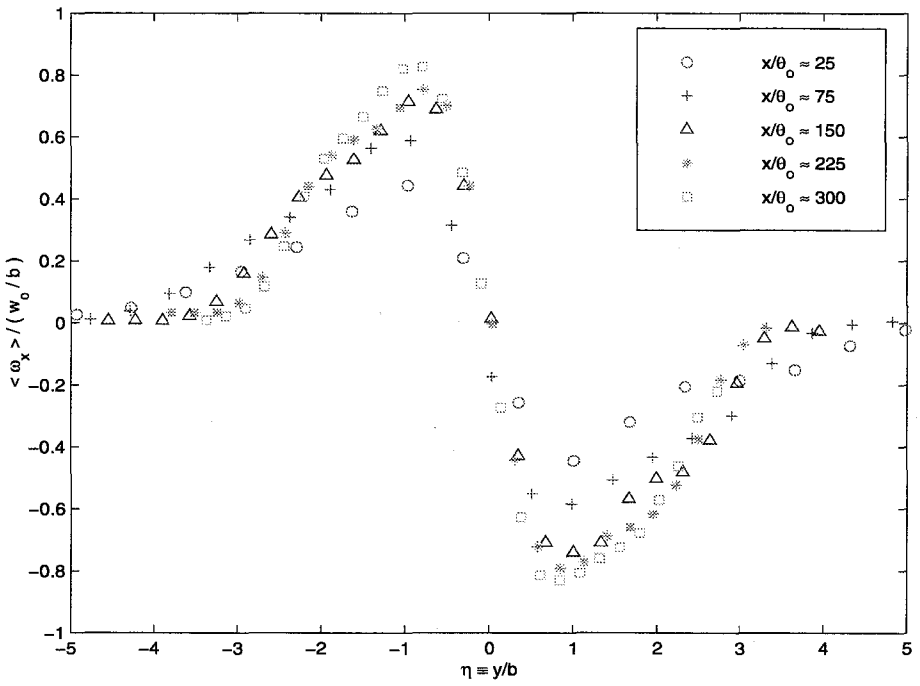
x/θo ≈ 25
x/θo ≈ 75
x/θo ≈ 150
x/θo ≈ 225
x/θo ≈ 300
< ωx > / (wo / b)
η ≡ y/b

(a)

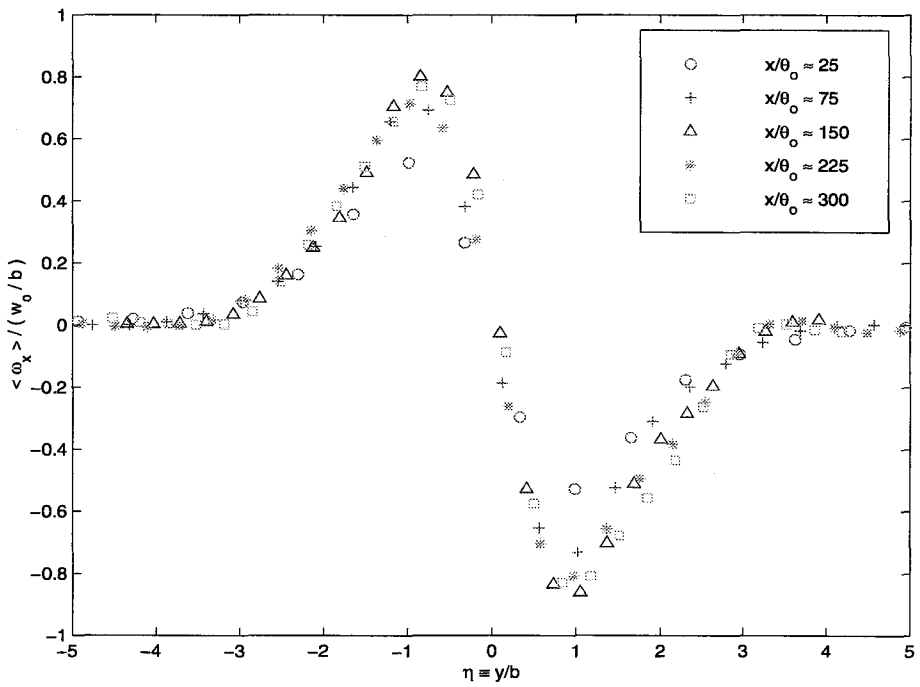
x/θo ≈ 25
x/θo ≈ 75
x/θo ≈ 150
x/θo ≈ 225
x/θo ≈ 300
< ωx > / (wo / b)
η ≡ y/b

(b)

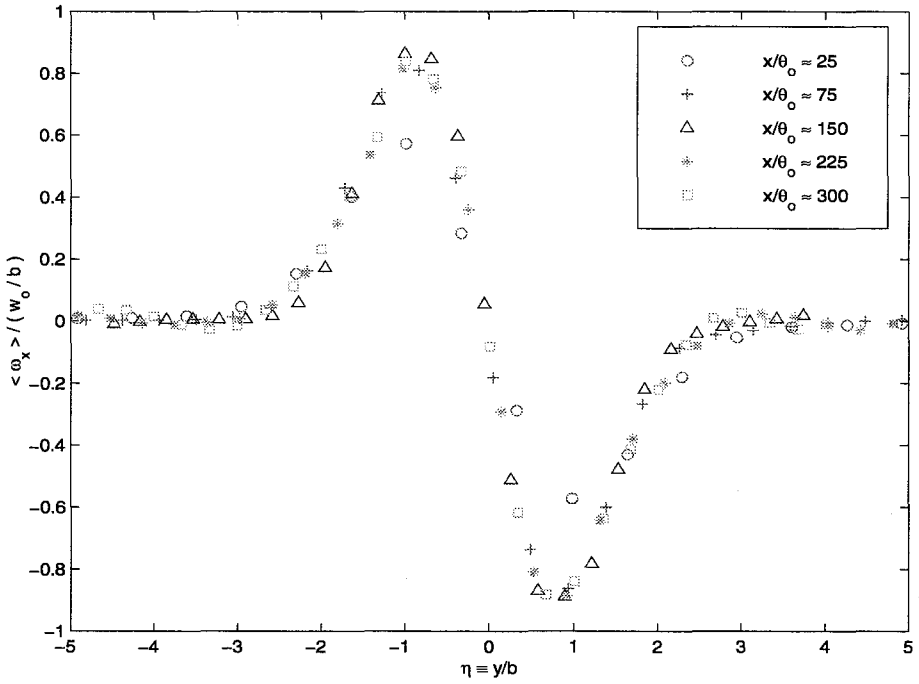

(c)

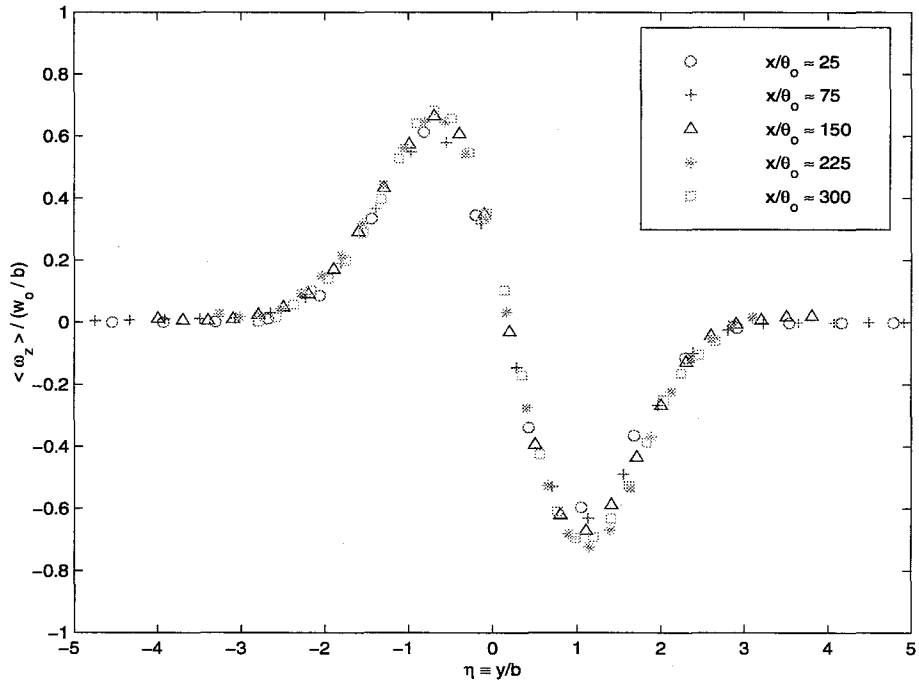

(d)

Fig. 4.3. Profiles of the normalized mean normal vorticity in the surface-parallel planes at: (a) $z/\theta_o \approx -1$, (b) $z/\theta_o \approx -2$, (c) $z/\theta_o \approx -4$, (d) $z/\theta_o \approx -100$

Profiles of the normalized turbulent Reynolds shear stress $-\overline{u'v'}/w_o^2$ are plotted in Fig. 4.4. The magnitude of $\left(-\overline{u'v'}/w_o^2\right)_{max}$ increases by about 35% with respect to its fully-submerged counterpart to a value of 0.135 at $z/\theta_o \approx -4$ before decreasing to 0.1 at $z/\theta_o \approx -2$ and 0.075 at $z/\theta_o \approx -1$, which corresponds to a decrease of 25% compared to the value attained in the fully-submerged wake (equal to about 0.1). In addition, the lateral extent of these profiles does vary consistently with the above findings (6b-wide wake at $z/\theta_o \approx -1$ versus 5b-wide wake at $z/\theta_o \approx -100$).

Profiles of the root-mean-square of the normalized normal vorticity fluctuations are plotted in Fig. 4.5. The magnitude of $\sqrt{\left(\overline{\omega_z'^2}\right)_{max}}/(w_o/b)$ increases by about 15% with respect to its fully-submerged counterpart to a value of 1.5 at $z/\theta_o \approx -4$ before decreasing to 1.3 at $z/\theta_o \approx -2$ and 1.2 at $z/\theta_o \approx -1$, which corresponds to the maximum value it attained in the fully-submerged wake. Furthermore, the lateral extent of these profiles does vary consistently with the above findings (6b-wide wake at $z/\theta_o \approx -1$ versus 5b-wide wake at $z/\theta_o \approx -100$). These results are consistent with the fact that only the surface-normal component of the vorticity remains at a flat free surface, which forces vortex lines to terminate normal to the surface. Thus, $\sqrt{\overline{\omega_z'^2}}/(w_o/b)$ increases — in lateral extent — as the free surface is reached as vortex filaments tend to connect to the free surface.

Results for both the turbulent Reynolds shear stress and the normal vorticity fluctuations unveil the presence of normal vortical structures at the edges of the wake. They are consistent with the increase of the wake's width by about 20%. This may be due to the outward motion of surface-normal vortical structures by the induced "surface currents" as well as the connection of surface-parallel vortical structures to the free surface.

Using flow-normal and surface-parallel measurements, profiles of the normalized turbulence kinetic energy $\dfrac{k}{w_o^2/2} \equiv \dfrac{\overline{u'^2}+\overline{v'^2}+\overline{w'^2}}{w_o^2}$ can be obtained at four downstream locations in each surface-parallel plane ($z/\theta_o \approx -1,-2,-4$ and -100). These profiles are shown in Fig. 4.6. Their variation in both width and magnitude agrees quite well with the previous findings. In particular, the kinetic energy of the turbulent fluctuations decreases by about 20% in maximum value between $z/\theta_o \approx -1$ and $z/\theta_o \approx -100$ but it is redistributed at the edges of the free-surface wake — its profile increases indeed by 20% in width. As shown previously, it is further redistributed from the fluctuations normal to the surface to those parallel to it.

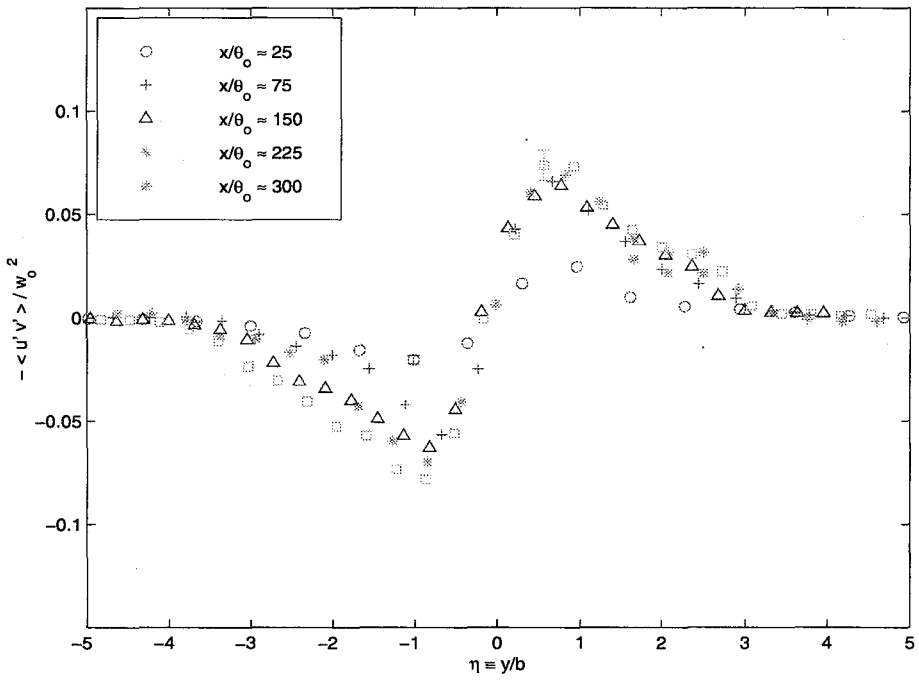
x/θo ≈ 25
x/θo ≈ 75
x/θo ≈ 150
x/θo ≈ 225
x/θo ≈ 300
0.1
0.05
0
−0.05
−0.1
−5
−4
−3
−2
−1
0
1
2
3
4
5
η ≡ y/b
− < u' v' > / wo 2

(a)

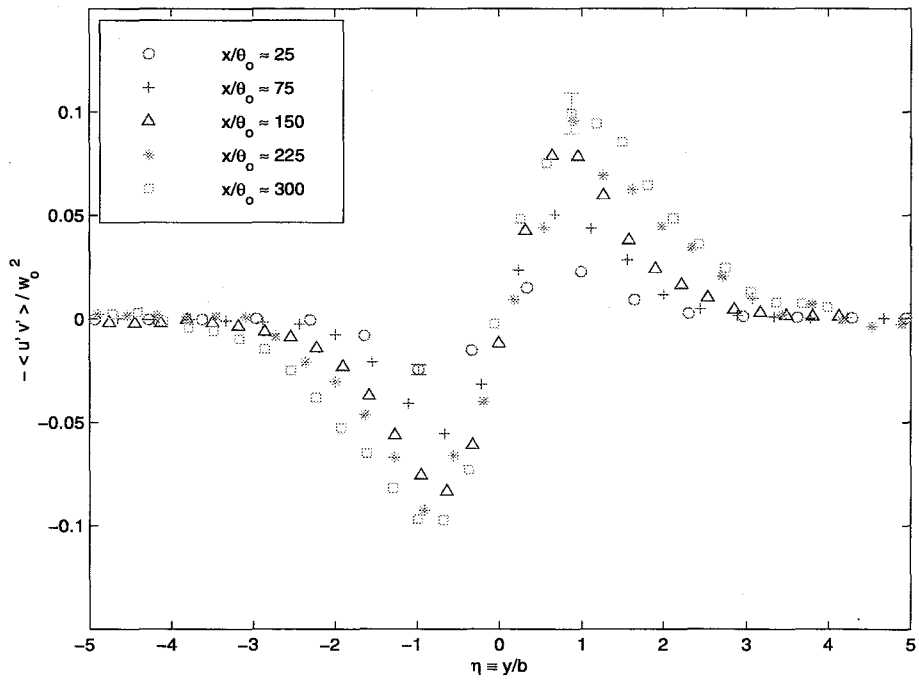
x/θo ≈ 25
x/θo ≈ 75
x/θo ≈ 150
x/θo ≈ 225
x/θo ≈ 300
0.1
0.05
0
−0.05
−0.1
−5
−4
−3
−2
−1
0
1
2
3
4
5
η ≡ y/b
− < u' v' > / wo 2

(b)

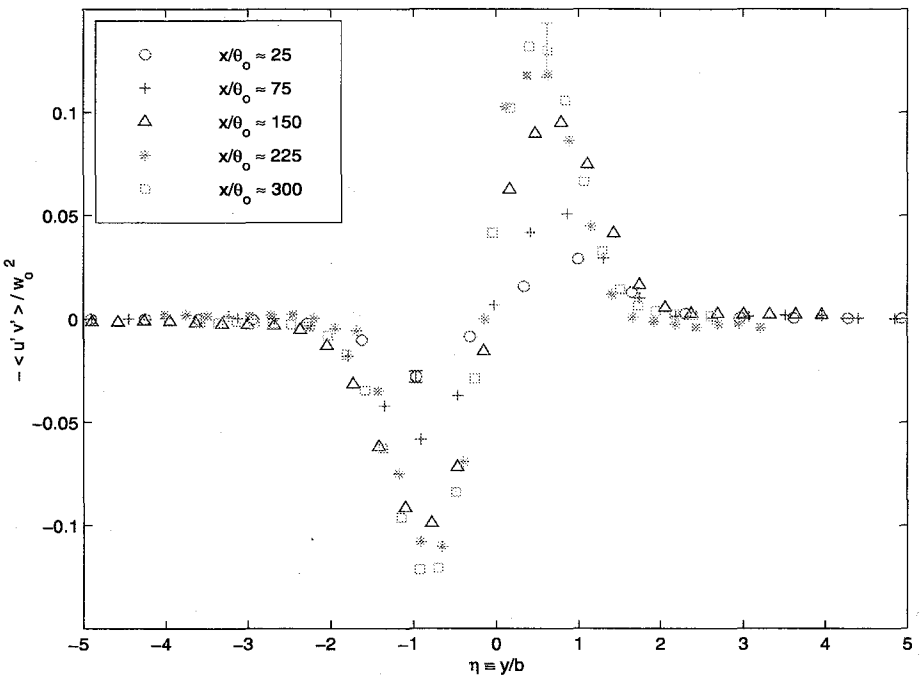

(c)

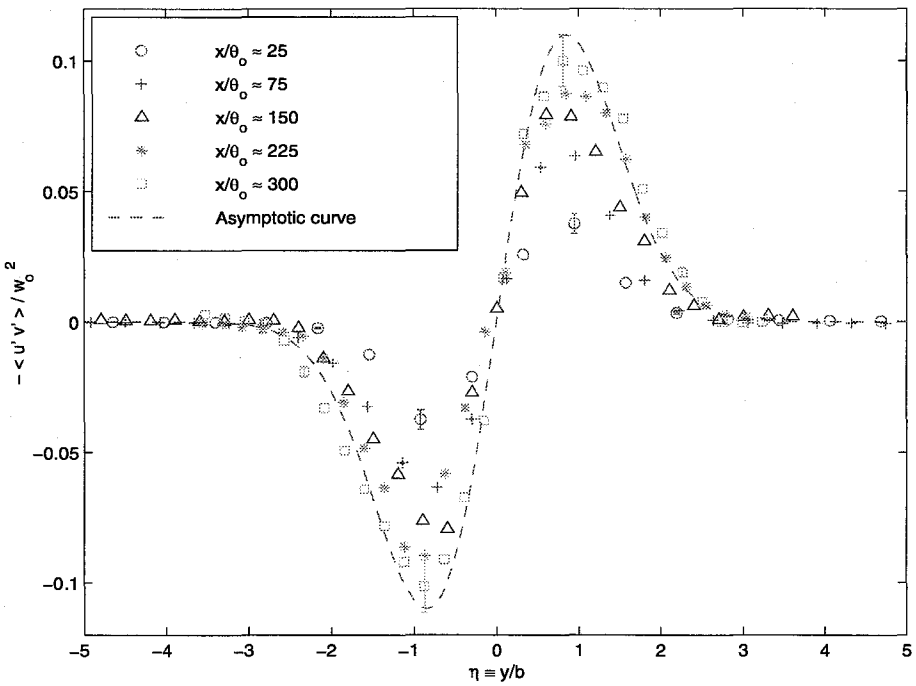

(d)

Fig. 4.4. Profiles of the normalized Reynolds turbulent shear stress in the surface-parallel planes at: (a) $z/\theta_o \approx -1$, (b) $z/\theta_o \approx -2$, (c) $z/\theta_o \approx -4$, (d) $z/\theta_o \approx -100$

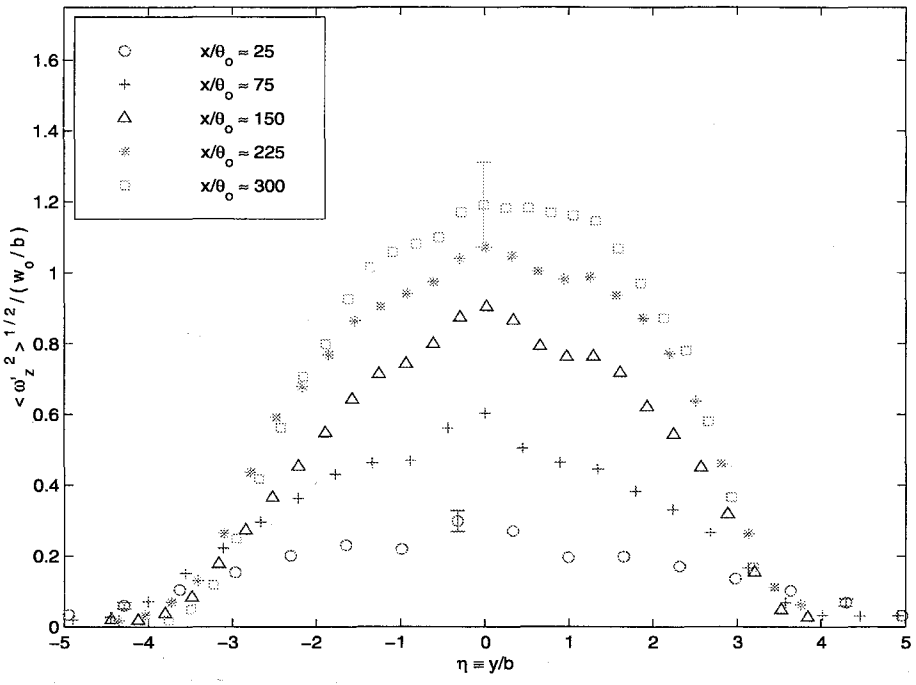
x/θo ≈ 25
x/θo ≈ 75
x/θo ≈ 150
x/θo ≈ 225
x/θo ≈ 300
<ω'z2>1/2/(wo/b)
η ≡ y/b

(a)

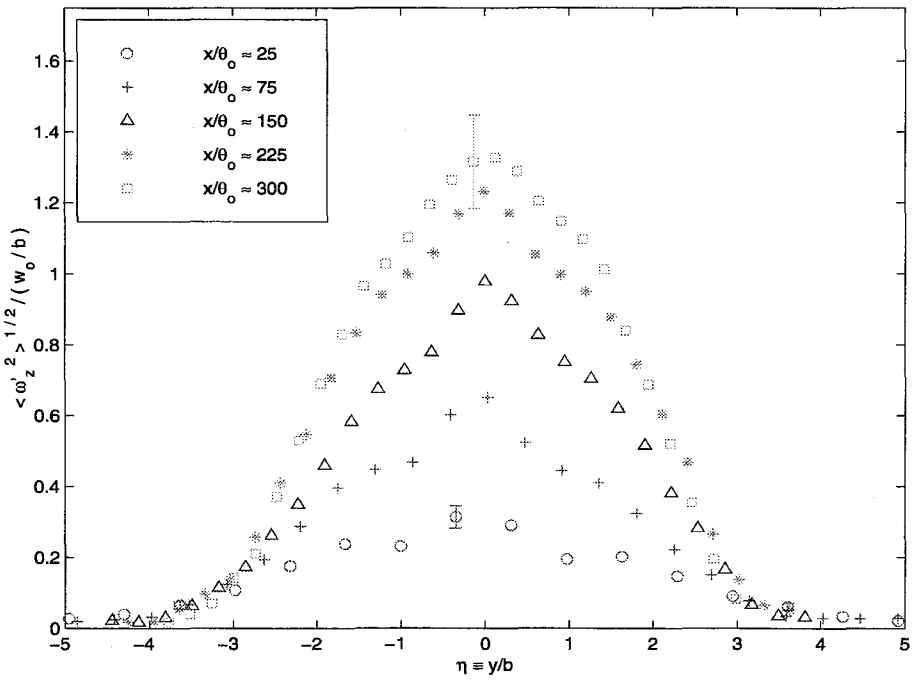
x/θo ≈ 25
x/θo ≈ 75
x/θo ≈ 150
x/θo ≈ 225
x/θo ≈ 300
<ω'z2>1/2/(wo/b)
η ≡ y/b

(b)

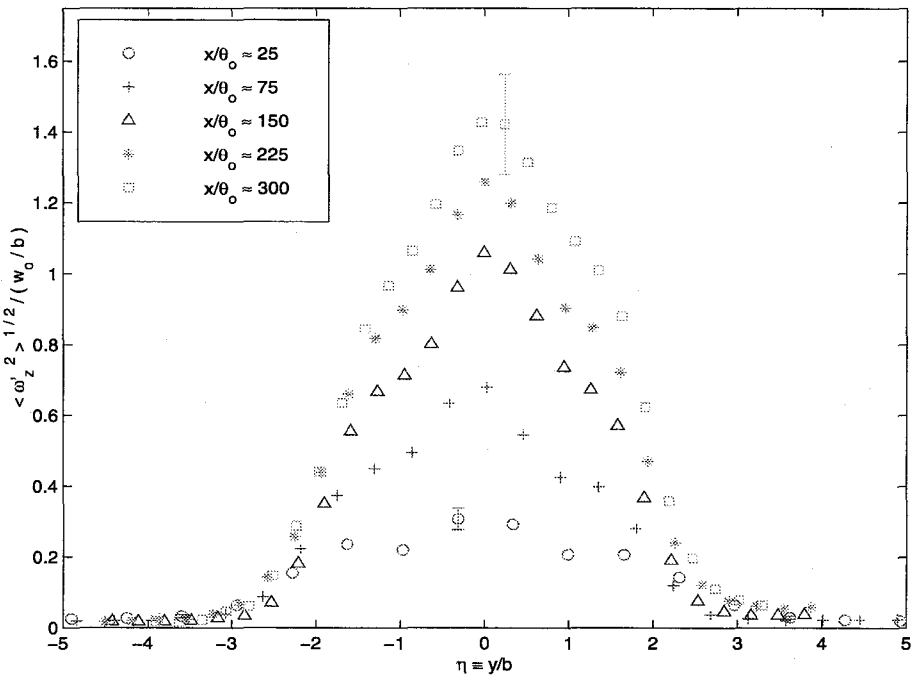

(c)

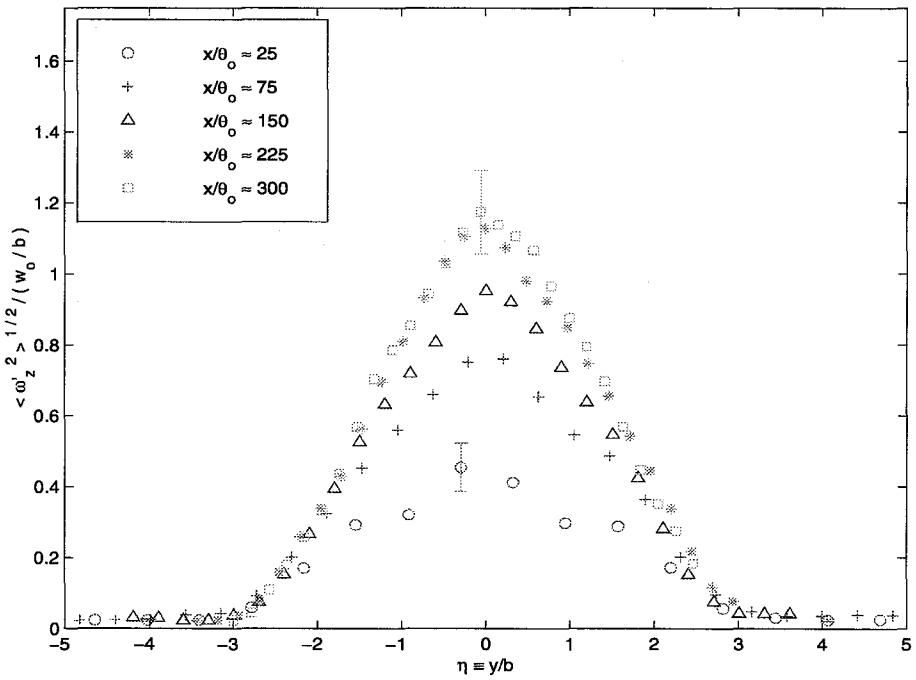

(d)

Fig. 4.5. Profiles of the normalized normal vorticity fluctuations in the surface-parallel planes at: (a) $z/\theta_o \approx -1$, (b) $z/\theta_o \approx -2$, (c) $z/\theta_o \approx -4$, (d) $z/\theta_o \approx -100$

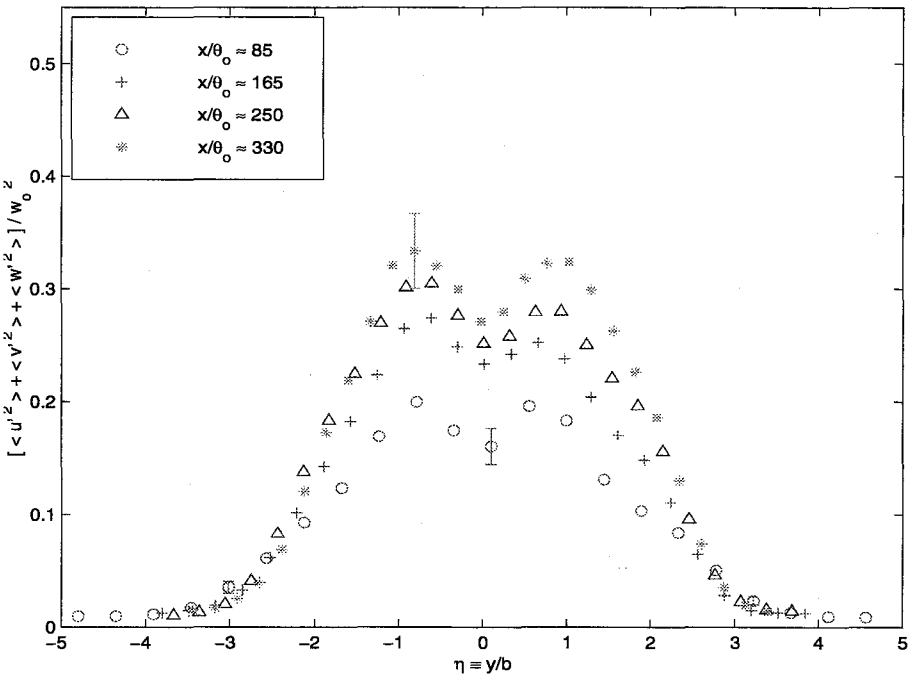
x/θo ≈ 85
x/θo ≈ 165
x/θo ≈ 250
x/θo ≈ 330
[< u'² > + < v'² > + < w'² >] / wo²
η ≡ y/b

(a)

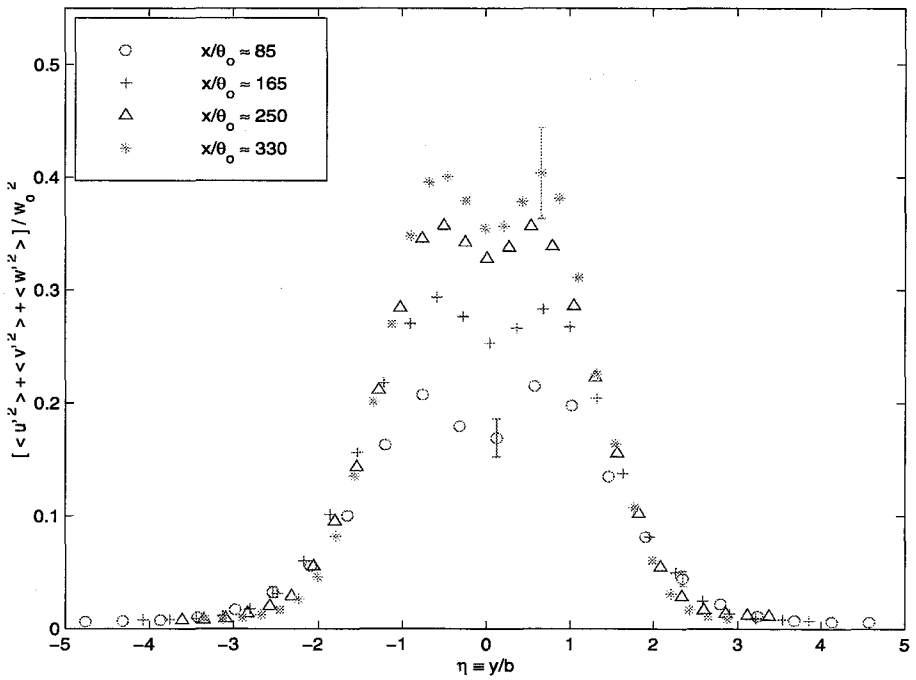
x/θo ≈ 85
x/θo ≈ 165
x/θo ≈ 250
x/θo ≈ 330
[< u'² > + < v'² > + < w'² >] / wo²
η ≡ y/b

(b)

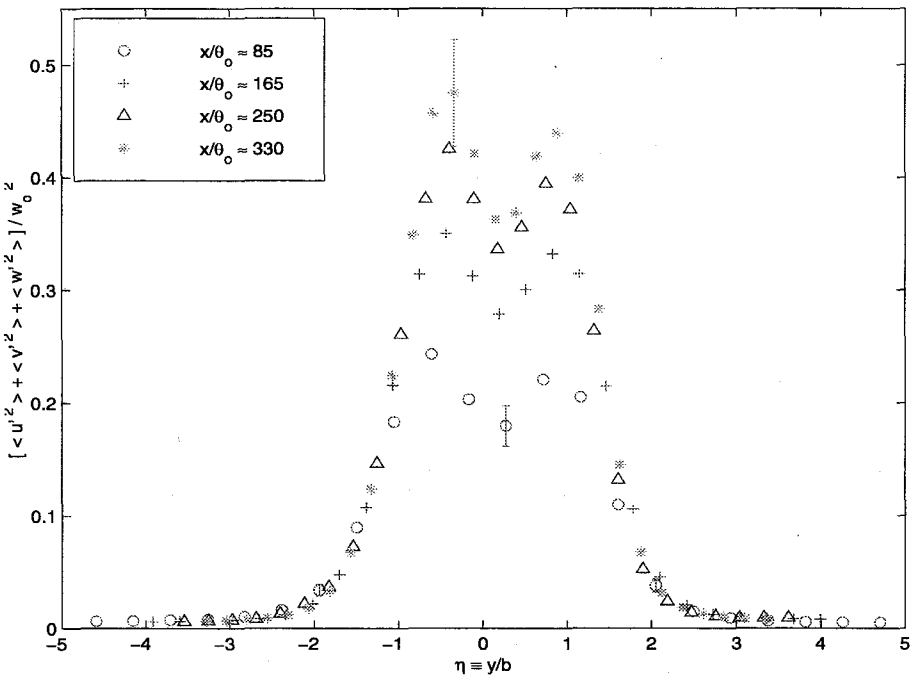

(c)

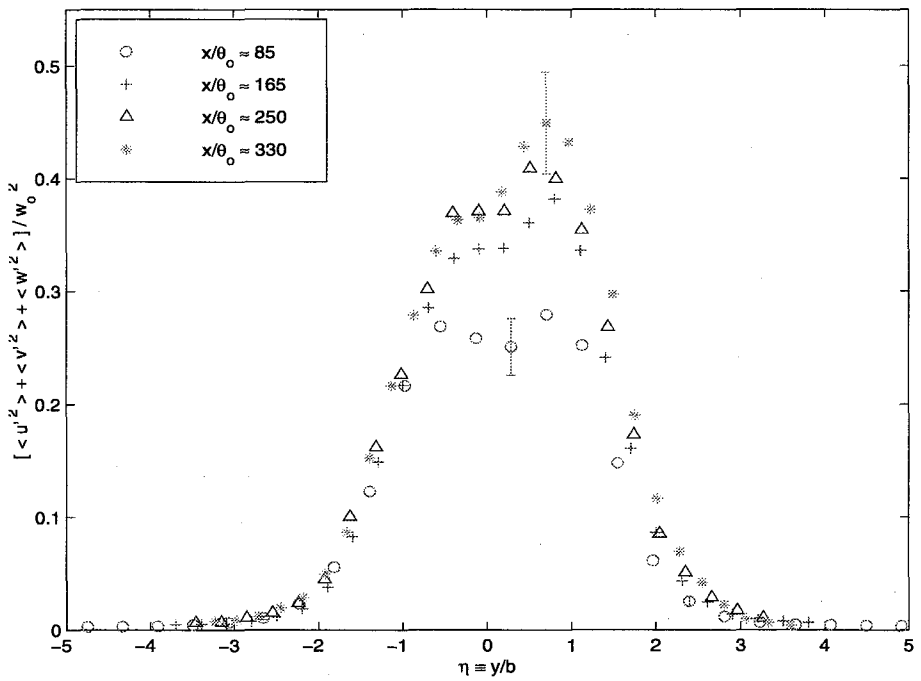

(d)

Fig. 4.6. Profiles of the normalized turbulent kinetic energy in the surface-parallel planes at: (a) $z/\theta_o \approx -1$, (b) $z/\theta_o \approx -2$, (c) $z/\theta_o \approx -4$, (d) $z/\theta_o \approx -100$

4.2.3. Secondary flows & turbulent features

(a) Secondary flows

(i) Introduction

The presence of secondary flows was unveiled in the near-surface edges of the wake by time averaging of flow-normal cross sections (see Fig. 4.2). This paragraph is concerned with the origin of these counter-rotating streamwise secondary *vortical* structures. As previously mentioned their effects on the turbulent shear flows were traced back to the plate's turbulent boundary layers where they are thus believed to originate. Recently, Longo et al.[17] (1997) examined the mixed-boundary corner problem by towing a surface-piercing flat plate in a water tank. A joint numerical / experimental study of turbulent flow along a corner formed by a vertical wall and a horizontal free surface was also undertaken by Grega et al.[18] (1995). The secondary streamwise vortical flows found in these studies were explained in terms of the anisotropy in the Reynolds stresses, i.e., Prandtl's secondary flows of the second kind. A simple analysis, similar to Hornung's[19] (1988) solid-solid corner flow, is made below of the physical mechanism for the streamwise structures and of free-surface effects on the Reynolds stresses.

(ii) The origin of the secondary flows

Consider a turbulent boundary layer formed by horizontal parallel flow of water along a partially submerged vertical solid wall. The free surface in this problem imposes an interesting set of boundary conditions. There is little or no shear at the free surface and vertical motion (i.e., perpendicular to the free surface) will be strongly attenuated. However, along the solid wall, the flow is constrained by the no-slip condition. Hence, this corner region is referred to as mixed-boundary corner or solid wall / free surface juncture. The analysis of secondary flows proves most fruitful when attention is concentrated on the component of vorticity in the chosen primary direction.

---

[17] Longo, J., Huang, H.P. & Stern, F. 1998 Solid / free-surface juncture boundary layer and wake. Exp. Fluids **25** (4), 283-297.

[18] Grega, L.M., Wei, T., Leighton, R.I. & Neves, J.C. 1995 Turbulent mixed-boundary flow in a corner formed by a solid wall and a free surface. J. Fluid Mech. **294**, 17-46.

[19] Hornung, H. 1988 Vorticity generation and secondary flow. First National Fluid Dyn. Congress. Cincinnati, 566-571.

In steady incompressible constant-flow property flow, the mean streamwise vorticity equation is

$$(\bar{u}\frac{\partial}{\partial x}+\bar{v}\frac{\partial}{\partial y}+\bar{w}\frac{\partial}{\partial z})\bar{\omega}_x=(\bar{\omega}_x\frac{\partial}{\partial x}+\bar{\omega}_y\frac{\partial}{\partial y}+\bar{\omega}_z\frac{\partial}{\partial z})\bar{u}+\nu\nabla^2\bar{\omega}_x$$
$$+\frac{\partial}{\partial x}(\frac{\partial\overline{u'v'}}{\partial z}-\frac{\partial\overline{u'w'}}{\partial y})+(\frac{\partial^2}{\partial z^2}-\frac{\partial^2}{\partial y^2})\overline{v'w'}+\frac{\partial^2}{\partial y\partial z}(\overline{v'^2}-\overline{w'^2})$$

where $\bar{\omega}_x=\frac{\partial\bar{w}}{\partial y}-\frac{\partial\bar{v}}{\partial z}$, $\bar{\omega}_y=\frac{\partial\bar{u}}{\partial z}-\frac{\partial\bar{w}}{\partial x}$ and $\bar{\omega}_z=\frac{\partial\bar{v}}{\partial x}-\frac{\partial\bar{u}}{\partial y}$.

This equation is most readily derived by eliminating the pressure, p, between the time-averaged Reynolds equations in the y and z directions.

If one assumes that the turbulent flow is fully-developed such that $\partial/\partial x \approx 0$, then

$$(\bar{\omega}_y\frac{\partial}{\partial y}+\bar{\omega}_z\frac{\partial}{\partial z})\bar{u}\approx\frac{\partial\bar{u}}{\partial z}\frac{\partial\bar{u}}{\partial y}-\frac{\partial\bar{u}}{\partial y}\frac{\partial\bar{u}}{\partial z}=0$$

In addition, measurements and simulations have shown that $\overline{v'w'}$ is negligibly small everywhere in the flow.

The mean streamwise vorticity equation reduces hence to

$$\underbrace{(\bar{v}\frac{\partial}{\partial y}+\bar{w}\frac{\partial}{\partial z})\bar{\omega}_x}_{\text{rate of change of vorticity}}=\underbrace{\nu(\frac{\partial^2}{\partial y^2}+\frac{\partial^2}{\partial z^2})\bar{\omega}_x}_{\substack{\text{diffusion of vorticity}\\ \text{due to viscosity}}}+\underbrace{\frac{\partial^2}{\partial y\partial z}(\overline{v'^2}-\overline{w'^2})}_{\substack{\text{production terms due to}\\ \text{Reynolds stress anisotropy}}}$$

The second term in the right-hand side indicates that mean streamwise vorticity is produced by an imbalance between gradients of the wall-normal and free-surface-normal turbulent fluctuations.

In order to understand the qualitative features of the secondary flow generated by the above equation, let us make some crude (but reasonable) assumptions about the amplitudes of the turbulent fluctuations. Since all fluctuating components disappear at the wall (particularly $\overline{v'^2} = 0$ and $\overline{w'^2} = 0$), we assume that their amplitudes increase monotonically with distance from the wall up to certain maxima. For simplicity (though this is not necessary), we assume the dependence on distance from the wall to be linear. After reaching these maximum values, they decrease exponentially toward their freestream values as has been verified by numerous boundary layer experiments (e.g., Nezu et al.[20]). Furthermore, we assume that the amplitude of the surface-parallel component increases more rapidly with distance from the wall than that of the wall-normal component. Finally, the free surface is treated as a flat, shear-free boundary. Based on previous results, we assume that the amplitude of the surface-parallel component significantly increases at the free surface while the amplitude of the surface-normal component strongly decreases as the free surface is reached.

We consider first the two lines in a quadrant of the cross section (y,z) of the corner flow (see Fig. 4.1) at distances $z = -a$ and $z = -2a$ from the free surface $z = 0$. Along the line $z = -a$, we start from the wall so that both fluctuating components increase to reach their maximum values after which they decrease toward their freestream values. Both full curves follow the same trend but the maximum value of $\overline{v'^2}$ is much larger than the one of $\overline{w'^2}$ since we are close to the free surface. The dashed lines represent the same turbulent fluctuations along the line $z = -2a$. However, as we move away from the free surface, the maximum value of $\overline{v'^2}$ is still much higher than the one of $\overline{w'^2}$, but it decreases while the maximum value of $\overline{w'^2}$ increases. This trend continues until both fluctuating turbulent intensities reach their asymptotic curves far away enough from the free surface. The next part of Fig. 4.1 shows a plot of the difference $\overline{v'^2} - \overline{w'^2}$ along the lines $z = -a$ (full) and $z = -2a$ (dashed) against y. It is important to note that this plot is in qualitative agreement with experimental results by Longo et al.[17] (1998). The difference between these two curves is an approximation for $\partial(\overline{v'^2} - \overline{w'^2})/\partial z$ along the line $z = -3a/2$. It is also plotted against y in Fig. 4.1. Finally, we plot the derivative of this quantity with respect to y and thus obtain the qualitative behavior of the production of longitudinal vorticity along the line $z = -3a/2$.

Free Surface

[20] Nezu, I. & Nakagawa, H. 1993 Turbulence in open-channel flows. AIRH monograph. ed. A.A. Balkema.

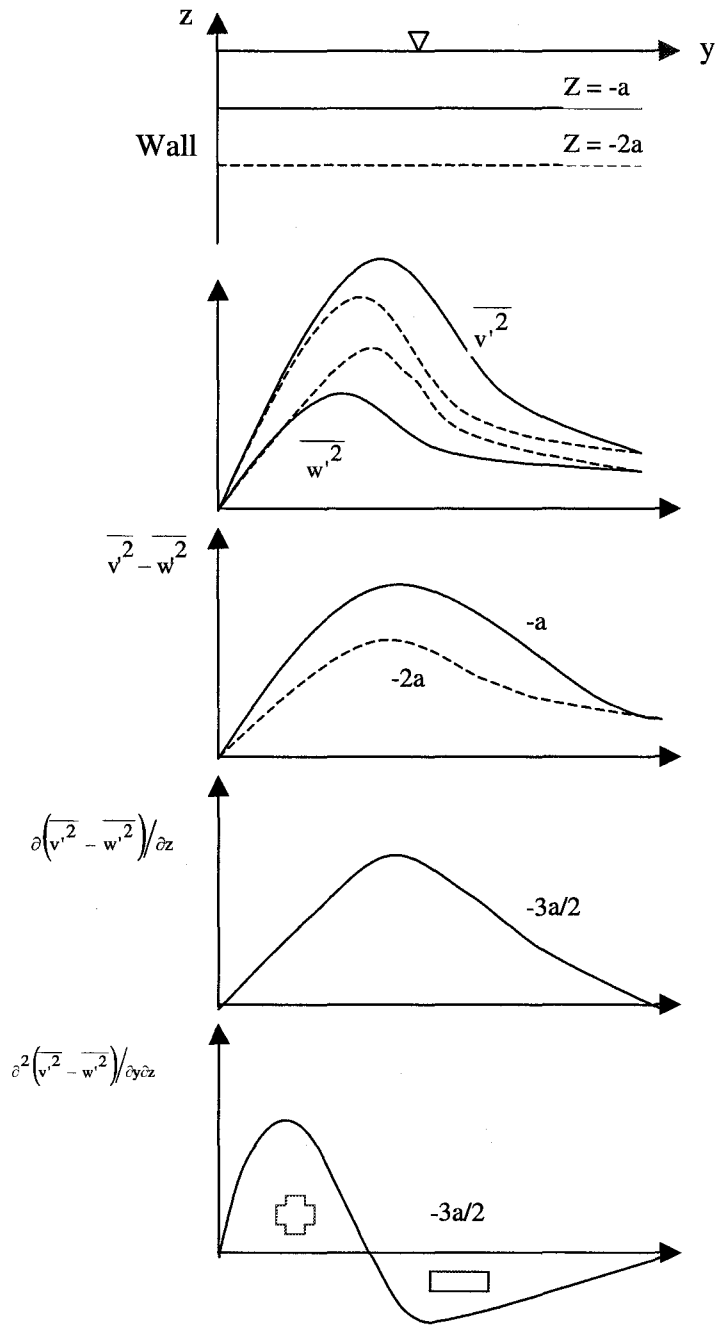

Fig. 4.1. Qualitative behavior of the secondary flows generated by Reynolds stress anisotropy

Positive vorticity is directed in the counterclockwise sense whereas negative vorticity is clockwise. In the near corner an inner secondary *vortex* whose motion is directed in toward the wall at the free surface and down away from the free surface at the wall (i.e., positive vorticity) is generated. To its right, an outer secondary *vortex* spinning in the opposite direction (i.e., negative vorticity) is also created (as shown in Fig. 4.2). The secondary *vortices* in a solid wall / free surface juncture, which are driven by the anisotropy in the local turbulent stresses, are similar to the ones obtained in a solid-solid corner. However, based on the above simple analysis, we can easily deduce that the inner secondary *vortex* is stronger than its outer counterpart. This latter is, in turn, larger and located farther away from the wall. Indeed, the inner secondary *vortex* is generated in the region where turbulent stresses reach linearly (for simplicity) their maximum values. On the other hand, the outer secondary *vortex* is created by anisotropy in the turbulent stresses as they exponentially decrease toward their freestream values. This qualitative behavior is in agreement with the numerical simulations carried out in Grega et al.[18]. Furthermore, the results presented in this simple analysis are altogether consistent with previous experimental and numerical results[17,18].

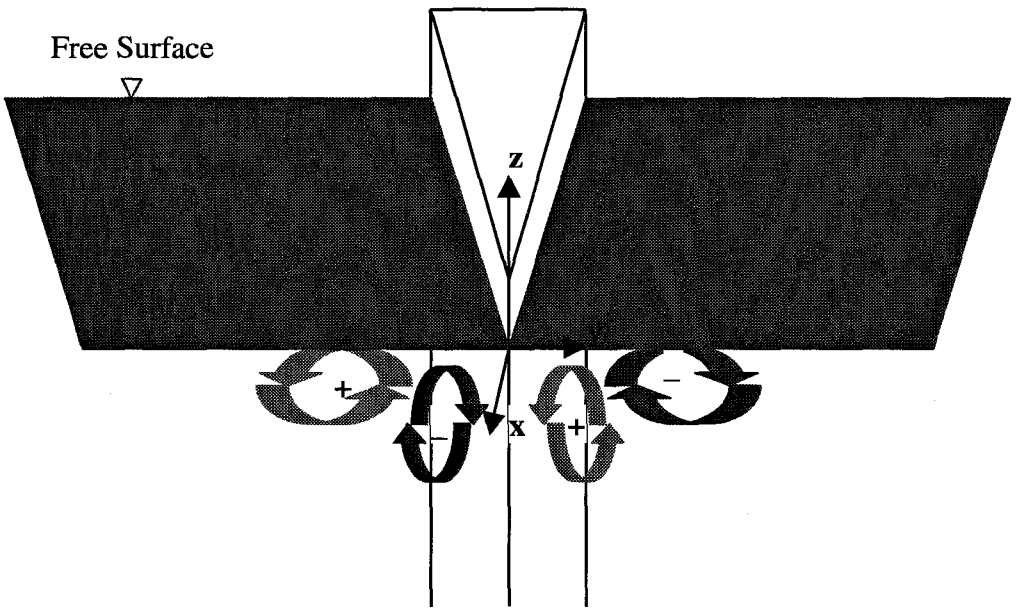

Fig. 4.2. Schematic drawing of the secondary vortical flows in the mixed-boundary corners

The above analysis obviously depicts a mean picture of the flow. LIF (laser-induced fluorescence) flow visualization (see in particular Grega et al.[18]) paints a much different instantaneous picture of this flow. It is composed of numerous surface-parallel and surface-normal turbulent structures. Both secondary *vortical* flows are the results of the mean behavior of these vortical structures. Their mutual interaction with their environment generates an anisotropy in the local turbulent stresses which, in turn, gives birth to two streamwise cellular vortex forms. In the next section, instantaneous data sequence obtained throughout the wake using the DPIV technique will shed light on the instantaneous flow structures and their relation to the mean flow field.

(b) The evolution of the secondary flows

(i) Mean flow patterns

A pair of counter-rotating streamwise secondary flows thus emerges from each mixed-boundary corner flow of the splitter plate as shown in Fig. 4.2. The sudden end of the plate has major impacts on the nature of the flow, as the turbulent boundary layers on the two sides of the plate merge slowly and transform into a wake. It does too on the secondary *vortical* flows.

The pair of outer secondary *vortices* are believed to be the counter-rotating streamwise secondary vortical flows unveiled in the near-surface edges of the wake by time averaging of flow-normal cross sections. These secondary *vortical* flows evolve away from one another but stay located at the edges of the wake feeding on the anisotropy of Reynolds stresses. As previously mentioned in section 4.2.1.(a), these secondary flows are consistent with the existence of the now well-known *surface currents*, which can be simply understood in terms of mean induced velocity field in this context. As pointed out by Walker[21], these *surface currents* appear to be ubiquitous features of turbulent free-surface flows. Plotting the mean transverse velocity profiles in the very near-surface region, that is, at $z/\theta_o \approx -1$, clearly shows the presence of these outward currents adjacent to the free surface. Fig. 4.1 shows that these near-surface velocity profiles are quite different and particularly of opposite sign from the mean transverse velocity profiles of the turbulent plane wake entraining fluid to enable its growth. The influence of the near-surface secondary flows and their associated free-surface currents on the development of the wake and its mean and turbulent properties at the free surface was quantified in sections 4.2.1 and 4.2.2.

[21] Walker, D.T. 1997 On the origin of the 'surface currents' in turbulent free-surface flows. J. Fluid Mech. **339**, 275-285.

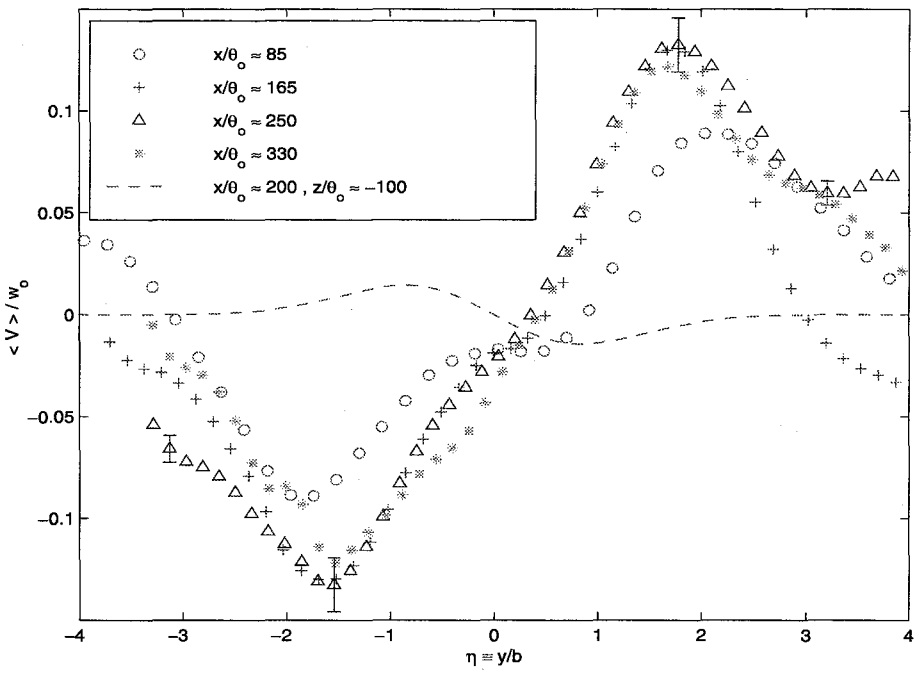

Fig. 4.1. Surface-normal measurements of the mean transverse velocity at $z/\theta_o \approx -1$

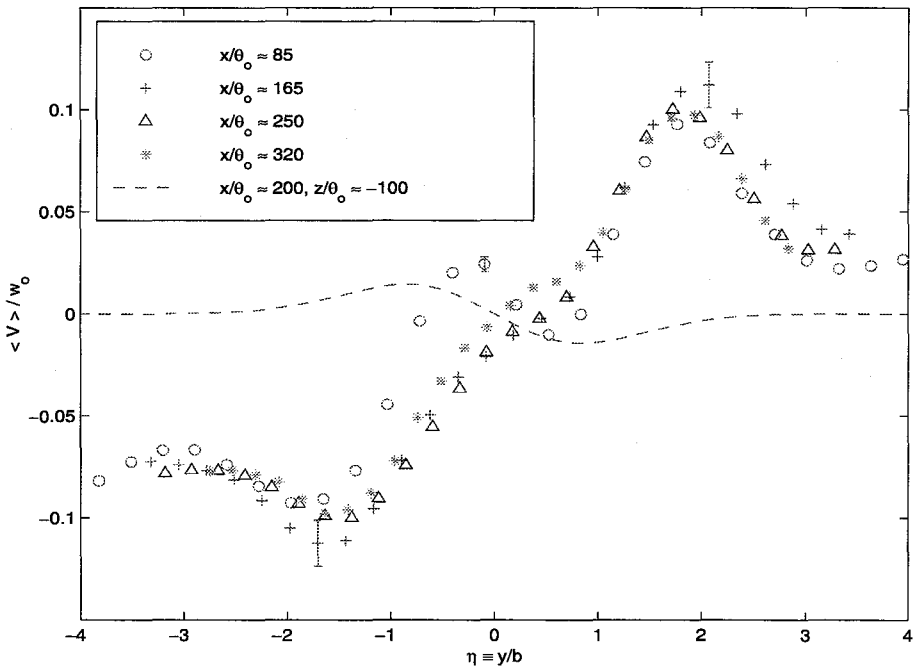

Fig. 4.2. Surface-parallel measurements of the mean transverse velocity at $z/\theta_o \approx -1$

On the other hand, the pair of inner secondary flows was not observed in any flow-normal cross sections from $x/\theta_o \approx 85$ on. Their disappearance should not be too surprising if we pause a moment to remember that each inner secondary *vortex* was fueled by the turbulent stress anisotropy close to the wall. As the flat plate ends, the anisotropy on which the inner *vortical* flows were feeding was expected to die out within the wake flow as the wall shear diffuses outward. This seems to be a reasonable explanation why these secondary flows do not appear in any of flow-normal Reynolds-averaged vorticity fields. However, this latter process is not instantaneous and should take some time to develop. Although no measurements were carried out in flow-normal planes upstream of $x/\theta_o \approx 85$, data was nevertheless obtained throughout the wake in surface-parallel planes. The measurements of the transverse velocity made in the near-surface-parallel plane ($z/\theta_o \approx -1$) reveal the presence of inward *surface currents* in the near-wake region (see Fig. 4.2 at $x/\theta_o \approx 65$ and also Fig. 4.1). These currents are believed to be the surface signatures of the inner *vortices* of the corner flows. Initially, as they emerge out of the solid wall / free surface juncture, their magnitude is larger than their outward counterparts in the near-wake region before it sharply decreases until their complete disappearance. These findings are consistent with the simple analysis made in section (a)(ii). Indeed, the inner *vortices* were found to be stronger than their outer counterparts, which would results in stronger inward *surface currents*, at least initially.

As the plate ends, the Reynolds-stress anisotropy, which gave birth to the pair of secondary flows unveiled in the juncture flows, is modified. The flow is confronted to new boundary conditions as the wall shear diffuses outward. The following paragraph uncovers the turbulent-stress field that ensues in the wake and how it is responsible for sustaining the two streamwise cellular vortex forms observed at its edges. Using similar arguments used in the previous section (4.2.3(a)(ii)), the mean streamwise vorticity equation can also be reduced to

$$\underbrace{\left(\bar{v}\frac{\partial}{\partial y}+\bar{w}\frac{\partial}{\partial z}\right)\overline{\omega_x}}_{\text{rate of change of vorticity}} = \underbrace{\nu\left(\frac{\partial^2}{\partial y^2}+\frac{\partial^2}{\partial z^2}\right)\overline{\omega_x}}_{\substack{\text{diffusion of vorticity}\\ \text{due to viscosity}}} + \underbrace{\frac{\partial^2}{\partial y \partial z}\left(\overline{v'^2}-\overline{w'^2}\right)}_{\substack{\text{production terms due to}\\ \text{Reynolds stress anisotropy}}}$$

A similar analysis as that made in section 4.2.3(a)(ii) could be performed. The reader can indeed convince himself that it will lead to the same results as the ones presented below. Measurements were indeed made in the flow-normal cross sections of the wake and shed all the light that is needed on this phenomenon.

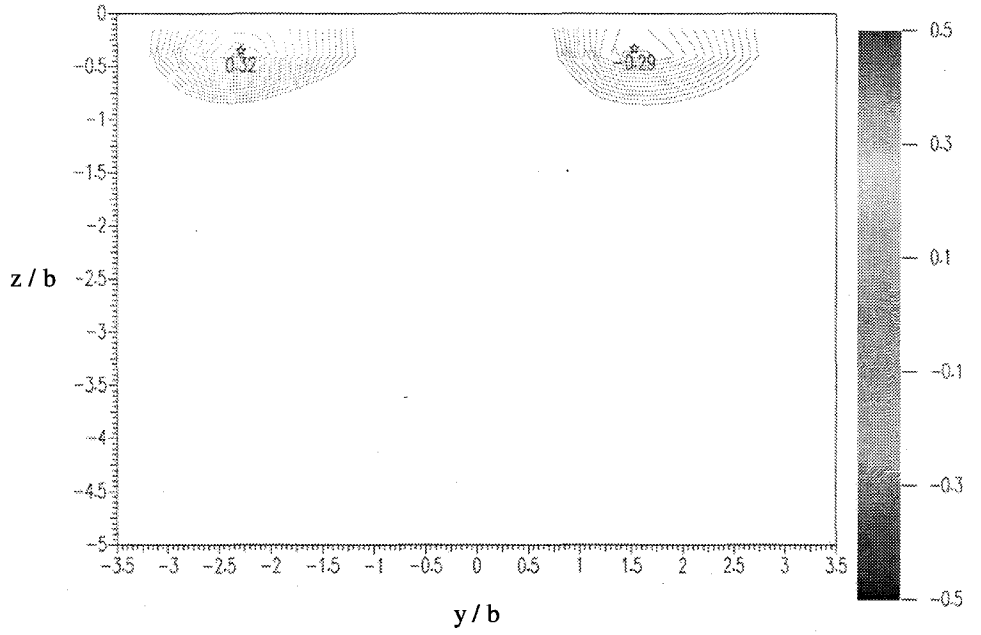

(a) Mean streamwise vorticity field $\overline{\omega_x}$

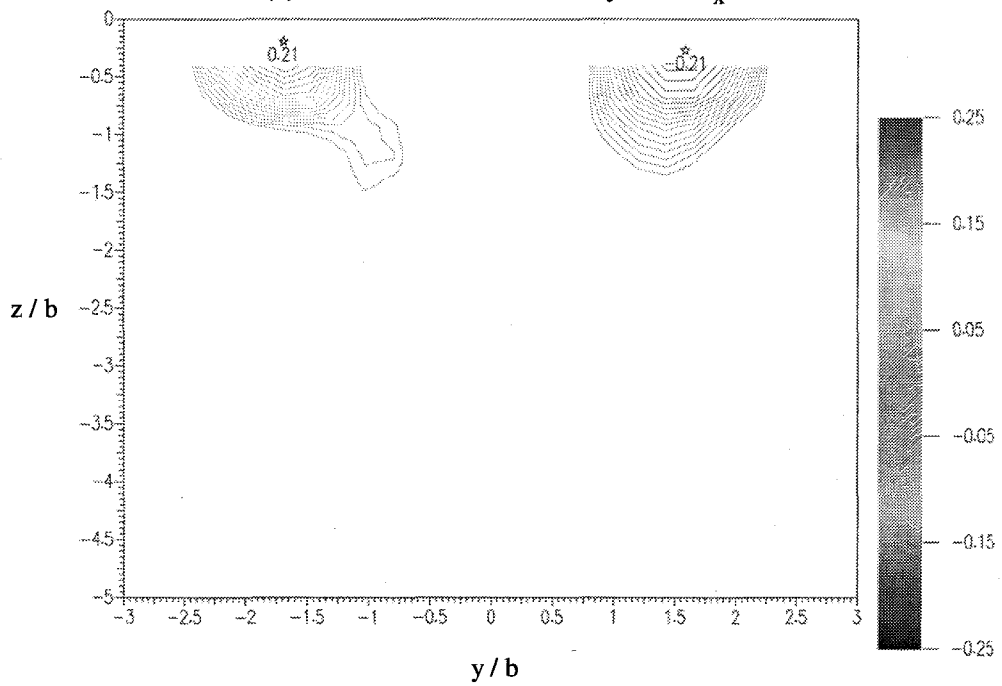

(b) $\partial^2\left(\overline{v'^2} - \overline{w'^2}\right)/\partial y \partial z$

Fig. 4.3. Mean streamwise vorticity and Reynolds-stress anisotropy in the wake

Fig. 4.3 displays a representative picture of the mean vorticity field and the associated production term due to Reynolds-stress anisotropy obtained in flow-normal measurement planes. Based on the $\partial^2 (\overline{v'^2} - \overline{w'^2})/\partial y \partial z$ field, we can easily deduce that two counter-rotating streamwise "secondary vortices" are generated at each edge of the wake. These results are in very good agreement with the mean streamwise vorticity field obtained throughout the wake.

It is worthwhile to point out that similar results would be obtained using the Reynolds-averaged Navier-Stokes equations combined with adequate simplifying assumptions, as brilliantly shown by Walker[21] for the free-surface turbulent jet.

(ii) Turbulent flow features

As was mentioned earlier, this analysis paints a picture of the mean flow patterns. It is also important to unravel the turbulent flow dynamics leading to these mean results. In contrast to most previous free-surface flow studies using single-point measurement techniques, new light can here be shed on the instantaneous flow features using the spatio-temporal information obtained through the intensive use of digital PIV.

Fig. 4.1 displays a representative sequence of instantaneous vortical fields captured in the measurement plane at $x/\theta_0 \approx 165$. Several fundamental observations can be readily made, pointing out the important differences existing between the instantaneous and averaged vortical fields. Indeed, streamwise vortical structures are present throughout the wake both in the deep and near-surface regions and are not only limited to the near-surface region. In addition, the near-surface structures have higher vorticity values and different locations, and appear to be intermittent. These instantaneous flow measurements thus indicate that these secondary flows are not caused by two coherent turbulent structures present at the edges of the wake. They are the result of a much more complex interaction of the wake turbulent structures with the free surface. Further inspection of the sequence provides explanations for the resulting mean flow patterns. The instantaneous streamwise structures present in the deep wake do not appear to be *locked-in* spatially. Actually, a positive streamwise vortex is as likely to be found at a certain position in the deep-wake region as is a negative one with similar vorticity value. And this point is further confirmed by the vorticity *cancellation* during the averaging process. However, this result was all but unexpected since one is to obtain a fully-submerged turbulent wake, two-dimensional in the mean.

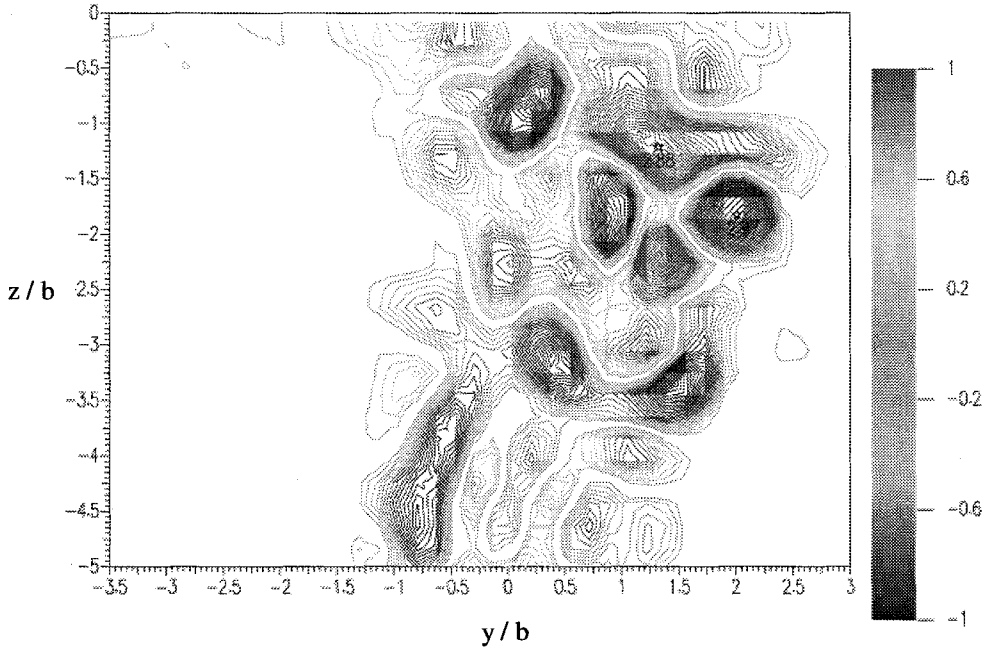
z / b
y / b
0
-0.5
-1
-1.5
-2
-2.5
-3
-3.5
-4
-4.5
-5
-3.5 -3 -2.5 -2 -1.5 -1 -0.5 0 0.5 1 1.5 2 2.5 3
1
0.6
0.2
-0.2
-0.6
-1

(a)

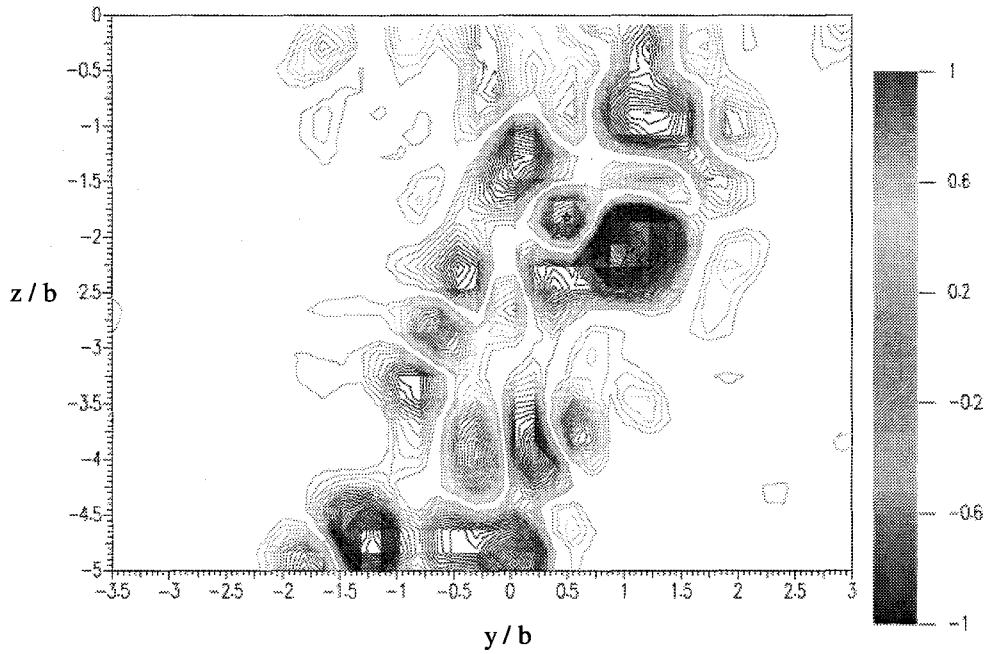
z / b
y / b
0
-0.5
-1
-1.5
-2
-2.5
-3
-3.5
-4
-4.5
-5
-3.5 -3 -2.5 -2 -1.5 -1 -0.5 0 0.5 1 1.5 2 2.5 3
1
0.6
0.2
-0.2
-0.6
-1

(b)

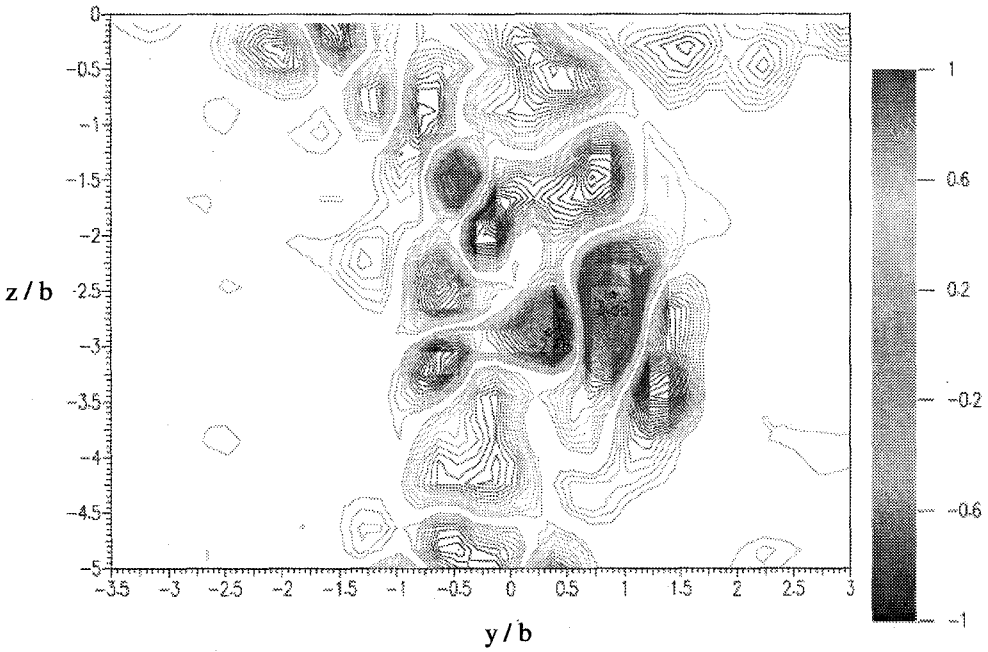
z / b
y / b
0
-0.5
-1
-1.5
-2
-2.5
-3
-3.5
-4
-4.5
-5
-3.5 -3 -2.5 -2 -1.5 -1 -0.5 0 0.5 1 1.5 2 2.5 3
1
0.6
0.2
-0.2
-0.6
-1

(c)

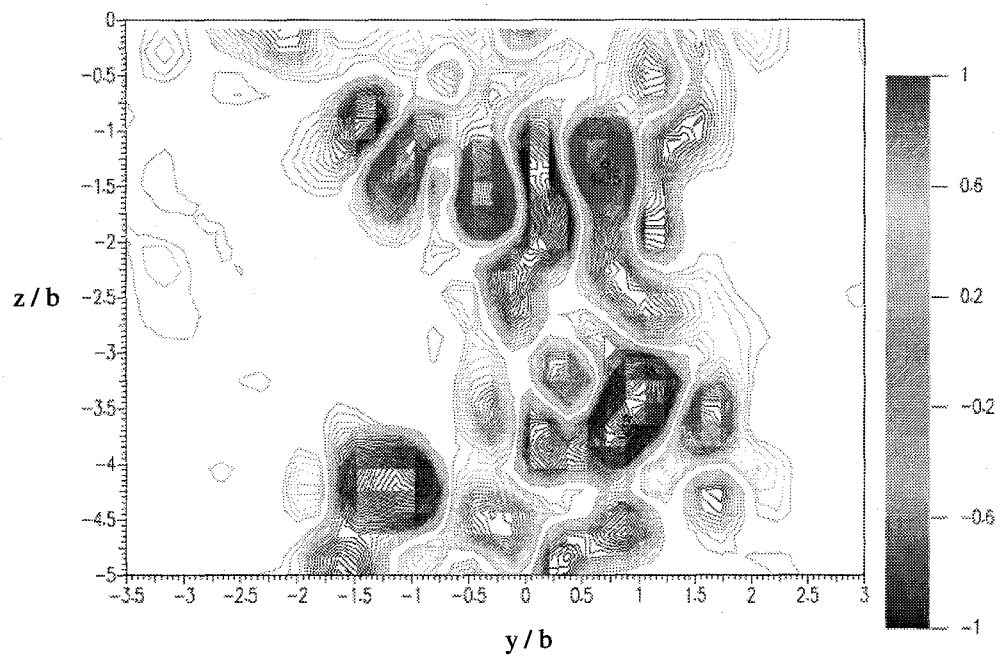
z / b
y / b
0
-0.5
-1
-1.5
-2
-2.5
-3
-3.5
-4
-4.5
-5
-3.5 -3 -2.5 -2 -1.5 -1 -0.5 0 0.5 1 1.5 2 2.5 3
1
0.6
0.2
-0.2
-0.6
-1

(d)

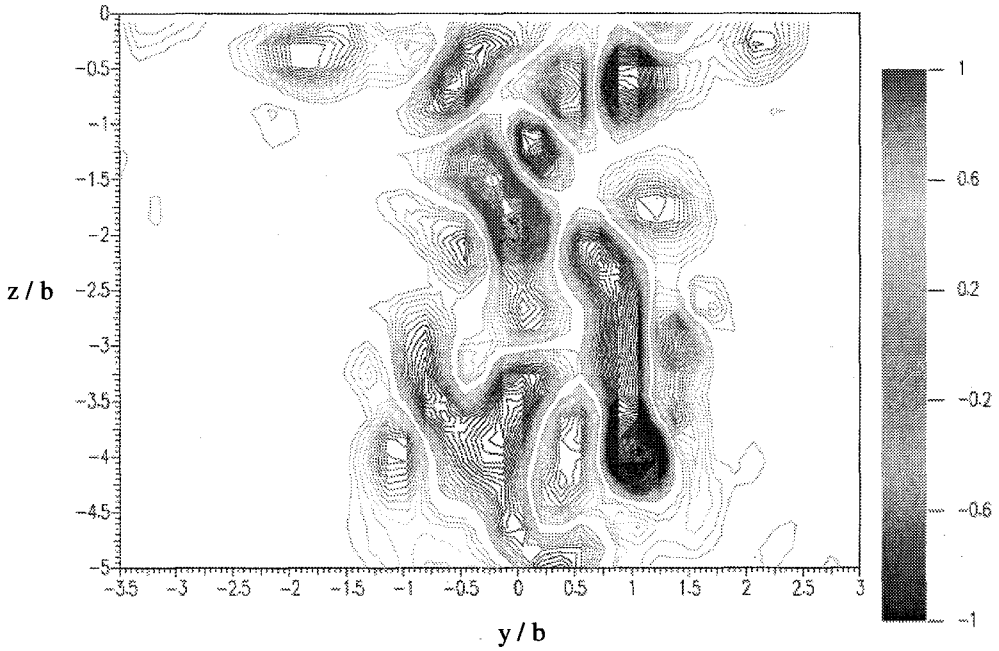
z / b
y / b
0
-0.5
-1
-1.5
-2
-2.5
-3
-3.5
-4
-4.5
-5
-3.5 -3 -2.5 -2 -1.5 -1 -0.5 0 0.5 1 1.5 2 2.5 3
1
0.6
0.2
-0.2
-0.6
-1

(e)

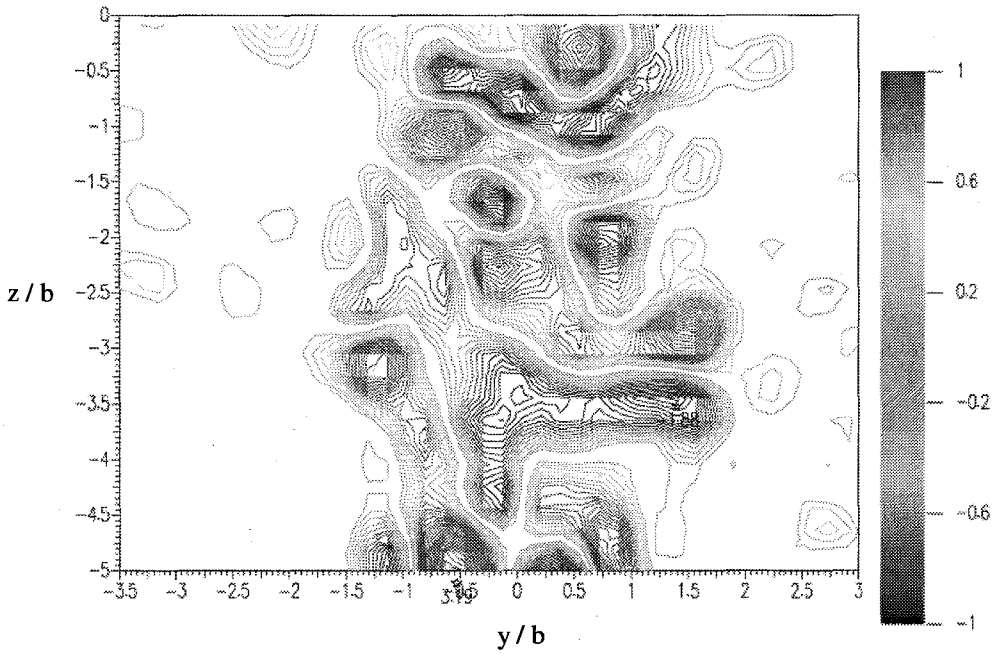
z / b
y / b
0
-0.5
-1
-1.5
-2
-2.5
-3
-3.5
-4
-4.5
-5
-3.5 -3 -2.5 -2 -1.5 -1 0 0.5 1 1.5 2 2.5 3
1
0.6
0.2
-0.2
-0.6
-1

(f)

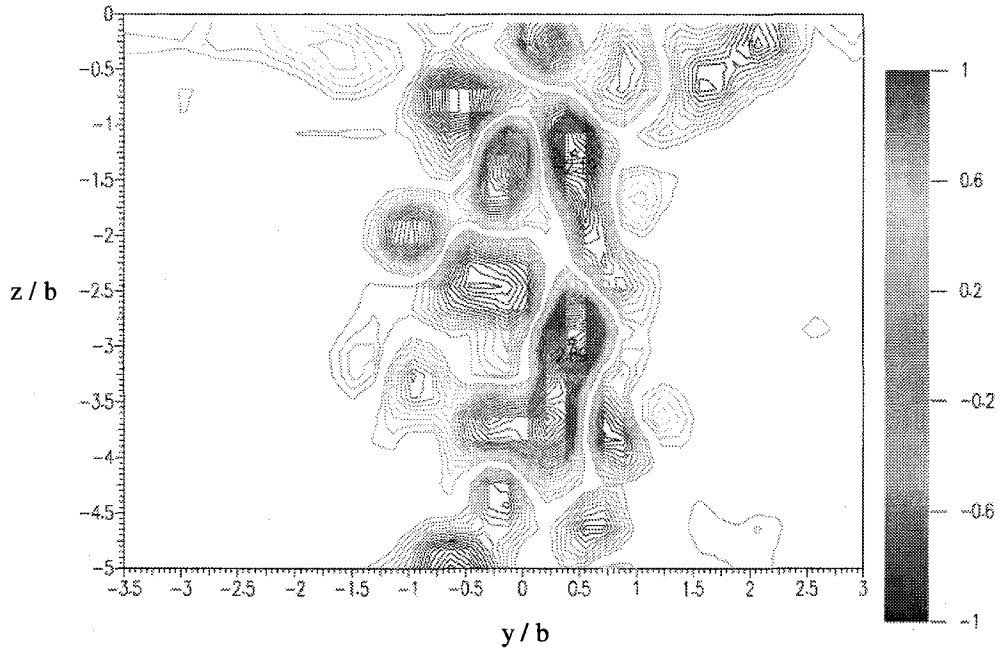
z / b
y / b
0
-0.5
-1
-1.5
-2
-2.5
-3
-3.5
-4
-4.5
-5
-3.5 -3 -2.5 -2 -1.5 -1 -0.5 0 0.5 1 1.5 2 2.5 3
1
0.6
0.2
-0.2
-0.6
-1

(g)

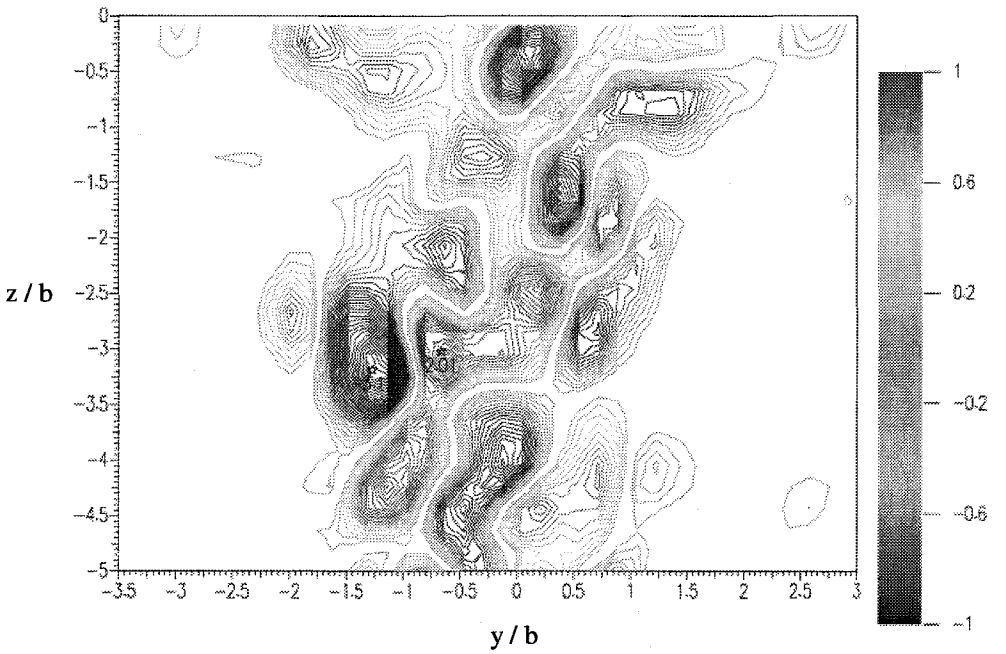
z / b
y / b
0
-0.5
-1
-1.5
-2
-2.5
-3
-3.5
-4
-4.5
-5
-3.5 -3 -2.5 -2 -1.5 -1 -0.5 0 0.5 1 1.5 2 2.5 3
1
0.6
0.2
-0.2
-0.6
-1

(h)

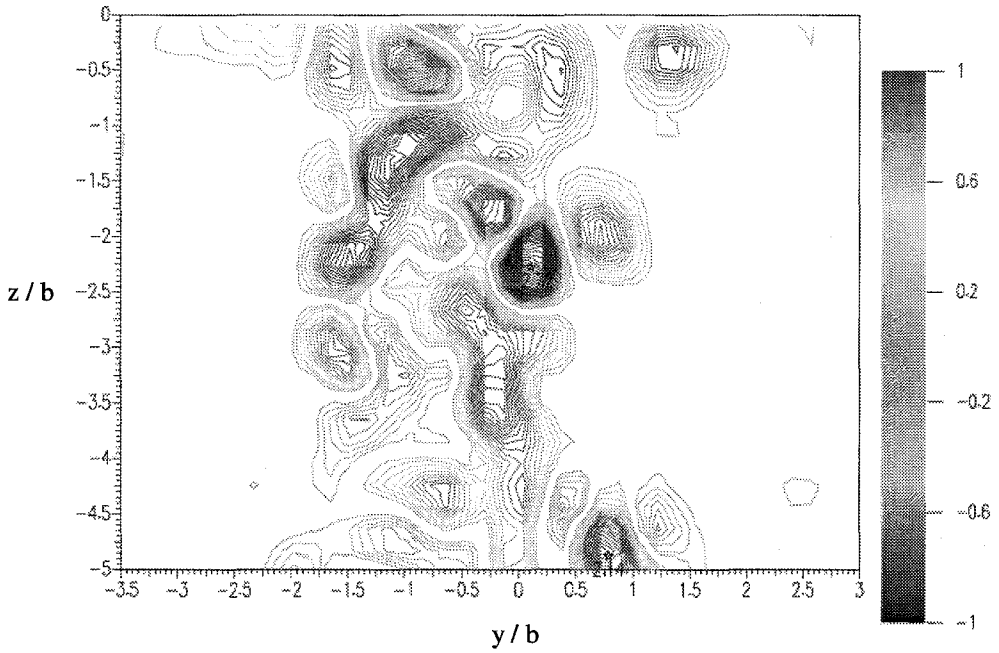

(i)

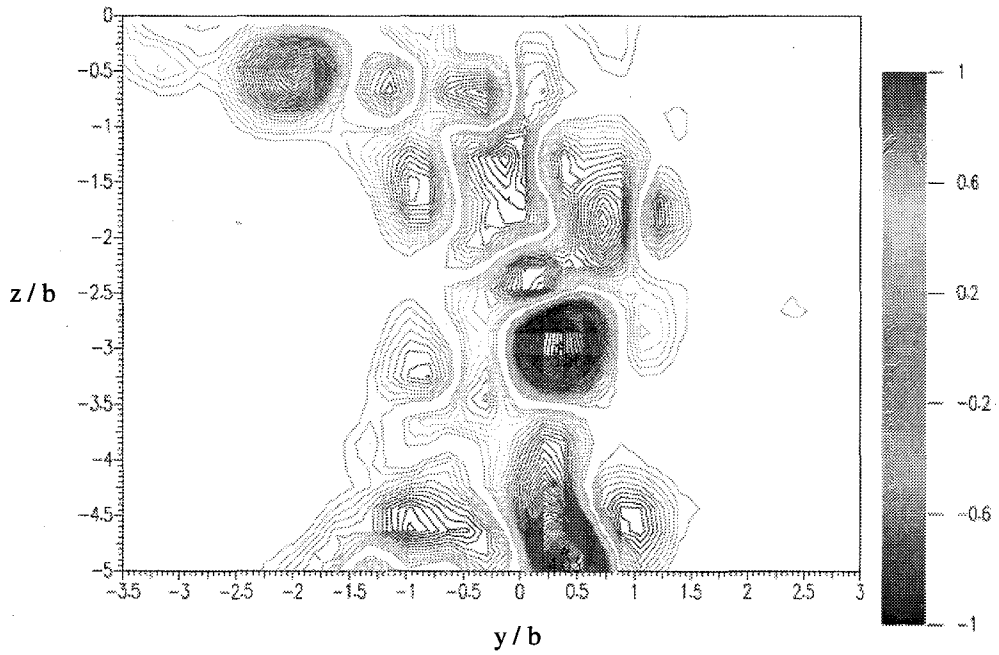

(j)

Fig. 4.1. Representative sequence of instantaneous vortical fields ($1/15$ sec $\approx \tau/4$ apart) in a flow-normal measurement plane ($x/\theta_o \approx 165$)

In addition, the wake contains relatively strong surface-parallel structures near the free surface and appears wider at the free surface in most of the vortical fields of this representative sequence. Besides, these near-surface vortical structures at the edges of the wake are of the same signs as the mean secondary flows: negative on the right edge of the wake and positive on the other edge. The streamwise vortical structures are believed to be the hairpin vortices originating from the plate's boundary layers and further advected in the wake. This explained the observed intermittency of these streamwise structures. The existence of the surface secondary flows can be easily understood by examining the interaction of the surface-parallel structures in the turbulent wake with their images above the free surface. Indeed, the mutually induced velocity by these structures and their images is directed outward which causes them to move away from the centerline. Streamwise structures of negative vorticity tend thus to evolve toward the $y > 0$ side of the wake, while those of positive vorticity move toward the $y < 0$ side. And, indeed, as previously pointed out, these near-surface vortical structures at the edges of the wake are of the same signs as the mean secondary flows: negative on the right edge of the wake and positive on the other edge. The time average of many instantaneous vorticity fields hence results in the mean secondary flow patterns and their associated mean *surface currents*.

We wish here to investigate more closely the combined effect of the streamwise vortices present at the edges of the wake. Short-time averages were thus obtained to shed light on this aspect. In particular, we are interested to assess the spatio-temporal coherence of the near-surface streamwise structures. Short-time averages clearly show that the constant stream of near-surface streamwise vortices originating from the plates' boundary layers, and now embedded into the wake turbulent structure, averages out into the secondary flows. Indeed, their *meandering* around a mean position at the edge of the wake gradually smoothes out into secondary *vortical* flows. Comparison with long-time averages shows the spatio-temporal coherence of these near-surface structures, as indicated by the similar positions, vorticity values and distributions. The near-surface streamwise vortices have the same size as the secondary flows to which they *quickly* averaged out to give birth. Indeed, the secondary vortical flows appear clearly after averaging only one second of data, that is 15 DPIV frames or about four integral time scales at this station. Similar near-surface secondary flows were also found using short-time averages at the edges of the free-surface jets as shown by both experimental and numerical results displayed in Fig. 4.3 (Liepmann et al.[22]) and (Mangiavacchi et al.[23]), even though their origin is slightly different.

[22] Liepmann, D. & Gharib, M. 1994 The vorticity and entrainment dynamics of near-surface jets. Free-surface turbulence ASME 1994, FED-**181**, 53-58.

[23] Mangiavacchi, N., Gundlapalli, R. & Akhavan, R. 1994 Dynamics of a turbulent jet interacting with a free surface. Free-surface turbulence ASME 1994, FED-**181**, 69-82.

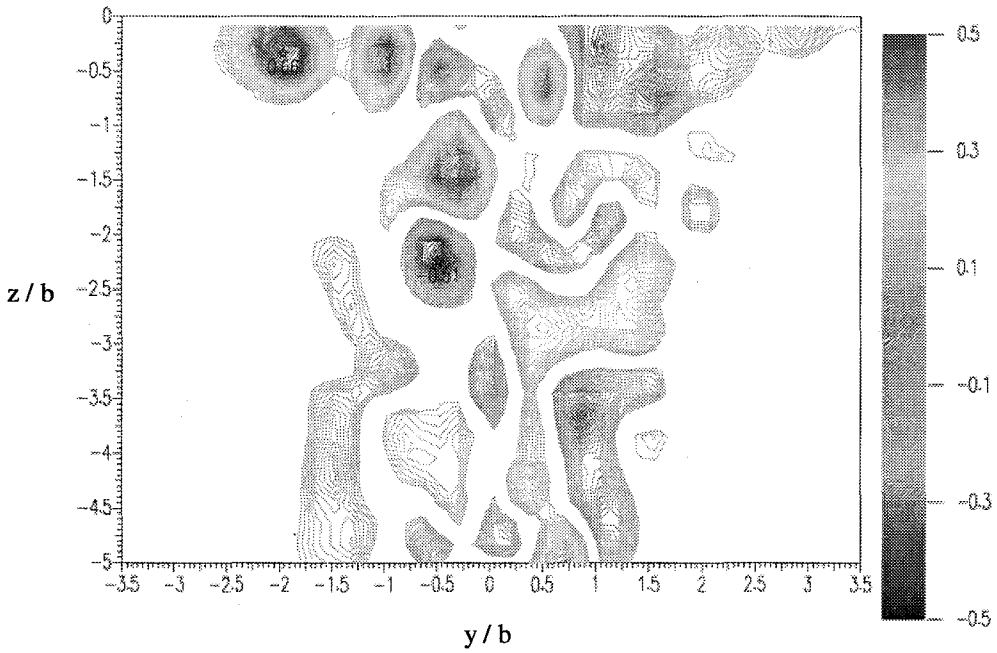
z / b
y / b
0
-0.5
-1
-1.5
-2
-2.5
-3
-3.5
-4
-4.5
-5
-3.5 -3 -2.5 -2 -1.5 -1 -0.5 0 0.5 1 1.5 2 2.5 3 3.5
0.5
0.3
0.1
-0.1
-0.3
-0.5

(a)

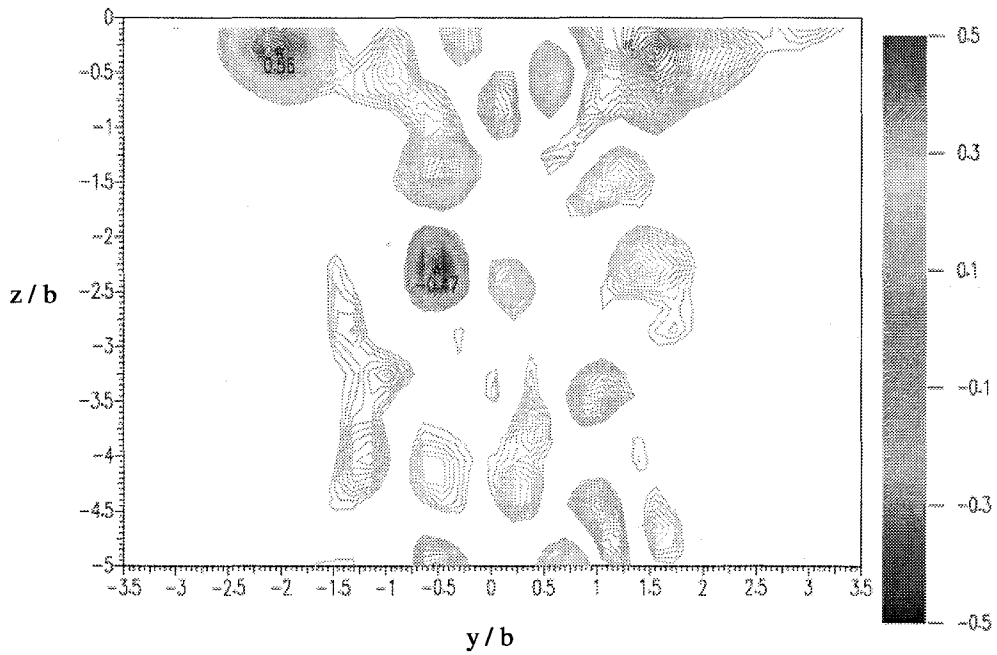
z / b
y / b
0
-0.5
-1
-1.5
-2
-2.5
-3
-3.5
-4
-4.5
-5
-3.5 -3 -2.5 -2 -1.5 -1 -0.5 0 0.5 1 1.5 2 2.5 3 3.5
0.5
0.3
0.1
-0.1
-0.3
-0.5

(b)

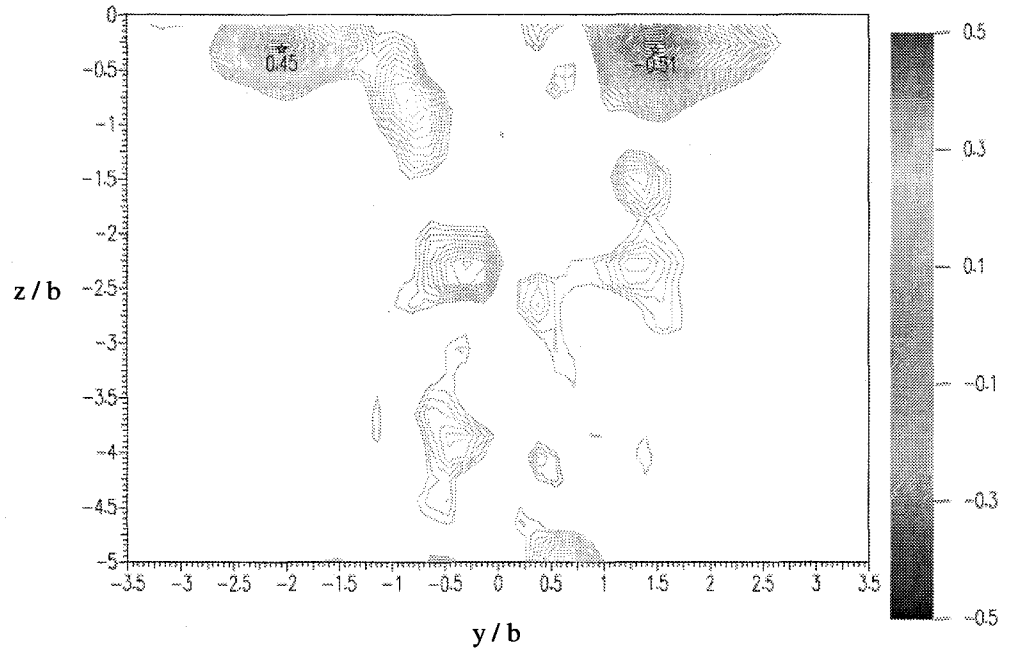

(c)

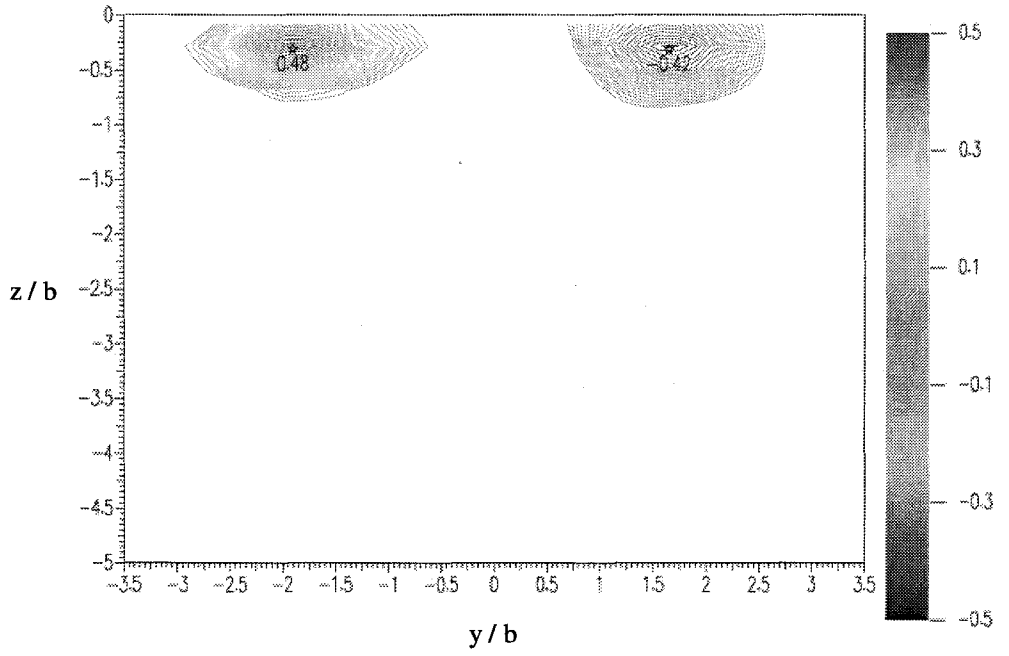

(d)

Fig. 4.2. Short-time and long-time averages of the vorticity field (e.g., at $x/\theta_o \approx 165$) for: (a) 4τ ($\approx$ 1 sec), (b) 8τ ($\approx$ 2 sec), (c) 20τ ($\approx$ 5 sec) and (d) 1200τ ($\approx$ 5 min)

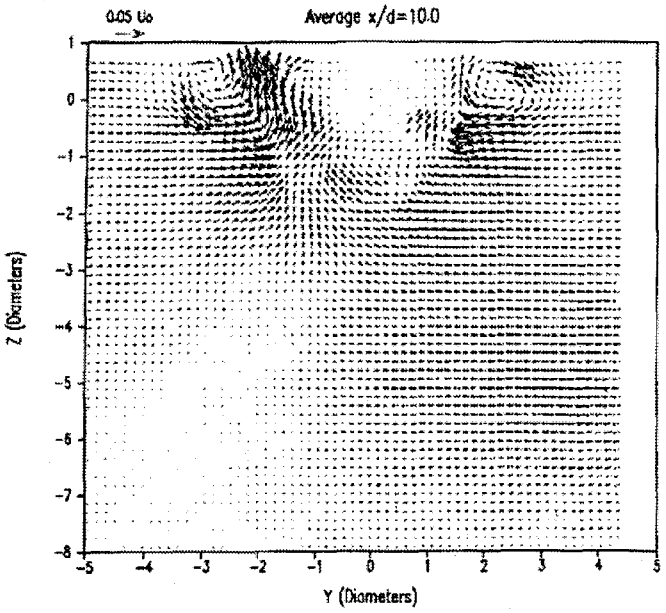

(a) Short-time average of the velocity field around a near-surface jet (Re=5,500) at $h/d = 1$ and $x/d = 10$. From Liepmann et al. (1994)

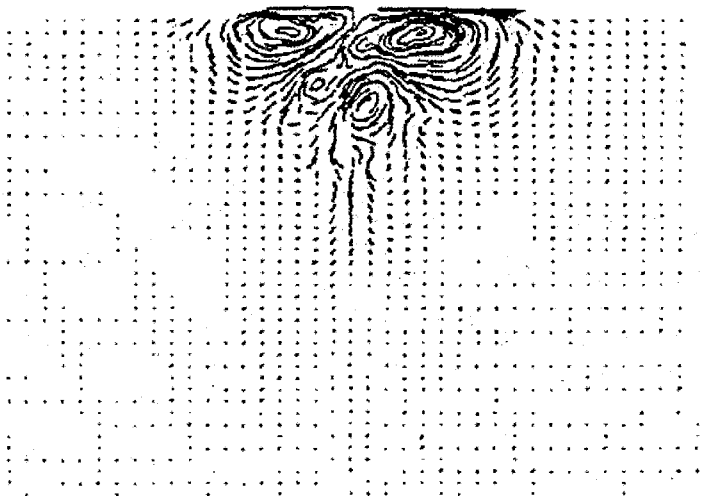

(b) Mean secondary flows established in the jet, visualized by particle trajectories. From Mangiavacchi et al. (1994)

Fig. 4.3. Experimental and numerical results of the mean velocity and vorticity fields of the free-surface turbulent jet

(c) Turbulence structure

The remaining question is to determine how this interaction between the turbulent vorticity field and the free surface manifests itself in the measurements of turbulence structure. This last issue is addressed by looking at the interaction of tangential vorticity with a free surface, similarly to Walker et al.[16] for free-surface jet flows. One of the main effects of the free surface is to cause a reduction in the $\overline{w'^2}$ Reynolds stress near the surface. We can examine this by writing the transport equation for the normal turbulent stress for which a good approximation is:

$$\frac{\partial}{\partial z}\overline{w'^2} = \frac{\partial}{\partial z}k - \left(\overline{u'\omega_y'} - \overline{v'\omega_x'}\right)$$

Based on this equation, we can see that the gradient in $\overline{w'^2}$ equals the gradient in the turbulence kinetic energy k, minus a contribution from the correlation of the orthogonal components of the fluctuating tangential velocities and vorticities, $\overline{u'\omega_y'}$ and $\overline{v'\omega_x'}$.

To interpret these velocity-vorticity correlations, we examine a vortical element as it approaches a free surface. For a flat horizontal free surface, the behavior will be as indicated in Fig. 4.1. For a vortex with purely x-direction vorticity (ω_x'), the vortex will develop a y-direction velocity as it approaches the free surface. For $\omega_y' > 0$, $u' > 0$ and for $\omega_y' < 0$, $u' < 0$ (see Fig. 4.1 (a)). As a result, near the free surface $\overline{u'\omega_y'}$ will be positive. Similarly for $\omega_x' > 0$, $v' < 0$ and vice versa (see Fig. 4.1 (b)) so $\overline{v'\omega_x'}$ will be negative. This behavior will cause the entire velocity-vorticity correlation term in the above equation to be positive near a flat horizontal free surface. The interaction, then, of the turbulent vorticity field with the free surface will cause a negative gradient in $\overline{w'^2}$.

The energy lost from the $\overline{w'^2}$ fluctuations due to the interaction of vorticity with the free surface must appear elsewhere. Using the definition of k, we can write the previous equation as

$$\frac{\partial}{\partial z}\left(\overline{u'^2} + \overline{v'^2}\right) = \frac{\partial}{\partial z}k + \left(\overline{u'\omega_y'} - \overline{v'\omega_x'}\right)$$

This shows that the energy that is lost from $\overline{w'^2}$ appears in the other two Reynolds normal stresses. Hence, the vorticity / free-surface interaction serves to redistribute the energy from the surface-normal to tangential velocity fluctuations.

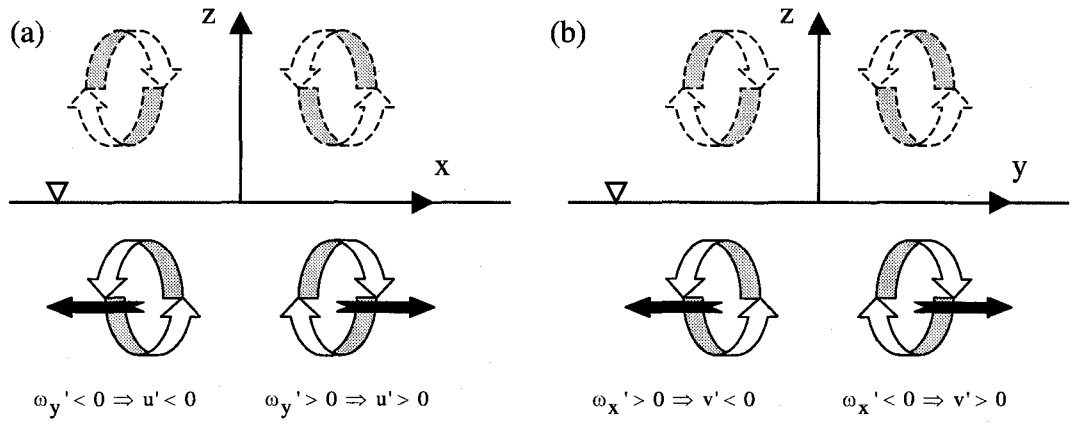

Fig. 4.1. Schematics of the interaction of tangential vorticity with the free surface:
(a) interaction of $\pm\omega_y'$ with the surface showing $\overline{u'\omega_y'} > 0$;
(b) interaction of $\pm\omega_x'$ with the surface showing $\overline{v'\omega_x'} < 0$.

The transport equation for the normal turbulent stress can also be written as:

$$\frac{\partial}{\partial z}(k - \overline{w'^2}) = \overline{u'\omega_y'} - \overline{v'\omega_x'}.$$

This equation shows that the velocity-vorticity correlations are equal to the normal gradient of $(k - \overline{w'^2})$. Fig. 4.2 shows transverse profiles of $(k - \overline{w'^2})$ obtained at four different depths $(z/\theta_o \approx -1, -2, -4 \text{ and } -100)$. The normal gradient can thus be estimated in the "surface layer" as $\Delta(k - \overline{w'^2})/\Delta z$ using these profiles. As a result, the normal gradient of $(k - \overline{w'^2})$ is found to be positive at the edges of the wake $(|y/b| \geq 1)$, leading to $\overline{u'\omega_y'} - \overline{v'\omega_x'} \geq 0$. This confirms the previous analysis at the edges of the wake, where the secondary flows are present. However, these velocity-vorticity correlations were also found to be negative in a smaller central portion of the wake $(|y/b| \leq 1)$. Nevertheless, these negative correlations are smaller in magnitude by a factor 3 to 4 than their positive counterparts and are confined to a smaller area of the flow. Similar results were obtained by Walker et al.[16] for turbulent free-surface jets, that is, $\overline{u'\omega_y'} - \overline{v'\omega_x'} \leq 0$ on the jet's axis, but were not addressed by the authors.

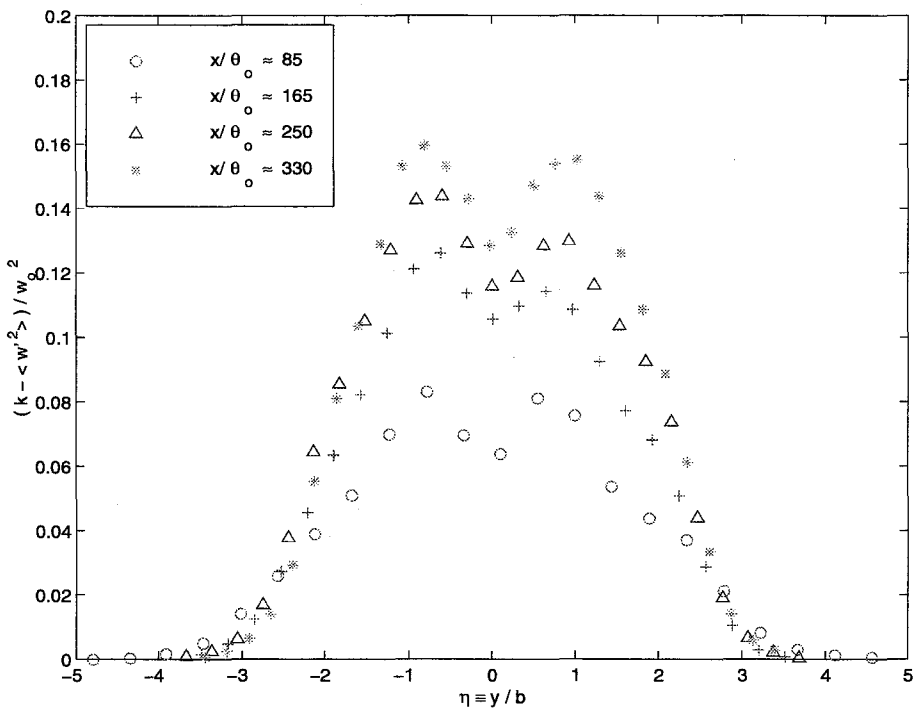
x/θo ≈ 85
x/θo ≈ 165
x/θo ≈ 250
x/θo ≈ 330
(k − <w'2>) / w0 2
η ≡ y / b

(a)

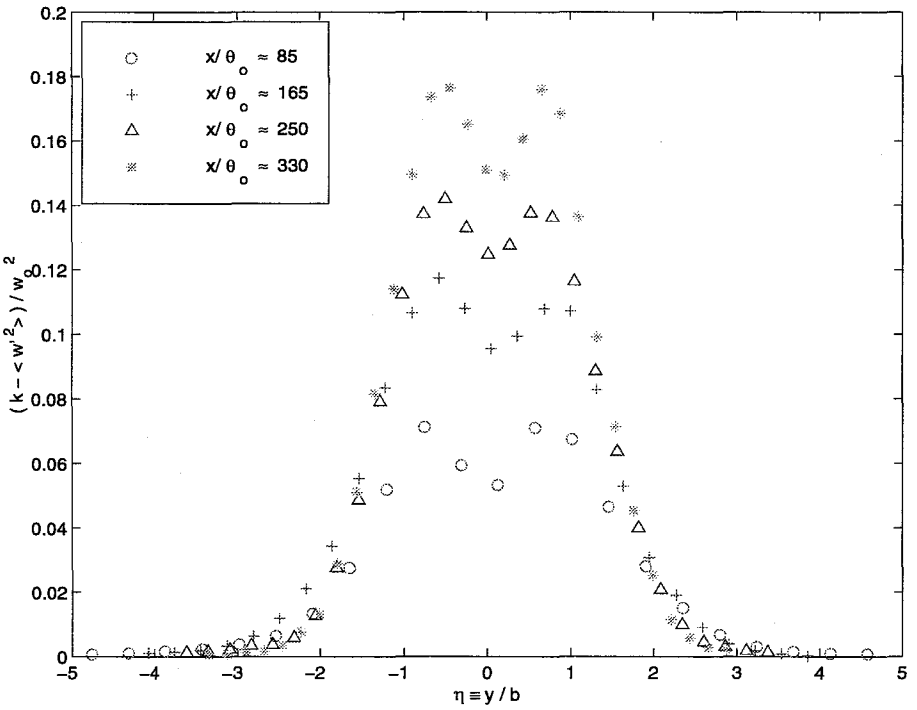
x/θo ≈ 85
x/θo ≈ 165
x/θo ≈ 250
x/θo ≈ 330
(k − <w'2>) / w0 2
η ≡ y / b

(b)

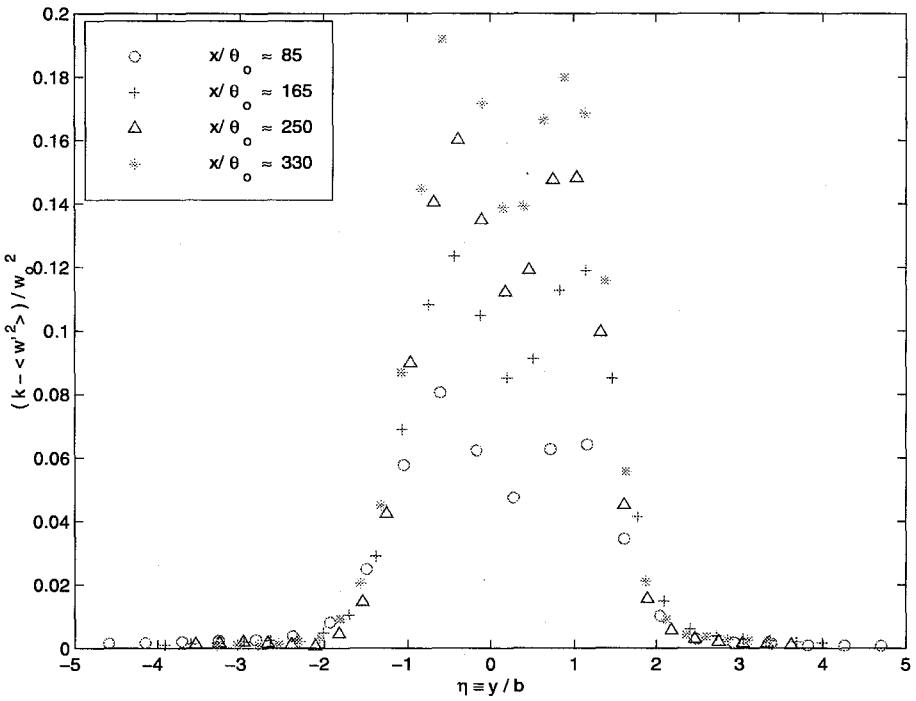

(c)

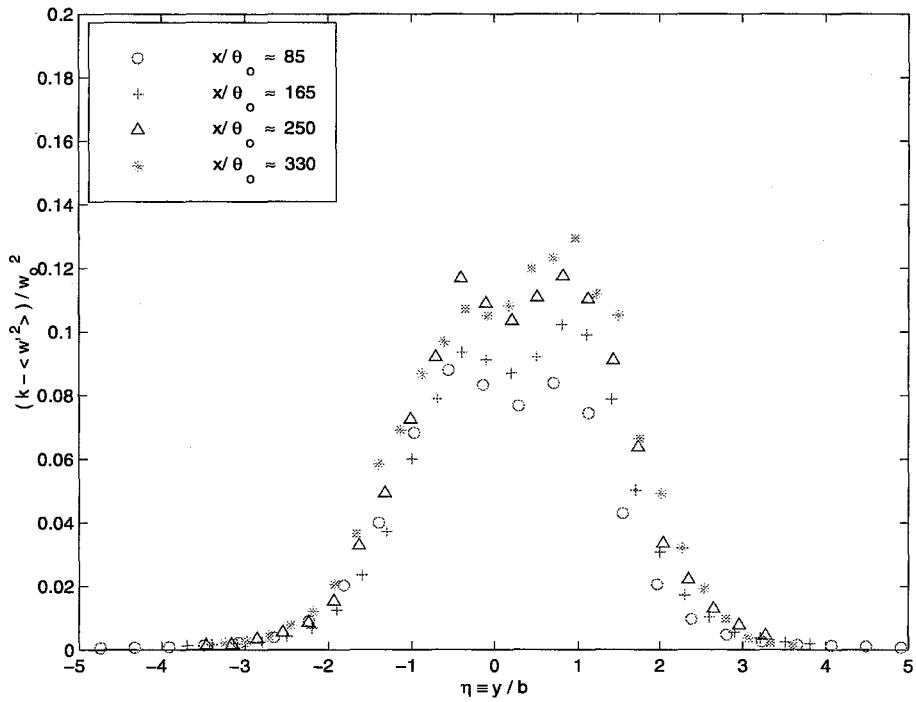

(d)

Fig. 4.2. Profiles of $\left(k - \overline{w'^2}\right)/w_o$ in the surface-parallel planes at:
(a) $z/\theta_o \approx -1$, (b) $z/\theta_o \approx -2$, (c) $z/\theta_o \approx -4$, (d) $z/\theta_o \approx -100$

4.3. Conclusions

The dynamics of low Froude number, free surface turbulence has been investigated by experiments of a turbulent wake behind a surface-piercing splitter plate.

The plate extended far enough below the surface to produce a wake that became nearly *two-dimensional* with depth, that is, away from the free surface, the turbulence quantities became homogeneous in the vertical direction. The measurements performed in the deep wake ($z/\theta_o \approx -100$) showed good agreement with the well-established theory for two-dimensional turbulent wake flows. However, the values obtained in this study were quite different from those found in the literature. In particular, the lateral spreading rate of the wake was increased by about 40%. It is believed that the nature of the inflow conditions, and in particular the state of the boundary layers, turbulent but not fully-developed, and the relatively low value of the Reynolds number are some of the important conditions resulting in such different, but self-consistent, wake parameters.

The free surface was found to affect the dynamics of turbulence within a *surface layer* on the order of one half-width of the submerged wake. Within this layer, the vertical velocity fluctuations were inhibited and the turbulence kinetic energy was redistributed to the horizontal components. The self-induced motion of surface-parallel vortical structures under the influence of their images was shown to lead to large-scale symmetric streamwise secondary flows and associated outward *surface currents*. This motion was the origin of the significantly higher (20%) lateral spreading rates of these surface shear flows compared to the spreading rates of their fully-submerged counterparts. In addition, the evolution of the streamwise and surface-normal enstrophy components within the *surface layer* was consistent with the normal connection of vortical structures required at a free surface.

The influence of the secondary flows was tracked back to the splitter plate's turbulent boundary layers where they were hence deduced to originate. A simple analysis of the mixed-boundary corner flows of the splitter plate made using the mean streamwise vorticity equation coupled with the evolution of the values of the transverse velocity confirmed the latter. In this picture of the mean flow, the secondary flows present in the near-surface edges of these shear flows were related to the pair of outer secondary *vortices* generated thereby. Furthermore, using a simplified equation for the surface-normal Reynolds stress, it was shown that the mutual interaction of the surface-parallel vortical structures with their images yielded a decrease in vertical velocity fluctuations as the free surface was approached. This

equation shed further light on the redistribution of the vertical kinetic energy of turbulence into the other two Reynolds normal stresses. The resulting free-surface Reynolds-stress anisotropy in turn gave birth to the two streamwise secondary flows.

"Knowledge comes from noticing resemblances and recurrences in the events that happen around us."
Wilfred Trotter

TURBULENT SHEAR LAYERS

CHAPTER V

5. Turbulent shear layers

5.1. Fully-submerged shear layers

5.1.1. Two-dimensional, turbulent shear layers

Like the *two-dimensional*, turbulent wake flows studied previously, plane, turbulent free-shear-layer flows provide a useful arena in which generic phenomena can be addressed. This interest is due, in large part, to their inherent geometric simplicity. At the confluence of two flows of different mean velocities, the velocity difference gives rise to instabilities in the fluid motion resulting in the development of a mixing (or shear) layer. On a practical note, as a relatively efficient mixer of initially separated streams, this flow plays a critical role in the performance of many industrial devices, ranging from chemical lasers to envisaged hypersonic-propulsion engines. In the natural environment mixing layers can be found at the confluence of rivers, harbor entrances, sudden expansion of flow geometries... Indeed, since a mixing layer is the interface between two initially separated flows, any exchange of material and momentum between the two flows will be mediated by its specific properties. A vast amount of literature exists concerning numerous details of turbulent structures in plane mixing layers (Ho & Huerre[1] 1984; Wygnanski and Petersen[2] 1987). Although the term plane suggests two-dimensionality, many features of the turbulent motions in such a mixing layer are essentially three-dimensional.

The discussion here will be limited to incompressible, subsonic, plane, turbulent shear layers, formed between two uniform free streams of unequal velocity, of equal density, at sufficiently high Reynolds numbers (see Fig. 5.1). The local Reynolds number is given by

$$\mathrm{Re}_\delta \equiv \frac{\delta\,\Delta U}{\nu}$$

where δ is some measure of the (local) transverse extent of the turbulent shear flow region, $\Delta U = U_1 - U_2$ is the velocity difference across the shear layer, and ν is the flow kinematic viscosity.

[1] Ho, C.M. & Huerre, P. 1984 Perturbed free shear layers. Ann. Rev. Fluid Mech. **16**, 365-424.
[2] Wygnanski, I.J. & Petersen, R.A. 1987 Coherent motion in excited free shear flows. AIAA **25**, 201-213.

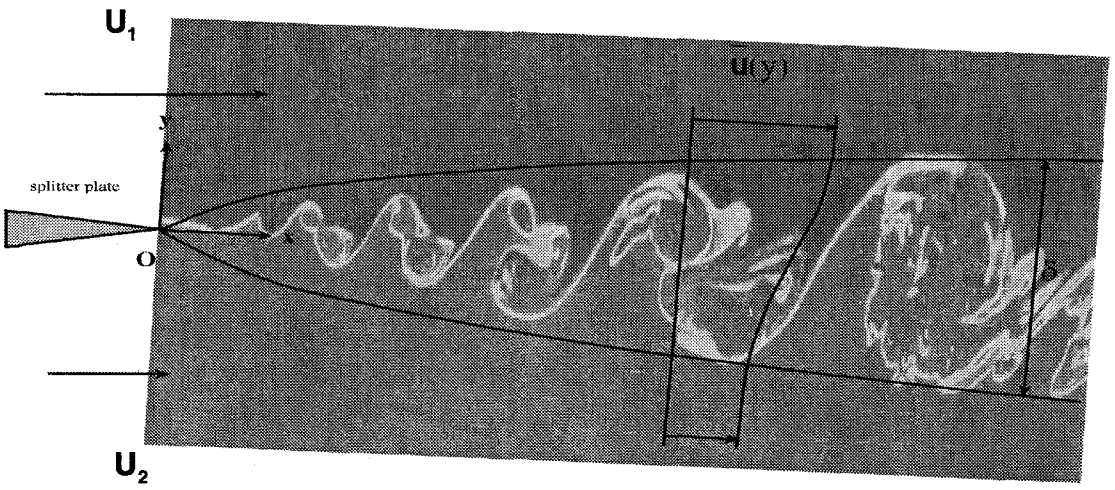

Fig. 5.1. Schematic of a subsonic turbulent shear-layer flow. The subscript $()_1$ refers to the properties of the high-speed freestream flow, and the subscript $()_2$ refers to those of the low-speed freestream flow.

There are several ways of defining the local transverse extent δ of the sheared region. The *visible* shear layer width δ_{vis} is the distance between the shear layer edges, as would be measured in a shadowgraph picture of the layer. It is very close to the 1% width, δ_1, defined as the distance between the two points across the layer where the mean velocity has dropped or increased by 1% of its freestream value. Here we will mainly use the vorticity (or maximum slope) thickness δ_ω, which is defined in terms of the mean streamwise velocity profile $\bar{u}(y)$ as

$$\delta_\omega \equiv \frac{\Delta U}{\left[\dfrac{d\bar{u}(y)}{dy}\right]_{max}} = \frac{\int_{-\infty}^{\infty} |\overline{\omega_z}|\, dy}{|\overline{\omega_z}|_{max}}$$

where $\overline{\omega_z} = -\partial\bar{u}/\partial y$. In addition to being convenient, the vorticity thickness is appropriate, the problem of the growth of the turbulent mixing layer being basically the kinematic problem of the unstable motion induced by the vorticity.

Abramovich[3] and Sabin[4] proposed an expression for the shear-layer growth rate given by

$$\frac{\delta}{x} \approx C_\delta \frac{1-r}{1+r}$$

where δ is some measure of the local scale of the flow, $r \equiv \frac{U_2}{U_1}$ is the freestream velocity ratio and C_δ is taken as a constant. This is an expression that can be argued for on similarity grounds for a temporally growing shear layer. Indeed, in a frame moving with the convection velocity U_C, we must have $\delta/t \propto \Delta U$, where $\Delta U = U_1 - U_2$. The growth rate equation above then follows if $U_C = (U_1 + U_2)/2$, which is found to be the case for $\rho_1 = \rho_2$, if we transform back to the laboratory coordinates, i.e., $x = t/U_C$ and normalize all velocities with U_1. This equation is found to be in reasonable agreement with experimental data of incompressible shear layers with equal freestream densities, as shown in the seminal experiments by Brown and Roshko[5] (1974).

For a fully-submerged shear layer with no external disturbances, there is substantial variance in inferred values of C_δ, especially between experiments performed in different facilities, i.e.,

$$0.25 \leq C_\delta \leq 0.45^{6}$$

for the total thickness δ, or roughly half that for the maximum slope thickness δ_ω. It is not clear why such a large spread of values of the coefficient C_δ do exist. However, it is speculated that inflow conditions may significantly affect the far-field properties of turbulence, including growth rate, as pointed out in a recent mixing-layer study[7].

[3] Abramovich, G.N. 1963 The theory of turbulent jets. MIT Press, Cambridge, MA.

[4] Sabin, C.M. 1965 An analytical and experimental investigation of the plane, incompressible, turbulent free-shear layer with arbitrary velocity ratio and pressure gradient. Trans. ASME D **87**, 421-428.

[5] Brown, G.L. & Roshko, A. 1974 On density effects and large structures in turbulent mixing layers. J. Fluid Mech. **64**, 775-816.

[6] Dimotakis, P.E. 1991 Turbulent free shear layer mixing and combustion. Progress in Aeronautics and Aeronautics. Vol **137**, Ed. S.N.B. Murphy and E.T. Curran.

[7] Slessor, M.D. 1998 Aspects of turbulent-shear-layer dynamics and mixing. Ph.D. thesis, California Institute of Technology, Pasadena.

It was indeed proposed by Bradshaw[8] (1966) that the shear layer is sensitive to its initial conditions. Bradshaw suggested that a minimum of several hundred of the initial momentum thickness is required for the shear layer to assume its asymptotic behavior. Dimotakis and Brown[9] (1986) argued that this estimate may not be conservative enough in light of the dynamics and interactions of the large-scale flow structures. Nevertheless, sufficient experimental data exist to suggest that a turbulent shear layer will exhibit linear growth, even within the Bradshaw specification, but that the growth rate may not be a unique function of the freestream velocity ratio r.

An important conclusion drawn by Konrad[10] was that a mixing layer entrains fluid from each of the two streams in an asymmetric way, even for equal freestream densities. As a result, the shear layer spreads preferentially into the low velocity stream. The mixing layer centerline defined by $\overline{u} = U_C \equiv (U_1 + U_2)/2$ or $(\overline{\omega_z}) = (\overline{\omega_z})_{max}$ (i.e., location of the velocity profile's inflection point) hence deflects toward the low-speed side.

5.1.2. Fully-submerged shear-layer measurements

Digital PIV measurements were made in the deep shear layer ($z/\theta_o \approx -60$) of the surface-piercing splitter plate to determine its mean flow field, turbulent intensities, and Reynolds stresses. The two inlet sections were separated by a splitter plate of 3m in length, that allowed the transition of the boundary layers of both the high-speed (U_1 = 39 cm/sec) and the low-speed (U_2 = 25 cm/sec) sides to turbulence. Evidence for the state of the boundary layers at separation was obtained by dye visualization. Similarly to the wake-flow study, the boundary layers were not tripped either to avoid triggering any undesired free-surface effects. Measurements carried out in the fully-submerged shear layer showed that the Reynolds number computed in the middle of the test section ($\delta \approx$ 80mm), i.e., $Re_\delta \equiv \frac{\Delta U \delta}{\nu}$, was 11200. The initial integral thickness θ_i used to normalize the downstream distance was measured at the origin x = 0 and was found to be $\theta_i \approx$ 4.8mm. In this investigation, surface wave amplitudes were small and the water surface remained free of surfactant, and

[8] Bradshaw, P. 1966 The effect of initial conditions on the development of a shear layer. J. Fluid Mech. **26**, 225-236.

[9] Brown, G.L. & Dimotakis, P.E., 1976 The mixing layer at high Reynolds number: Large- structure dynamics and entrainment. J. Fluid Mech. **78**, 535-560.

[10] Konrad, J.H. 1976 An experimental investigation of mixing in two-dimensional turbulent shear flows with applications to diffusion-limited chemical reactions. Ph.D. thesis, California Institute of Technology, Pasadena.

consequently neither of those effects was expected to be significant. The water depth yielded a mean aspect ratio (width to depth) of about 10. As a result of the velocity difference, a mixing layer starts to develop downstream of the splitter plate. The mixing layer and its growth can be further characterized by a single parameter $\lambda \equiv \frac{1-r}{1+r} = \frac{U_1 - U_2}{U_1 + U_2}$, which has a value of 0.22 in the present case ($r \approx 0.64$), and does not vary in the region of observation up to 2m downstream of the splitter plate.

The parameters of the mixing layer were carefully chosen such that it can develop over a large distance without any side wall interference.

(a) behavior of the mean flow in the shear layer

At various positions downstream of the splitter plate, streamwise velocity profiles were obtained to determine the width of the mixing layer and the position of its centerline. The mixing layer centerline defined by $\bar{u} = U_C \equiv (U_1 + U_2)/2$ or $(\overline{\omega_z}) = (\overline{\omega_z})_{max}$ is seen to deflect toward the low-speed side as anticipated (cf Fig. 5.1). The mixing layer therefore spreads preferentially into the low velocity stream. The experimental results are presented in a coordinate system following the mixing layer growth (corresponding to the centerline deflection).

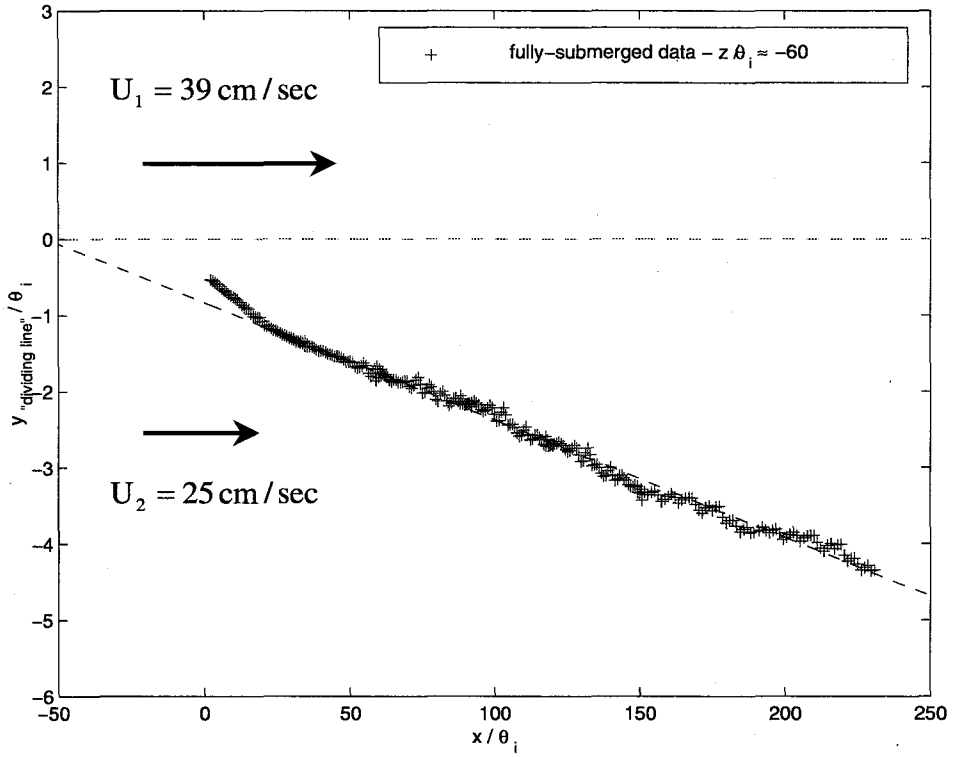

Fig. 5.1. Location of the "dividing line" for the fully-submerged shear layer

Fig. 5.2 shows, in the normalized variables $\left(\overline{u} - U_C\right)/(\Delta U/2)$ and $\eta \equiv y/\delta_\omega$, representative streamwise velocity profiles obtained for several downstream stations. In order to compare the characteristic profiles and to assess the self-similarity of the mixing layer, the lateral distances are scaled using the mixing layer vorticity thickness δ_ω. The profile at $x/\theta_i \approx 25$ from the splitter plate clearly shows the presence of a wake due to the boundary layers that have developed at the splitter plate. The effects can still be noticed at $x/\theta_i \approx 75$ but have completely disappeared by $x/\theta_i \approx 125$. The presence of this wake disturbance might affect the initial development of the mixing layer (Mehta[11] 1991; Oster and Wygnanski[12] 1982). Apart from the wake effects, the measured data show good similarity. Indeed, the remaining profiles ($x/\theta_i \geq 125$) collapse quite neatly onto a single curve, which can be described by the traditional Görtler's error function.

[11] Mehta, R.D. 1991 Effect of velocity ratio on plane mixing layer development; Influence of the splitter plate wake. Exp. Fluids **10**, 194-204.

[12] Oster, D. & Wygnanski, I.J. 1982 The forced mixing layer between parallel streams. J. Fluid Mech. **123**, 91-130.

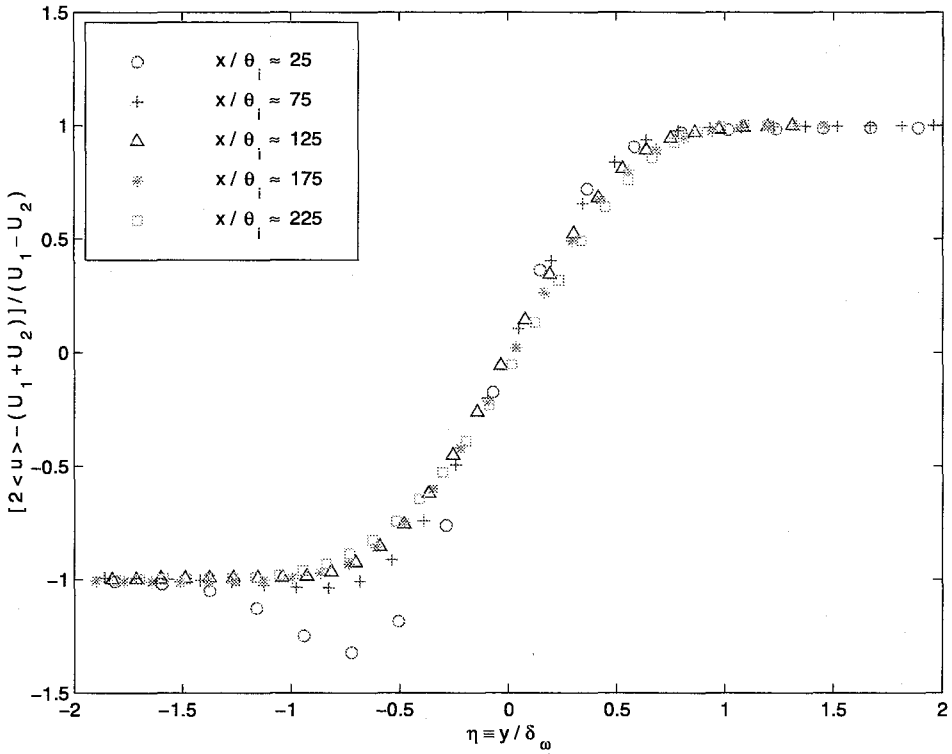

Fig. 5.2. Mean streamwise velocity profiles for the fully-submerged shear layer

The mean normal vorticity distribution, when plotted with a normalized lateral coordinate (see Fig. 5.3 below), also approaches an equilibrium state. For both velocity and vorticity distributions, independence seems to be established beyond 125 initial momentum thicknesses.

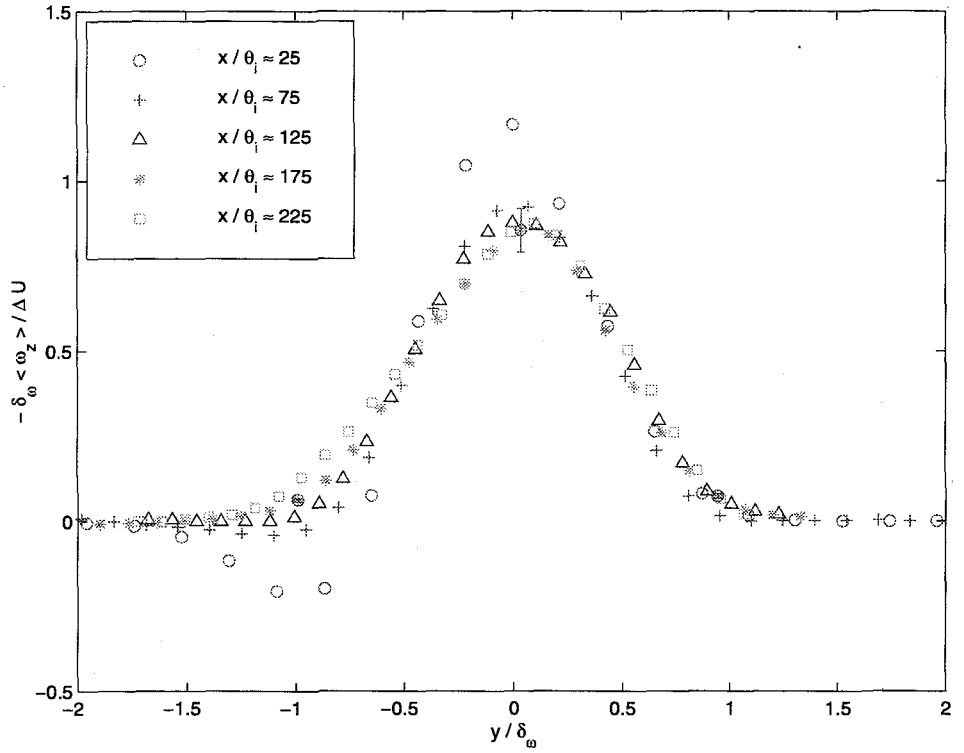

Fig. 5.3. Mean normal vorticity profiles for the fully-submerged shear layer

From the same data the growth rate of the mixing layer can be determined using the definition of the vorticity thickness δ_ω (see section 5.1.1.). It is useful to consider the development of two-dimensional turbulent mixing layers in terms of the non-dimensional parameter

$$\Delta \equiv \frac{\delta_\omega}{x}$$

à la Narasimha and Prabhu (see section 4.1.1.). Indeed, it is expected that "sufficiently" far from the splitter plate (large x/θ_i) the above parameter will tend asymptotically to a certain constant value, say Δ^*. Fig. 5.4 presents the evolution of the non-dimensional growth-rate parameter Δ, as defined above, with the normalized downstream distance.

One of the important issues that arise in the discussion of mixing-layer development is concerned with the downstream distance from the trailing edge beyond which the mixing layer can be regarded as having reached an asymptotic state. By the asymptotic self-preserving state, we also mean here that the mean velocity and the Reynolds-stress distributions are independent of the streamwise

position when normalized by the same velocity and length scales. The importance of this issue, whether it is for the wake or the shear layer, is reinforced by the fact that the present values are quite different from those obtained in earlier studies. The value attained by the growth-rate parameter in the last measurement region does not vary by more than 5% of its mean value in this region, which is found to be $\Delta \approx 0.058$. The curve still slightly decreases but the value attained by Δ is close to its asymptotic value Δ^*. Taking Δ^* to be 0.058, this leads to a constant C_{δ_ω} of value

$$0.058 = \Delta^* \equiv \left(\frac{\delta_\omega}{x}\right)^* \approx C_{\delta_\omega} \frac{1-r}{1+r} = 0.22\, C_{\delta_\omega} \quad \Rightarrow \quad C_{\delta_\omega} \approx 0.265$$

which is considerably higher (about 18%) than the upper limit of the interval values $0.125 \leq C_{\delta_\omega} \leq 0.225$[6] obtained in previous investigations.

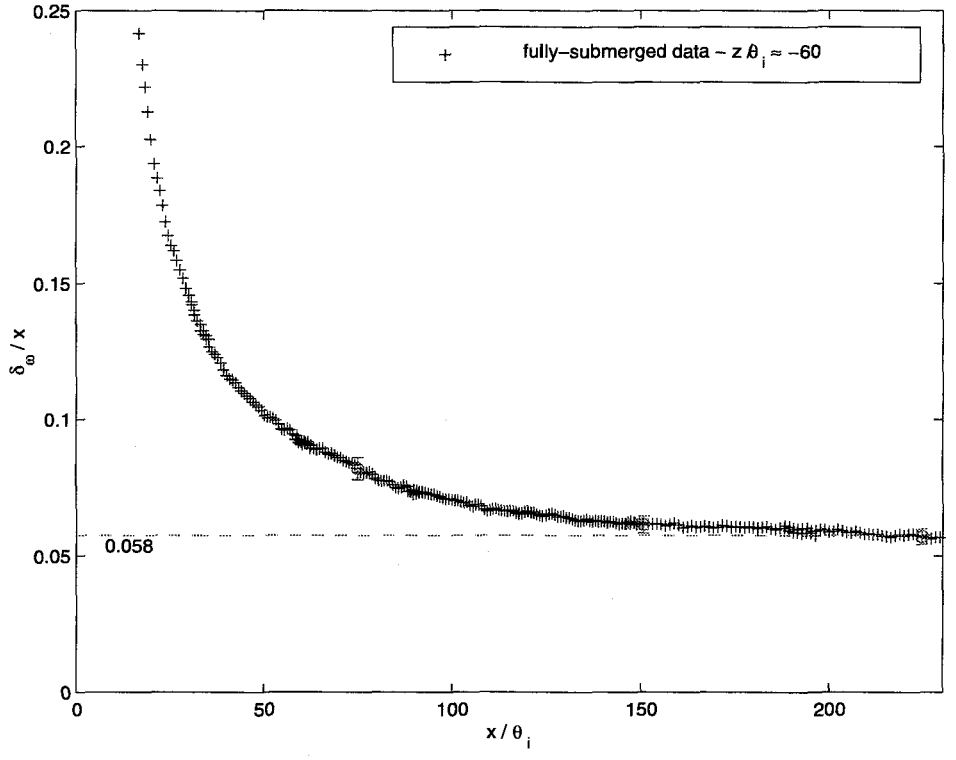

Fig. 5.4. Evolution of the growth rate parameter with the normalized downstream distance

Thus, the vorticity thickness growth rate for the fully-submerged mixing layer is:

$$\frac{\delta_\omega}{x} \approx 0.265 \frac{1-r}{1+r} = 0.265\,\lambda$$

which is higher than the value, between 0.162λ and 0.181λ, suggested by Brown and Roshko[5].

If δ_ω is divided by $x-x_o$ instead of x, as suggested by Dr. Leonard, then C_{δ_ω} reaches a lower value of 0.221. This value is still higher than the range of values suggested by Brown and Roshko[5] but is in the range of values compiled by Dimotakis[6].

One possible reason for this higher value might be the fact that Δ has not reached its asymptotic value Δ^* just yet and is indeed still decreasing. However, in light of its evolution, it is unlikely that its value would change by as much as 30% further downstream. The boundary layers at the splitter plate are more likely to affect the difference in growth rate found. In their seminal work, Browand and Latigo[13] (1979) showed that the growth rate of a mixing layer with tripped boundary layers (0.150λ) was significantly smaller than with untripped boundary layers (0.170λ). This result has been confirmed in more recent works, notably by Bell and Mehta[14] (1990) and Slessor[7] (1998). Chu and Babarutsi[15], who found a doubling of the initial mixing layer growth with respect to the plane mixing layer data, used a setup for which the boundary layers at the splitter plate were not expected to be fully-developed at the position where the mixing layer starts to develop.

(b) turbulence structure in the shear layer

The measured distributions of the normalized root-mean-square of the streamwise and transverse velocity fluctuations are plotted at several downstream stations in Fig. 5.1 and Fig. 5.2 respectively. The degree to which the mixing layer approaches a self-preserving state can be determined from Fig. 5.3, which shows the downstream variation of $\sqrt{\overline{v'^2}_{max}}/\Delta U$. For a self-preserving state, this statistic should be a constant, independent of x. The present results show that this does not appear to be the case at the end of the last measurement region ($x/\theta_i \geq 230$). On the basis of the

[13] Browand, F.K. & Latigo, B.O. 1979 Growth of the two-dimensional mixing layer from a turbulent and nonturbulent boundary layer. Phys. Fluids **22(6)**, 1011-1019.

[14] Bell, J.H. & Mehta, R.D. 1990 Development of a two-stream mixing layer from tripped and untripped boundary layers. AIAA **28**, 2034-2042.

[15] Chu, V.H. & Babarutsi, S. 1988 Confinement and bed-friction effects in shallow turbulent mixing layers. J. Hydraulic Eng. **114**, 775-816.

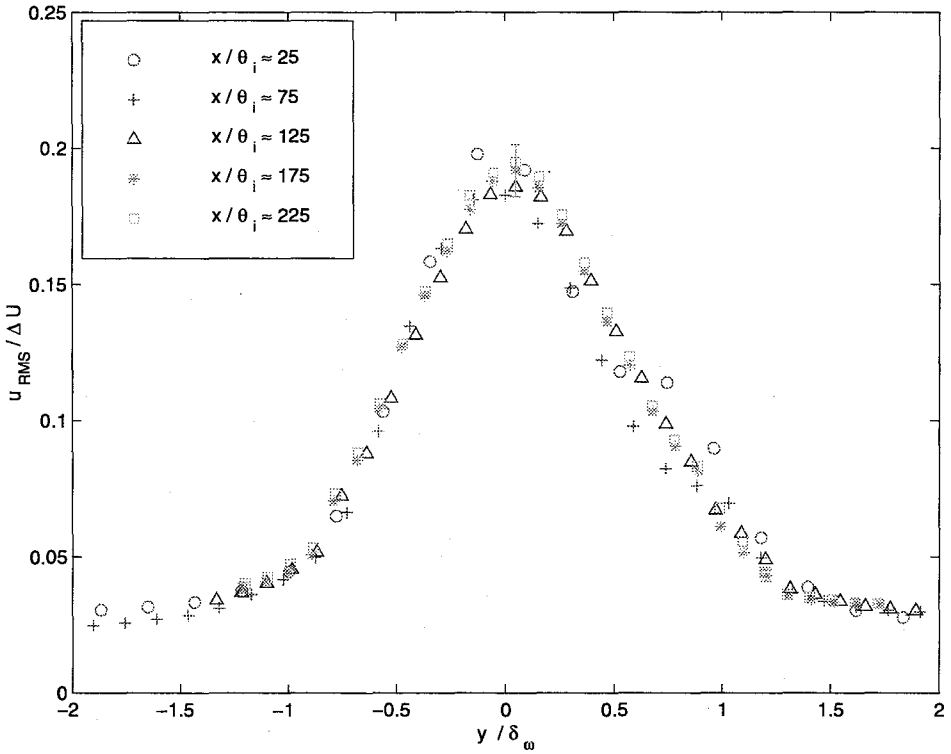

Fig. 5.1. Distribution of the streamwise velocity fluctuations at several downstream stations

results presented here, it is believed that the distributions of the second-order turbulence quantities have not achieved an equilibrium state yet. This does, however, not seem surprising in light of previous experimental results which estimate that a minimum of several hundred of the initial momentum thickness is required for a shear layer to assume its asymptotic behavior (e.g., about 800 θ_i for Browand and Latigo[13]). It is interesting to note that the maximum normalized transverse velocity fluctuation first sharply decreases (until $x/\theta_i \approx 50$) before it starts increasing toward its far-field value. The maximum normalized streamwise velocity fluctuation follows the exact same trend. It is speculated that this sharp decrease can be associated with the presence of the wake of the splitter plate, with which it correlates quite well. Furthermore, in previous mixing-layer experiments[13], these values were found to increase with the downstream distance for nonturbulent boundary layers whereas they were found to decrease for turbulent boundary layers. As for the wake-flow study, it is speculated that the state of the boundary layers, that is turbulent but not fully-developed, could be an important factor in the evolution of the shear layer since this was a major difference between this and the other studies.

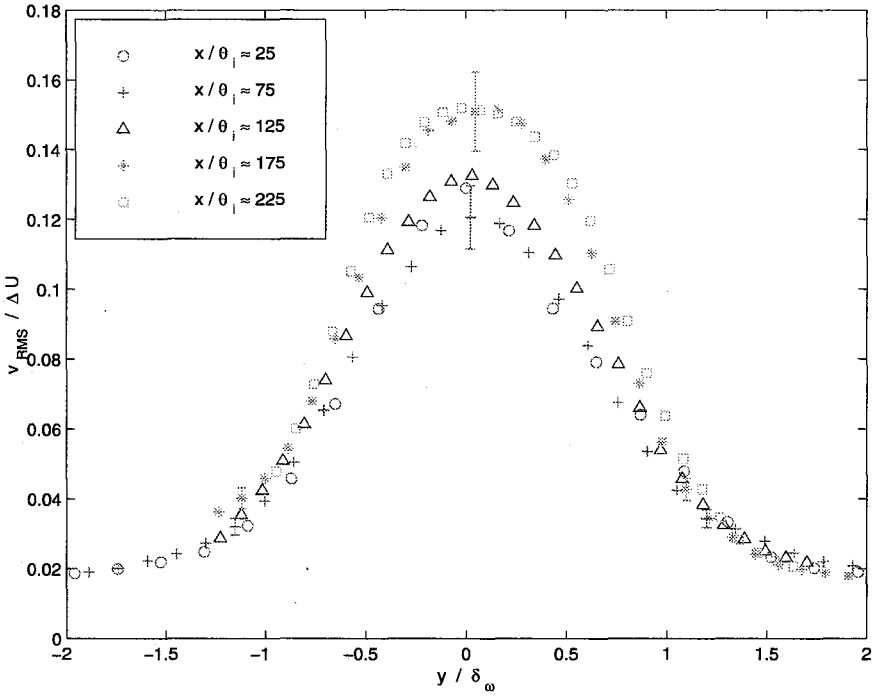

Fig. 5.2. Distribution of the transverse velocity fluctuations at several downstream stations

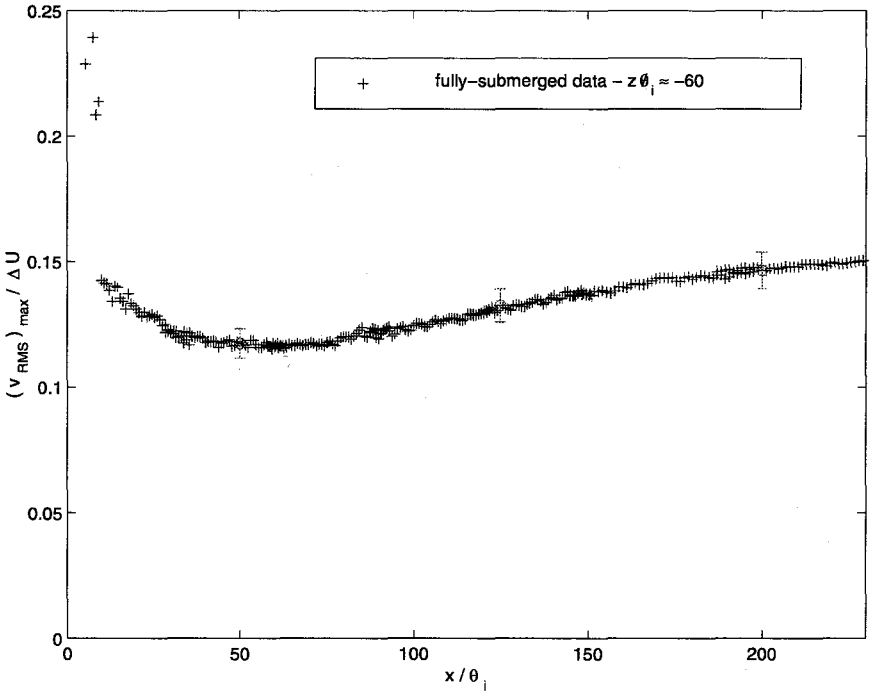

Fig. 5.3. The downstream variation of $\sqrt{\overline{v'^2_{max}}}/\Delta U$ for the fully-submerged shear layer

Similar results were obtained for the distributions of the normalized Reynolds stresses, as shown in Fig. 5.4. The maximum normalized Reynolds stress first sharply decreases (until $x/\theta_i \approx 50$) before it starts increasing toward its far-field value. The asymmetric double-peak profile at $x/\theta_i \approx 25$ from the splitter plate clearly shows the presence of a wake due to the boundary layers that have developed at the splitter plate. These "wake" effects have disappeared by $x/\theta_i \approx 125$. After that point, the profiles spread in width and increase in values. However, the Reynolds stress profile does not appear either to attain its asymptotic profile at the end of the last measurement region just yet. This is not surprising in light of previous experimental results discussed above.

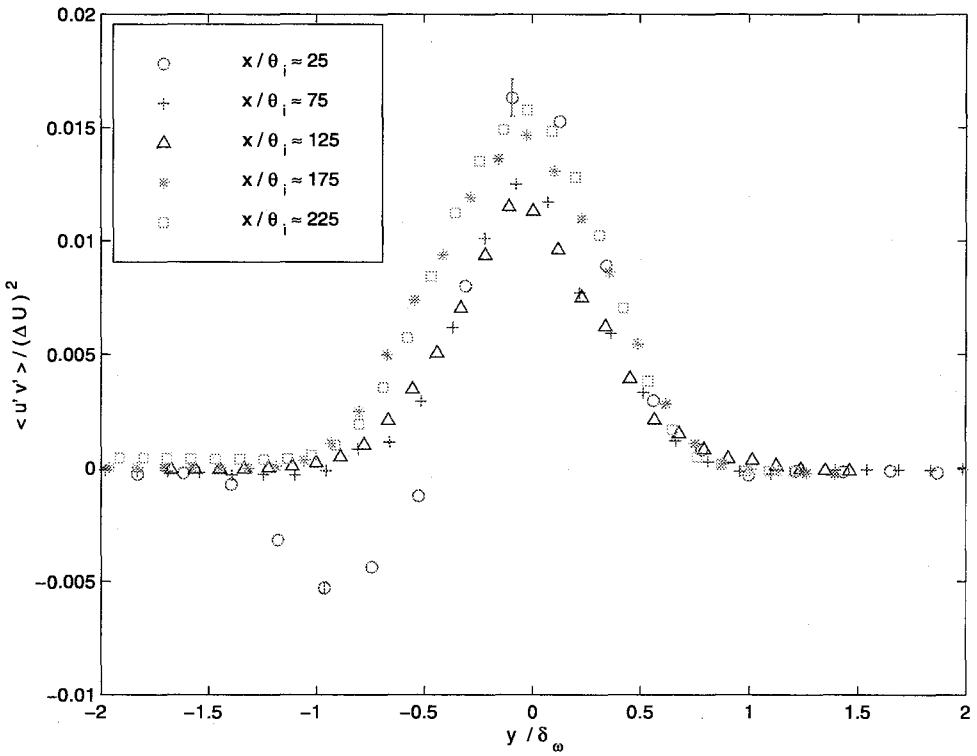

Fig. 5.4. The measured distribution of the turbulent Reynolds stress at several downstream stations

It is interesting to point out that, except for the vorticity thickness growth rate, the present values are in very good agreement with those obtained by Browand and Latigo[13].

5.2. Free-surface turbulent shear layers

5.2.1. Flow-normal plane measurements

Data were acquired in y-z flow-normal planes at different downstream stations ($x/\theta_i \approx 105, 155$ and 210) in order to probe the spatial extent of the free-surface influence on the underlying turbulent mixing layer and guide the positioning of our x-y surface-parallel plane in the near-surface region.

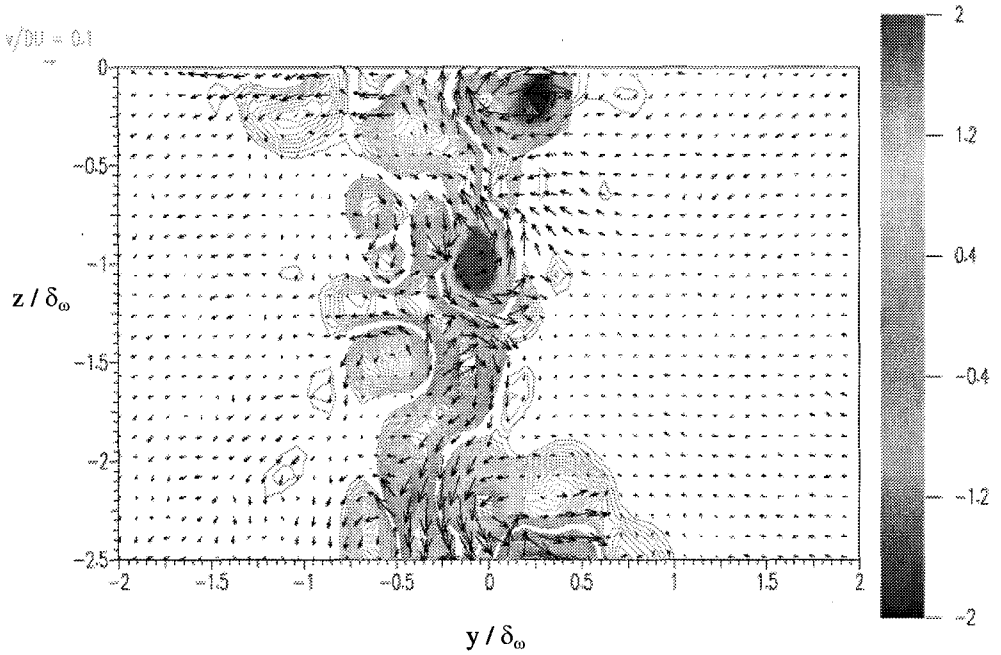

Fig. 5.1. Instantaneous velocity & vorticity fields in the flow-normal plane at $x/\theta_i \approx 155$

Fig. 5.1 shows a representative instantaneous vorticity field on which its associated velocity field is superimposed obtained in such a flow-normal plane at $x/\theta_i \approx 155$. The flow is evolving out of the page; y and z, respectively the width and depth with z = 0 being the mean free-surface level, are normalized by the vorticity thickness δ_ω. Contour plots of the normalized streamwise vorticity $(\omega_x/(\Delta U/\delta_\omega))$ indicate that the shear layer is composed of numerous streamwise vortical structures believed to originate from the plate's turbulent boundary layers. It also appears from this instantaneous flow picture that the shear layer widens at the free surface. These instantaneous measurements presented here are representative of the shear-layer flow, but they do not necessarily encompass all possible flow features observed in the shear

layer. To get a more quantitative information on this turbulent shear flow, thousands of such images were acquired to obtain well-converged Reynolds-averaged quantities at each measurement plane ($x/\theta_i \approx 105, 155$ and 210).

(a) behavior of the mean flow in the shear layer

Long-time averages (of six minutes, that is, about 5,000 image pairs) clearly reveal the presence of two counter-rotating streamwise secondary flows in the near-surface region throughout the shear layer as shown in Fig. 5.1. The following contours and vector fields were not corrected for the small deflection of the mixing layer toward the low-speed side. Indeed, the reader will notice that the "dividing line" (located approximately where the transverse velocity changes sign) is not found to be at y=0 in these plots. This is simply due to the fact that this correction is not systematic as the position of the mixing-layer centerline is affected by the free-surface dynamics, as shall be seen shortly (cf section 5.2.2. (a)). However, this should not affect the results too much, as the deflection is rather small. In contrast, the profiles were plotted in their respective mixing-layer coordinate systems.

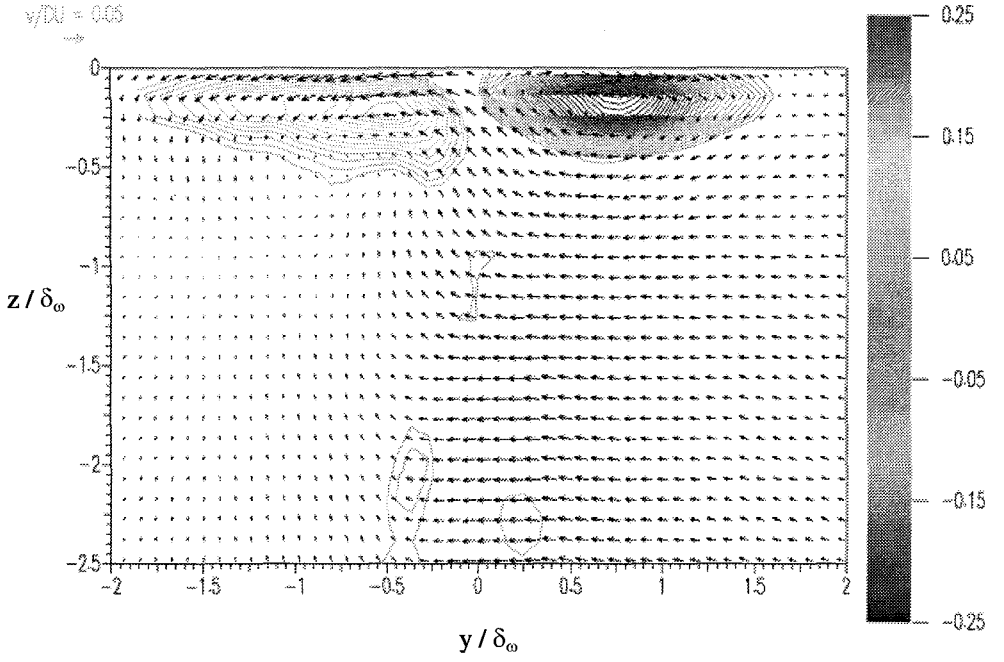

(a)

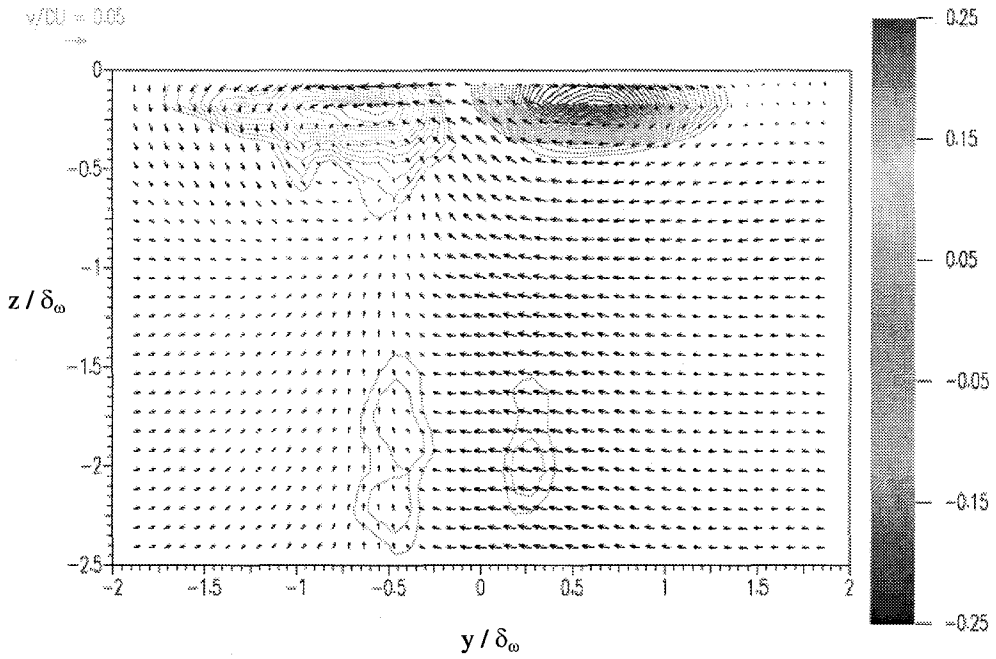

(b)

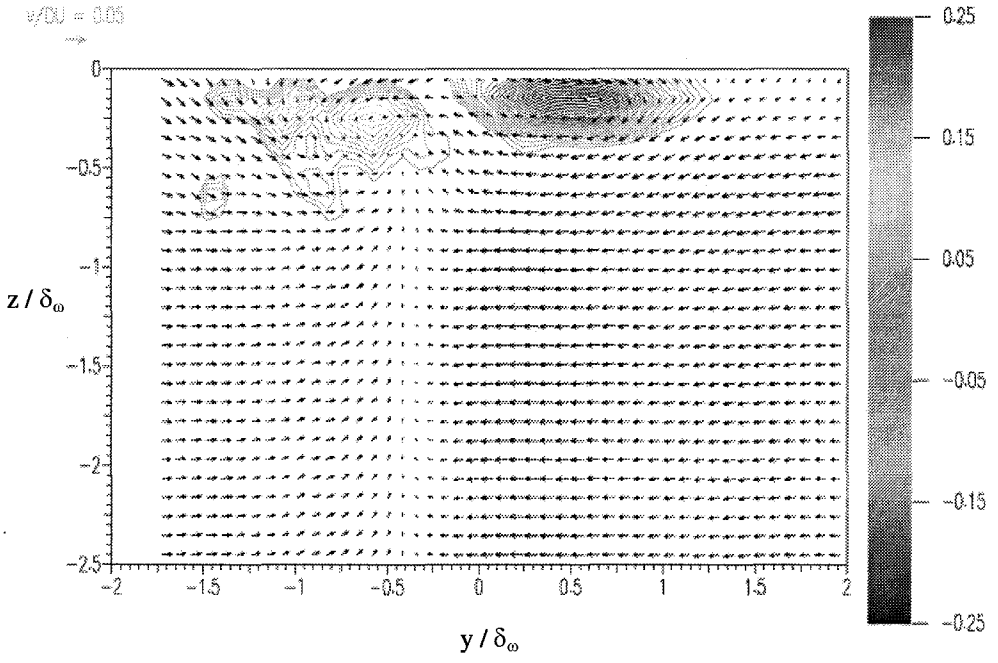

(c)

Fig. 5.1. Normalized Reynolds-averaged velocity & vorticity fields obtained in the flow-normal planes: (a) $x/\theta_i \approx 105$, (b) $x/\theta_i \approx 155$, (c) $x/\theta_i \approx 210$

Fig. 5.2 shows the distributions of the mean streamwise vorticity along a transverse cut running through the core centers ($z/\theta_i \approx -0.25$) and Fig. 5.3 depicts them along normal cuts running through each core center from the free surface to the fluid bulk ($y/\delta_\omega \approx -0.5$ and $y/\delta_\omega \approx 0.66$). The first figure indicates that the mean streamwise vorticity profiles appear to reach self-similarity for $x/\theta_i \geq 105$ with $\left(\overline{\omega_x}\right)_{max}/(\Delta U/\delta_\omega) \approx 0.18$ at $(y/\delta_\omega, z/\delta_\omega) \approx (-0.5, -0.25)$ and $\left(\overline{\omega_x}\right)_{min}/(\Delta U/\delta_\omega) \approx -0.3$ at $(y/\delta_\omega, z/\delta_\omega) \approx (0.66, -0.25)$. These values are much smaller than that obtained for $\left(\overline{\omega_z}\right)_{min}/(\Delta U/\delta_\omega)$ (≈ -0.75) (see Fig. 5.3). The next figure quantifies the mean extent of the near-surface secondary flows, that is about $0.5\delta_\omega$ or roughly $6\theta_i$ in the mean (at the middle of the test section). The latter result is primordial to position the x-y surface-parallel measurement plane in the near-surface region and thus investigate the free-surface shear layer. The instantaneous vortical structures present in the deep mixing layer canceled out during the averaging process as hinted by their "broken up" appearance as well as expected if one is to obtain a fully-submerged turbulent shear flow two-dimensional in the mean. The issue of the origin of these secondary flows has been tackled extensively in section 4.2.3.

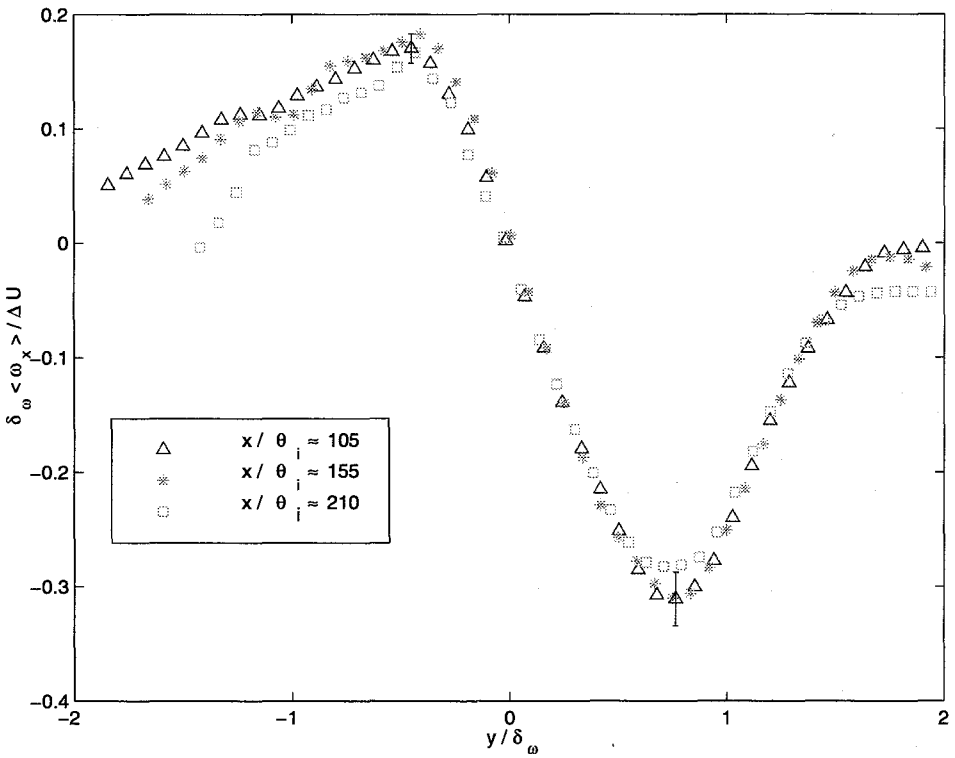

Fig. 5.2. Distribution of the mean streamwise vorticity along $z/\delta_\omega \approx -0.25$

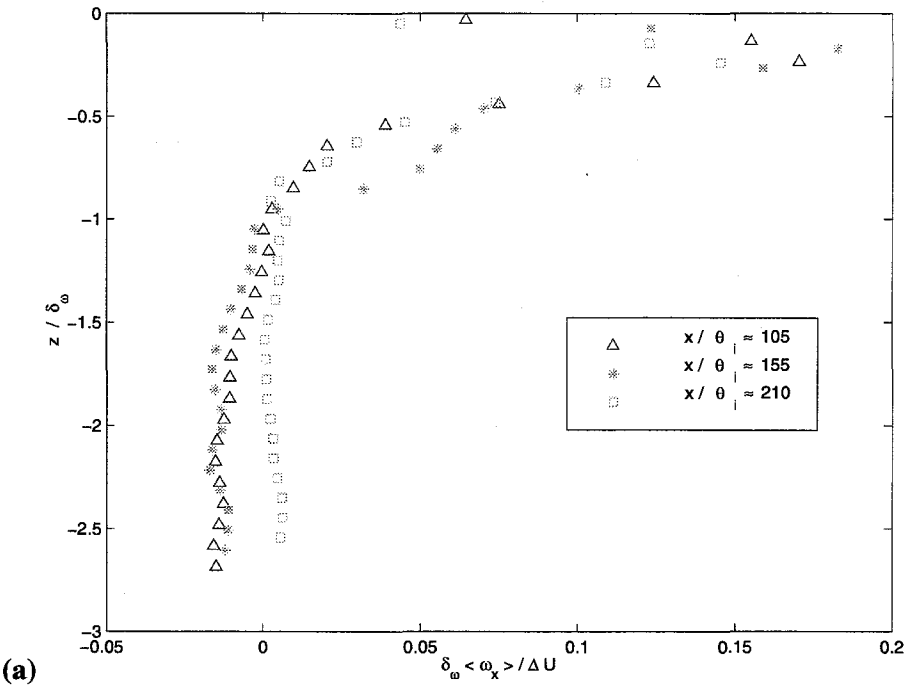

(a)

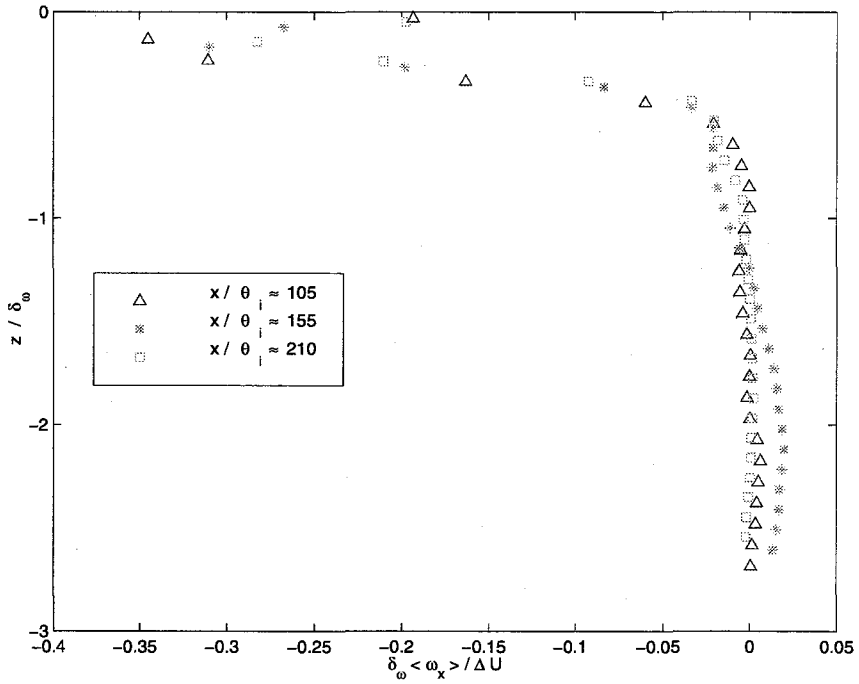

(b)

Fig. 5.3. Distribution of the mean streamwise vorticity along :
(a) $y/\delta_\omega \approx -0.5$, (b) $y/\delta_\omega \approx 0.75$

These secondary flows are consistent with the existence of the *surface currents*, which can be simply understood in terms of mean induced velocity field in this context. These *surface currents* are indeed ubiquitous features of turbulent free-surface flows, as pointed out by Walker[16]. Plotting the mean transverse velocity profiles in the very near-surface region, that is $z/\theta_i \approx -1$, clearly shows the presence of these outward currents adjacent to the free surface. Fig. 5.4 shows that these near-surface velocity profiles are quite different and particularly of opposite sign from the mean transverse velocity profiles of the turbulent plane mixing layer entraining fluid to enable its growth. Therefore, one issue that naturally arises is concerned with the influence of the near-surface secondary flows and their associated free-surface currents on the development of the shear layer and its mean and turbulent properties at the free surface. This question will be tackled in the following section with the help of surface-parallel measurements in the very near-surface region.

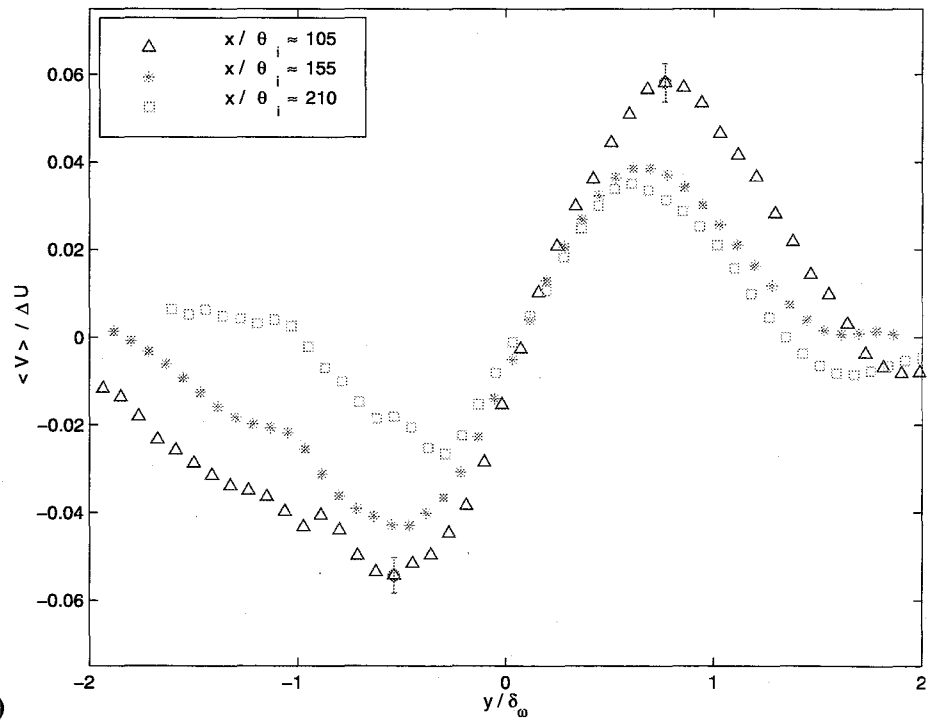

(a)

[16] Walker, D.T. 1997 On the origin of the 'surface currents' in turbulent free-surface flows. J. Fluid Mech. **339**, 275-285.

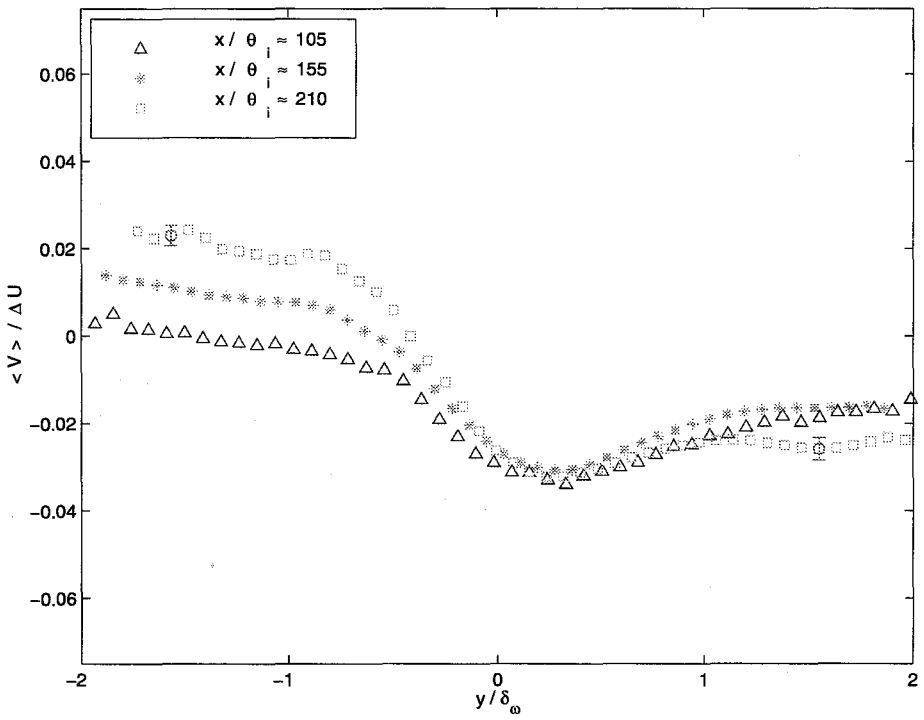

(b)

Fig. 5.4. Profiles of the Reynolds-averaged transverse velocity at:
(a) $z/\theta_i \approx -1$, (b) $z/\theta_i \approx -20$

(b) turbulence structure in the shear layer

Measurements of the turbulent transverse and normal velocity fluctuations as well as the streamwise vorticity fluctuations were also obtained in these flow-normal planes. As previously mentioned, these contours were not corrected for the small deflection of the mixing layer toward the low-speed side, whereas profiles were plotted in their respective mixing-layer coordinate systems.

The contours of the root-mean-square of the normalized transverse velocity fluctuations are plotted in Fig. 5.1. As indicated earlier, it is possible to conclude that the distributions of the second-order turbulence quantities have not achieved an equilibrium state yet. In particular, the maximum value of $\sqrt{\overline{v'^2}}/\Delta U$ doubles while its lateral extent increases by about 30% as the flow evolves downstream from $x/\theta_i \approx 105$ to $x/\theta_i \approx 210$. However, similar features can be found in each flow-normal plane. The magnitude of $\sqrt{\overline{v'^2}}/\Delta U$ remains essentially constant with the depth in the central region of the fully-submerged shear layer.

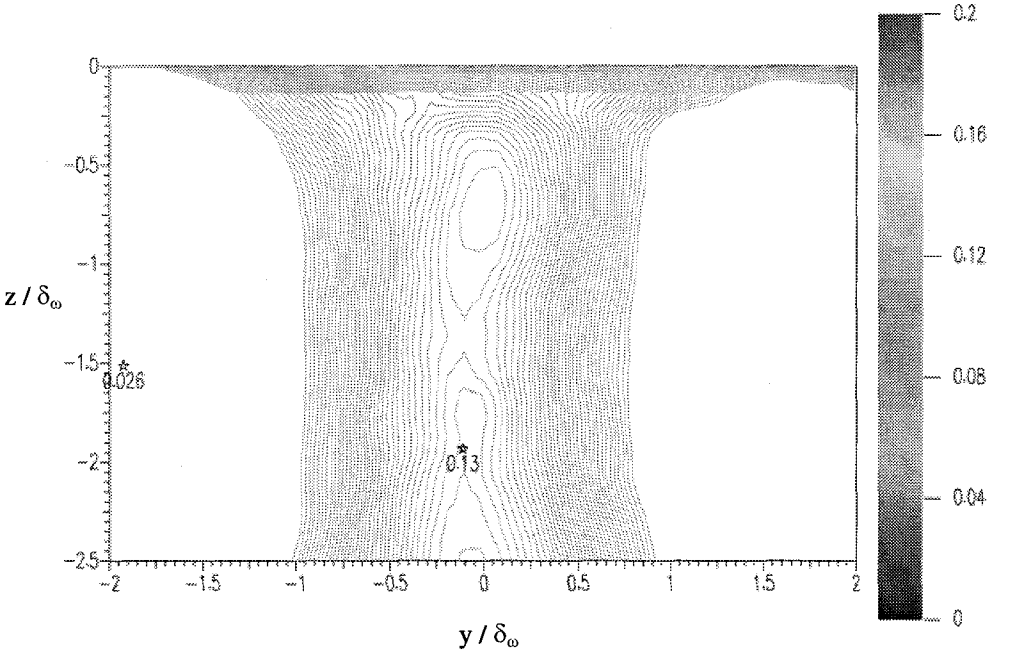
0.2
0.16
0.12
0.08
0.04
0
0
-0.5
-1
-1.5
-2
-2.5
z / δω
0.026
0.13
-2
-1.5
-1
-0.5
0
0.5
1
1.5
2
y / δω

(a)

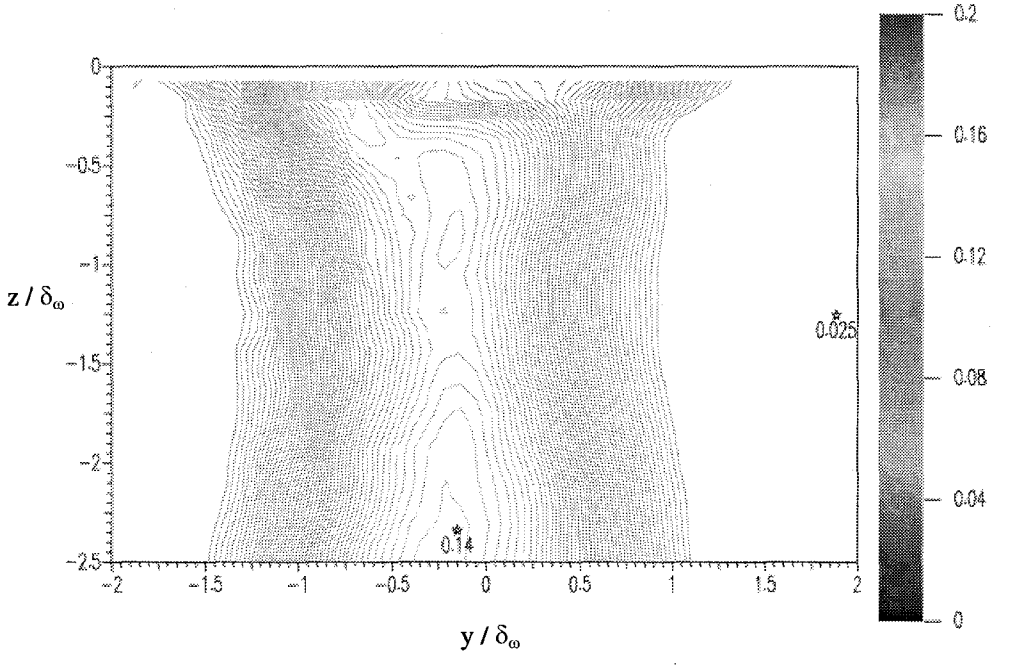
0.2
0.16
0.12
0.08
0.04
0
0
-0.5
-1
-1.5
-2
-2.5
z / δω
0.025
0.14
-2
-1.5
-1
-0.5
0
0.5
1
1.5
2
y / δω

(b)

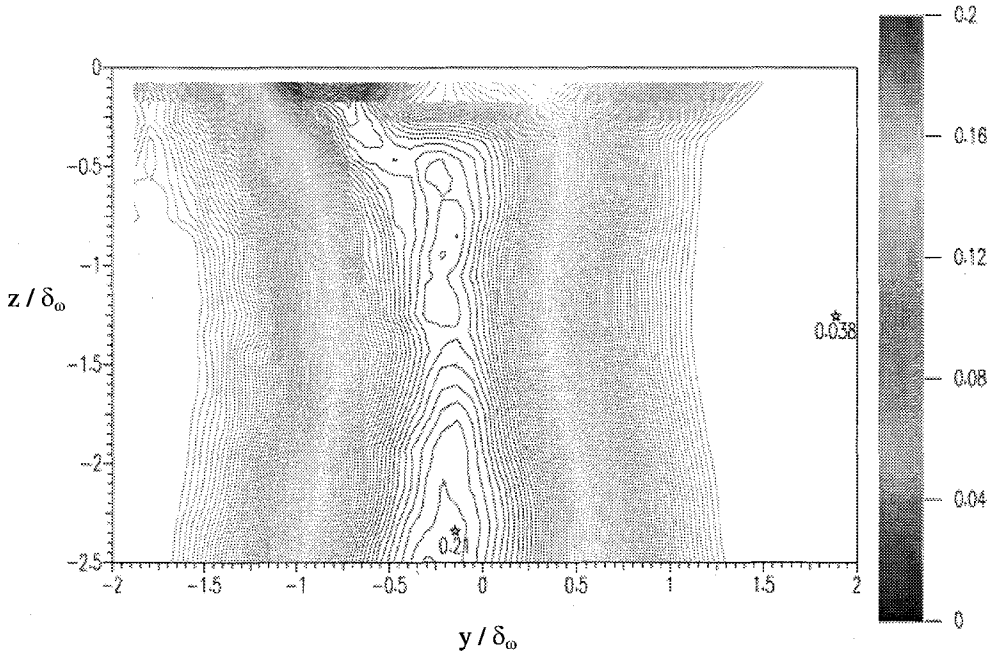

(c)

Fig. 5.1. Contours of the normalized transverse velocity fluctuations in the flow-normal planes: (a) $x/\theta_i \approx 105$, (b) $x/\theta_i \approx 155$, (c) $x/\theta_i \approx 210$

However, it increases along the edges of the mixing layer and its maximum shifts toward the low-speed side as the free surface is approached ($|z/\delta_\omega| \leq 0.25$).

Comparison between the profiles of the root-mean-square of the normalized transverse velocity fluctuations at constant depth near the free surface ($z/\theta_i \approx -1$) and in the fluid bulk ($z/\theta_i \approx -20$) confirms this analysis. Furthermore, Fig. 5.2 also reveals the difference in shape between the profiles of the free-surface shear layer and its fully-submerged counterpart. Indeed, $\sqrt{\overline{v'^2}}/\Delta U$ has a Gaussian-shaped profile evolving toward its asymptotic curve in the fully-submerged shear layer while its profile at the free surface is asymmetric and much fuller (by about 25%) ranging from about $-1.5\delta_\omega$ to $2.5\delta_\omega$ with a non-Gaussian characteristic shape. Furthermore, its maximum is slightly higher by about 10% and located further toward the low-speed side (about $-0.5\delta_\omega$).

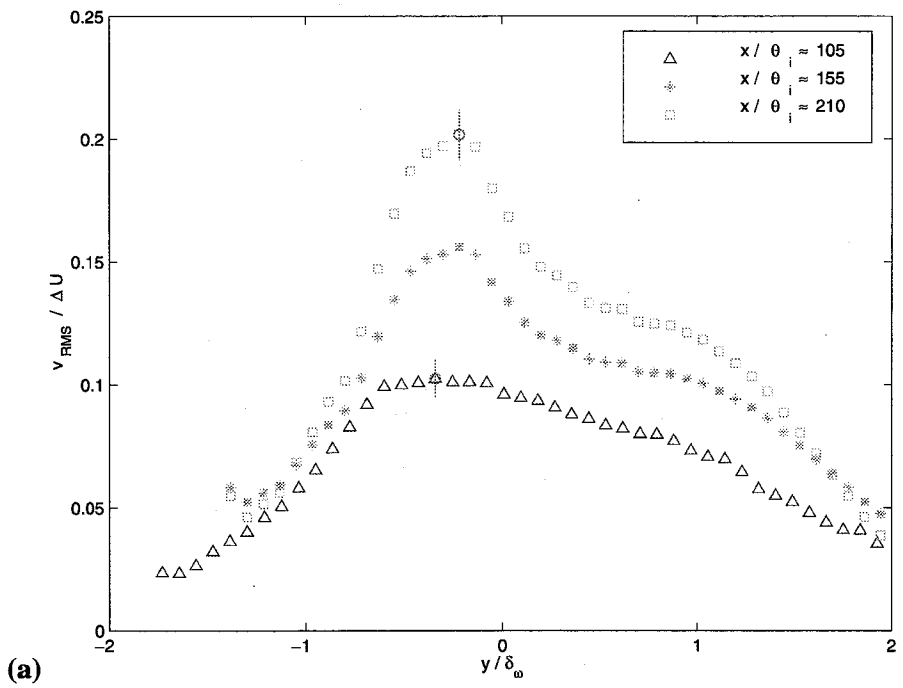

(a)

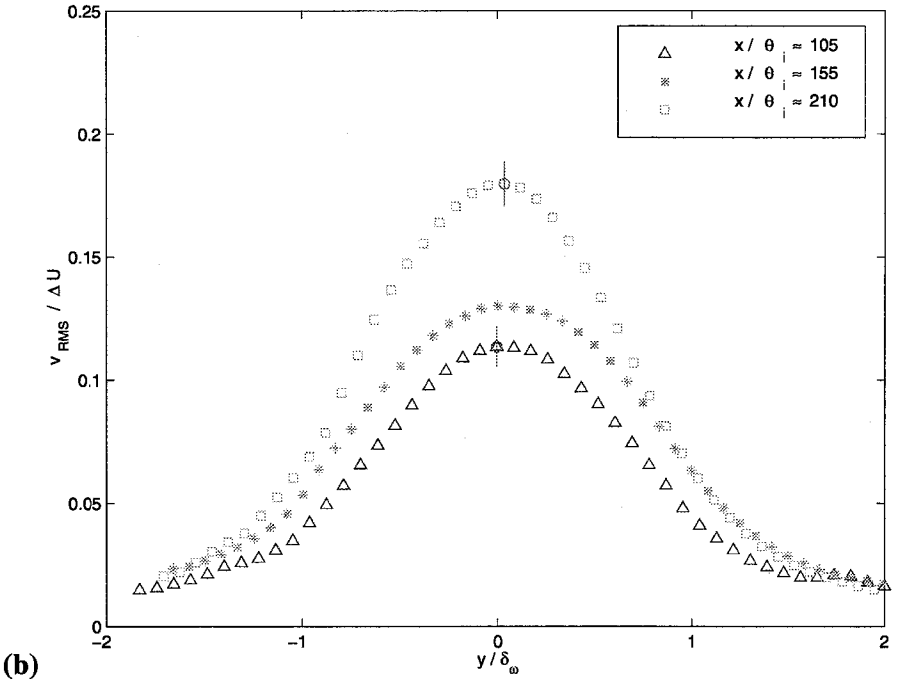

(b)

Fig. 5.2. Profiles of the normalized transverse velocity fluctuations in the flow-normal planes at: (a) $z/\theta_i \approx -1$, (b) $z/\theta_i \approx -20$

The contours of the root-mean-square of the normalized normal velocity fluctuations are also plotted in Fig. 5.3. The distribution of the normal velocity fluctuations has not achieved an equilibrium state yet either, as its maximum value doubles and its lateral extent increases by about 30% (from $x/\theta_i \approx 105$ to $x/\theta_i \approx 210$). However, similar features can also be found in each flow-normal plane. The magnitude of $\sqrt{\overline{w'^2}}/\Delta U$ remains essentially constant with the depth in the central region of the fully-submerged shear layer. However, as the free surface is approached ($|z/\delta_\omega| \leq 0.25$), it sharply decreases except in a narrow region of the low-speed side located at about $-0.5\delta_\omega$. Similar comparison between the profiles of the root-mean-square of the normalized normal velocity fluctuations at constant depth near the free surface ($z/\theta_i \approx -1$) and in the fluid bulk ($z/\theta_i \approx -20$) confirms this analysis. The value of $\sqrt{\overline{w'^2_{max}}}/\Delta U$ decreases by about 15% but would drop by more than 50% if not for this narrow region of the low-speed side located at about $-0.5\delta_\omega$. Furthermore, Fig. 5.4 also reveals the difference in shape between the profiles of the free-surface shear layer and its fully-submerged counterpart.

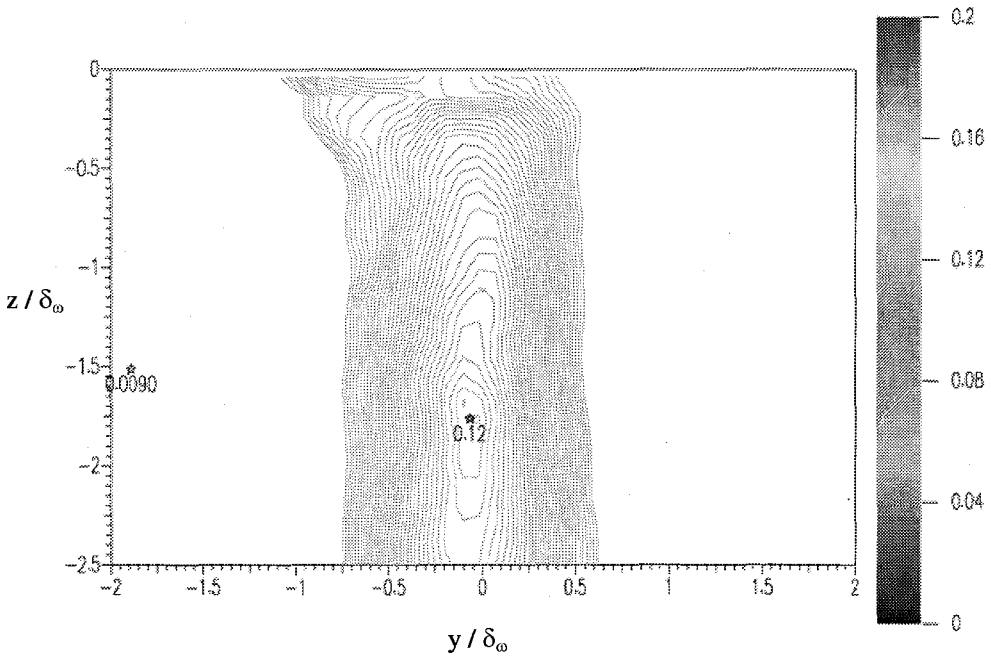

(a)

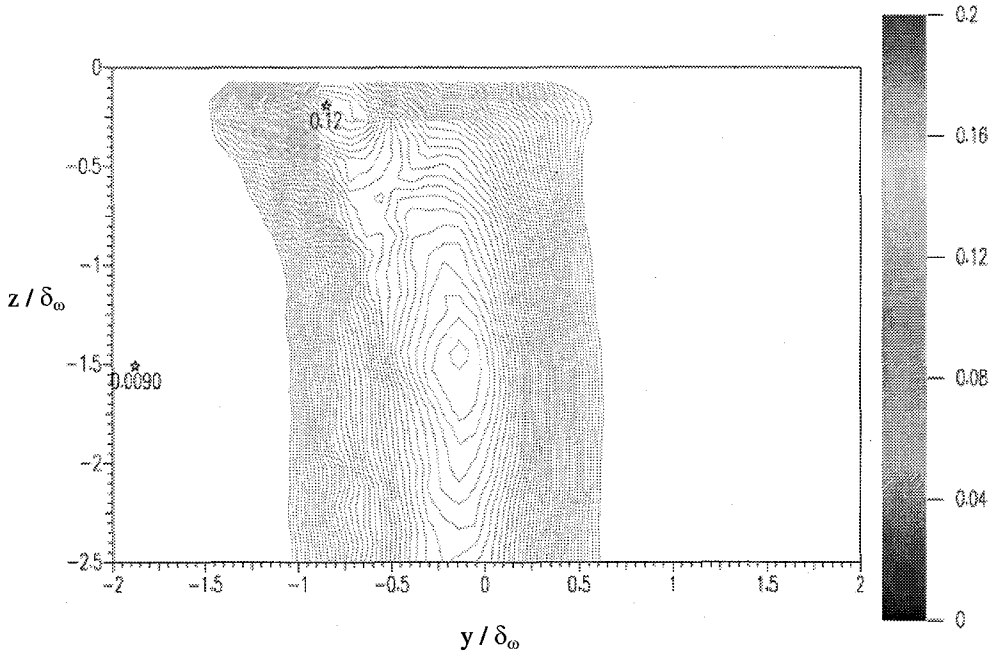

(b)

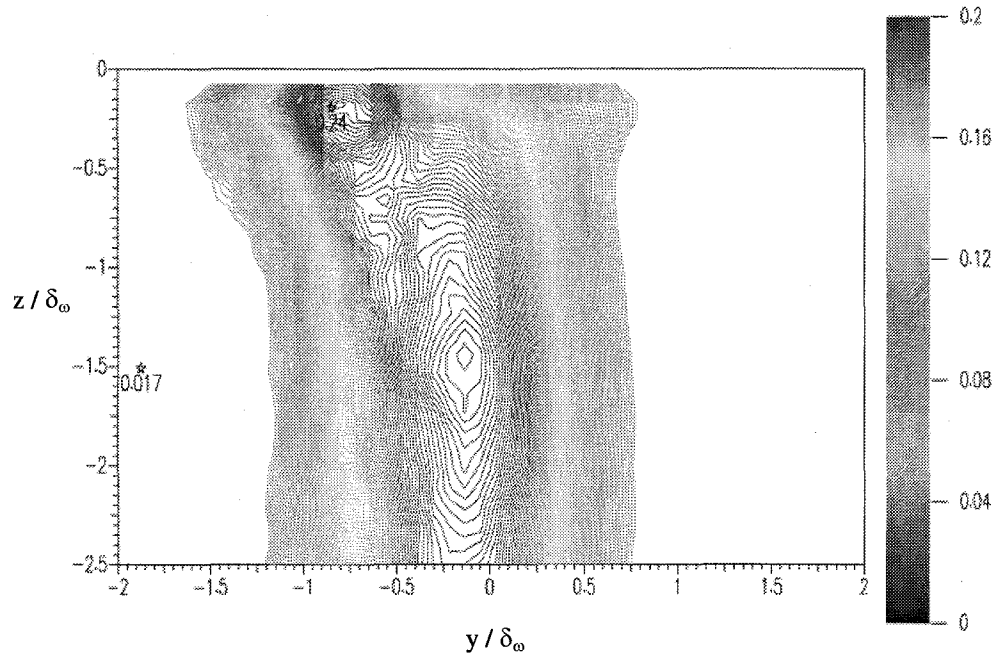

(c)

Fig. 5.3. Contours of the normalized normal velocity fluctuations in the flow-normal planes: (a) $x/\theta_i \approx 105$, (b) $x/\theta_i \approx 155$, (c) $x/\theta_i \approx 210$

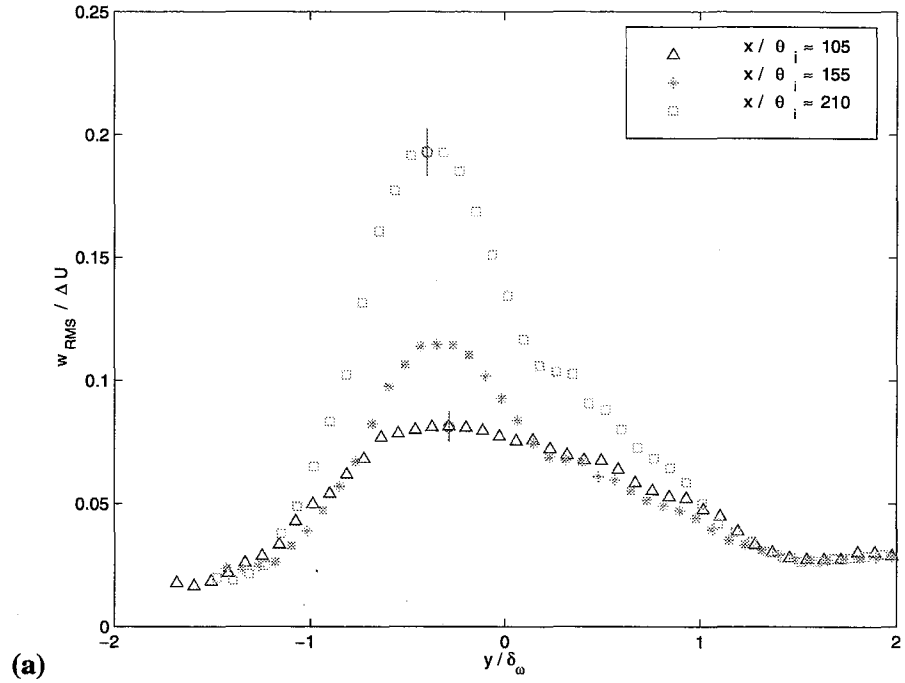

(a)

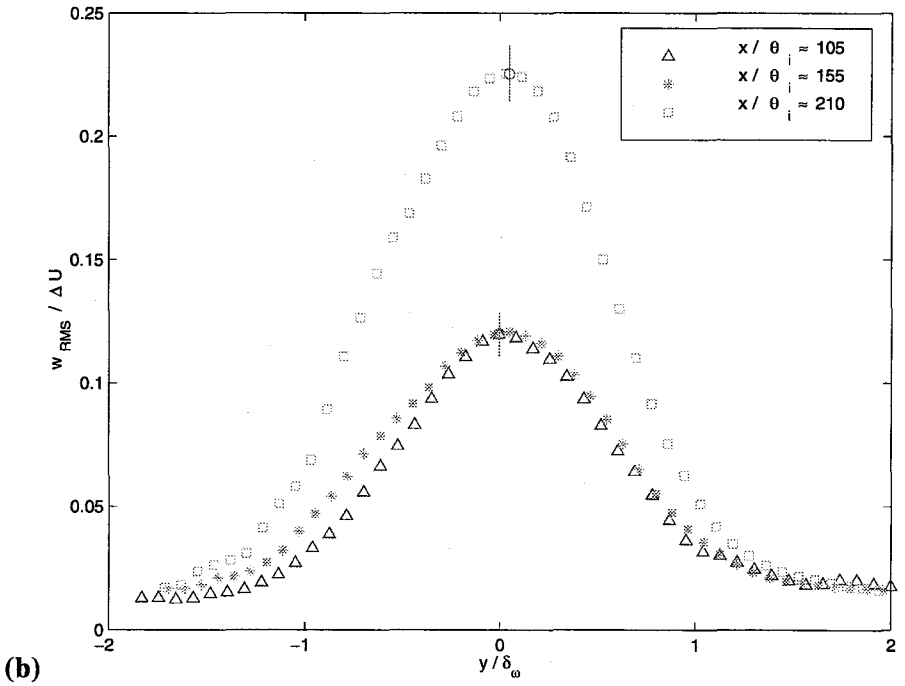

(b)

Fig. 5.4. Profiles of the normalized normal velocity fluctuations in the flow-normal planes at: (a) $z/\theta_i \approx -1$, (b) $z/\theta_i \approx -20$

Indeed, $\sqrt{\overline{w'^2}}/\Delta U$ has a Gaussian-shaped profile evolving toward its asymptotic curve in the fully-submerged shear layer while its profile at the free surface is asymmetric and much fuller (by about 25%) ranging from about $-1.5\delta_\omega$ to $2.5\delta_\omega$ with a non-Gaussian characteristic shape and its maximum is shifted toward the low-speed side (about $-0.5\delta_\omega$).

These results clearly show the anisotropy that exists at the free surface. However, the reduction in $\sqrt{\overline{w'^2}}/\Delta U$ is far less pronounced than it was for the free-surface wake.

Fig. 5.5 shows the contours of the root-mean-square of the normalized streamwise vorticity fluctuations. The magnitude of $\sqrt{\overline{\omega_x'^2}}/(\Delta U/\delta_\omega)$ remains essentially constant with the depth until the near-free-surface region ($|z/\delta_\omega| \le 0.25$). As the free surface is approached, it increases along the edges of the mixing layer and its maximum shifts toward the low-speed side at about $-0.5\delta_\omega$.

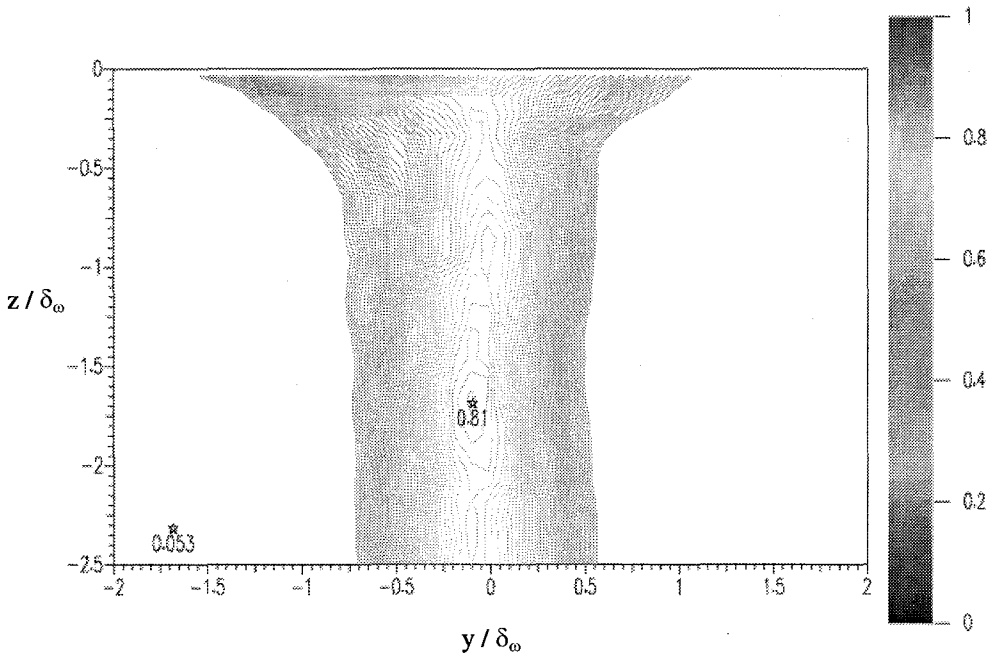

(a)

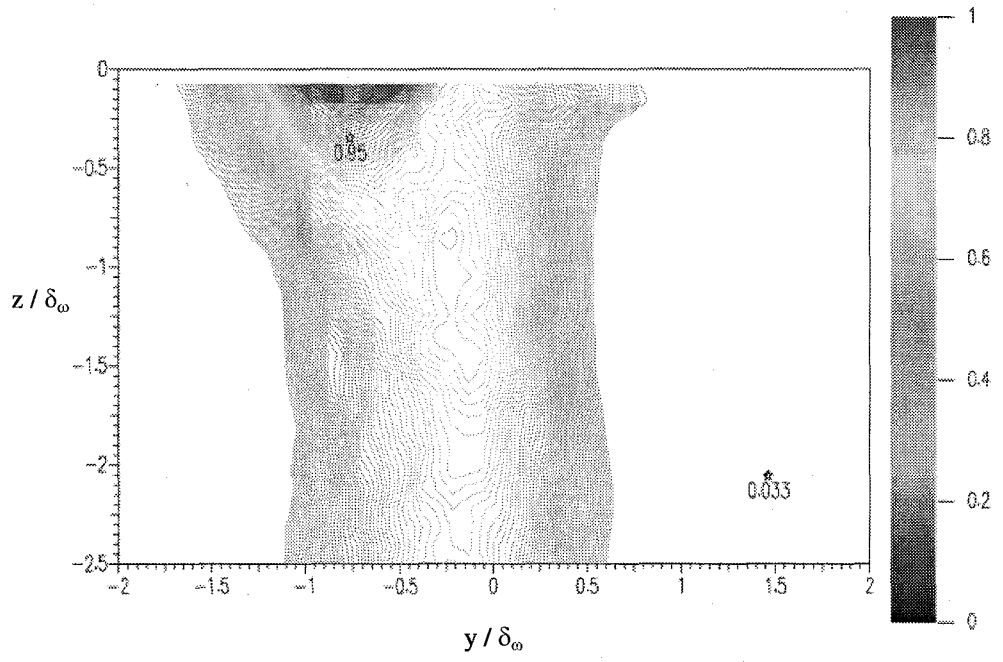

(b)

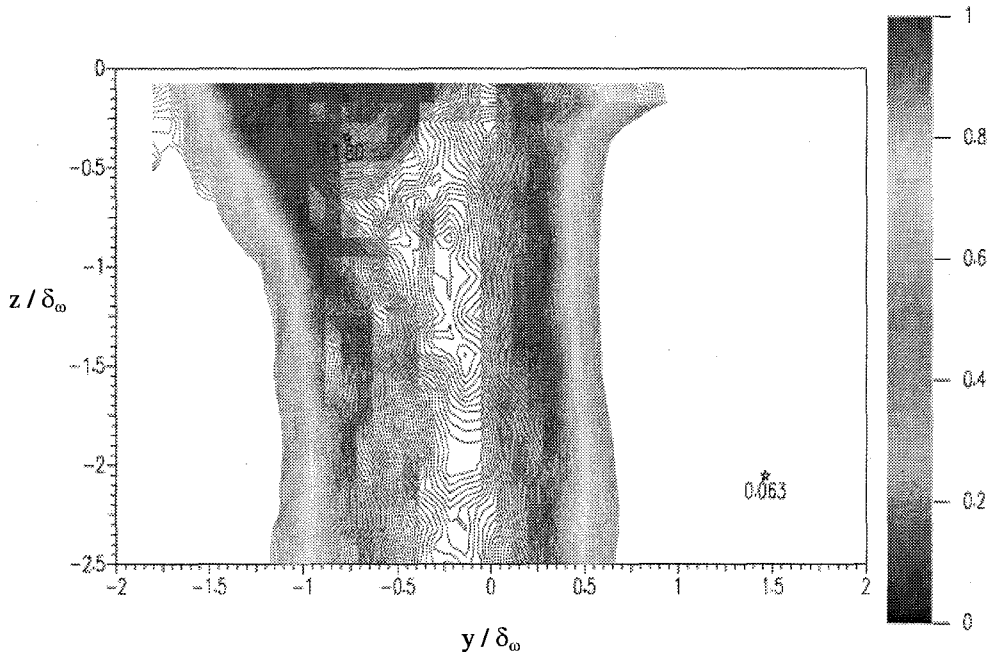

(c)

Fig. 5.5. Contours of the normalized streamwise vorticity fluctuations in the flow-normal planes: (a) $x/\theta_i \approx 105$, (b) $x/\theta_i \approx 155$, (c) $x/\theta_i \approx 210$

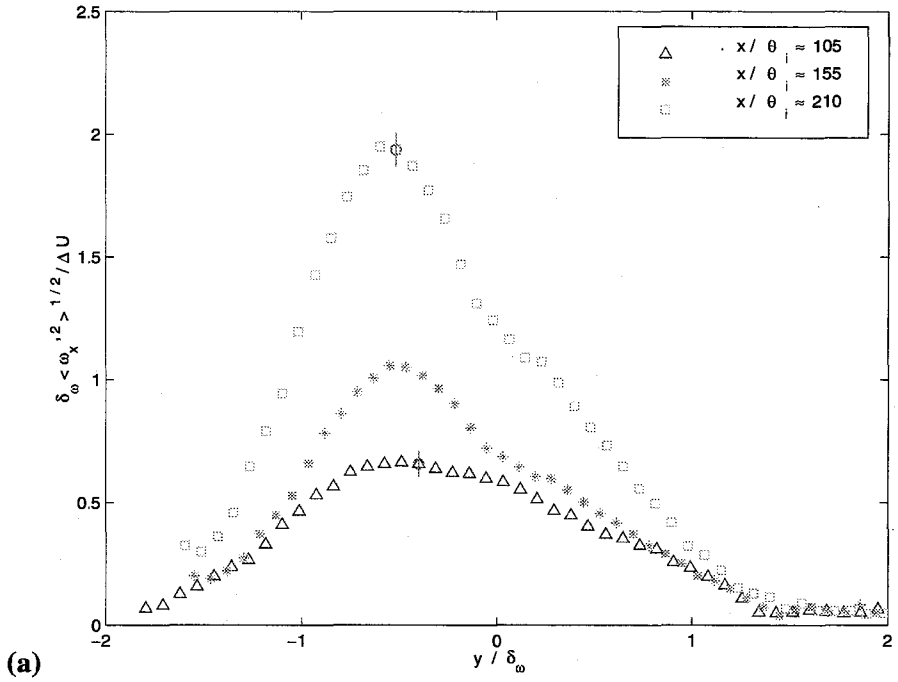

(a)

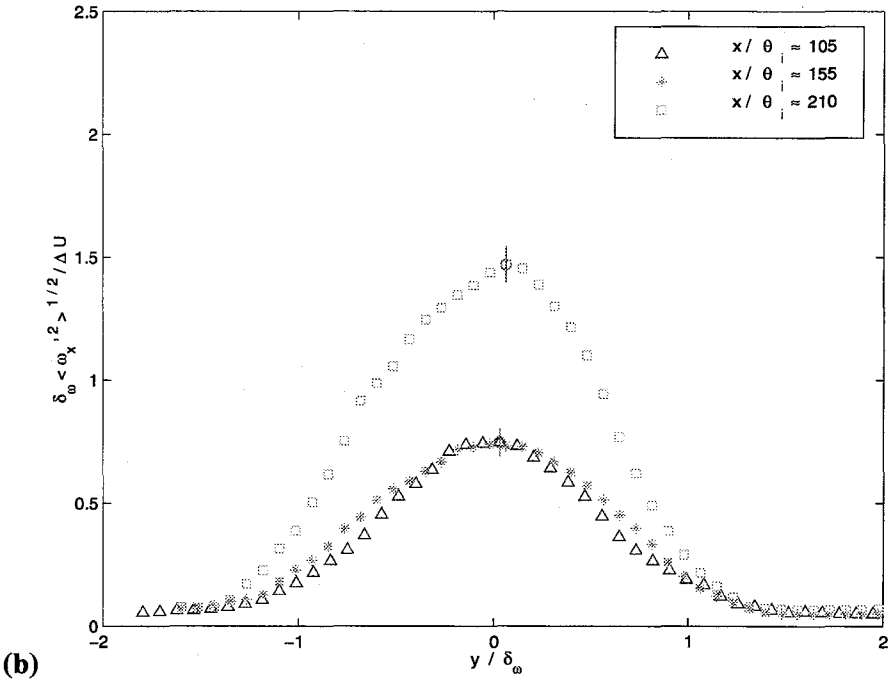

(b)

Fig. 5.6. Profiles of the normalized streamwise vorticity fluctuations in the flow-normal planes at: (a) $z/\theta_i \approx -1$, (b) $z/\theta_i \approx -20$

Comparison between the profiles of the root-mean-square of the normalized normal vorticity fluctuations at constant depth near the free surface ($z/\theta_i \approx -1$) and in the fluid bulk ($z/\theta_i \approx -20$) can be assessed in Fig. 5.6. The value of $\sqrt{\overline{(\omega'^2_x)}}_{max}/(\Delta U/\delta_\omega)$ increases by about 30%. Furthermore, $\sqrt{\overline{(\omega'^2_x)}}/(\Delta U/\delta_\omega)$ has a Gaussian-shaped profile evolving toward its asymptotic curve in the fully-submerged shear layer. On the other hand, its profile at the free surface is asymmetric and much fuller (by about 25%) ranging from about $-1.5\delta_\omega$ to $2.5\delta_\omega$ with a non-Gaussian characteristic shape and its maximum is shifted toward the low-speed side (about $-0.5\delta_\omega$).

The presence of higher values of $\sqrt{\overline{\omega'^2_x}}/(\Delta U/\delta_\omega)$ at the edges of the surface layer ($|z/\delta_\omega| \leq 0.25$) is consistent with the discovery of streamwise vortical structures present at the edges of the mixing layer at the free surface. These present results are also consistent with the normal connection of vortical structures at the free surface, except in a narrow region of the low-speed side located at about $-0.5\delta_\omega$ where the value of the normalized surface-parallel enstrophy component is increased by about 30%.

5.2.2. Free-surface plane measurements

(a) behavior of the mean flow in the shear layer

One surface-parallel measurement plane was then positioned in the estimated region of influence of the near-surface secondary flows to investigate their influence on the underlying turbulent shear layer. Data was thus acquired in a x-y surface-parallel plane in the very near-surface at $z/\theta_i \approx -1$.

At various positions downstream of the splitter plate, streamwise velocity profiles were obtained to determine the width of the free-surface mixing layer and the position of its centerline. The free-surface mixing layer also deflects toward the low-speed side and thus spreads preferentially into the low velocity stream. However, as shown in Fig. 5.1, the deflection of the free-surface mixing layer is smaller than its fully-submerged counterpart, as it is influenced by the near-surface secondary flows. Indeed, the secondary flow on the high-speed side is stronger by about 35%. The experimental results are presented in a coordinate system following the mixing layer growth (corresponding to the centerline deflection of the free-surface shear layer).

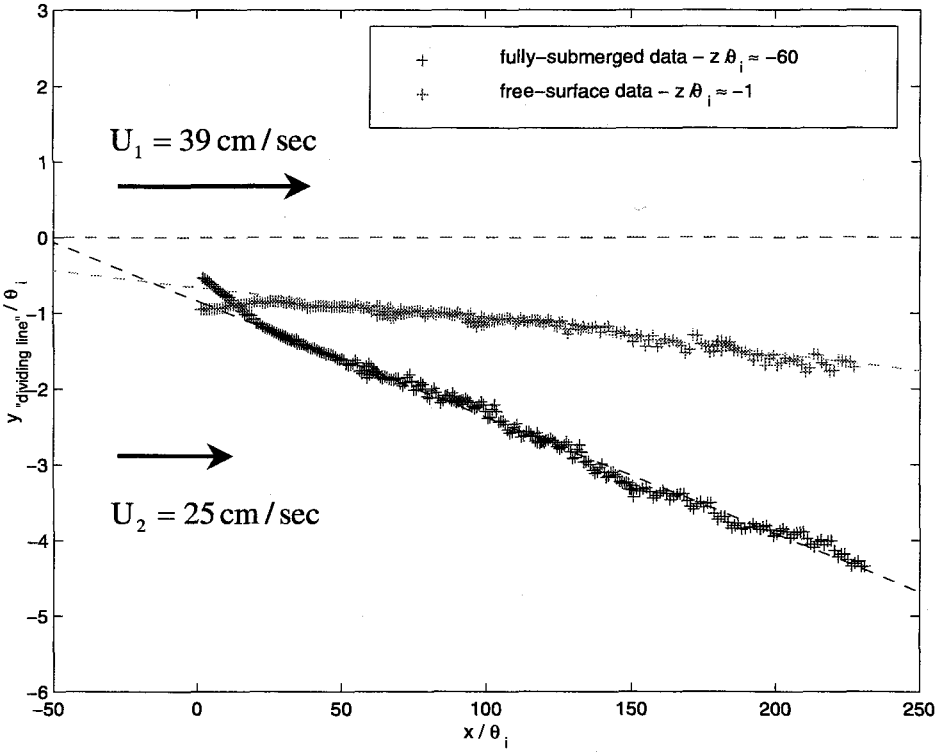

Fig. 5.1. Location of the dividing line for the free-surface and the fully-submerged shear layers

Values of the growth-rate parameter Δ were obtained throughout the very near-surface-parallel plane ($z/\theta_i \approx -1$). Fig. 5.2 depicts its evolution at the free surface. Its fully-submerged counterpart is also plotted on this figure for reference. The value attained by the growth-rate parameter in the last measurement region does not vary by more than 5% of its mean value in this region, which is found to be $\Delta \approx 0.073$. The curve still slightly decreases but the value attained by Δ is close to its asymptotic value Δ^*. Taking Δ^* to be 0.073, this leads to a constant C_{δ_ω} of value

$$0.073 = \Delta^* \equiv \left(\frac{\delta_\omega}{x}\right)^* \approx C_{\delta_\omega} \frac{1-r}{1+r} = 0.22\, C_{\delta_\omega} \quad \Rightarrow \quad C_{\delta_\omega} \approx 0.334$$

which is considerably higher (about 25%) than the value attained by the same parameter in the deep mixing layer (i.e., 0.265). This simply means that the free-surface shear layer grows 1.25 times faster than its fully-submerged counterpart.

The distributions of the second-order turbulence quantities presented above suggest that the mixing layer did not reach its equilibrium state just yet. However, as for the wake flow, mean-flow quantities reach their asymptotic values much faster. Thus, the results obtained hereby should hold, as the mixing layer evolves downstream.

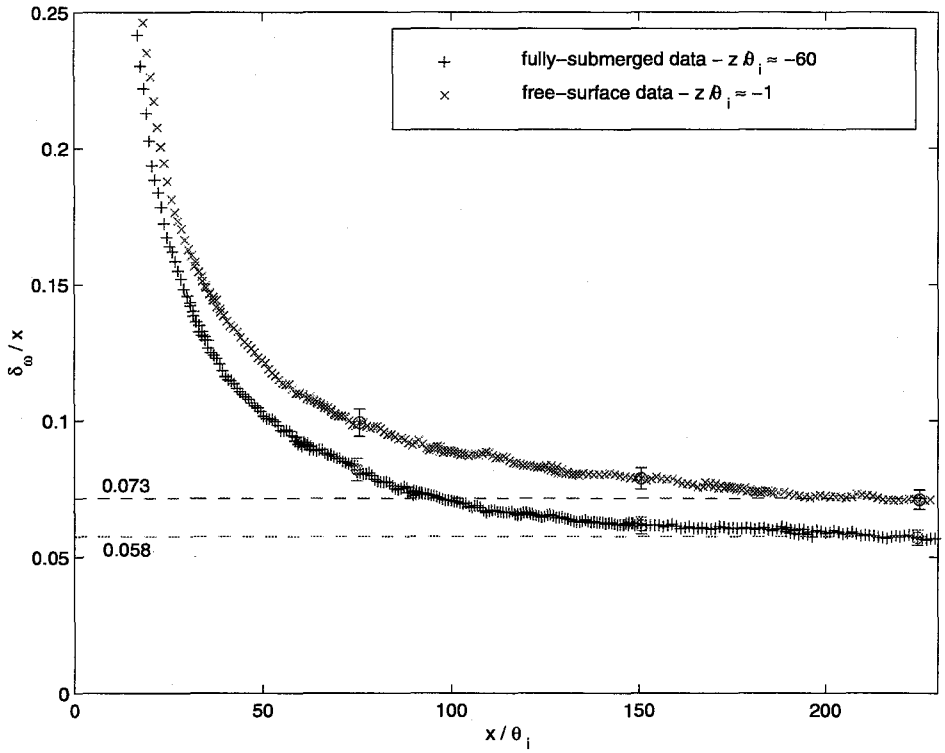

Fig. 5.2. Evolution of the growth rate parameters with the normalized downstream distance

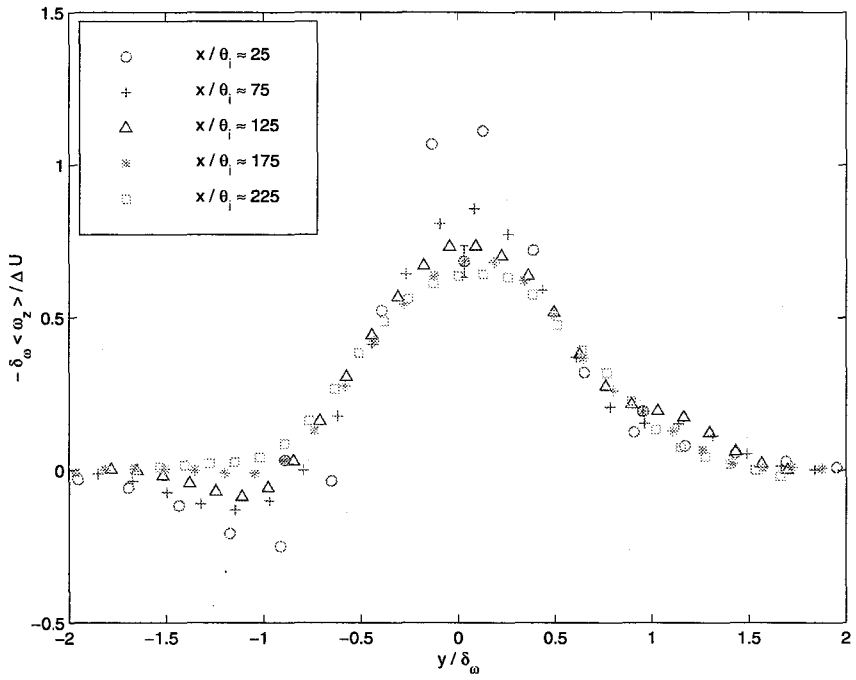

(a)

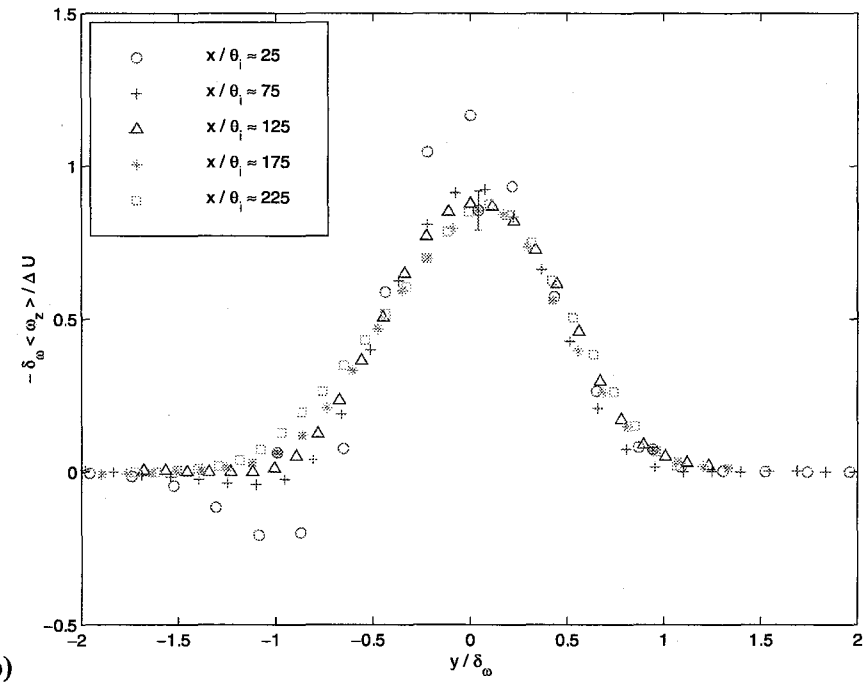

(b)

Fig. 5.3. Mean normal vorticity profiles for: (a) the free-surface shear layer ($z/\theta_i \approx -1$), (b) the fully-submerged shear layer ($z/\theta_i \approx -60$)

(b) turbulence structure in the shear layer

The distributions of the normalized root-mean-square of the streamwise and transverse velocity fluctuations measured in the very-near plane ($z/\theta_i \approx -1$) are plotted at several downstream stations in Fig. 5.1 and Fig. 5.2 respectively. The distributions obtained for the fully-submerged mixing layer ($z/\theta_i \approx -60$) are also plotted on these figures to enable easier comparison. As indicated earlier, the distributions of these second-order turbulence quantities have not reached an equilibrium state yet. In particular, the maximum value of $\sqrt{\overline{v'^2}}/\Delta U$ doubles while its lateral extent increases by about 25% as the flow evolves downstream from $x/\theta_i \approx 75$ to $x/\theta_i \approx 225$. Fig. 5.1 depicts the profiles of $\sqrt{\overline{u'^2}}/\Delta U$ near the free surface ($z/\theta_i \approx -1$) and in the fluid bulk ($z/\theta_i \approx -60$). The value of $\sqrt{\overline{u'^2_{max}}}/\Delta U$ slightly increases by about 10%. Furthermore, its profile is fuller at the free surface (by about 20%) and the location of its maximum is shifted by about $-0.5\delta_\omega$. The results concerning the distribution of the normalized root-mean-square of the transverse velocity fluctuations are consistent with the flow-normal measurements presented above. Fig. 5.2 confirms the difference in shape between the profiles of $\sqrt{\overline{v'^2}}/\Delta U$ at the free surface and in the deep flow. Its profile is indeed much fuller at the free surface (by about 25%), ranging from about $-1.5\delta_\omega$ to 2.5 and its maximum value is both shifted in location (about $-0.5\delta_\omega$) and increased in value (about 10 %).

Fig. 5.3 presents the distributions of the normalized turbulent Reynolds shear stress at the same downstream stations. Similarly, its maximum value slightly increases by 10% while its width is much fuller by about 25%. Profiles of the root-mean-square of the normalized normal vorticity fluctuations are plotted in Fig. 5.4. The magnitude of $\sqrt{\left(\overline{\omega'^2_z}\right)_{max}}/(w_o/b)$ is similar to that of its fully-submerged counterpart. However, the lateral extent of these profiles does vary consistently with the higher lateral spreading rate (25%) of the shear layer at the free surface. These results are consistent with the fact that only the surface-normal component of the vorticity remains at a flat free surface, which forces vortex lines to terminate normal to the surface. Thus, $\sqrt{\overline{\omega'^2_z}}/(w_o/b)$ increases — in lateral extent — as the free surface is reached as vortex filaments tend to connect to the free surface.

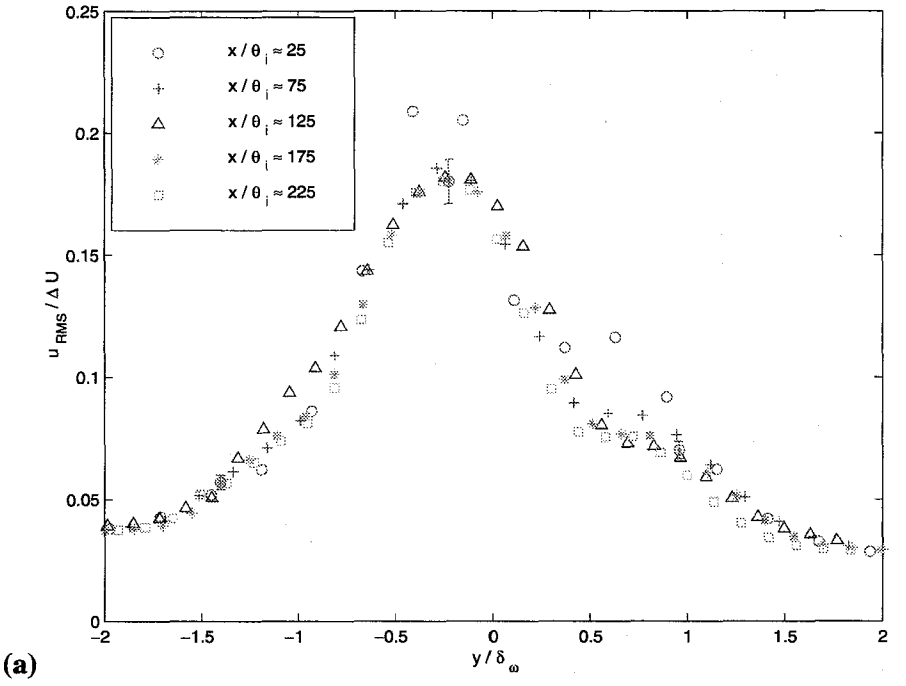

(a)

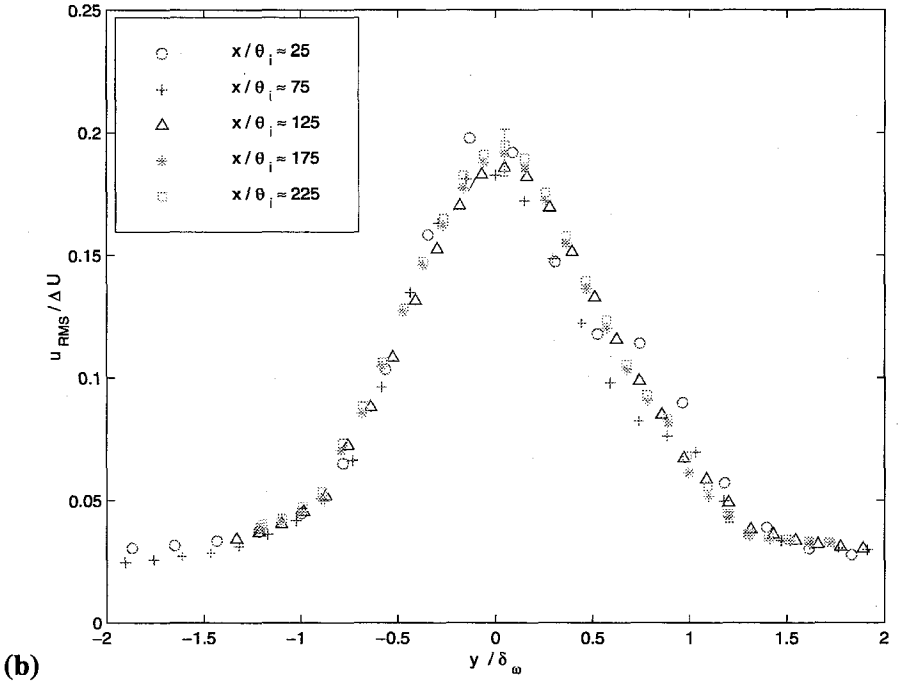

(b)

Fig. 5.1. Distribution of the streamwise velocity fluctuations for: (a) the free-surface shear layer ($z/\theta_i \approx -1$), (b) the fully-submerged shear layer ($z/\theta_i \approx -60$)

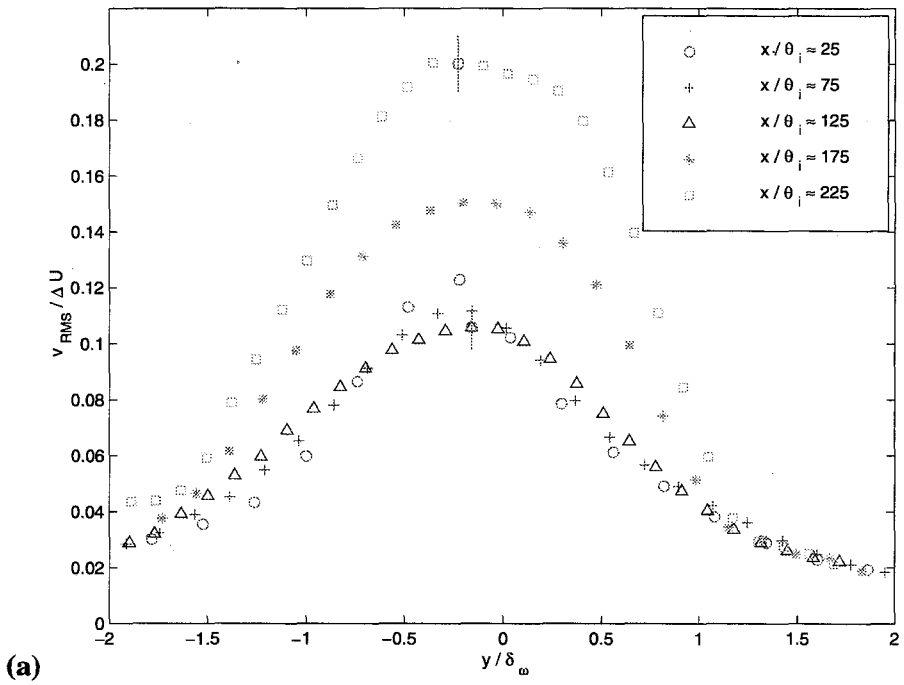

(a)

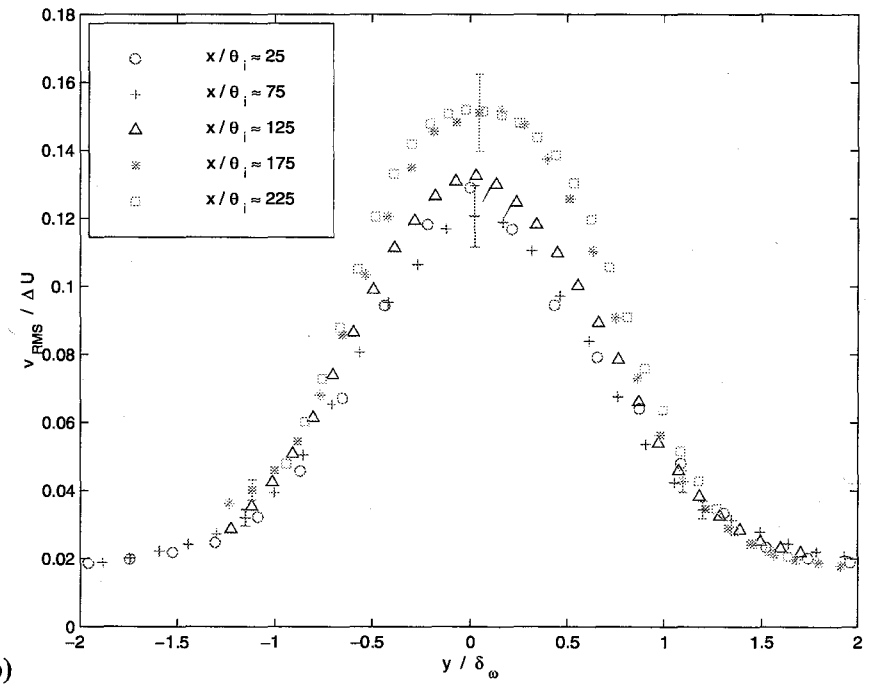

(b)

Fig. 5.2. Distribution of the transverse velocity fluctuations for: (a) the free-surface shear layer ($z/\theta_i \approx -1$), (b) the fully-submerged shear layer ($z/\theta_i \approx -60$)

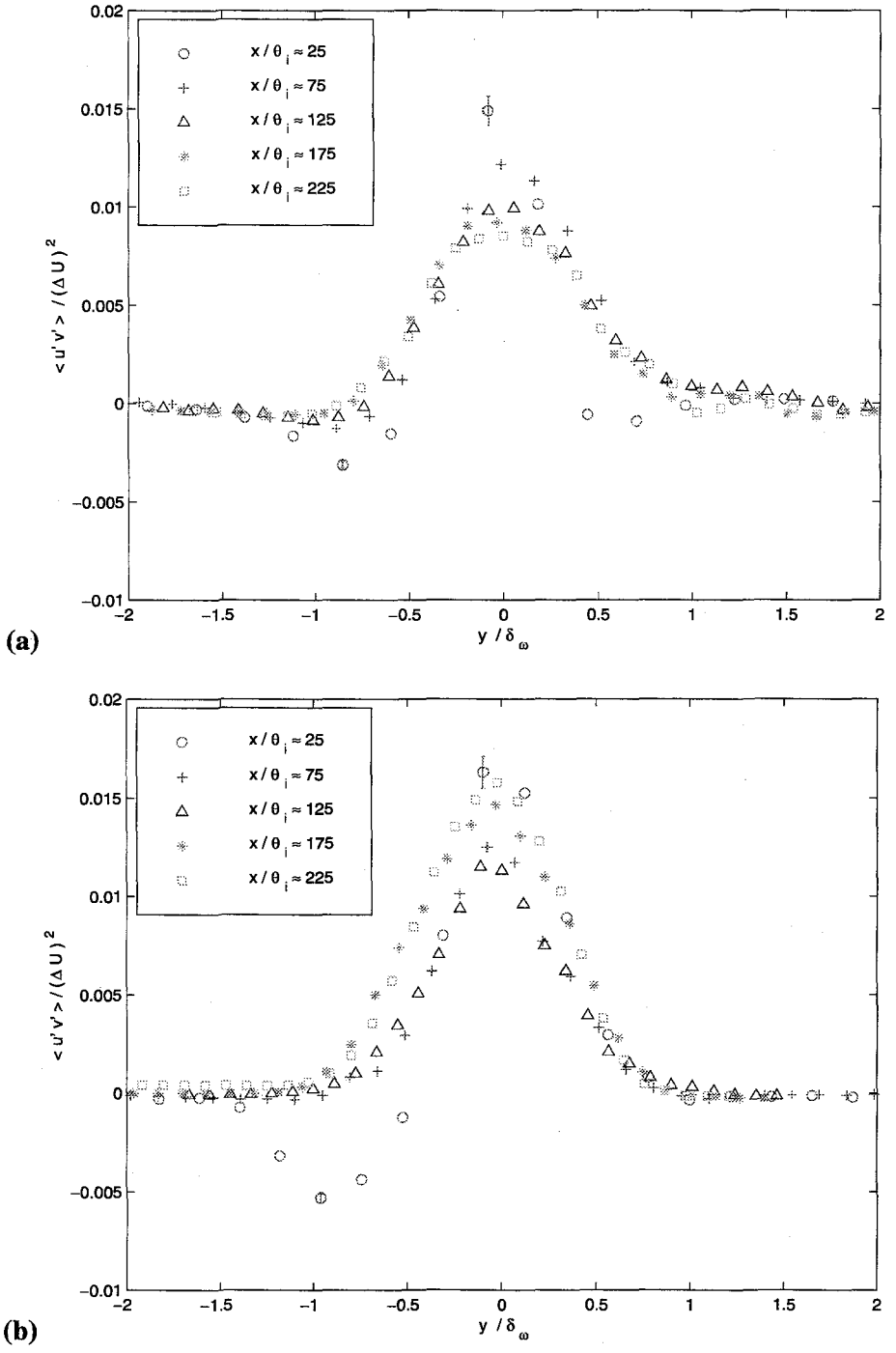

Fig. 5.3. Distribution of the Reynolds turbulent shear stress for: (a) the free-surface shear layer ($z/\theta_i \approx -1$), (b) the fully-submerged shear layer ($z/\theta_i \approx -60$)

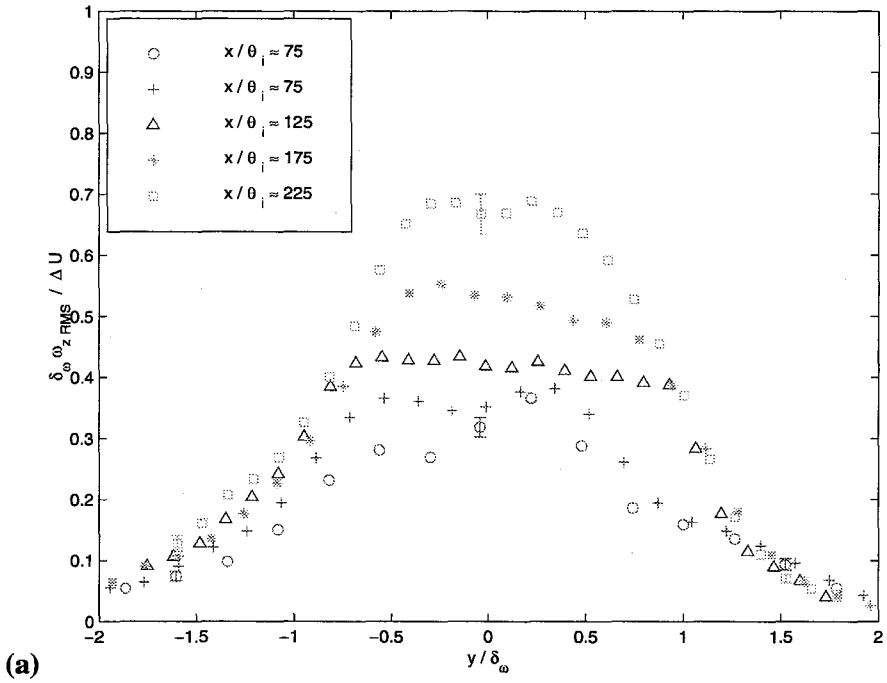

(a)

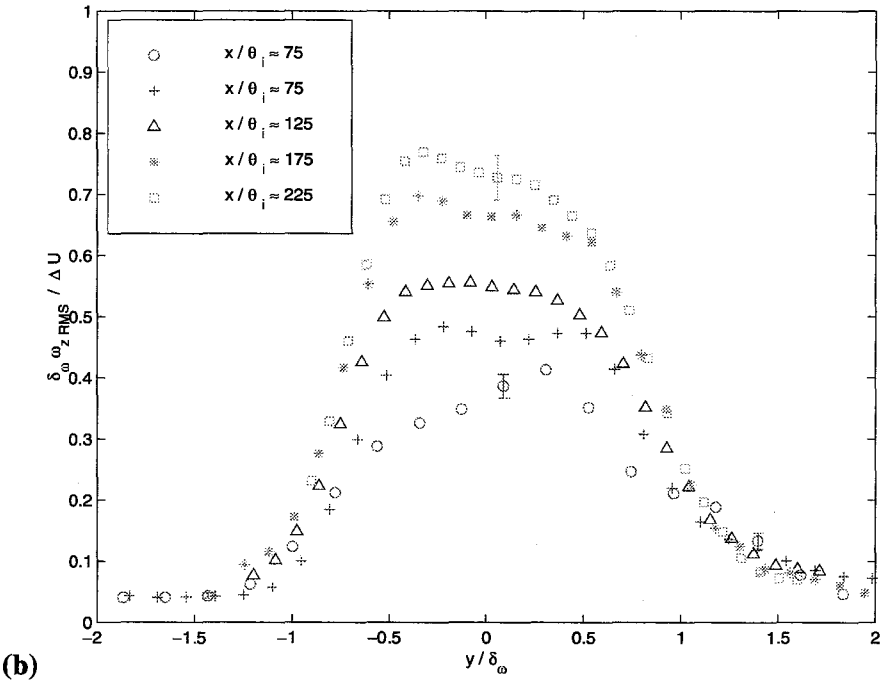

(b)

Fig. 5.4. Distribution of the normal vorticity fluctuations for: (a) the free-surface shear layer ($z/\theta_i \approx -1$), (b) the fully-submerged shear layer ($z/\theta_i \approx -60$)

5.3. Conclusions

The dynamics of low Froude number, free surface turbulence has been investigated by experiments of a turbulent shear layer behind a surface-piercing splitter plate.

The plate extended far enough below the surface to produce a shear layer that became nearly *two-dimensional* with depth, that is, away from the free surface, the turbulence quantities became homogeneous in the vertical direction. The measurements performed in the deep shear layer ($z/\theta_i \approx -60$) showed good agreement with the well-established theory for two-dimensional turbulent shear-layer flows. However, the values obtained in this study were quite different from those found in the literature. In particular, the lateral spreading rate of the shear layer was increased by about 40%. It is believed that the nature of the inflow conditions, and in particular the state of the boundary layers, turbulent but not fully-developed, is also responsible for these different parameters.

The free surface was found to affect the dynamics of turbulence within a *surface layer* on the order of one half of the local vorticity thickness of the submerged shear layer. Within this layer, the vertical velocity fluctuations were inhibited and the turbulence kinetic energy was redistributed to the horizontal components. The self-induced motion of surface-parallel vortical structures under the influence of their images was shown to lead to large-scale asymmetric streamwise secondary flows and associated outward *surface currents*. This motion was the origin of the significantly higher (25%) lateral spreading rates of these surface shear flows compared to the spreading rates of their fully-submerged counterparts. In addition, the evolution of the surface-normal enstrophy components within the *surface layer* was consistent with the normal connection of vortical structures required at a free surface.

The influence of the secondary flows was tracked back to the splitter plate's turbulent boundary layers and similar arguments made in the wake flow can be used to account for their origins and evolution. These arguments are further reinforced by the asymmetry of the secondary flows.

"Chance favors only those who know how to court her."
Charles Nicolle.

CONCLUSIONS

CHAPTER VI

6. Conclusions

The dynamics of low Froude number, free surface turbulence has been investigated by experiments of turbulent wakes and shear layers behind a surface-piercing splitter plate.

The plate extended far enough below the surface to produce shear flows that became nearly *two-dimensional* with depth, that is, away from the free surface, the turbulence quantities became homogeneous in the vertical direction. The measurements performed in the deep shear flows showed good agreement with the well-established theory for two-dimensional turbulent shear flows. However, the values obtained in this study were quite different from those found in the literature. In particular, the lateral spreading rates of the wake and shear layer were both increased by about 40%. It is believed that the nature of the inflow conditions, and in particular the state of the boundary layers, turbulent but not fully-developed, and the relatively low value of the Reynolds number are some of the important conditions resulting in such different parameters.

The free surface was found to affect the dynamics of turbulence within a *surface layer* on the order of one half-width of the submerged wake and one half of the local vorticity thickness of the submerged shear layer. Within this layer, the vertical velocity fluctuations were inhibited and the turbulence kinetic energy was redistributed to the horizontal components. The self-induced motion of surface-parallel vortical structures under the influence of their images was shown to lead to large-scale streamwise secondary flows and associated outward *surface currents* — symmetric for the wake and asymmetric for the shear layer. This motion was the origin of the significantly higher lateral spreading rates of these surface shear flows compared to the spreading rates of their fully-submerged counterparts — 20% and 25% for the wake and shear layer respectively. In addition, the evolution of the streamwise and surface-normal enstrophy components within the *surface layer* was consistent with the normal connection of vortical structures required at a free surface.

The influence of the secondary flows was tracked back to the splitter plate's turbulent boundary layers where they were hence deduced to originate. A simple analysis of the mixed-boundary corner flows of the splitter plate made using the mean streamwise vorticity equation coupled with the evolution of the values of the transverse velocity confirmed the latter. In this picture of the mean flow, the secondary flows present in the near-surface edges of these shear flows were related to the pair of outer secondary *vortices* generated thereby. Furthermore, using a simplified equation for the surface-normal Reynolds stress, it was shown that the

mutual interaction of the surface-parallel vortical structures with their images yielded a decrease in vertical velocity fluctuations as the free surface was approached. This equation shed further light on the redistribution of the vertical kinetic energy of turbulence into the other two Reynolds normal stresses. The resulting free-surface Reynolds-stress anisotropy in turn gave birth to the two streamwise secondary flows.

Finally, many of the flow phenomena observed here are found to occur in the wakes of surface ships. Indeed, observations by Johnston and Walker[1] (1991) have shown a turbulent layer, which spreads more rapidly in the wake of a ship model. Quantitative measurements of the velocity field and surface deformations in the wakes of surface ships, as well as investigations of the influence of other factors, such as surfactants, ambient waves and currents, and breaking waves and bubble entrainment, on the nature and persistence of the wake signature, are necessary to obtain a better understanding of this complicated problem.

[1] Johnston, V.G. & Walker, D.T. 1991 Experimentally observed features of the turbulent near-wake of a model ship. Univ. of Michigan Tech. report **92-1**.

"Unless you feel it, you will never achieve it.
If it doesn't flow from your soul
With natural easy power,
Your listeners will not believe it ...
How can anyone cling to such trash
Keep any hope in one's head?"
Goethe.

APPENDICES

APPENDIX A: LDV measurements

LDV measurements were made to calibrate the speed controllers' settings and to check the flow uniformity. The experimental setup and methodology are presented in chapter 3. The frequency of each speed controller was varied, and the mean streamwise velocity component was measured. The calibration data are shown in Fig. A.1, along with the calibration curves resulting from linear regression fits.

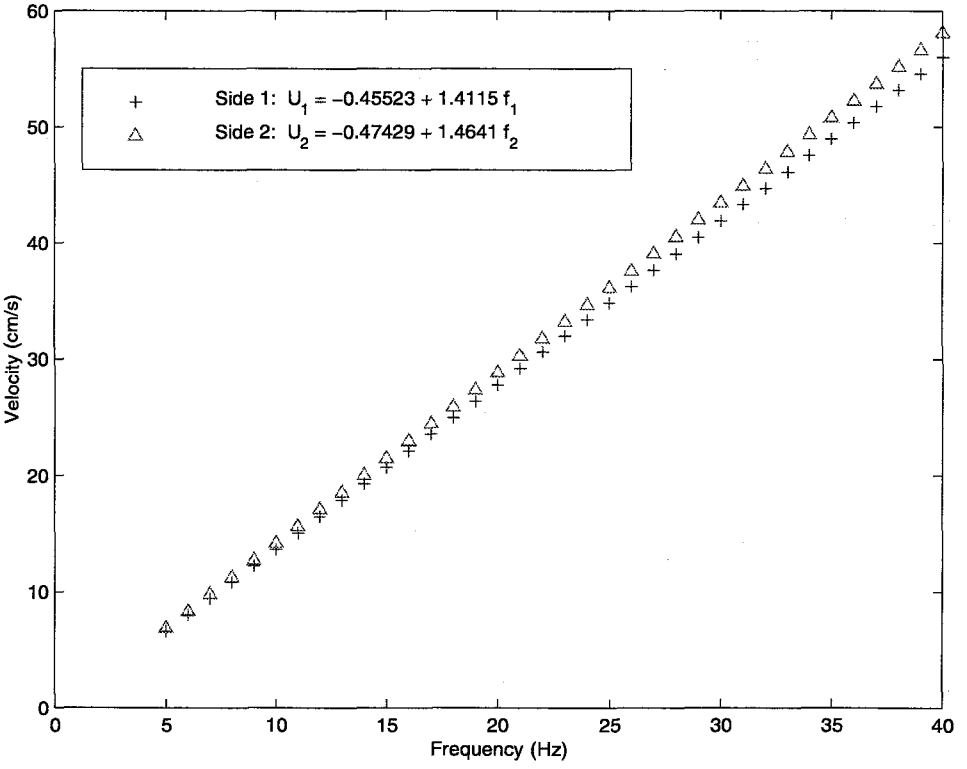

Fig. A.1. Speed calibration of both channels of the watertunnel

No flow is obtained below 5 Hz. Above 40 Hz, strong bath-tube vortices form in the downstream settling chamber causing air entrainment and the appearance of bubbles in the flow. The calibration curves were considered adequate for the experiments conducted in this facility and agree very well with subsequent DPIV measurements.

The measuring volume was then traversed along the length x, the width y and the depth z of both channel flows to probe their uniformity. The next three figures show the variation of the mean streamwise velocity component obtained on both sides at 35 cm/s with respect to y, z and x respectively.

The flow non-uniformity along the channel width was found to be less than 3% outside of the boundary layer (see Fig. A.2). However, this relatively high value does not totally reflect the flow quality since, the dividing plate's tip being tapered, the mean flow progressively inclines by 4.5° until it becomes parallel to the splitter plate.

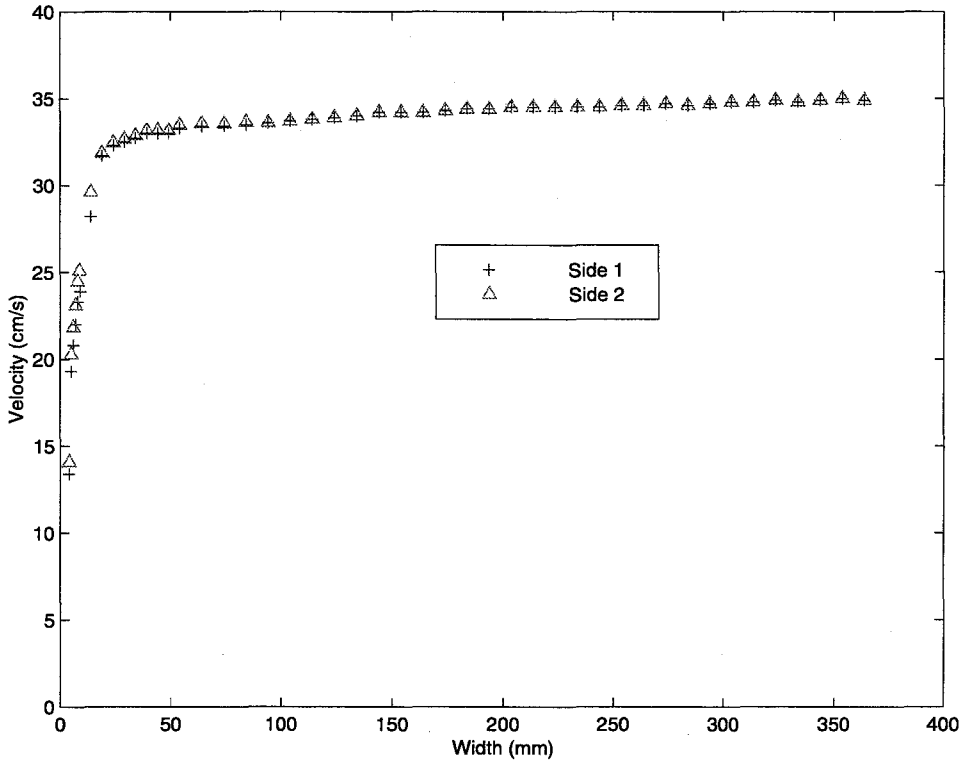

Fig. A.2. Variation of the freestream velocity with the width of the channel

The flow was found to be relatively uniform with the depth. Indeed, the flow non-uniformity along the channel depth was less than 1%, as shown in Fig. A.3.

Finally, the flow non-uniformity along the channel length was found to be less than 2.5% (see Fig. A.4). This value corresponds to the variation of the channel area due to the tapering of the splitter plate.

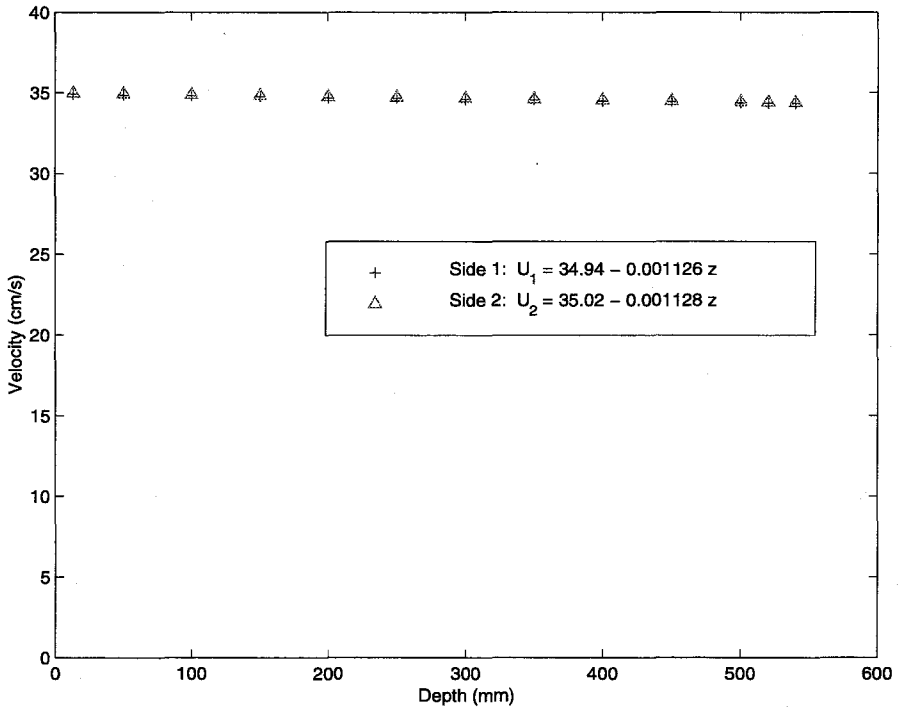

Fig. A.3. Variation of the freestream velocity with the depth of the channel

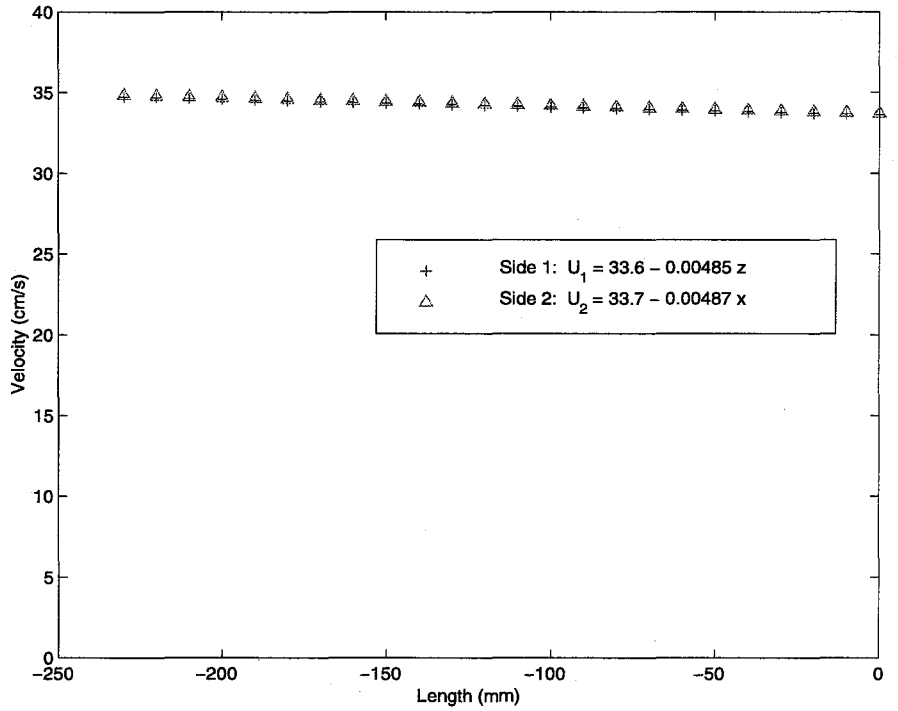

Fig. A.4. Variation of the freestream velocity with the length of the channel

APPENDIX B: Hot-film measurements

Hot-film measurements were made in both streams to measure the freestream turbulence level. The facility and experimental setup are presented in Chapter 3. The aim of these measurements being the quantification of each freestream turbulence level, the hot-film probe was not calibrated and the velocity fluctuations were found in the following manner.

King's law provides a relationship between the mean probe voltage E and the mean flow velocity U :

$$E^2 = A + B\sqrt{U}$$

where A and B are two constants.

At rest $U = 0$, i.e., $E^2 = E_o^2 = A$, thus King's law can be written as

$$E^2 - E_o^2 = B\sqrt{U}\,.$$

Differentiating this equation, we obtain

$$2E\,dE = \frac{B}{2\sqrt{U}}\,dU \;\Rightarrow\; \frac{dU}{U} = 4\frac{E\,dE}{E^2 - E_o^2}\,.$$

With $E = \langle E \rangle + e'$ and $U = \langle U \rangle + u'$, where $dE = e'$ and $dU = u'$, and in the approximation of $e' \ll \langle E \rangle$ and $u' \ll \langle U \rangle$,

an expression of the turbulence level is obtained:

$$T \equiv \frac{\sqrt{\overline{u'^2}}}{\langle U \rangle} = 4\frac{\langle E \rangle}{\langle E \rangle^2 - \langle E_o \rangle^2}\sqrt{\overline{e'^2}}\,.$$

The table presenting the freestream turbulence levels in Chapter 3 was obtained using the above formula.

APPENDIX C: DPIV uncertainty

The overall measurement accuracy in PIV is a combination of a variety of aspects extending from the recording process all the way to the methods of evaluation. In practice, the total measurement error ε_{tot} can be expressed as the sum of a bias error ε_{bias} and a random error or measurement uncertainty, ε_{rms}:

$$\varepsilon_{tot} = \varepsilon_{bias} + \varepsilon_{rms}.$$

Each displacement vector is associated with a certain degree of over or underestimation, hence a bias error ε_{bias}, and some degree of random error $\pm\varepsilon_{rms}$.

(a) Systematic error

The systematic errors comprise all errors which arise due to optical aberrations affecting the image quality, the effects of out-of-plane motions, the inadequacy of the statistical method of cross-correlation in the evaluation of a PIV record ... Only the elements relevant to the present study will be here discussed. For a more complete discussion on this subject, the reader is referred to Huang & Gharib[1,2] (1997, 1998), Royer & Stanislas[3] (1996) and Raffel et al.[4] (1998) to name a few.

(i) optical distortion

The effects caused by lens distortion (e.g., barrel or pillow form distortion) can be compensated by a set of parameters modeling radial and tangential distortion (Brown[5], 1971):

$$x_d + D_x = x_u$$
$$y_d + D_y = y_u$$

[1] Huang, H., Dabiri, D. & Gharib, M. 1997 On errors of digital particle image velocimetry. Meas. Sci. Technol. **8**, 1427-1440.
[2] Huang, H. & Gharib, M. 1998 Errors of DPIV applying to turbulence. In preparation.
[3] Royer, H. & Stanislas, M. 1996 Stereoscopic and holographic approaches to get the third velocity component in PIV. Lectures series **1996-03**, Von Karman Institute for fluid dynamics.
[4] Raffel, M., Willert, C. & Kompenhans, J. 1998 Particle Image Velocimetry: a practical guide. Springer.
[5] Brown, D. 1971 Close-range camera calibration. Photogrametric Eng. **37-8**.

where (x_d, y_d) is the distorted, or real, image and (x_u, y_u) is the undistorted image with

$$D_x = \underbrace{x_d\,(\kappa_1 r^2 + \kappa_2 r^4 + \kappa_3 r^6 + \ldots)}_{\text{radial distortion}} + \underbrace{p_1(r^2 + 2x_d^2) + 2p_2 x_d y_d + \ldots}_{\text{tangential distortion}}$$

$$D_y = \overbrace{y_d\,(\kappa_1 r^2 + \kappa_2 r^4 + \kappa_3 r^6 + \ldots)}^{\text{radial distortion}} + \overbrace{2p_1 x_d y_d + p_2(r^2 + 2y_d^2) + \ldots}^{\text{tangential distortion}}$$

$$\text{where} \quad r = \sqrt{x_d^2 + y_d^2} \ .$$

Although there exist two types of optical distortion, radial and tangential (Born and Wolf[6], 1980), which can both be expressed in terms of infinite series, experience shows that only the first coefficient in the radial distortion series is of importance. Thus, only this first-order coefficient κ_1 needs to be calibrated.

(ii) perspective

1. conventional planar PIV technique

The measured flow quantities are unbiased if we would truly measure the in-plane displacement at each location. However, this not necessarily the case, due to a perspective effect that causes the out-of-plane motion of the tracer particles to contribute to the measured in-plane displacement (Lourenco and Whiffen[7], 1986). The following paragraph describes and quantifies the effects of perspective projection.

To fully explain the influence of a velocity component perpendicular to the light sheet on the location of the image points in the coordinate system x,y,z (Fig. C.1), the imaging through the lens must be taken into account. Ideal imaging is assumed for this calculation. In the (camera-) world coordinate system, the image displacement $\mathbf{d} = \mathbf{x_i'} - \mathbf{x_i}$ corresponding to a certain displacement Δ can be obtained by:

$$x_i' - x_i = -\,M\,(\Delta_x + \Delta_z x_i'/z_0\,)$$
$$y_i' - y_i = -\,M\,(\Delta_y + \Delta_z y_i'/z_0\,)$$

[6] Born, M. & Wolf, E. 1980 Principles of optics. Pergamon press.

[7] Lourenco, L.M. & Whiffen, M.C. 1986 Laser speckle methods in fluid dynamics application. Laser Anem. in fluid mech. **II** (Adrian et al. eds.), Instituto Superior Tecnico, Lisbon, 51-68.

As can be seen from these equations, a particle displacement in the Z-direction influences the particle image displacement, especially for large magnitudes of X_i' and Y_i' at the edges of the observation field. Conventional PIV, which was at the beginning suitable only for measurements of flow fields with weak out-of-plane components, has been adapted also for use in highly three-dimensional flows over the last decade. This effect introduces an uncertainty in measuring the in-plane velocity components, because it cannot be separated from the in-plane components. This uncertainty will turn into a systematic error if it is assumed that PIV determines just the in-plane components particularly for larger viewing angles.

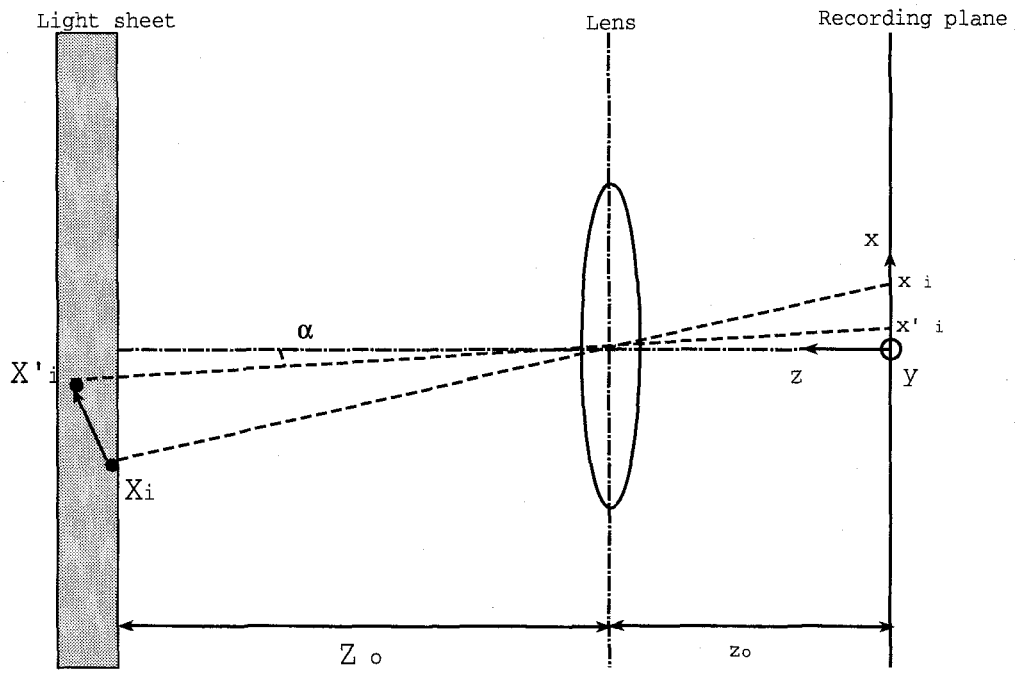

Fig. C.1. Imaging of a particle within the light sheet on the recording plane

2. flow-normal PIV technique

A flow-imaging technique had to be devised for convective flows. Measurements in y-z flow-normal planes had to be performed to probe the spatial extent of the free surface on the underlying turbulent shear flow and thus guide the positioning of the x-y surface-parallel planes in the very near-surface region. The concept of this technique is not new by any means and it has already been applied

successfully in experimental studies particularly in tow-tanks and most recently in a watertunnel[8]. The optical configuration of the digital PIV system allowed for measurements in which the mean flow was normal to the plane of the light sheet, as depicted in Chapter 3. The laser beams were made into individual light sheets using the sheet-generating optical system also presented in Chapter 3. In this case, however, the two sheets were spaced a few millimeters apart. The sheet thickness of the first sheet was about 1mm while that of the second depended on the normal flow field (typically a few millimeters). This was necessary in order that the same particles were imaged in successive frames of each frame pair. However, this setup led to a systematic error as a result of perspective, as shown in Fig. C.2. A particle image was synthetically obtained through numerical simulation, in which randomly distributed particles were generated. This particle image was carefully positioned in each light plane and numerous recordings were made by the CCD sensor. These image sets were then processed using the DPIV software, and the "source-like" velocity field due to this perspective (also called parallax) effect was obtained and subsequently digitally removed.

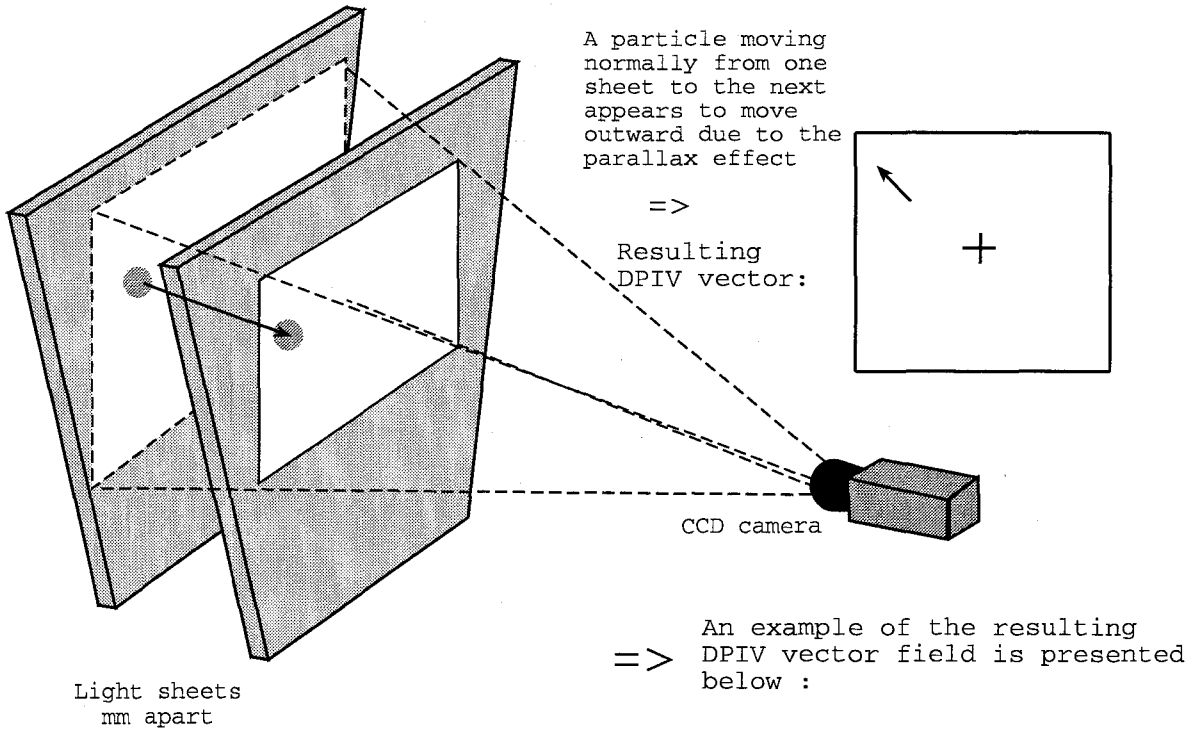

[8] Kuzo, D.M. 1996 An experimental study of the turbulent transverse jet. Ph.D. thesis, California Institute of Technology, Pasadena.

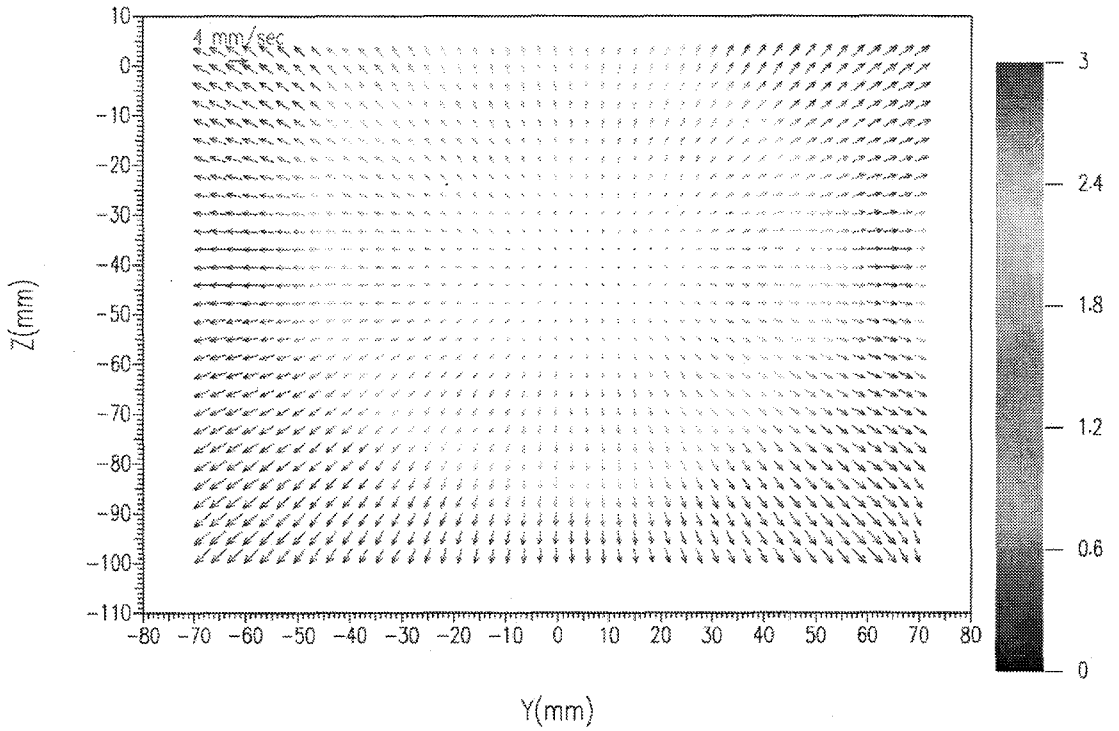

Fig. C.2. Effect of parallax (or perspective) on the particle displacements

(b) Random error

The measurement uncertainty in digital PIV can be assessed in a variety of ways. One approach is to use actual PIV recordings for which the displacement data is known reliably. For instance, PIV recordings obtained of a static (quiescent) flow can be used in determining the measurement accuracy in the cross-correlation evaluation of single exposed particle image pairs. Although this approach is likely to provide the most realistic estimate for the measurement uncertainty, it only permits a limited study of how specific parameters, such as the particle diameter and background noise, influence the measurement precision. An alternative approach taken by a number of researchers is based on numerical simulations. By varying only a single parameter at a time, artificial particle image recordings of known content can be generated, evaluated and compared with the known result.

These measurements were performed by Willert & Gharib[9] (1991) and Huang et al.[1] (1997) for this particular digital PIV system and Westerweel[10] (1993) on a

[9] Willert, C.E. & Gharib, M. 1991 Digital particle image velocimetry. Exp. in Fluids **10**, 181-193.

similar PIV system. Numerical simulations were also made, particularly by Keane & Adrian[11] (1991) using Monte-carlo schemes. Reasonable estimates can be found in these papers. However, real error uncertainties depend on the specific advanced digital interrogation and post-processing techniques as well as the flow itself. In this study, the sampling errors for the RMS velocities and Reynolds stresses were quantified using the power spectra (cf Fig. C.3, Fig. C.4 and Fig. C.5). We may indeed use the signal-to-noise (SNR) values to assess the measurement errors. The SNR ratio is found by dividing the total signal power by the estimated total noise power. The measurement error for the RMS velocities is then estimated as the inverse of the square-root of the SNR of their associated turbulence intensities while the measurement error for the Reynolds stresses is estimated as the inverse of its associated SNR.

The systematic and random errors were estimated for these measurements using the large data sets obtained, and the resulting DPIV uncertainties are presented in the tables of Chapter 3.

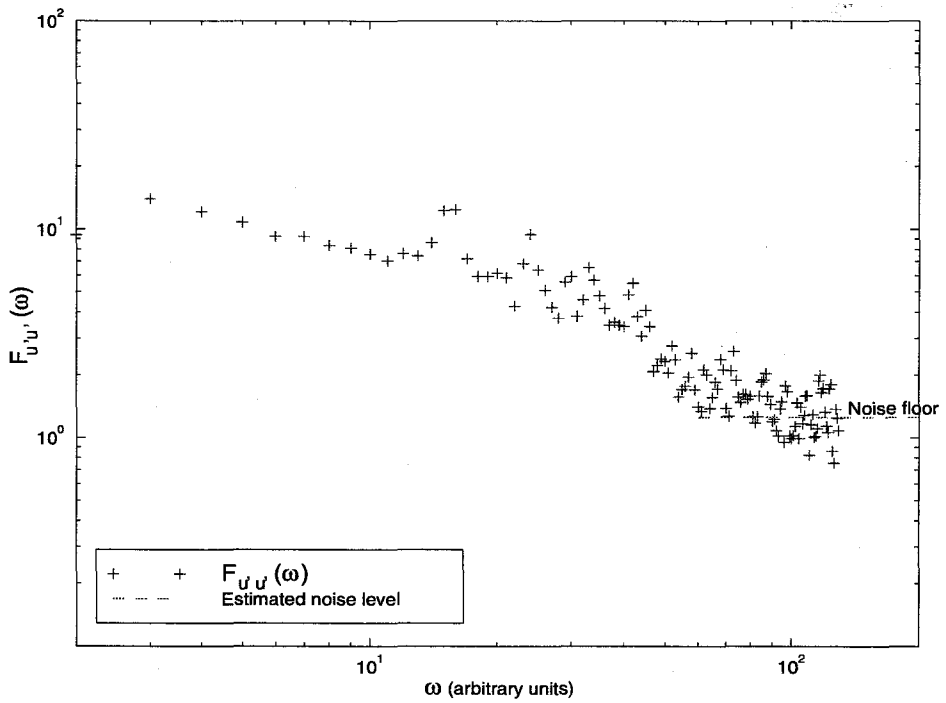

Fig. C.3. Power spectrum of the streamwise fluctuating velocities

[10] Westerweel, J. 1993 Digital Particle Image Velocimetry - Theory and Application. Delft: Delft University Press.

[11] Keane, R.D. & Adrian, R.J. 1991 Optimization of particle image velocimeters. Part II: Multiple-pulsed systems. Meas. Sci. Technol. **2**, 963-974.

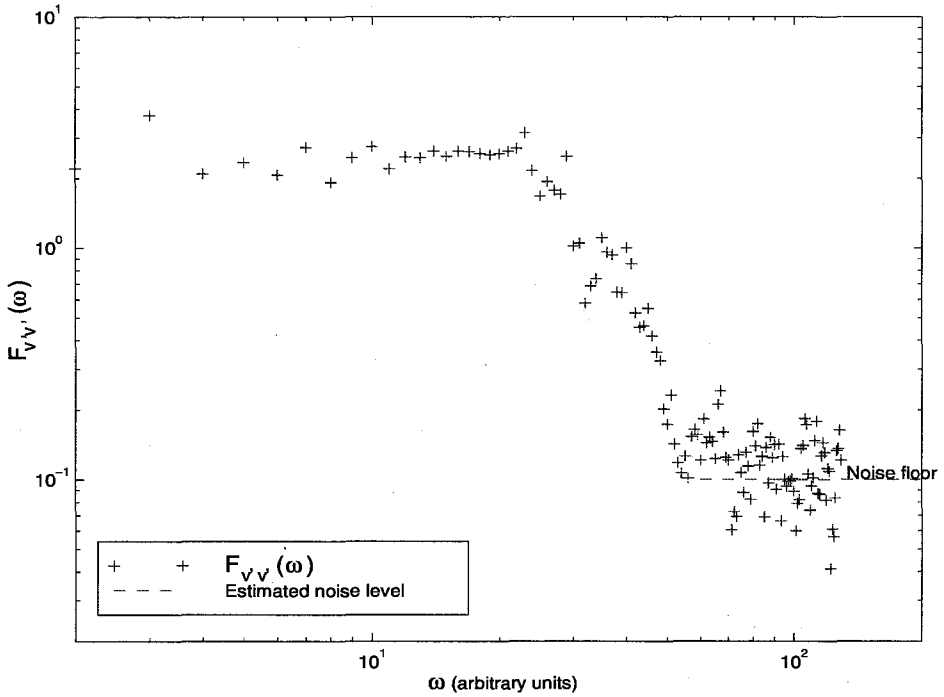

Fig. C.4. Power spectrum of the transverse fluctuating velocities

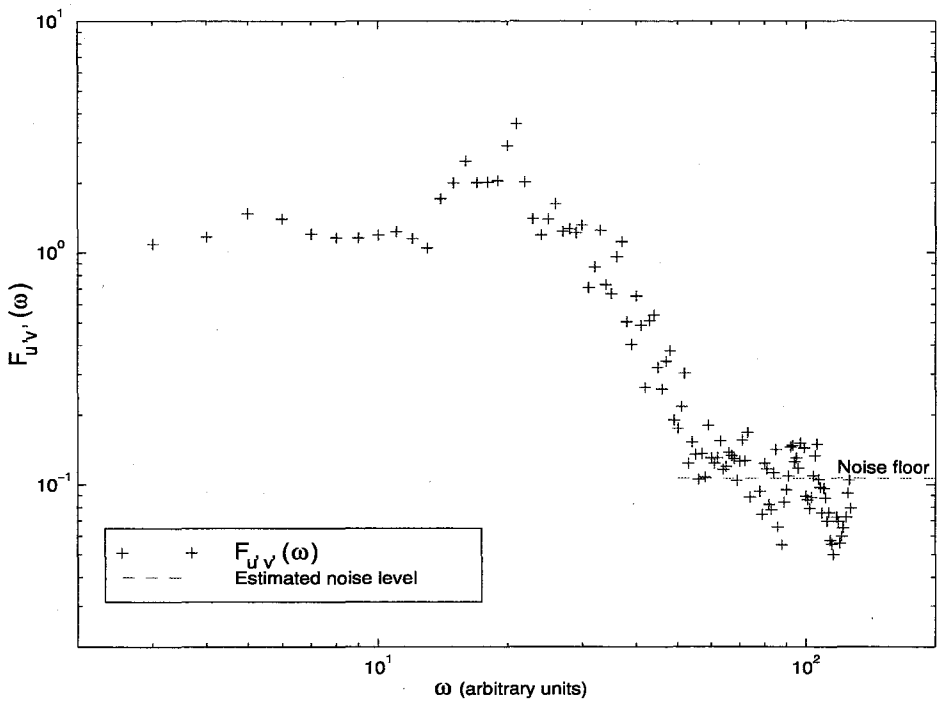

Fig. C.5. Power spectrum of the turbulent Reynolds stresses

"Il est beaucoup plus intéressant de savoir un peu de tout que de tout savoir d'une seule chose."

Blaise Pascal.

REFERENCES

Abramovich, G.N. 1963 The theory of turbulent jets. MIT Press, Cambridge, MA.
Adrian, R.J. 1991 Particle-imaging techniques for experimental fluid mechanics. Ann. Rev. Fluid Mech. **23**, 261-304.
Anthony, D.G. & Willmarth, W.W. 1992 Interaction of a submerged jet with a free surface. J. Fluid Mech. **243**, 699-720.
Bernal, L.P. & Kwon, J.T. 1989 Vortex ring dynamics at a free surface. Phys. Fluids A **1**, 449-451.
Bernal, L.P. & Roshko, A. 1986 Streamwise vortex structure in plane mixing layers. J. Fluid Mech. **170**, 499-525.
Born, M. & Wolf, E. 1980 Principles of optics. Pergamon press.
Bradshaw, P. 1966 The effect of initial conditions on the development of a shear layer. J. Fluid Mech. **26**, 225-236.
Browand, F.K. & Latigo, B.O. 1979 Growth of the two-dimensional mixing layer from a turbulent and a nonturbulent boundary layer. Phys. Fluids **22(6)**.
Brown, D. 1971 Close-range camera calibration. Photogrametric Eng. **37-8**.
Brown, G.L. & Dimotakis, P.E., 1976 The mixing layer at high Reynolds number: Large-structure dynamics and entrainment. J. Fluid Mech. **78**, 535-560.
Brown, G.L. & Roshko, A. 1974 On density effects and large structures in turbulent mixing layers. J. Fluid Mech. **64**, 775-816.
Brumley, B. & Jirka, H. 1987 Near-surface turbulence in a grid stirred tank. J. Fluid Mech. **183**, 235-263.
Chevray, R. & Kovasznay, L.S.G. 1969 Turbulence measurements in the wake of a thin flat plate. AIAA J. **7**, 1641-1643.
Chu, V.H. & Babarutsi, S. 1988 Confinement and bed-friction effects in shallow turbulent mixing layers. J. Hydraulic Eng. **114**, 1257-1274.
Davis, M.R. & Winarto, H. 1980 Jet diffusion from a circular nozzle above a solid wall. J. Fluid Mech. **101**, 201-221.
Dimotakis, P.E. 1993 Some issues on turbulent mixing and turbulence. GALCIT report **FM93-1a**.
Dimotakis, P.E. 1991 Turbulent free shear layer mixing and combustion. Progress in Aeronautics and Aeronautics. Vol **137**, Ed. S.N.B. Murphy and E.T. Curran.
Dommermuth, D.G. 1992 The formation of U-shaped vortices on vortex tubes impinging on a wall with applications to free surfaces. Phys. Fluids A **4**, 757-769.
Elghobashi, S. 1994 On predicting particle-laden turbulent flows. Appl. Sci. Res. **52**, 309-329.
Gessner, F.B. & Jones, J.B. 1965 On some aspects of fully-developed turbulent flow in rectangular channels. J. Fluid Mech. **23**, 689-713.
Gharib, M. 1994 On some aspects of near vortices. In Proc. Twelfth US National Congress of Applied Mechanics, June 1994, Seattle, WA (ed. A.S. Kobayashi), Appl. Mech. Rev. **47**, S157-S162.

Gharib, M. and Weigand, A. 1996 Experimental studies of vortex disconnection and connection at a free surface. J. Fluid Mech. **321**, 59-86.
Grega, L.M., Wei, T., Leighton, R.I. & Neves, J.C. 1995 Turbulent mixed-boundary flow in a corner formed by a solid wall and a free surface. J. Fluid Mech. **294**, 17-46.
Handler, R.A., Swean, T.F. Jr., Leighton, R.I. & Swearingen, J.D. 1993 Length scales and the energy balance for turbulence near a free surface. AIAA J. **31**, 1998-2007.
Ho, C.M. & Huerre, P. 1984 Perturbed free shear layers. Ann. Rev. Fluid Mech. **16**, 365-424.
Hoekstra, M. 1991 Macro wake features of a range of ships. MARIN Rep. 410461-1-P. Maritime Research Institute Netherlands.
Hornung, H. 1988 Vorticity generation and secondary flow. First National Fluid Dyn. Congress. Cincinnati, 566-571.
Huang, H. & Gharib, M. 1997 On errors of digital particle image velocimetry. Meas. Sci. Technol. **8**, 1427-1440.
Huang, H. & Gharib, M. 1998 Errors of DPIV applying to turbulence. In preparation.
Hunt, J. & Graham, J. 1978 Free stream turbulence near plate boundaries. J. Fluid Mech. **84**, 178-209.
Johnston, V.G. & Walker, D.T. 1991 Experimentally observed features of the turbulent near-wake of a model ship. Univ. of Michigan Tech. report **92-1**.
Keane, R.D. & Adrian, R.J. 1991 Optimization of particle image velocimeters. Part II: Multiple-pulsed systems. Meas. Sci. Technol. **2**, 963-974.
Konrad, J.H. 1976 An experimental investigation of mixing in two-dimensional turbulent shear flows with applications to diffusion-limited chemical reactions. Ph.D. thesis, California Institute of Technology, Pasadena.
Kuzo, D. 1996 An experimental study of the turbulent transverse jet. Ph.D. thesis, California Institute of Technology, Pasadena.
Lam, K. & Banerjee, S. 1992 On the conditions of streak formation in a bounded turbulent flow. Phys. Fluids A **4** (2), 306-320.
Launder, B.E. & Rodi, W. 1983 The turbulent wall jet measurements and modelling. Ann. Rev. Fluid Mech. **15**, 429-459.
Liepmann, D. 1990 The near-field dynamics and entrainment field of submerged and near-surface jets. Ph.D. thesis, University of California, San Diego.
Liepmann, D. & Gharib, M. 1994 The vorticity and entrainment dynamics of near-surface jets. Free-surface turbulence ASME 1994, FED-**181**, 53-58.
Logory, L.M., Hirsa, A. & Anthony, D.G. 1996 Interaction of wake turbulence with a free surface. Phys. Fluids **8** (3), 805-815.
Longo, J., Huang, H.P. & Stern, F. 1998 Solid / free-surface juncture boundary layer and wake. Exp. Fluids. **25** (4), 283-297.

Lourenco, L.M. & Whiffen, M.C. 1986 Laser speckle methods in fluid dynamics application. Laser Anem. in fluid mech. **II** (Adrian et al. eds.), Instituto Superior Tecnico, Lisbon, 51-68.

Lugt, H.J. 1987 Local flow properties at a viscous free surface. Phys. Fluids **30**, 3647-3652.

Lugt, H.J. 1988 Fundamental viscous flow properties at a free surface. Fluid Dyn. Trans. **14**, 1-20.

Lundgren, T.S. 1988 A free surface vortex method with weak viscous effects. Proceedings of the Workshop on Mathematical Aspects of Vortex Dynamics, Leesburg, VA, 68-79.

Mangiavacchi, N., Gundlapalli, R. & Akhavan, R. 1994 Dynamics of a turbulent jet interacting with a free surface. Free-surface turbulence ASME 1994, FED-**181**, 69-82.

Mehta, R.D. 1991 Effect of velocity ratio on plane mixing layer development; Influence of the splitter plate wake. Exp. Fluids **10**, 194-204.

Meiburg, E. & Lasheras, J.C. 1988 Experimental and numerical investigation of the three-dimensional transition in plane wakes. J. Fluid Mech. **190**, 1-37.

Milgram, J.H. 1988 Theory of radar backscatter from short waves generated by ships, with application to radar (SAR) imagery. J. Ship Res. **32**, 54-69.

Munk, W.H., Scully-Power, P. & Zachariasen, F. 1987 Ships from space. Proc. R. Soc. Lond. A **412**, 231-254.

Narasimha, R. & Prabhu, A. 1972 Equilibrium and relaxation in turbulent wakes. J. Fluid Mech. **54**, 1-17.

Nezu, I. & Nakagawa, H. 1993 Turbulence in open-channel flows. AIRH monograph. ed. A.A. Balkema.

Ochadlick, A.R. Jr., Cho, P. & Evans-Morgis, J. 1992 Synthetic aperture radar observations of currents colocated with slicks. J. Geophys. Res. **97**, 5325-5330.

Ohring, S. & Lugt, H.J. 1995 Interaction of a viscous vortex pair with a free surface. J. Fluid Mech. **227**, 47-70.

Oster, D. & Wygnanski, I.J. 1982 The forced mixing layer between parallel streams. J. Fluid Mech. **123**, 91-130.

Peltzer, R.D., Griffin, O.M., Barger, W.R. & Kaiser, J.A.C. 1992 High-resolution measurement of surface-active film redistribution in ship wakes. J. Geophys. Res. C **104**, 245-258.

Perkins, H.J. 1970 The formation of streamwise vorticity in turbulent flow. J. Fluid Mech. **44**, 721-740.

Pot, P.J. 1979 Measurements in a 2-D wake and in a 2-D wake merging into a boundary layer. Data report, NLR TR-79063 U, the Netherlands.

Raffel, M., Willert, C. & Kompenhans, J. 1998 Particle Image Velocimetry: a practical guide. ed. Springer.

Ramaprian, B.R., Patel, V.C. & Sastry, M.S. 1982 The symmetric turbulent wake of a flat plate. AIAA J. **20**, 1228-1235.

Reed, A.M., Beck, R.F. Griffin, O.M. & Peltzer, R.D. 1990 Hydrodynamics of remotely sensed surface-ship wakes. Trans. Soc. Naval Archit. Mech. Engrs **98**, 319-363.

Rood, E.P. 1995 Free surface vorticity. In Fluid Vortices, ed. S.I. Green, 687-730. Norwell, MA: Kluwer.

Royer, H. & Stanislas, M. 1996 Stereoscopic and holographic approaches to get the third velocity component in PIV. Lecture series **1996-03**, Von Karman Institute for fluid dynamics.

Sabin, C.M. 1965 An analytical and experimental investigation of the plane, incompressible, turbulent free-shear layer with arbitrary velocity ratio and pressure gradient. Trans. ASME D **87**, 421-428.

Sarpkaya, T. & Henderson, D.O. 1985 Free surface scars and striations due to trailing vortices generated by a submerged lifting surface. AIAA Paper 85-0445.

Schlichting, H. 1979 Boundary-Layer Theory, 7th ed. (reissued 1987) McGraw-Hill.

Scully-Power, P. 1986 Navy oceanographer shuttle observations, Mission report, Rep. STSS 41-G, NUSC Tech. Doc. 7611, Nav. Underwater Syst. Cent., Newport, R.I., March 26, 1986.

Shemdin, O.H. 1987 SAR imaging of ship wakes in the Gulf of Alaska. Final Rep. N00014-84-WRM-2212, Office of Naval Research, Arlinton, VA.

Slessor, M.D. 1998 Aspects of turbulent-shear-layer dynamics and mixing. Ph.D. thesis, California Institute of Technology, Pasadena.

Sreenivasan, K.R. 1981 Approach to self-preservation in plane turbulent wakes. AIAA J.**19**, 1365-1367.

Sreenivasan, K.R. & Narasimha, R. 1982 Equilibrium parameters for two-dimensional turbulent wakes. J. Fluid Eng. **104**, 167-170.

Stern, F., Choi, J.E. & Hwang, W.S. 1993 Effects of waves on the wake of a surface-piercing flat plate: experiment and theory. J. Ship Res. **37**, 102-118.

Swean, T.F. Jr., Ramberg, S.E. & Miner, E.W. 1991 Anisotropy in a turbulent jet near a free surface. J. Fluid Eng. **113**, 430-438.

Townsend, A.A. 1947 Measurements in the turbulent wake of a cylinder. Proc. R. Soc. Lond. A **190**, 551-561.

Townsend, A.A. 1949 The fully developed turbulent wake of a circular cylinder. Austral. J. Sci. Res. **2**, 451-468.

Townsend, A.A. 1956 The structure of turbulent shear flows. Cambridge University Press, Cambridge.

Vesecky, J.F. & Stewart, R.H. 1982 The observation of ocean surface phenomena using imagery from the Seasat synthetic aperture radar: an assessment. J. Geophys. Res. **87** (C5), 3397-3430.

Walker, D.T. & Johnson, V.G. 1991 Observations of turbulence near the free surface in the wake of a model ship. In Dynamics of bubbles and vortices near a free surface (ed. I. Sahin & G. Tryggvason), ASME AMD-**119**.

Walker, D.T., Chen, C.-Y. & Willmarth, W.W. 1995 Turbulent structure in free-surface jet flows. J. Fluid Mech. **291**, 223-261.

Walker, D.T., Leighton, R.I. & Garza-Rios, L.O. 1996 Shear-free turbulence near a flat free surface. J. Fluid Mech. **320**, 19-51.

Walker, D.T. 1997 On the origin of the 'surface currents' in turbulent free-surface flows. J. Fluid Mech. **339**, 275-285.

Warncke, A. 1997 The effects of surfactants on free-surface flows. Ph.D. thesis, California Institute of Technology, Pasadena.

Willert, C.E. & Gharib, M. 1991 Digital particle image velocimetry. Exp. in Fluids **10**, 181-193.

Weigand, A. and Gharib, M. 1995 Turbulent vortex ring/surface interaction. J. Fluid Eng. Trans. ASME **117**, 374-381.

Westerweel, J., Flör, J.B. & Nieuwstadt, F.T.M 1991 Measurement of dynamics of coherent flow structures using particle image velocimetry. Appl. Laser Tech. Fluid Mech. (eds Adrian, R.J. et al.), Berlin: Springer, 476-499.

Westerweel, J. 1993 Digital Particle Image Velocimetry – Theory and Application. Delft: Delft University Press.

Westerweel, J. 1994 Efficient detection of spurious vectors in particle image velocimetry data sets. Exp. Fluids **16**, 236-247.

Westerweel, J., Dabiri, D. & Gharib M. 1997 The effect of a discrete window offset on the accuracy of cross-correlation analysis of digital PIV recordings. Exp. Fluids **23**, 20-28.

Wygnanski, I., Champagne, F. & Marasli, B. 1986 Structures in two-dimensional, small-deficit, turbulent wakes. J. Fluid Mech. **168**, 31-71.

Wygnanski, I.J. & Petersen, R.A. 1987 Coherent motion in excited free shear flows. AIAA **25**, 201-213.

Zhang, C. & Yue, D.P. 1996 On vortex connection at a free surface. Private communication.